Composite Behavior of Geosynthetic Reinforced Soil Mass

PUBLICATION NO. FHWA-HRT-10-077

JULY 2013

U.S. Department of Transportation
Federal Highway Administration

Research, Development, and Technology
Turner-Fairbank Highway Research Center
6300 Georgetown Pike
McLean, VA 22101-2296

FOREWORD

Through the Federal Highway Administration's (FHWA) Every Day Counts initiative, geosynthetic reinforced soil (GRS) was distinguished apart from traditional mechanically stabilized Earth technology. The separation is based on the reinforcement spacing, with GRS referred to as alternating layers of closely spaced (≤ 12 inches (300 mm)) geosynthetic reinforcement and a compacted granular fill material. The close reinforcement spacing increases the soil-geosynthetic interaction, leading to full composite behavior. This study investigated the composite behavior of GRS.

A major finding of this study was a new method to evaluate the required reinforcement strength based on the results of full-scale plane strain testing conducted at FHWA's Turner-Fairbank Highway Research Center. This semi-empirical equation was subsequently selected by FHWA for inclusion in the new internal stability design method presented in the *Geosynthetic Reinforced Soil Integrated Bridge System Interim Implementation Guide*.[1] The methodology and testing that led to this new design equation are presented in this report, along with further documentation regarding the composite behavior of GRS and the new FHWA GRS design method.

Jorge E. Pagán-Ortiz
Director, Office of Infrastructure
Research and Development

TECHNICAL REPORT DOCUMENTATION PAGE

1. Report No. FHWA-HRT-10-077	2. Government Accession No.	3. Recipient's Catalog No.
4. Title and Subtitle Composite Behavior of Geosynthetic Reinforced Soil Mass		5. Report Date July 2013
		6. Performing Organization Code:
7. Author(s) Jonathan T.H. Wu, Thang Q. Pham, and Michael T. Adams		8. Performing Organization Report No.
9. Performing Organization Name and Address Department of Civil Engineering University of Colorado Denver 1200 Larimer Street Denver, CO 80217-3364		10. Work Unit No. 11. Contract or Grant No.
12. Sponsoring Agency Name and Address Office of Infrastructure Research and Development Federal Highway Administration 6300 Georgetown Pike McLean, VA 22101-2296		13. Type of Report and Period Covered 14. Sponsoring Agency Code

15. Supplementary Notes
The FHWA Contracting Officer's Technical Representative (COTR) was Mike Adams, HRDI-40.

16. Abstract
This study investigated the composite behavior of a geosynthetic reinforced soil (GRS) mass. Many studies have been conducted on the behavior of GRS structures; however, the interactive behavior between the soil and geosynthetic reinforcement in a GRS mass has not been fully elucidated. Current design methods consider the reinforcement in a GRS structure as tiebacks and adopt a design concept that the reinforcement strength and reinforcement spacing produce the same effects on the performance of a GRS structure. This has encouraged designers to use stronger reinforcement at a larger spacing to reduce time and effort in construction.

A series of large-size generic soil geosynthetic composite (GSGC) tests were designed and conducted to examine the behavior of a GRS mass under well-controlled conditions. The tests clearly demonstrated that reinforcement spacing has a much stronger impact than reinforcement strength on the performance of the GRS mass. An analytical model was established to describe the relative contribution of reinforcement strength and reinforcement spacing. Based on the analytical model, equations were developed to calculate the apparent cohesion of a GRS composite, the ultimate load-carrying capacity of a GRS mass, and the required tensile strength of reinforcement for a prescribed value of spacing. The equations were verified using measured data from the GSGC tests and measured data from large-size experiments by other researchers, as well as by results of the finite element (FE) method of analysis.

Due to the popularity of GRS walls with modular block facing, an analytical procedure was developed for predicting the walls' lateral movement. This procedure also allows the required tensile strength of the reinforcement to be determined by simple calculations. In addition, compaction-induced stresses, which have usually been ignored in design and analysis of GRS structures, were investigated. An analytical model for estimating compaction-induced stresses in a GRS mass was proposed. Preliminary verification of the model was made by using results from the GSGC tests and FE analysis. The dilative behavior of a GRS composite was also examined. The presence of geosynthetic reinforcement has a tendency to suppress dilation of the surrounding soil and reduce the angle of dilation of the soil mass. The dilative behavior offers a new explanation of the reinforcing mechanism, and the angle of dilation may be used to reflect the degree of reinforcing of a GRS mass.

17. Key Words	18. Distribution Statement
Geosynthetic reinforced soil, GRS, Retaining walls, Analysis, Design, Composite, Compaction	No restrictions. This document is available to the public through the National Technical Information Service, Springfield, VA 22161.

19. Security Classif. (of this report)	20. Security Classif. (of this page)	21. No. of Pages	22. Price
Unclassified	Unclassified	211	

Form DOT F 1700.7 (8-72) Reproduction of completed page authorized

SI* (MODERN METRIC) CONVERSION FACTORS

APPROXIMATE CONVERSIONS TO SI UNITS

Symbol	When You Know	Multiply By	To Find	Symbol
		LENGTH		
in	inches	25.4	millimeters	mm
ft	feet	0.305	meters	m
yd	yards	0.914	meters	m
mi	miles	1.61	kilometers	km
		AREA		
in^2	square inches	645.2	square millimeters	mm^2
ft^2	square feet	0.093	square meters	m^2
yd^2	square yard	0.836	square meters	m^2
ac	acres	0.405	hectares	ha
mi^2	square miles	2.59	square kilometers	km^2
		VOLUME		
fl oz	fluid ounces	29.57	milliliters	mL
gal	gallons	3.785	liters	L
ft^3	cubic feet	0.028	cubic meters	m^3
yd^3	cubic yards	0.765	cubic meters	m^3
	NOTE: volumes greater than 1000 L shall be shown in m^3			
		MASS		
oz	ounces	28.35	grams	g
lb	pounds	0.454	kilograms	kg
T	short tons (2000 lb)	0.907	megagrams (or "metric ton")	Mg (or "t")
		TEMPERATURE (exact degrees)		
°F	Fahrenheit	5 (F-32)/9 or (F-32)/1.8	Celsius	°C
		ILLUMINATION		
fc	foot-candles	10.76	lux	lx
fl	foot-Lamberts	3.426	$candela/m^2$	cd/m^2
		FORCE and PRESSURE or STRESS		
lbf	poundforce	4.45	newtons	N
lbf/in^2	poundforce per square inch	6.89	kilopascals	kPa

APPROXIMATE CONVERSIONS FROM SI UNITS

Symbol	When You Know	Multiply By	To Find	Symbol
		LENGTH		
mm	millimeters	0.039	inches	in
m	meters	3.28	feet	ft
m	meters	1.09	yards	yd
km	kilometers	0.621	miles	mi
		AREA		
mm^2	square millimeters	0.0016	square inches	in^2
m^2	square meters	10.764	square feet	ft^2
m^2	square meters	1.195	square yards	yd^2
ha	hectares	2.47	acres	ac
km^2	square kilometers	0.386	square miles	mi^2
		VOLUME		
mL	milliliters	0.034	fluid ounces	fl oz
L	liters	0.264	gallons	gal
m^3	cubic meters	35.314	cubic feet	ft^3
m^3	cubic meters	1.307	cubic yards	yd^3
		MASS		
g	grams	0.035	ounces	oz
kg	kilograms	2.202	pounds	lb
Mg (or "t")	megagrams (or "metric ton")	1.103	short tons (2000 lb)	T
		TEMPERATURE (exact degrees)		
°C	Celsius	1.8C+32	Fahrenheit	°F
		ILLUMINATION		
lx	lux	0.0929	foot-candles	fc
cd/m^2	$candela/m^2$	0.2919	foot-Lamberts	fl
		FORCE and PRESSURE or STRESS		
N	newtons	0.225	poundforce	lbf
kPa	kilopascals	0.145	poundforce per square inch	lbf/in^2

*SI is the symbol for the International System of Units. Appropriate rounding should be made to comply with Section 4 of ASTM E380.
(Revised March 2003)

TABLE OF CONTENTS

LIST OF FIGURES

LIST OF TABLES

CHAPTER 1. INTRODUCTION

1.1 PROBLEM STATEMENT

Over the past two decades, geosynthetic reinforced soil (GRS) structures, including retaining walls, slopes, embankments, roadways, and load-bearing foundations, have gained increasing popularity in the United States and abroad. In construction, GRS structures have demonstrated several distinct advantages over their conventional counterparts. Generally, GRS structures require less over-excavation and are more ductile, more flexible (hence more tolerant to differential settlement and to seismic loading), more adaptable to low-permeability backfill, easier to construct, and more economical than conventional Earth structures.[2–4]

Among the various types of GRS structures, GRS walls have seen far more applications than other types of reinforced soil structures. A GRS wall comprises two major components: a facing element and a GRS mass. Figure 1 shows a schematic diagram of a typical GRS wall with a modular block facing.

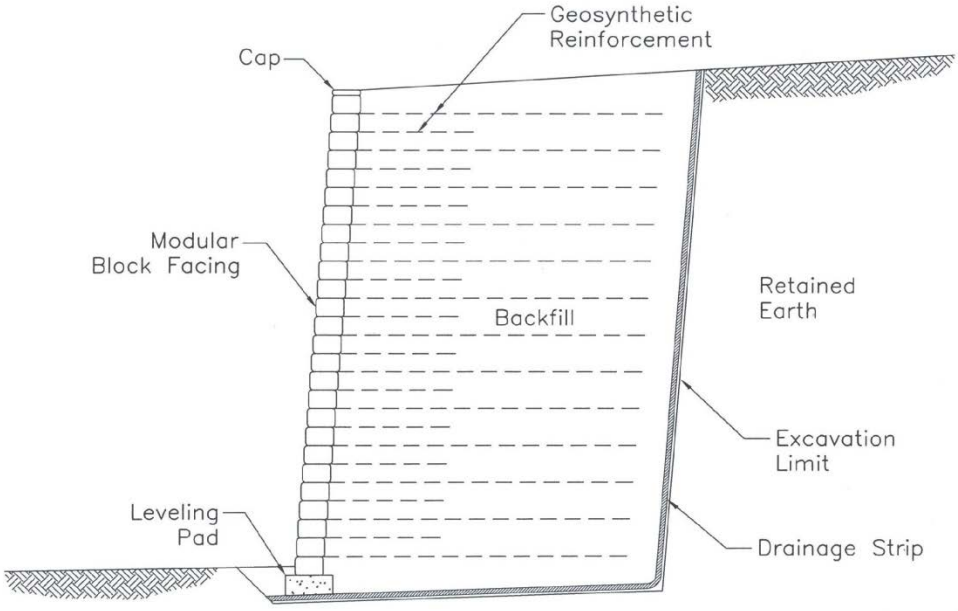

Figure 1. Illustration. Typical cross section of a GRS wall with modular block facing.

The GRS wall facing may be of various shapes and sizes. It may also be made of different materials. However, the other component of a GRS wall, the GRS mass, is always a compacted soil mass reinforced by layers of geosynthetic reinforcement.

Soil is weak in tension and relatively strong in compression and shear. In a reinforced soil, the soil mass is reinforced by incorporating an inclusion (or reinforcement) that is strong in tensile resistance. Through soil reinforcement interface bonding, the reinforcement restrains lateral deformation of the surrounding soil, increases its confinement, reduces its tendency for dilation, and, consequently increases the stiffness and strength of the soil mass.

Many studies have been conducted on the behavior of GRS structures; however, the interactive behavior between soil and reinforcement in a GRS mass has not been fully elucidated. This has resulted in design methods that are fundamentally deficient.[5] Perhaps the most serious deficiency is that the current methods ignore the composite nature of the GRS mass and consider the reinforcement as tiebacks added to the soil mass. The reinforcement strength is determined by requiring that the reinforcement be sufficiently strong to resist Rankine, Coulomb, or at-rest pressure that is assumed not to be affected by the configuration of the reinforcement. Specifically, the design strength of the reinforcement, $T_{required}$, has been determined by multiplying an assumed lateral Earth pressure at a given depth, σ_h, by the value of reinforcement spacing, S_v, and a safety factor, F_s, as shown by the equation in figure 2.

$$T_{required} = \sigma_h * S_v * F_s$$

Figure 2. Equation. Design strength.

Figure 2 implies that as long as the reinforcement strength is kept linearly proportional to the reinforcement spacing, all walls with the same σ_h (walls of a given height with the same backfill compacted to the same density) will behave the same. In other words, a GRS wall with reinforcement strength T at spacing S_v will behave the same as one with twice the reinforcement strength ($2 \times T$) at twice the spacing ($2 \times S_v$). Figure 2 has important practical significance in that it has encouraged designers to use stronger reinforcement at larger spacing because the use of larger spacing will generally reduce construction time and effort.

Some engineers, however, have learned that figure 2 cannot be true. In actual construction, reinforcement spacing appears to play a much greater role than reinforcement strength in the performance of a GRS wall. Researchers at the Turner-Fairbank Highway Research Center (TFHRC) conducted a series of full-scale experiments in which a weak reinforcement at a small spacing and a strong reinforcement (with several times the strength of the weak reinforcement) at twice the spacing were load-tested.[6,7] The former was found to be much stronger than the latter. An indepth study on the relationship between reinforcement spacing and reinforcement stiffness/ strength in regards to their effects on the behavior of a GRS mass is of critical importance to the design of GRS structures.

The effects of compaction-induced stress (CIS) in unreinforced soil masses and Earth structures have been the subject of many studies. (See references 8–14.) These studies indicated that CIS would significantly increase the lateral stresses in soil (also known as the locked-in lateral stresses or residual lateral stresses) provided that there is sufficient constraint to lateral movement of the soil during compaction. The increase in lateral stresses will increase the stiffness and strength of the compacted soil mass.

The effect of CIS is likely to be more significant in a soil mass reinforced with layers of geosynthetics than in an unreinforced soil mass. This is because the interface bonding between the soil and reinforcement will increase the degree of restraint to lateral movement of the soil mass during fill compaction. With greater restraint to lateral movement, the resulting locked-in lateral stresses are likely to become larger.

In most studies, the effects of CIS in numerical analysis of Earth structures have been either overly simplified or ignored. (See references 15–18.) In the case of GRS walls, failure to account

for CIS may have led to the erroneous conclusion by many numerical studies that the equation in figure 2 is completely or approximately valid. Evaluation of CIS is an important issue in the study of GRS structures.

In addition, GRS walls with modular block facing are rather flexible. Thus, the design of these structures should consider not only the stresses in the GRS mass but also the deformation. The Jewell-Milligan method is recognized as the best available method for estimating lateral movement of GRS walls.[19] However, it only applies to walls with little or no facing rigidity. With the increasing popularity of GRS walls with modular block facing where facing rigidity should not be ignored, an improvement over the Jewell-Milligan method for calculating lateral wall movement is needed.

1.2 RESEARCH OBJECTIVES

The objectives of this study were fourfold. The first objective was to investigate the composite behavior of GRS masses with different reinforcing configurations. The second objective was to examine the relationship between reinforcement strength and reinforcement spacing with regard to their effects on the behavior of a GRS mass. The third objective was to develop an analytical model for evaluating CIS in a GRS mass. The fourth objective was to develop an analytical model for predicting lateral movement of a GRS wall with a modular block facing.

1.3 RESEARCH TASKS

To achieve the research objectives, the following tasks were carried out in this study:

1. **Reviewed previous studies on the composite behavior of a GRS mass, CIS in a soil mass, and the reinforcing mechanism of GRS structures.** Previous studies on composite behavior of a GRS mass were reviewed. The review included theoretical analyses as well as experimental tests. Studies on CIS in an unreinforced soil mass were also reviewed, including simulation models for fill compaction. In addition, a literature study on reinforcing mechanisms of GRS structures was conducted.

2. **Developed a hand computation analytical model for estimation of CIS in a GRS mass.** An analytical model for simulation of CIS in a GRS mass was developed. The compaction model was developed by modifying an existing fill compaction simulation model for unreinforced soil. The model allows CIS in a GRS mass to be estimated by hand computations.

3. **Developed an analytical model for the relationship between reinforcement strength and reinforcement spacing and derived an equation for calculating composite strength properties.** An analytical model for describing the relationship between reinforcement strength and reinforcement spacing was developed. Based on the model and the average stress concept for a GRS mass, an equation for calculating the composite strength properties of a GRS mass was derived.[20] The model represents a major improvement over the existing current design methods used and more precisely reflects the role of reinforcement spacing versus reinforcement strength on the performance of a GRS mass. The equation allows the strength properties of a GRS mass to be evaluated by a simple hand computation method.

4. **Designed and conducted laboratory experiments on a generic soil geosynthetic composite (GSGC) to investigate the performance of GRS masses with different reinforcing conditions.** A GSGC plane-strain test was designed by considering several factors culled from previous studies. A series of finite element (FE) analyses were performed to determine the dimensions of the test specimen that would yield stress-strain and volume change behavior representative of a very large GSGC mass. Five GSGC tests with different reinforcement strengths, reinforcement spacing, and confining pressures were conducted. These tests allowed direct observation of the composite behavior of a GRS mass in various reinforcing conditions. They also provided measured data for verification of analytical and numerical models for investigating the behavior of a GRS mass (including the models developed in tasks 2 and 3).

5. **Performed FE analyses to simulate the GSGC tests and analyze the behavior of the GRS mass.** FE analyses were performed to simulate the GSGC tests conducted in task 4. The analyses allowed the stresses in the soil and forces in the reinforcement to be determined. They also allowed an investigation of the behavior of GRS composites under conditions different from those employed in the GSGC tests of task 4.

6. **Verified the analytical models developed in tasks 2 and 3 by using the measured data from the GSGC tests and relevant test data in the literature.** The compaction model developed in task 2 was employed to determine the CIS for the GSGC tests. The results were incorporated into an FE analysis to calculate the global stress-strain relationship and then compared to the measured results. The measured data from the GSGC tests, relevant test data available in the literature, and results from FE analyses were also used to verify the analytical models developed in task 3 for calculating composite strength properties of a GRS mass and for calculating required tensile strength of reinforcement based on the forces induced in the reinforcement.

7. **Developed an analytical model for predicting lateral movement of GRS walls with modular block facing.** An analytical model was developed for predicting the lateral movement of GRS walls with a modular block facing. The model was based on an existing model for reinforced soil walls without a modular block facing.[19] The results obtained from the model were compared with measured data from a full-scale experiment of a GRS wall with modular block facing. The analytical model can also be used in design for determining the required design strength of reinforcement under a prescribed value of maximum allowable lateral wall movement.

CHAPTER 2. LITERATURE REVIEW

A GRS mass is a soil mass that is embedded with layers of geosynthetic reinforcement. These layers are typically placed horizontally with a vertical spacing of 8 to 12 inches (200 to 300 mm). Under vertical loads, a GRS mass exhibits significantly higher stiffness and strength than an unreinforced soil mass. This chapter presents a review of previous studies on the mechanics of reinforced soil, the composite behavior of a GRS mass, and CIS in a reinforced soil mass.

2.1 MECHANICS OF REINFORCED SOIL

In literature, three concepts have been proposed to explain the mechanical behavior of a GRS mass: (1) the concept of enhanced confining pressure, (2) the concept of enhanced material properties, and (3) the concept of reduced normal strains. (See references 21–32.)

The mechanics of a GRS mass have been explained by Schlosser and Long and Yang using two concepts: the concept of apparent cohesion and the concept of apparent confining pressure.[25,21]

2.1.1 Concept of Apparent Cohesion

In this concept, a reinforced soil is said to increase the major principle stress at failure from σ_1 to σ_{1R} (with an apparent cohesion C'_R) due to the presence of the reinforcement, as shown by the Mohr stress diagram in figure 3. If a series of triaxial tests on unreinforced and reinforced soil elements were conducted, the failure envelopes of the unreinforced and reinforced soils would allow the apparent cohesion C'_R to be determined. Yang indicated that the ϕ value for unreinforced sand and reinforced sand were about the same as long as slippage at the soil-reinforcement interface did not occur.[21]

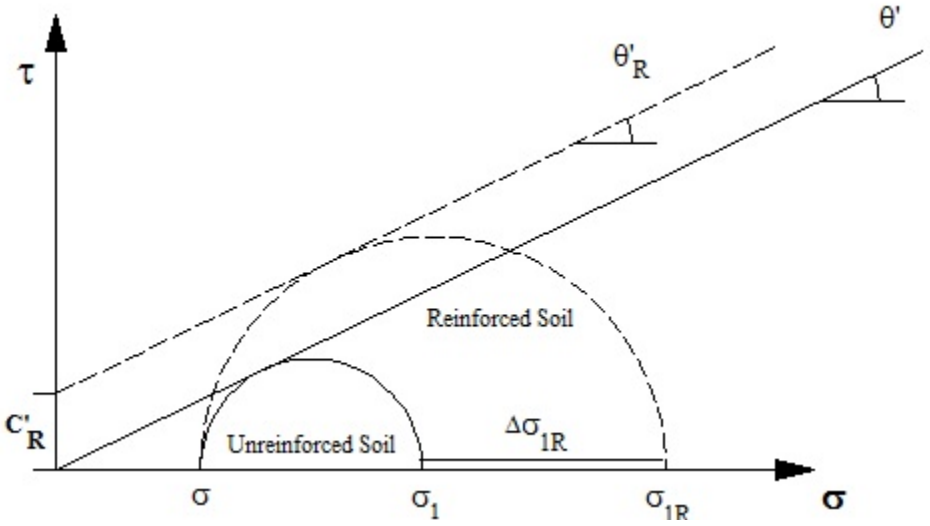

Figure 3. Illustration. Concept of apparent cohesion due to the presence of reinforcement.

2.1.2 Concept of Apparent Confining Pressure

In this concept, a reinforced soil is said to increase its axial strength from σ_1 to σ_{1R} (with an increase of confining pressure, $\Delta\sigma_{3R}$), as shown in figure 4, due to the tensile inclusion. The value of $\Delta\sigma_{3R}$ can also be determined from a series of triaxial tests by assuming that ϕ will remain the same.

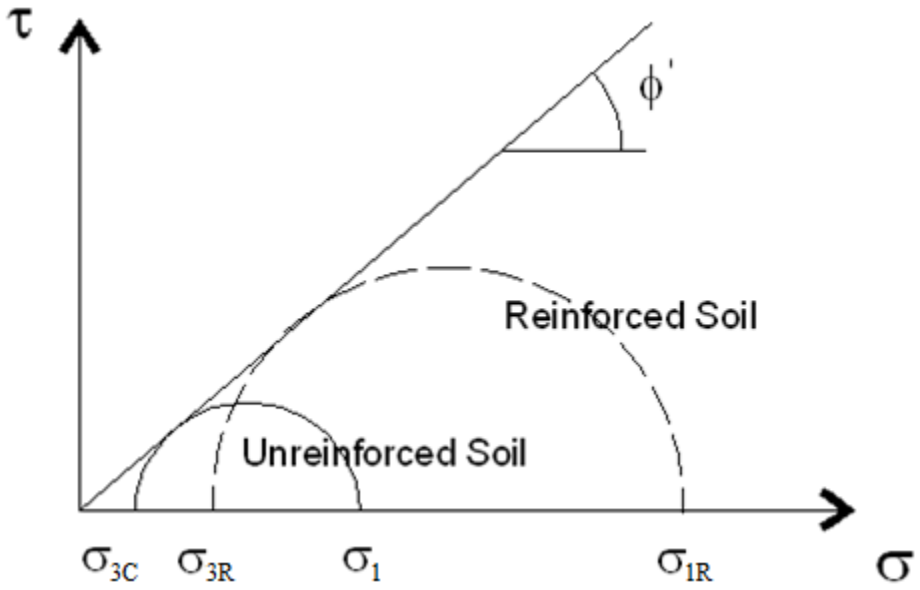

Figure 4. Illustration. Concept of apparent confining pressure due to the presence of reinforcement.

Note that the concept of apparent confining pressure allows the apparent cohesion to be determined with only the strength data for the unreinforced soil, as shown in figure 5 through figure 13.[25]

Consider a GRS mass with equally spaced reinforcement of strength T_f and vertical spacing S_v. It is assumed that the increase in confining pressure due to the tensile inclusion, $\Delta\sigma_{3R}$, can be calculated using the equation in figure 5.

$$\Delta\sigma_{3R} = \frac{T_f}{S_v}$$

Figure 5. Equation. Increase in confining pressure as a function of reinforcement strength and spacing.

From figure 3 and figure 4 and using Rankine's Earth pressure theory to equate the principal stress at failure, σ_{1R} can be calculated using figure 6.

$$\sigma_{1R} = \sigma_{3C} K_P + 2c_R' \sqrt{K_P}$$

Figure 6. Equation. Principle stress at failure for reinforced soil.

$$\sigma_{1R} = \sigma_{3R} K_P$$

Figure 7. Equation. Principle stress at failure for reinforced soil with zero cohesion.

$$\sigma_{3R} = \sigma_{3C} + \Delta\sigma_{3R}$$

Figure 8. Equation. Total confining stress of reinforced soil.

Using figure 8, figure 7 can be written as figure 9.

$$\sigma_{1R} = \sigma_{3R} K_P = (\sigma_{3C} + \Delta\sigma_{3R}) K_P$$

Figure 9. Equation. Principle stress at failure for reinforced soil substituting the components derived in figure 8.

Equating figure 6 to figure 9, figure 10 is obtained.

$$c'_R = \frac{\Delta\sigma_{3R}\sqrt{K_P}}{2}$$

Figure 10. Equation. Apparent cohesion for reinforced soil in terms of increase in confining stress.

Substituting figure 5 into figure 10 results in figure 11.

$$c'_R = \frac{T_f\sqrt{K_P}}{2S_v}$$

Figure 11. Equation. Apparent cohesion in terms of reinforcement strength and spacing.

Figure 11 may be useful for evaluating the stability of a reinforced soil mass. Given a granular soil with strength parameters c ($c = 0$) and ϕ, figure 11 allows the strength parameters of a reinforced soil mass (c'_R and ϕ_R) to be determined as a function of T and S_v.

It should be noted that the validity of figure 11 is questionable. There is a key assumption involved in the derivation—the assumption of figure 5, which implies that an increase in T_f has the same effect as a proportional decrease in S_v.

Note that figure 12 represents the increase in confining pressure based on the explanation given by Schlosser and Long and Yang (see figure 4), while figure 13 represents the same increase in Hausmann's study, where $R_T \equiv T_f$.[22,25,26]

$$\Delta\sigma_3 = \frac{R_T}{S_v}$$

Figure 12. Equation. Increase of confining pressure due to reinforcement.

$$\Delta\sigma_3 \leq \frac{R_T}{S_v}$$

Figure 13. Equation. Increase of confining pressure by Hausmann.[26]

2.2 COMPOSITE BEHAVIOR OF GRS MASS

The behavior of GSGC has been investigated through different types of laboratory experiments including small-size (1.9-inch (50-mm)-diameter) triaxial compression tests with a specimen diameter no greater than 6 inches (150 mm), large-size (19-inch (500-mm)-diameter) triaxial compression tests, large-size (30-inch (760-mm)-diameter) unconfined compression tests, unconfined compression tests with cubical specimens, and plane-strain tests. (See references 6, 7, 20, 31, and 33–35.)

The effects of reinforcement layers on the stiffness and strength of GSGCs has been investigated, and the results suggest that unless the reinforcement is placed at locations where lateral deformation of the soil occurs, there will not be any reinforcing effect.[33]

There are questions concerning the applicability of these small-size triaxial tests because the reinforcement in these tests is very small compared to the typical field installation, and factors such as gravity, soil arching, and CIS are not simulated properly. For these reasons, several larger triaxial tests and plane-strain tests have been conducted. Elton and Patawaran conducted seven unconfined compression tests on 2.5-ft (0.76-m)-diameter and 5-ft (1.53-m)-high specimens with different types of reinforcement and spacing (see figure 14 and figure 15).[31] Six types of reinforcement were used in the tests with spacing of 6 and 12 inches (150 and 300 mm). Figure 16 shows the stress-strain curves of the specimens reinforced by Tensar® TG500 at spacings of 6 and 12 inches (150 and 300 mm). As shown in the figure, the strength of the GSGC was much higher at the 6-inch (150-mm) spacing than at the 12-inch (300-mm) spacing.

Figure 14. Photo. Unconfined test specimen before testing.[31]

Figure 15. Photo. Unconfined test specimen after testing.[31]

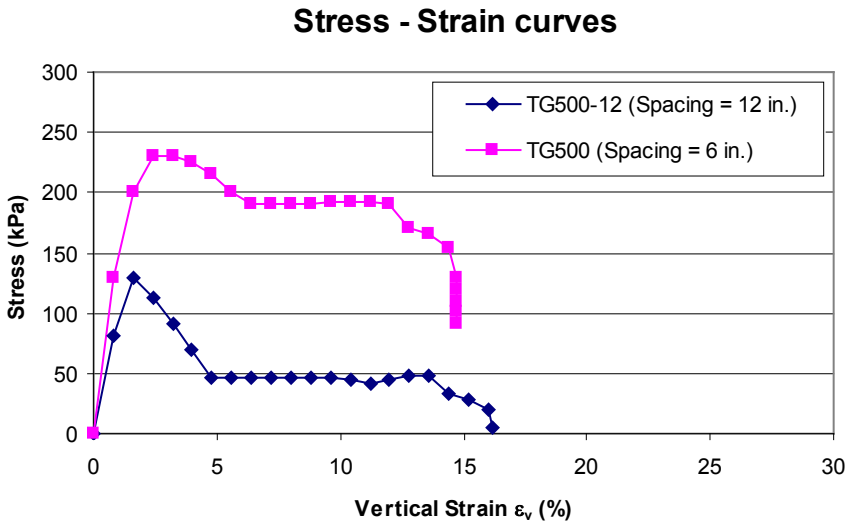

1 kPa = 0.145 psi
1 mm = 0.039 inches

Figure 16. Graph. Stress-strain curves of specimens reinforced at spacings of 6 and 12 inches (150 and 300 mm) in large, unconfined compression test.[31]

Five unconfined mini-pier experiments were conducted by Adams and his associates.[6,7] The dimensions of the specimen were 6.6 ft (2.0 m) high, 3.3 ft (1.0 m) wide, and 3.3 ft (1.0 m) deep. The test results showed that the load-carrying capacity was strongly affected by the spacing of the reinforcement and was not significantly affected by the strength of the reinforcement. Figure 17 shows a photo of the mini-pier experiment, and table 1 shows the material properties and conditions for the tests. The stress-strain curves from the tests are presented in figure 18. The effect of reinforcement spacing and reinforcement strength on the behavior of the mini-piers can be seen in the figure by comparing the difference between curve B (at 1.3-ft (0.4-m) spacing) and curve D (at 0.7-ft (0.2-m) spacing) and the difference between curve C (reinforcement

strength = 1.4 kip/ft (21 kN/m)) and curve D (reinforcement strength = 4.8 kip/ft (70 kN/m)). The effect of reinforcement spacing is much more pronounced than the effect of reinforcement strength.

Figure 17. Photo. Mini-pier experiments.[6]

Table 1. Properties of materials for the mini-pier experiments.[7]

Experiment	Fill Average Density (kN/m^3)	Geotextile Reinforcement Schedule		
		Polypropylene Type	Strength (kN/m)	Spacing (m)
MP NR	22.4	None	None	None
MP A	23.0	A2044	70.0	0.4–0.6
MP B	22.7	A2044	70.0	0.4
MP C	N/A	A2000	21.0	0.2
MP D	22.8	A2044	70.0	0.2
MP NR	22.4	None	None	None

MP = Mini-pier and NR = Not reinforced.
1 kN/m^3 = 0.0064 kip/ft^3
1 m = 3.28 ft
N/A = Not available.

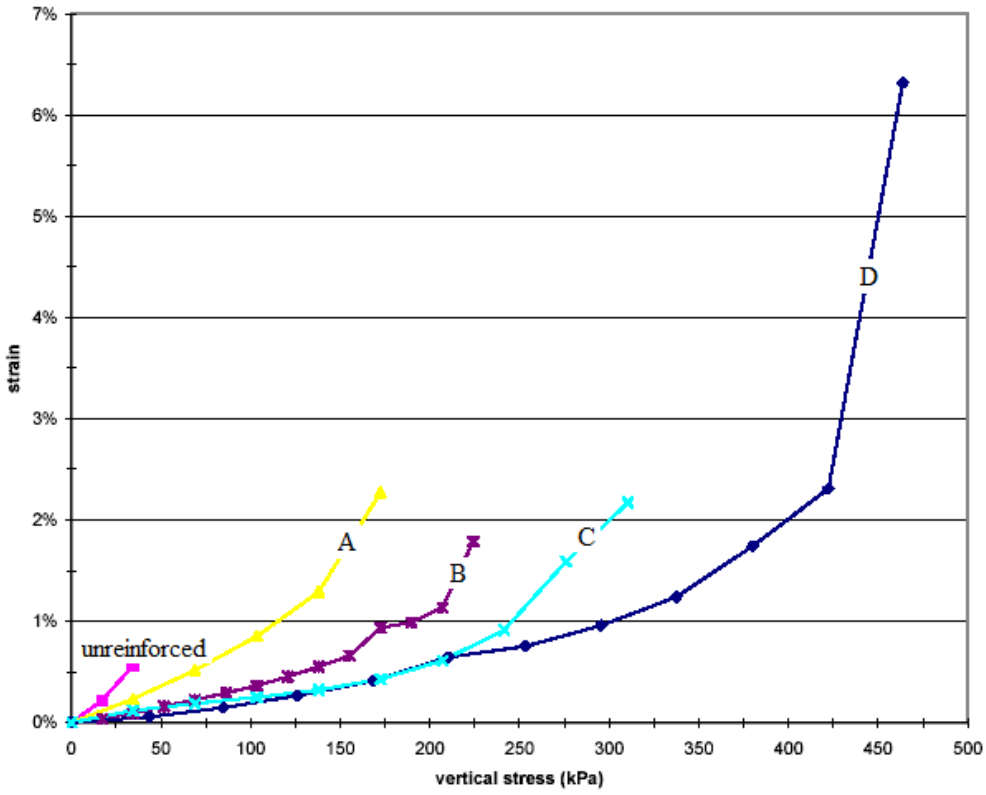

1 kPa = 0.145 psi

Figure 18. Graph. Stress-strain curves of mini-pier experiments.[7]

Figure 19 and figure 20 show the setup of the large-size triaxial tests conducted by Ziegler et al.[35] The specimens were 1.6 ft (0.5 m) in diameter and 3.6 ft (1.1 m) high. The results also show the behavior of the GRS specimens was strongly affected by reinforcement spacing. Figure 21 shows the relationship between the applied loads and vertical strains of the test specimens. The strength of the specimen increased with an increasing number of reinforcement layers. The stiffness of the specimen also increased with an increasing number of reinforcement layers for strains of more than about 1 percent. Below 1 percent, the stiffness was not affected by the reinforcement layers.

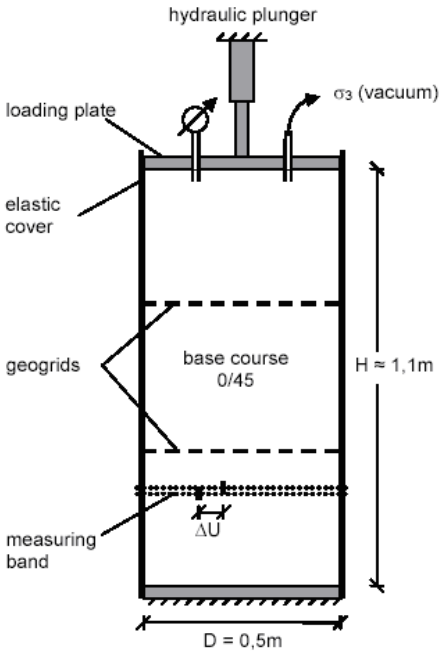

1 m = 3.28 ft

Figure 19. Illustration. Schematic of large-size triaxial tests with specimens 3.6 ft (1.1 m) high and 1.6 ft (0.5 m) in diameter.[(35)]

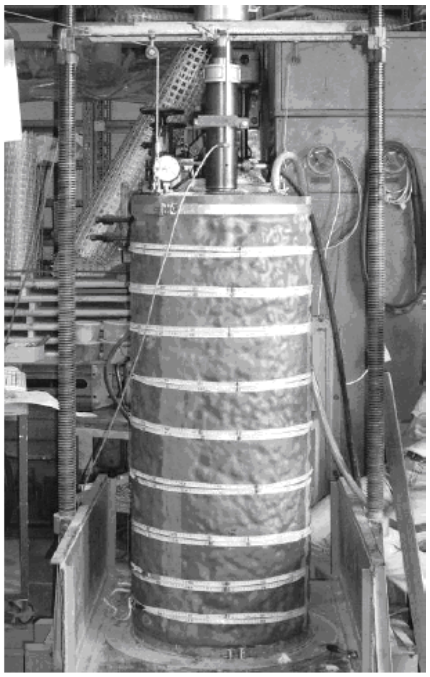

Figure 20. Photo. Setup of large-size triaxial tests with specimens 3.6 ft (1.1 m) high and 1.6 ft (0.5 m) in diameter.[(35)]

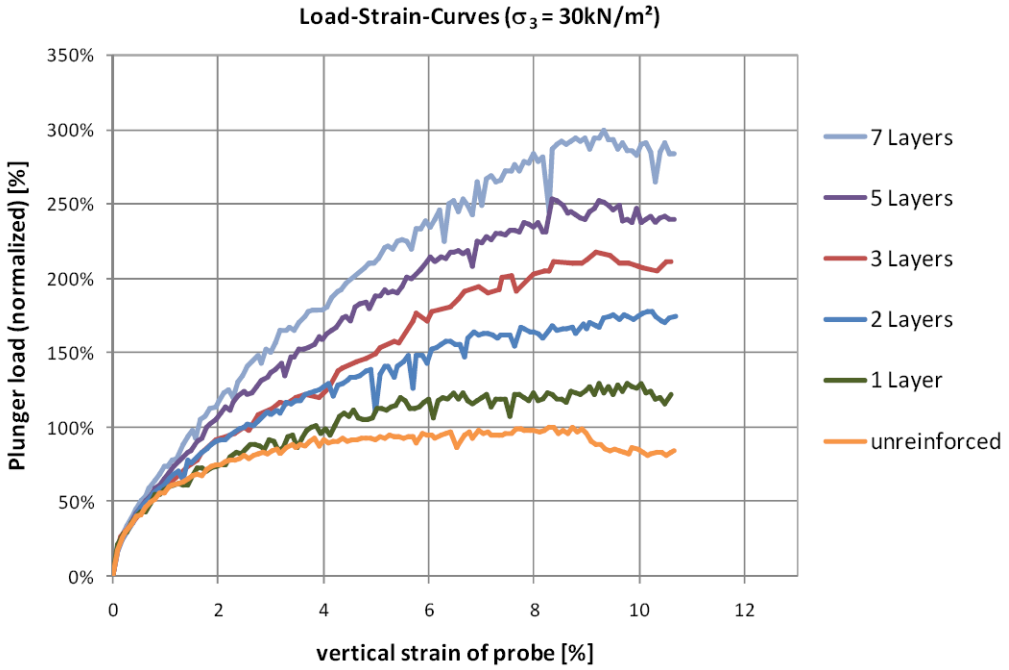

1 kN/m^2 = 0.021 kip/ft^2

Figure 21. Graph. Large-size triaxial test results.[35]

The behavior of GSGCs has also been investigated through numerical analysis. (See references 20 and 36–40.)

Vulova and Leshchinsky conducted a series of analyses using the two-dimensional (2D) finite difference program Fast Lagrangian Analysis of Continua (FLAC) Version 3.40.[40,41] From the analyses, it was concluded that reinforcement spacing was a major factor controlling the behavior of GRS walls. The analysis of GRS walls with reinforcement spacing from 0.7 to 3.3 ft (0.2 to 1.0 m) showed that the critical wall height (defined as a general characteristic of wall stability) always increased when reinforcement spacing decreased. Reinforcement spacing also controlled the mode of failure of GRS walls. In these analyses, CIS in soil was not included.

Comparisons of the stress distribution in a soil mass with and without reinforcement were made by Ketchart and Wu.[20] The reinforcement was a medium-strength woven geotextile with wide-width strength of 4.8 kip/ft (70 kN/m). The backfill was a compacted road base material, and the reinforcement spacing was 1 ft (0.3 m). Figure 22, figure 23, and figure 24 show the vertical, horizontal, and shear stress distributions, respectively, at a vertical load of 1.3 kip (6 kN). The presence of the reinforcement layers in the soil mass altered the horizontal and shear stress distributions but not the vertical stress distribution. The horizontal and shear stresses increased significantly near the reinforcement. The largest stresses occurred near the reinforcement and reduced with increasing distance from the reinforcement. The extent of appreciable influence was only about 0.33–0.49 ft (0.1–0.15 m) from the reinforcement. With the increased lateral stress, the stiffness and strength of the soil became larger. Ketchart and Wu emphasized the importance of keeping reinforcement spacing less than 1 ft (0.3 m) for GRS walls.

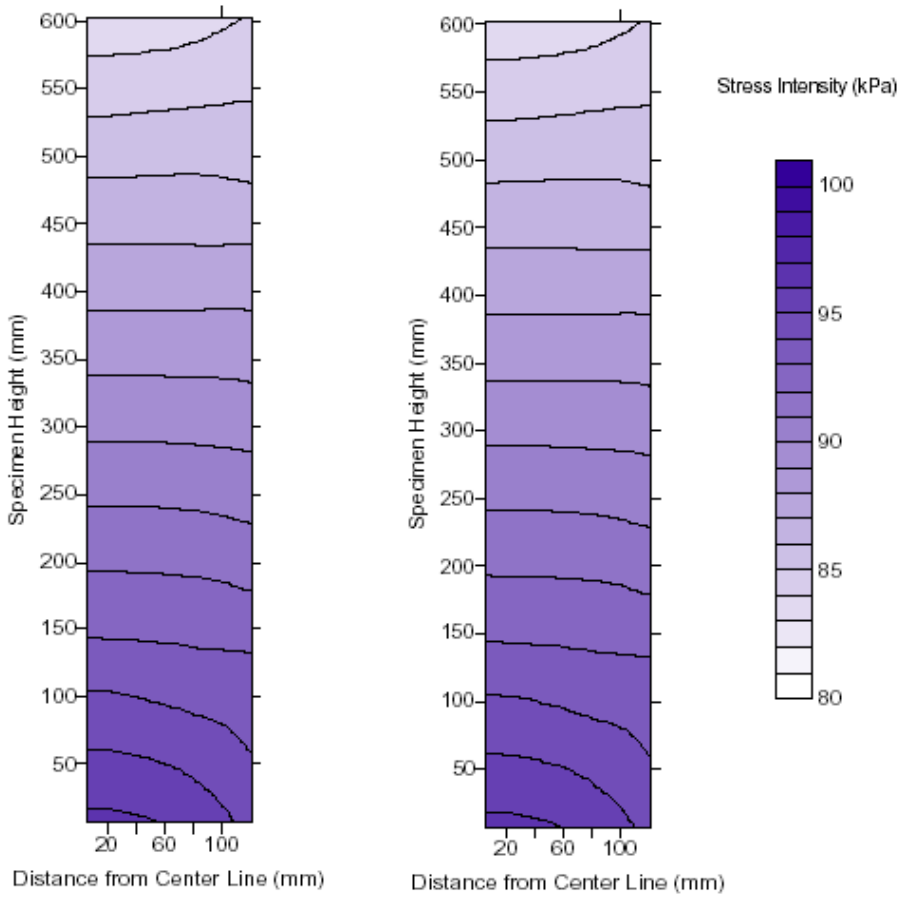

(a) Vertical Stress at 6 kN of Test P-M-RB

(b) Vertical Stress at 6 kN of Test P-M-(RB+2044)

1 kPa = 0.145 psi
1 mm = 0.039 inches

Figure 22. Graph. Vertical stress distributions at 1.3-kip (6-kN) vertical load of the GRS masses without and with reinforcement.[(20)]

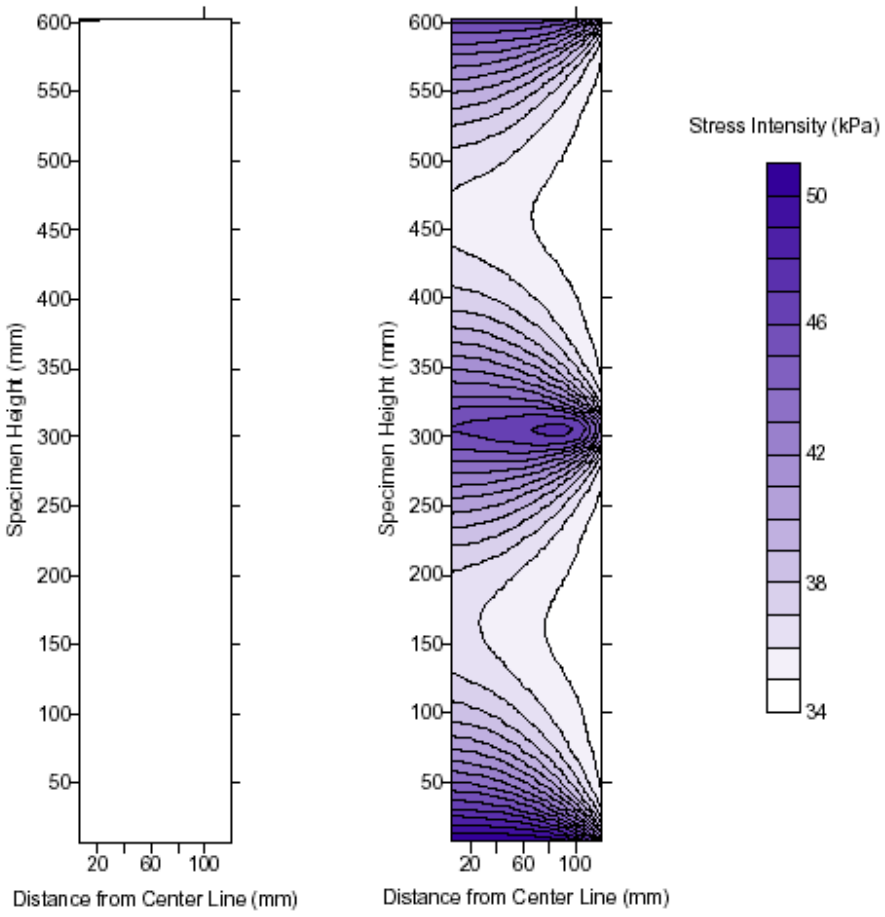

(a) Horizontal Stress at 6 kN of Test P-M-RB

(b) Horizontal Stress at 6 kN of Test P-M-(RB+2044)

1 kPa = 0.145 psi
1 mm = 0.039 inches

Figure 23. Graph. Horizontal stress distribution at 1.3-kip (6-kN) vertical load of the GRS masses without and with reinforcement.[20]

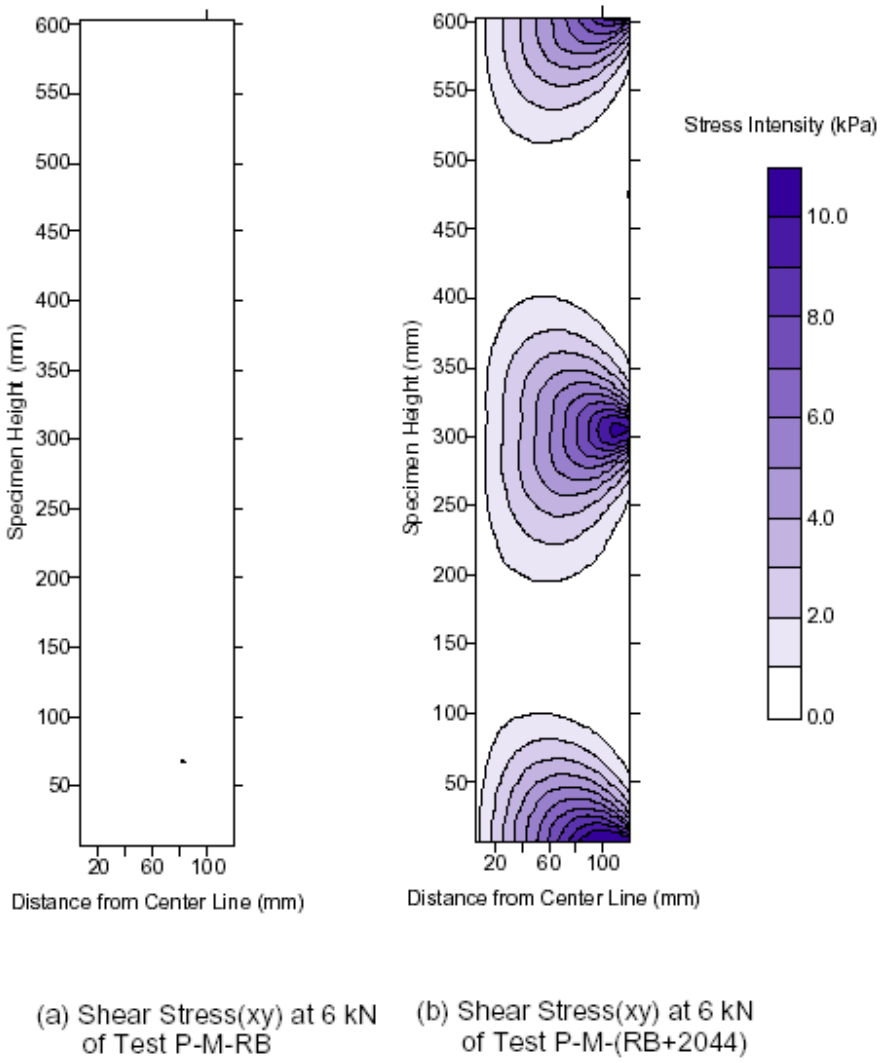

1 kPa = 0.145 psi
1 mm = 0.039 inches

Figure 24. Graph. Shear stress distribution at 1.3-kip (6-kN) vertical load of the GRS masses without and with reinforcement.[20]

2.3 CIS IN AN UNREINFORCED SOIL MASS

Many studies have been conducted to address CIS in a soil mass. As early as 1943, Terzaghi noted that compaction significantly affected lateral Earth pressures.[42] In 1954, Rowe calculated lateral Earth pressures for conditions of wall deflection intermediate between the at-rest, fully active, and fully passive states.[8] Rowe's work did not directly address CIS, but it contributed to a later study by Broms on compaction-induced Earth pressures.[9] Seed and Seed and Duncan developed a simulation model called the "bi-linear hysteretic loading/unloading model" to simulate the compaction effect on vertical, non-deflecting structures.[11,43] Duncan and Seed and Duncan et al. also developed a procedure to determine lateral Earth pressure due to compaction.[12,13] These studies were considered to have a strong impact on the determination of CIS.

2.3.1 Lateral Earth Pressure Estimation

The lateral Earth pressure estimation study by Rowe was not directly related to CIS, but it addressed lateral Earth pressures for conditions of wall deflection between the at-rest, fully active, and fully passive states.[8] Rowe's stress-strain theory for calculations of lateral pressures exerted on structures by cohesionless soils was based on the following hypotheses:

- The degrees of mobilization of the soil friction angle ϕ and the soil-wall friction angle δ depend on the degrees of interlocking of the soil grains, which in turn depend on the fractional movement of the shear planes or slip strain (defined as the ratio of relative shear displacement to total slip plane length). The friction angle increases from a relatively low value to a higher limiting or ultimate value as slip strain increases.

- Earth pressures acting on a retaining wall or structure may be calculated by conventional limiting equilibrium methods (i.e., gravity analyses of sliding wedges) using the developed fractional ϕ and δ values.

The basic mechanics of Rowe's theory are essentially a simple Coulomb analysis of sliding wedges. A sample wedge adjacent to a wall or structure is considered. When the structure deflects, slip strain occurs along planes AB and AC. Assuming no soil compression, slip strain along each plane is calculated as the ratio of shear displacement along the plane to the length of the plane. The forces acting on the typical sliding wedge are the weight of the soil, the force exerted on a sliding wedge by the underlying soil, and the force exerted on the sliding wedge by the wall.

Rowe substantiated his theory by performing a series of direct shear tests on different sands, recording the friction angle developed at various levels of slip strain, and using these values to calculate lateral Earth pressures for sample problems. By considering tamping or compaction as application and removal of surcharge pressure γh_o (γ = unit weight of soil and h_o = surcharge head), Rowe postulated that slip strains would be induced by the load application. He suggested that in the compression and shear tests, unloading causes relatively small strain reversals. Thus, after tamping a fill behind a wall, the lateral pressure will be almost as great as the value, which acted under the preconsolidation pressure. From that, the pressure coefficient (K'_o) could be expressed as shown in the equation in figure 25.

$$K_o^{'} = K_o\left(1+\frac{h_o}{h}\right)$$

Figure 25. Equation. At-rest Earth pressure coefficient.

Where h_o is the surcharge head removed and h is the overburden head ($h = \sigma_v / \gamma$). In any case, $K_o \le K_P$, where K_p is the coefficient of passive Earth pressure at limiting condition.

It is interesting to note the similarity between Rowe's early equation for residual compaction-induced lateral Earth pressures and an equation proposed later by Schmidt to explain residual lateral Earth pressures resulting from over-consolidation of soils under conditions of no lateral strain (i.e., the K_o condition).[44] Schmidt's equation, which empirically allows for some degree of relaxation of lateral stresses following surcharge removal, can be expressed in figure 26.

$$K_o' = K_o \left(1 + \frac{h_o}{h}\right)^{\alpha}$$

Figure 26. Equation. Schmidt's equation for residual lateral Earth pressures.[44]

Where:

α = 0.3 to 0.5 for most sands.
α = 1.2 $\sin\phi'$ for initially normally consolidated clays.

2.3.2 Stress Path Theory by Broms and Extension of Broms' Work by Ingold[9,45]

Broms developed a stress path theory to explain residual lateral Earth pressure on rigid, vertical, non-yielding structures resulting either from compaction or surcharge loading that is subsequently removed.[9] The theoretical basis for Broms' theory is illustrated in figure 27. An element of soil at some depth is considered to exist at some initial stress state represented by point A with horizontal and vertical effective stresses of σ'_{ho} and σ'_{vo}. Compaction of the soil is considered a process of loading followed by unloading. When the overburden pressure is increased (i.e., loading), there is little change in lateral pressure until the ratio of lateral to vertical effective stresses is equal to K_o (denoted by point B in figure 27), where K_o is the coefficient of Earth pressure at rest. Thereafter, increased vertical stress is accompanied by an increased lateral stress according to figure 28, corresponding to primary (or virgin) loading.

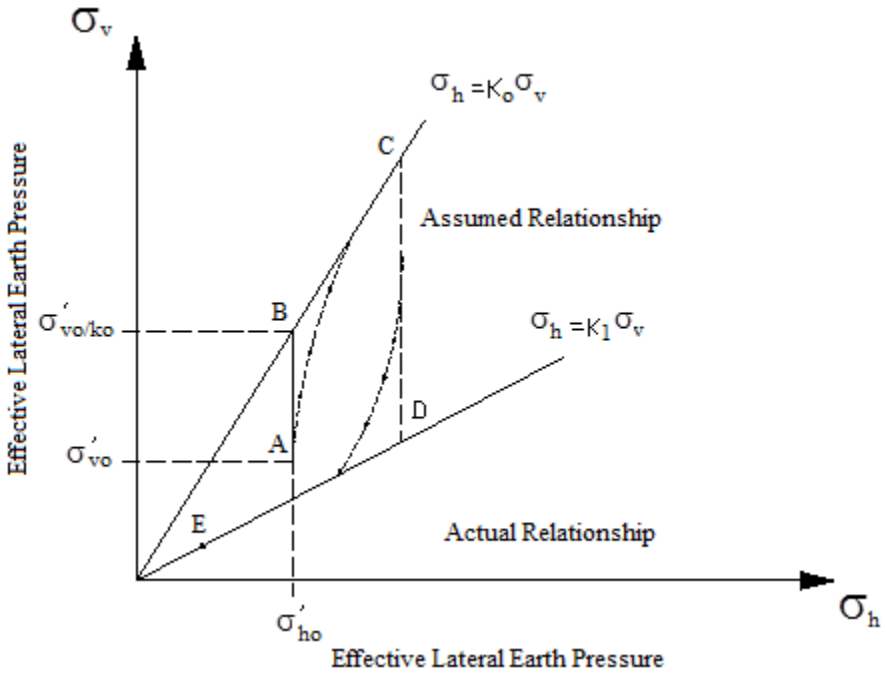

Figure 27. Illustration. Hypothetical stress path during compaction.

$$\sigma'_h = K_o \, \sigma'_v$$

Figure 28. Equation. Lateral Earth pressure at rest.

When the overburden pressure is subsequently decreased (e.g., from point C), the corresponding decrease in lateral pressure is small until the ratio of lateral to vertical effective stresses is equal

to some limiting constant K_1 (denoted by point D in figure 27). Thereafter, a continued decrease in vertical pressure is accompanied by a decrease in lateral stress according to figure 29.

$$\sigma'_h = K_1 \sigma'_v$$

Figure 29. Equation. Lateral Earth pressure at K_1.

This idealized stress path is in agreement with Rowe's earlier hypothesis that stress relaxation with unloading is negligible until some limiting condition, defined by the K_1 line, is reached.[8] By following this type of stress path, an element of soil can be brought to a final state, which is represented by an effective coefficient $K_{effective}$, varying $K_o \leq K_{effective} \leq K_1$. Having made this idealized assumption of the stress path, Broms then postulated the actual stress path followed by a real soil element.[9] Rowe and Ingold both suggested that $K_1 = K_P$ (the coefficient of passive Earth pressure), reasoning that the limiting condition reached is essentially a form of passive failure.[8,45]

By employing this theory to estimate the lateral pressure exerted on a vertical, rigid, non-yielding structure with a compacted fill, Broms considered the compaction plant to present a load applied to the fill surface, inducing vertical stresses that may be approximated as twice as those calculated by the Boussinesq stress equation for an infinite half space.[9] Lateral Earth pressures acting against the wall were then calculated using figure 28. The resulting horizontal stress distribution calculated for a 11.25-T (10.2-t) smooth wheel roller is presented by Broms.[9]

By considering the backfill process as the placement of a series of soil layers each deposited and then compacted one after the other, the compaction-induced lateral pressure for each new layer will be surpassed in magnitude by the at-rest Earth pressures due to the static overburden.

Ingold applied the extension of Broms' theory in cases where wall deflection during backfilling was sufficient to induce an active condition in the lower layers of a backfill that is deposited and compacted in lifts by assuming the virgin loading path to be $\sigma'_h = K_A \sigma'_v$ instead of Broms' $\sigma'_h = K_o \sigma'_v$.[45] Ingold postulated that passive failure controlled the other limiting condition and therefore, $K_1 = K_p$.[45]

2.3.3 FE Analysis by Aggour and Brown[10]

Aggour and Brown were the first to model compaction-induced lateral Earth pressure by 2D FE analysis.[10] Aggour and Brown's analysis involved the following steps for simulation of compaction operation:

1. A layer of soil elements adjacent to a wall was modeled with some initial modulus, E_1.

2. Compaction was modeled as some increased vertical load acting uniformly over the entire surface of the soil. Simultaneously, the soil modulus was increased to some new and stiffer value, E_2, to reflect the increase in density during compaction.

3. The compaction load was then removed. The resulting strains, deflections, and stress redistributions were modeled using a stiffer unloading modulus, E^u_2.

4. A new layer of fill with modulus E_1 was added to the top of the preceding layer. This increased the vertical stresses in the underlying layer. These increased stresses in the underlying layer were modeled using the soil modulus E_2.

5. A surface load to model compaction of the new layer was applied, increasing the stresses in both these soil layers, and the modulus was increased to E_2.

6. The compacting load was removed and the resulting wall deflections, strains, and stress redistributions were modeled using the modulus E^u_2 for both soil layers.

7. The entire process was then incrementally repeated for subsequent soil layers.

Aggour and Brown used the procedure to model the soil moduli. The effects of increased number of compaction passes were modeled by increasing the soil modulus E_2. The soil modulus was greater for unloading than for reloading. Compaction loading was modeled as a uniform unit surface pressure of unit width acting at all points along the full length of the fill, from the wall to the right boundary of the FE mesh. The fill materials were placed in five 4-ft (1.22-m) lifts. The interface between the soil and the wall was assumed to remain bonded at all times.

The results of this analysis indicate the following:

- Increased wall deflections occurred with increased compactive effort (increased number of passes were modeled by increasing E_2 values).

- Increased residual lateral pressures near the top of the wall occurred with increased compactive effort.

The second sample problem analyzed by Aggour and Brown used the same soil and wall geometry, but only the last soil lift placed was compacted.[10] The effects of the compaction of the last soil layer were increased wall deflections and increased residual lateral Earth pressures near the top of the wall. These results were in agreement on a qualitative basis with field- and scale-model observations of the effects of compaction on structural deflections and residual lateral Earth pressures. The analyses suggest the potential value of FE analysis for determining compaction-induced Earth pressures on yielding structures.

2.3.4 CIS Models by Seed[11]

Seed proposed a method to estimate the effects of CIS and associated deflections.[11] The study represents the most indepth study on the subject of CIS and involved the following three areas:

- CIS due to different stress paths, including the first cycle K_o reloading stress path, typical K_o reloading stress path, multicycle K_o unloading/reloading stress path, and K_o unloading following reloading stress path.

- The nonlinear and bilinear hysteretic loading/unloading compaction models for simulation of fill compaction behind vertical, non-deflecting structures.

- FE analysis of fill compaction using the nonlinear and bilinear models.

2.3.4.1 First Cycle K_o Reloading Stress Path and Typical K_o Unloading/Reloading Stress Path

Seed proposed the first cycle K_o reloading model.[11] The model was derived from fitting available data. Upon loading, the stress path is assumed to follow the K_o line to point A, after which, the unloading stress path is followed by $K_o' = K_o (OCR)^{\alpha}$ to an arbitrary point B prior to reloading where *OCR* is the overconsolidation ratio, K_o is the at-rest coefficient of Earth pressure, α is an exponent determined from laboratory or in situ testing, and K_o' is the at-rest coefficient of Earth pressure accounting for stress history. Reloading is then assumed to follow a linear path to point *R*, the intersection of the reloading path with the K_o line and to follow the K_o line thereafter. Point *R*, the intersecting point of the reloading path with the virgin loading path, is determined as shown in figure 30 and figure 31.

$$\sigma^*_{h,r} = \sigma'_{h,\min} + \beta * \Delta$$

Figure 30. Equation. Horizontal residual stress after compaction.

$$\sigma^*_{v,r} = \frac{1}{K_o} \sigma^*_{h,r}$$

Figure 31. Equation. Vertical residual stress after compaction.

Where:

Δ = The decrease in horizontal effective stress from the maximum loading at point A to the minimum unloading at point B.
β = Assumed constant regardless of the degree of unloading that precedes reloading.
$\sigma'_{h,min}$ = Minimum horizontal stress.
$\sigma^*_{v,r}$ and $\sigma^*_{h,r}$ = Vertical and horizontal residual stress after compaction, respectively.

2.3.4.2 Multicycle K_o Unloading/Reloading Stress Path and K_o Unloading Following Reloading Stress Path

Seed proposed another model for multicycle K_o unloading/reloading conditions.[11] The values α and β are assumed to remain constant regardless of the number of loading-reloading cycles.

Three situations of unloading were considered. The first situation is for unloading after significant loading, the second situation is for unloading after intermediate reloading, and the third situation is for unloading after moderate reloading. Note that Seed also developed a nonlinear multicycle K_o unloading/reloading compaction model.

2.3.4.4 Simplified Bilinear Approximation to the Nonlinear Model

In this model, the α-type nonlinear unloading model for the first cycle unloading is approximated by a bilinear unloading path. The relationship between K_2 and *F* in the bilinear unloading model shows the relationship between K_3 (slope of reloading path) and β_3 of the model.

Seed also developed the following simplified hand-calculation procedure for computing CIS:[11]

1. Calculate the peak lateral compaction pressure profile (i.e., $\Delta\sigma'_{h,vc,p}$ versus depth relationship).

2. Multiply the $\Delta\sigma'_{h,vc,p}$ values with the bilinear model parameter, F.

3. Calculate the lateral residual stress as shown in figure 32.

$$\sigma'_{h,r} = K_0\sigma'_v + F\Delta\sigma'_{h,vc,p}$$

Figure 32. Equation. Lateral residual stress.

4. Reduce the near-the-surface portion of the $\sigma'_{h,r}$ distribution with $\sigma_{h,r}' \leq K_{1,\phi',B}\sigma_v'$ at all depths.

5. Increase the residual effective stress distribution such that $\sigma_{h,r}' \geq K_0\sigma_v'$ at all depths.

The compaction models developed by Seed were used to determine CIS for full-scale experiments and were reported by Duncan and Seed and Duncan et al.[11–13] The publications show that CIS could be calculated based on either the simplified method (i.e., the bilinear model) or the nonlinear model with the aid of FE analysis. The studies showed that the resulting lateral Earth pressures determined by the models are in good agreement with measured data.

2.4 CIS IN A REINFORCED SOIL MASS

Many researchers and engineers have suggested that if a granular backfill is well compacted, a GRS mass can usually carry many loads while experiencing little movement. Several studies on performance of GRS structures have used simplified and somewhat arbitrary procedures to simulate the effects of fill compaction. In past studies, CIS in the fills were ignored completely. CIS in a GRS mass is likely to be more pronounced than CIS induced in an unreinforced soil mass because soil reinforcement interface friction tends to restrain lateral deformation of the soil mass and result in greater values of CIS. A review of previous studies on GRS masses, including the effects of CIS, is presented in this section.

2.4.1 Ehrlich and Mitchell[46]

Ehrlich and Mitchell presented a procedure to include CIS in the analysis of reinforced soil walls and noted that CIS was a major factor affecting the reinforcement tensions.[46] The assumptions involved in the procedure were as follows:

- The stress path was as shown in figure 33.

- With the multicycle operations of soil placement and compaction during construction, the soil surrounding the reinforcement maximum tension point in each compaction lift was subjected to only one cycle of loading, as shown in figure 33.

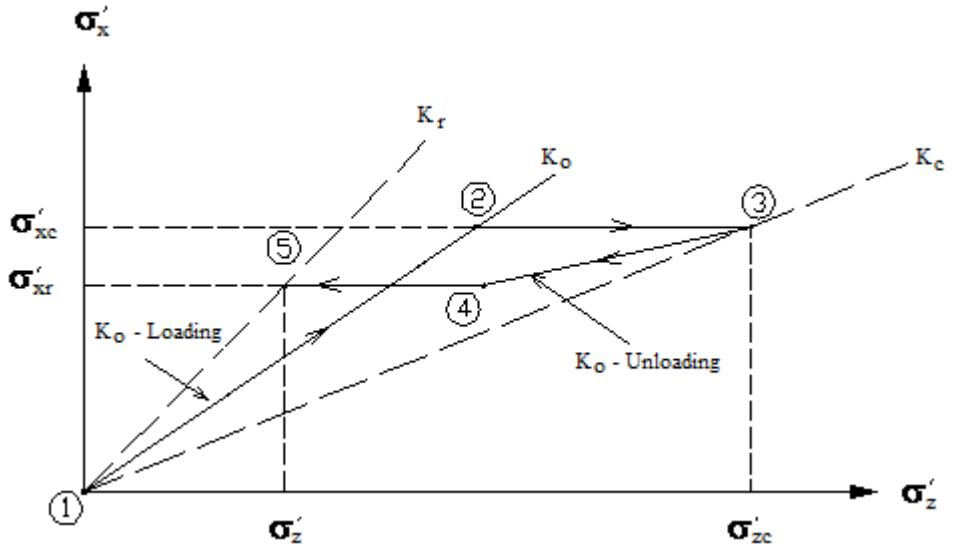

Figure 33. Illustration. Assumed stress path due to compaction-induced stress.

Loading due to the weight of overlying soil layers plus some equivalent increase in the stress state induced by the compaction operations is shown as paths 1–3 in figure 33. This is followed by unloading along paths 3–5 to the final residual stress-state condition at the end of construction. Ehrlich and Mitchell noted that by following this procedure, the stresses in each layer were calculated only once and that each layer calculation was independent of the others.[46]

The specific values of σ'_z and σ'_{zc} at point 3 in figure 33 represent the maximum stress applied to the soil at a given depth during the construction process. The maximum past equivalent vertical stress, including compaction at the end of construction (σ'_{zc}), can be estimated using a new procedure based on the method given by Duncan and Seed for conventional retaining walls.[12]

In figure 33, the value of σ'_{zc} can be estimated using figure 34 through figure 38.

$$\sigma_{zc}' = \frac{\sigma_{xp}'}{K_o}$$

Figure 34. Equation. Maximum vertical stress at a given depth during construction.

$$K_o = 1 - \sin\varphi'$$

Figure 35. Equation. Coefficient of Earth pressure at rest.[47]

$$\sigma_{xp}' = \nu_o \left(1 + K_A\right) \sqrt{\frac{0.5\gamma' Q N_\gamma}{L}}$$

Figure 36. Equation. Maximum lateral stress in terms of compaction and effective soil unit weight.

Where:

Q = Maximum vertical operating force of the roller drum.
L = Length of the roller drum.
γ = Effective soil unit weight.

$$\upsilon_o = \frac{K_o}{1 - K_o}$$

Figure 37. Equation. Poisson's ratio under K_o condition.

$$N_\gamma = \tan\left(45^o + \frac{\phi'}{2}\right)\left[\tan^4\left(45^o + \frac{\phi'}{2}\right) - 1\right]$$

Figure 38. Equation. Bearing capacity factor.

The effects of CIS on compaction and reinforcement stiffness in GRS walls were investigated by Ehrlich and Mitchell.[46] Their conclusions were as follows:

- The soil shearing resistance parameters, the soil unit weight, the depth, the relative soil reinforcement stiffness index S_i, and the compaction, were the major factors determining reinforcement tensions (typical S_i for metallic reinforcement = 0.500 to 3.200, plastic reinforcement = 0.030 to 0.120, and geotextile reinforcement = 0.003 to 0.012).

- Increasing S_i usually means increased lateral Earth pressure and reinforcement tension, but at shallow depths, the opposite effect can occur depending on compaction conditions.

- The coefficient of horizontal Earth pressure, K, can be greater than K_o at the top of the wall and can be greater than K_A to depths of more than 20 ft (6.1 m) depending on the relative soil reinforcement stiffness index and the compaction load.

- K_o is the upper limit for the coefficient of horizontal Earth pressure, K, if there is no compaction of the backfill.[46]

2.4.2 Hatami and Bathurst[17]

Hatami and Bathurst noted that fill compaction has two effects on the soil: it increases the lateral Earth pressure and it reduces the effective Poisson's ratio.[17] They suggested that the first effect can be modeled in a numerical analysis by applying a uniform vertical stress (1.2 and 2.3 psi (8 and 16 kPa) depending on compaction load) to the entire surface of each newly placed soil layer before analysis and removing it afterwards. This procedure was based on a recommendation by Gotteland et al., who simulated the compacting effect by loading and unloading a uniform surcharge of 7.3 and 14.5 psi (50 kPa and 100 kPa) on the top of the wall.[48]

For the second effect of compaction on the reduction of Poisson's ratio, Hatami and Bathurst used the numerical simulation to find the minimum Poisson's ratio, ν_{min}, from matching measured and analysis data.[17] The results (wall lateral movement and reinforcement forces)

obtained from the numerical analysis, including compaction effects, were in good agreement with the measured data.

In the numerical analyses, the compaction effects were also accounted for by increasing the elastic modulus number, K_e, from triaxial test results by a factor of 2.25 for walls 1 and 2.

2.4.3 Morrison et al.[18]

Morrison et al. simulated the effects of fill compaction of shored mechanically stability Earth walls.[18] A 7.3-psi (50-kPa) inward pressure was applied to the top, bottom, and exposed faces of each lift to simulate the effects of fill compaction. The inward pressure was then reduced to 1.5 psi (10 kPa) on the top and bottom of a soil lift prior to placement of the next lift to simulate vertical relaxation or unloading following compaction. The inward pressure acting on the exposed face was maintained at 7.3 psi (50 kPa) because this produced the most reasonable model deformation behavior compared with that observed in the field-scale test. It was considered that the inward maintained pressures were "locking-in" stresses in soil due to compaction.

The stiffness of soil was increased by a factor of 10 to consider CIS in the GRS mass. This factor was about 2.25 in Hatami and Bathurst.[17]

Figure 39 shows the model for FE analysis by Morrison et al.[18] The figure shows the simulation of fill compaction of lift 5 by the applying uniform pressures.

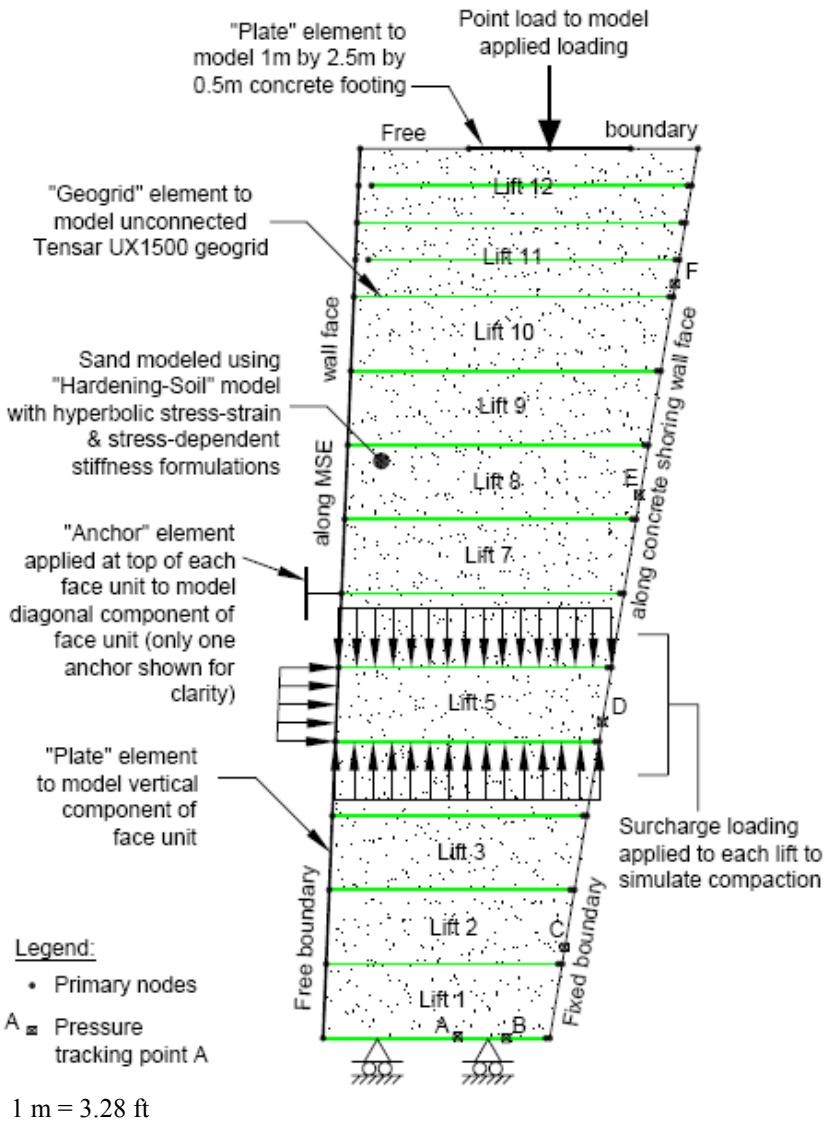

Figure 39. Illustration. FE model for FE analysis.[18]

The results of the lateral movement and reinforcement forces showed a good qualitative agreement with the measured data. However, general application of the procedure may be questionable because neither the method of analysis nor the magnitude of the applied inward pressure was properly justified.

2.5 HIGHLIGHTS OF COMPACTION-INDUCED EARTH PRESSURES IN THE LITERATURE

Several important highlights regarding compaction-induced lateral Earth pressures in the literature include the following:

- Compaction of soil against a rigid, vertical, non-yielding structure appears to result in the following residual lateral pressure distribution:

  - The lateral pressure near the surface increases rapidly with depth, exceeding the at-rest value, but limited to passive failure pressures.[9,11]
  - At intermediate depths, the lateral pressures exceed the at-rest value and increase less rapidly with depth or remain fairly constant with depth.[9,11]
  - At greater depths, the lateral pressures appear to be the simple at-rest pressures, showing no affects of compaction.[9,11]

- Compaction of soil against deflecting structures appears to increase near the surface.

- The compaction-induced residual Earth pressures are significantly affected by the compaction equipment. For compaction by small hand-operated rollers, the increase in the lateral pressure occurs within a depth of about 10 to 13 ft (3 to 4 m), but for very large rollers, the effect of compaction can be up to 49 to 82 ft (15 to 25 m).[12]

- Structural deflections away from the soil, which occur during fill placement and compaction, will reduce the residual lateral Earth pressures. Reduction in pressures appears to occur more rapidly in heavily compacted cohesionless soil.[11]

- Compaction-induced residual lateral Earth pressures in cohesive soils appear to dissipate with time, even against non-deflecting structures, and eventually approach at-rest values.

- There is some evidence suggesting that the direction of rolling with the compactor can have a significant effect on compaction-induced Earth pressures.[46]

- Field observations indicate that available overburden pressures are sufficient that possible passive failure does not limit residual lateral Earth pressure and a high percentage of the peak lateral Earth pressures induced during compaction may be retained as residual pressures. In previously compacted soil, however, additional compaction can result in only small increases in peak pressures and at negligible fractions.[10]

- A number of simulation models have been proposed to explain and evaluate the residual lateral Earth pressures induced by compaction. Common to all of these theories is the idea that compaction represents a form of over-consolidation wherein stresses resulting from a temporary or transient loading condition are retained to some extent following removal of this peak load.

- Many researchers have simulated fill compaction by application and removal of a surface surcharge pressure. (See references 8, 9, 17, and 48.)

- Broms proposed a theory to calculate compaction-induced residual lateral Earth pressures against a rigid, vertical, frictionless, non-yielding wall.[9] The simulation results somewhat agree with available field data for walls sustaining minimal deflections. Broms assumed that unloading results in no decrease in lateral stress until a limiting passive-failure-type condition is reached and reloading results in no increase in lateral stress until the virgin K_0-loading stress path is regained.[9] This type of model does not predict well

the peak lateral stresses induced by fill compaction and is not suited for computing lateral stresses induced by a surface compaction plant of finite lateral dimensions (not the entire surface). But Broms' theory is very easy to apply.[9] Some researchers have adopted this theory for analysis of GRS structures.[17,18,48]

- Seed developed two models for simulation of fill compaction: a nonlinear model and a bilinear model.[11] They are well suited for simulation of compaction operations in GRS structures. The simulation results of the two models are rather similar, and both agree well with measured data of unreinforced Earth retaining walls. The bilinear model is easy to apply using hand calculation. Both models are based on the K_o condition and are very useful for estimating CIS for soil only. To use it for GRS structures, indepth studies need to be carried out.

CHAPTER 3. ANALYTICAL MODEL FOR CALCULATING LATERAL DISPLACEMENT OF A GRS WALL WITH MODULAR BLOCK FACING

Over the past two decades, GRS walls have gained increasing popularity in the United States and abroad. In actual construction, GRS walls have demonstrated a number of distinct advantages over the conventional cantilever and gravity retaining walls. Generally, GRS walls require less over-excavation and are more ductile, more flexible (hence more tolerant to differential settlement and to seismic loading), more adaptable to low permeability backfill, easier to construct, and significantly more economical than conventional Earth structures.[2–4]

A GRS wall comprises two major components: a facing element and a GRS mass. GRS wall facing elements have been constructed with different types of material and in different forms including wrapped geotextile facing, timber facing, modular concrete block facing, precast concrete panel facing, and cast-in-place rigid facing. Among the various facing types, modular concrete block facing has been the most popular in North America, mainly because of its ease of construction, availability, and low cost. The other component of a GRS wall, the GRS mass, is a compacted soil mass reinforced with layers of geosynthetic reinforcement. Figure 40 shows the schematic diagram of a typical GRS wall with a modular block facing.

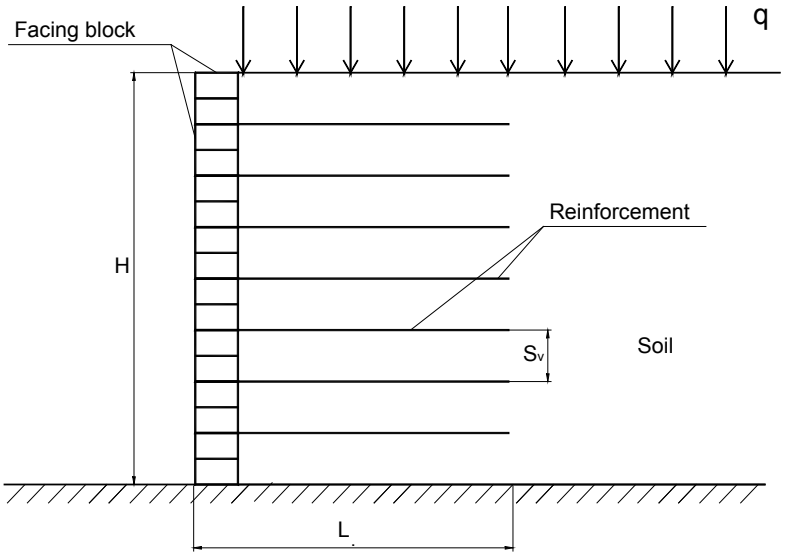

Figure 40. Illustration. Basic components of a GRS wall with a modular block facing.

Current design methods for GRS walls consider only the stresses and forces in the wall system. Even though a GRS wall with a modular block facing is a fairly flexible wall system, movement of the wall is not accounted for in current designs. A number of empirical and analytical methods have been proposed for estimating lateral movement of GRS walls. Although many full-scale experiments, numerical analyses, and field experience have clearly indicated the importance of facing rigidity on wall movement, most methods do not address the rigidity of the facing. (See references 49–52.)

The prevailing methods for estimating the maximum lateral displacement of GRS walls include the Federal Highway Administration (FHWA) method, the Geoservices method, the Colorado

Transportation Institute (CTI) method, and the Jewell-Milligan method. (See references 2, 19, 53, and 54.) Among these methods, the Jewell-Milligan method has been found to give the closest agreement with FE analysis.[55] However, the method ignores the effect of facing rigidity. Strictly speaking, the method is only applicable to reinforced soil walls where there is little facing rigidity, such as a wrapped-faced GRS wall.

A study aimed at developing an analytical model for calculating lateral movement of a GRS wall with modular block facing was undertaken.[19] The analytical model is a modification to the Jewell-Milligan method by including the rigidity of facing element. This analytical model can be used in routine design by determining the required reinforcement strength for a limiting value of maximum allowable wall movement.

To verify the analytical model, the lateral wall displacements calculated by the analytical model were compared with the results of the Jewell-Milligan method for GRS walls with negligible facing rigidity.[19] In addition, the lateral wall displacements obtained from the analytical model were compared with the measured data of a full-scale experiment using a GRS wall with modular block facing.[16,17]

In addition to lateral displacement profiles, an equation for determining facing connection forces (i.e., the forces in reinforcement immediately behind the facing) is introduced.[19]

3.1 EXISTING METHODS FOR ESTIMATING MAXIMUM WALL MOVEMENT

The most prevalent methods for estimating the maximum lateral displacement of GRS walls are the FHWA method, the Geoservices method, the CTI method, and the Jewell-Milligan method. (See references 2, 19, 53, and 54.) A summary of each method is presented in this section.

3.1.1 The FHWA Method[53]

The FHWA method correlates the reinforcement length/wall height (L/H) ratio with the lateral displacement of a reinforced soil wall during construction. Figure 41 shows the relationship between L/H and δ_R, the empirically derived relative displacement coefficient. Based on 20-ft (6-m)-high walls, the δ_R value increases by 25 percent for every 3 psi (20 kPa) of surcharge. For higher walls, the surcharge effect may be greater. The curve in figure 41 has been approximated by a fourth-order polynomial for $0.3 \le \frac{L}{H} \le 1.175$, as shown in figure 42**.**

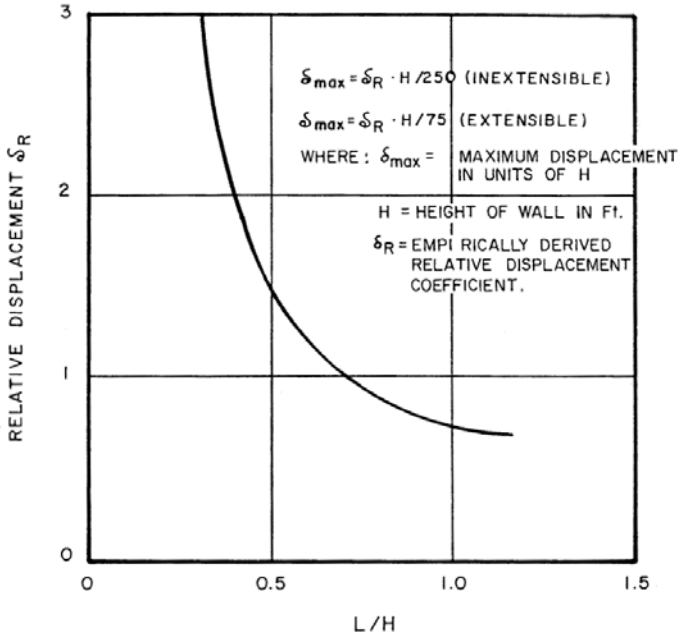

1 m = 3.28 ft

Figure 41. Graph. Empirical curve for estimating maximum wall movement during construction in the FHWA method.[53]

$$\delta_R = 11.81\left(\frac{L}{H}\right)^4 - 42.25\left(\frac{L}{H}\right)^3 + 57.16\left(\frac{L}{H}\right)^2 - 35.45\left(\frac{L}{H}\right) + 9.471$$

Figure 42. Equation. Relative displacement coefficient.

For extensible reinforcement, the maximum lateral wall displacement, δ_{max}, can be calculated using figure 43 (δ_{max} is in units of wall height (H)).

$$\delta_{\max} = \delta_R \left(\frac{H}{75}\right)$$

Figure 43. Equation. Maximum lateral wall displacement during construction for extensible reinforcement.

The FHWA method was developed empirically by determining a displacement trend from numerical analysis and adjusting the curve to fit with field-measured data. The method provides a quick estimate of the maximum lateral displacement. Note that the maximum lateral displacement, δ_{max}, as obtained from figure 43, has been corrected for a wall with a different height and surcharge.

3.1.2 The Geoservices Method[54]

The Geoservices method relies on limit equilibrium analyses to calculate the length of the required reinforcement to satisfy a suggested factor of safety with regard to three presumed external failure modes (e.g., bearing capacity failure, sliding, and overturning). The method provides a procedure for calculating the lateral wall displacement.

The lateral displacement is calculated by first choosing a strain limit for the reinforcement. This strain limit is usually less than 10 percent and depends on a number of factors, such as the type of wall facing, the displacement tolerances, and the type of geosynthetic to be used as reinforcement. Concrete facing panels, for example, would not allow much lateral displacement without showing signs of distress. Therefore, a low strain limit (1–3 percent) should be selected.

Geosynthetics have a wide range of material properties depending on, among other factors, the way they are manufactured. Non-woven geotextile exhibits low modulus characteristics. If such a geosynthetic was chosen as a reinforcement for a wall, design would necessarily imply that a large design strain is to be considered.

Once the strain limit has been selected, the method assumes a distribution of strain in the reinforcement, as shown in figure 44, for calculating wall movement.

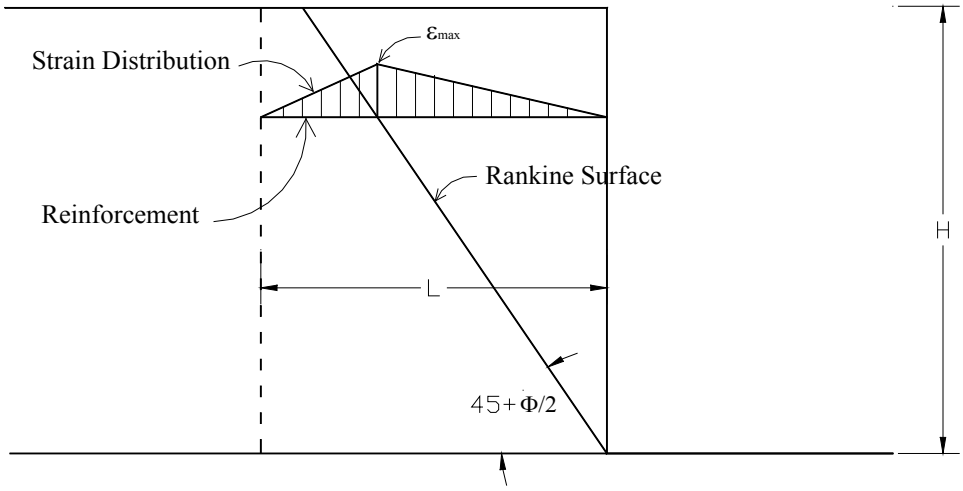

Figure 44. Illustration. Assumed strain distribution in the Geoservices method.[54]

The horizontal displacement, δ_h, is calculated as shown in figure 45.

$$\delta_h = \frac{\varepsilon_d L}{2}$$

Figure 45. Equation. Horizontal displacement.

Where:

ε_d = Strain limit (ε_{max}).
L = Reinforcement length.

3.1.3 The CTI Method[2]

Differing from all other design methods based on ultimate strength of the geosynthetic reinforcement, the CTI method is a service-load-based design method. The reinforcement requirements are made in terms of stiffness at a design limit strain as well as the ultimate strength.

In most cases, the designer will select a design limit strain of 1–3 percent for the reinforcement. The maximum lateral displacement of a wall, δ_{max}, can be estimated by the empirical equation in figure 46.

$$\delta_{\max} = \varepsilon_d \left(\frac{H}{1.25} \right)$$

Figure 46. Equation. Maximum lateral wall displacement according to CTI method.

Where:

ε_d = Design limit strain (typically 1–3 percent for H less than or equal to 30 ft (0.9 m)).
H = Wall height.

If the maximum wall displacement exceeds a prescribed tolerance for the wall, a smaller design limit strain should be selected so that the maximum lateral displacement of the wall will satisfy the performance requirement. Figure 46 applies only to walls with very small facing rigidity, such as wrapped-faced walls. Walls with significant facing rigidity will have smaller maximum lateral displacement. For example, a modular block GRS wall will have δ_{max} about 15 percent smaller than that calculated in figure 46.

3.1.4 The Jewell-Milligan Method

Jewell and Jewell and Milligan proposed a procedure for calculating wall displacement based on analysis of stresses and displacements in a reinforced soil mass.[56,19] The method describes a link between soil stresses (stress fields) in a reinforced soil mass in which a constant mobilized angle of friction is assumed with the resulting displacements (velocity fields). There are two parameters for plane-strain plastic deformation of soil: the plane-strain angle of friction, ϕ_{ps}, and the angle of dilation, ψ. The planes on which the maximum shearing resistance ϕ_{ps} is mobilized are called the "stress characteristics" and are inclined at $\left(45^\circ + \varphi_{ps}/2\right)$ to the direction of major principal stress, as shown in figure 47. The directions along which there is no linear extension strain in the soil are called the "velocity characteristics" and are inclined at $\left(45^\circ + \psi/2\right)$ to the direction of major principal stress, as shown in figure 47.

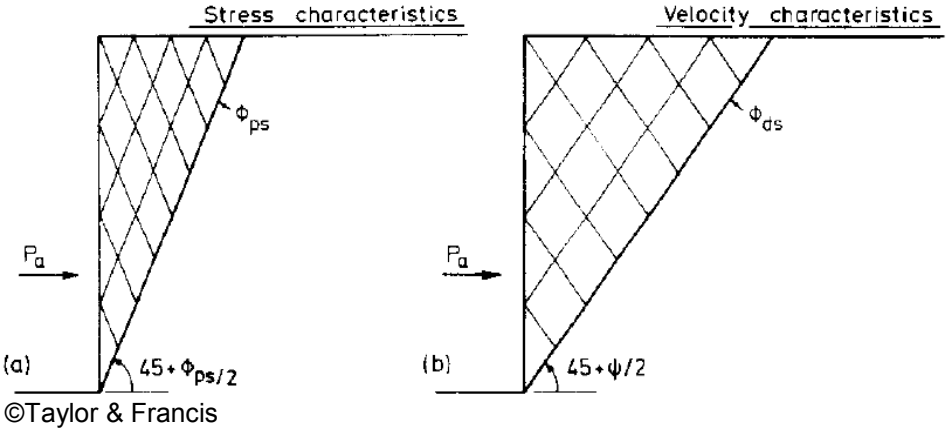

Figure 47. Illustration. Stress and velocity characteristics behind a smooth retaining wall rotating about the toe.[19]

Jewell and Milligan noted from limiting equilibrium analyses that there are three important zones in a reinforced soil wall, as illustrated in figure 48.[19] The boundary between zone 1 and 2 is at an angle $\left(45^{\circ}+\psi/2\right)$ to the horizontal, and the boundary between zone 2 and 3 is at an angle ϕ_{ds}. Large reinforcement forces are required in zone 1 to maintain stability across a series of critically inclined planes. In zone 2, the required reinforcement forces reduce progressively.

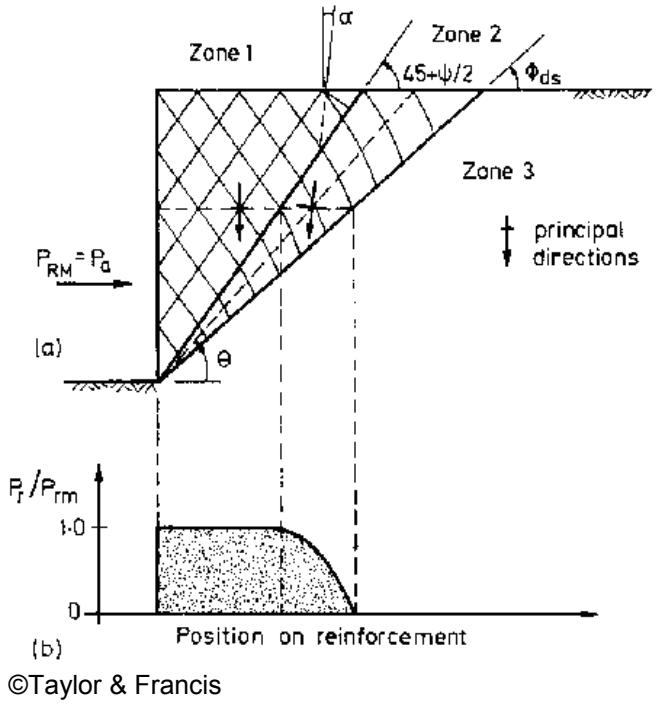

Figure 48. Illustration. Major zones of reinforcement forces in a GRS wall and the force distribution along reinforcement with ideal length.[19]

The assumptions of the Jewell-Milligan method for ideal length of reinforcement are as follows:

- The reinforcement length at every layer extends to the back of zone 2, the so-called ideal length.
- The horizontal movement of the facing can be calculated by assuming horizontal deflections starting at the fixed boundary between zones 2 and 3 and working to the face of the wall.
- The stability of the stress characteristics and the velocity characteristics is equally critical in soil. Hence, reinforcement must provide equilibrium for both. The consequence is that behind the Rankine active zone in a reinforced soil wall, the equilibrium is governed by ϕ_{ds}, mobilized on the velocity characteristics.

In figure 48, the maximum horizontal resultant force required for equilibrium, P_{rm}, is equal to the active force P_a, as shown in figure 49.

$$P_{rm} = P_a = K_a\left(\frac{\gamma H^2}{2} + q_s H\right)$$

Figure 49. Equation. Maximum horizontal resultant force required for equilibrium.

Where:

γ = Unit weight of the soil.
H = Wall height.
q_s = Uniform surcharge.
K_a = The active Earth pressure coefficient, which can be expressed as shown in figure 50.

$$K_a = \frac{(1-\sin\phi_{ps})}{(1+\sin\phi_{ps})} = \frac{\tan\left(45+\frac{\psi}{2}-\phi_{ds}\right)}{\tan\left(45+\frac{\psi}{2}\right)}$$

Figure 50. Equation. Active Earth pressure coefficient.

The required reinforcement force P_r in zone 2 at an angle θ, as shown in figure 48, can be estimated from the maximum reinforcement force, P_{rm}, as shown in figure 51.

$$\frac{P_r}{P_{rm}} = \frac{\tan(\theta-\phi_{ds})}{K_a \tan\theta}$$

Figure 51. Equation. Ratio of the required reinforcement force and the estimated maximum reinforcement force.

The results of the displacement analyses have been presented in the form of design charts in figure 52. The charts can be used to determine the distribution of lateral wall displacement along the wall face for different values of mobilized internal friction, ϕ_{ps}, and angles of dilation, ψ.

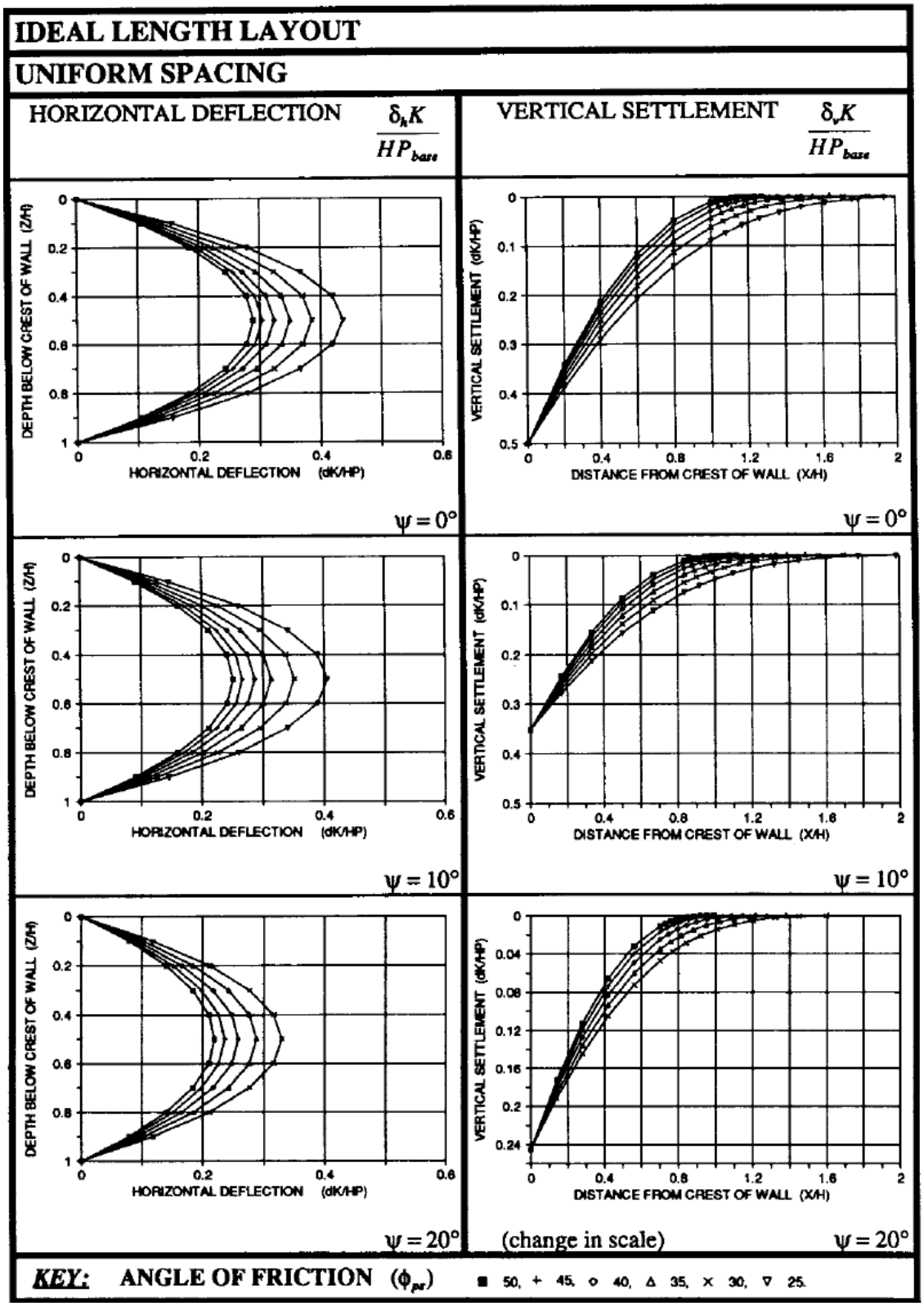

Figure 52. Illustration. Charts for estimating lateral displacement of GRS walls with the ideal length layout.[19]

To estimate the horizontal deflection at the GRS wall face for reinforcement with the ideal length and uniform spacing, the charts in figure 52 can be used. The horizontal deflection at the wall face depends on the wall height, H, the mobilized soil shearing resistance, ϕ_{ds}, the reinforcement force, P_r, and the reinforcement stiffness, K. Figure 52 can also be used to obtain a dimensionless factor, $\frac{\delta_h K}{HP_{base}}$. The horizontal displacement, δ_h, can be calculated from this factor. The reinforcement occurs at the base of the wall, P_{base}, in the dimensionless factor above. P_{base} is calculated using figure 53.

$$P_{base} = K_a \; s_v \left(\gamma \; H + q_s\right)$$

Figure 53. Equation. Reinforcement force at the base of the wall.

3.2 DEVELOPING AN ANALYTICAL MODEL FOR CALCULATING LATERAL MOVEMENT AND CONNECTION FORCES OF A GRS WALL

Jewell and Milligan presented design charts for estimating the deformation of reinforced soil walls where the rigidity of the facing can be ignored.[19] Rowe and Ho and Ho and Rowe pointed out that there is little variation in the reinforcement forces and the lateral wall deformation when L/H is equal to or greater than 0.7.[50,57,58] Note that L/H = 0.7 is commonly used in practice and is suggested by AASHTO.[59] Based on a series of numerical analyses of GRS walls, Rowe and Ho also showed that the maximum lateral deformation obtained by the Jewell-Milligan method with an ideal reinforcement length, as defined by Jewell and Milligan, is generally in good agreement with the numerical results for L/H = 0.7.[19,50] For this reason, the Jewell-Milligan method can be used to estimate lateral movement of a reinforced soil wall with L/H greater than or equal to 0.7. The analytical model developed in this study for GRS walls with modular block facing was based on the Jewell-Milligan method.

The derivation of the analytical model is provided in the following sections. It presents the derivation of the equations in the Jewell-Milligan method for predicting deformation of a reinforced soil wall with negligible facing rigidity, provides the derivation of the equations for determining connection forces in the reinforcement for walls with modular block facing, and provides equations for calculating lateral movement of GRS walls with modular block facing.

3.2.1 Lateral Movement of GRS Walls with Negligible Facing Rigidity

Figure 54 shows the three major zones in a GRS wall and the force distribution in the reinforcement at depth z_i used by Jewell and Milligan to develop an analytical model for determination of wall deformation.[19] Jewell and Milligan presented design charts based on the analytical model (without giving the derivation).[19] The following derivation is presented for completeness and for easier reference when showing the derivation of the analytical model developed for this study.

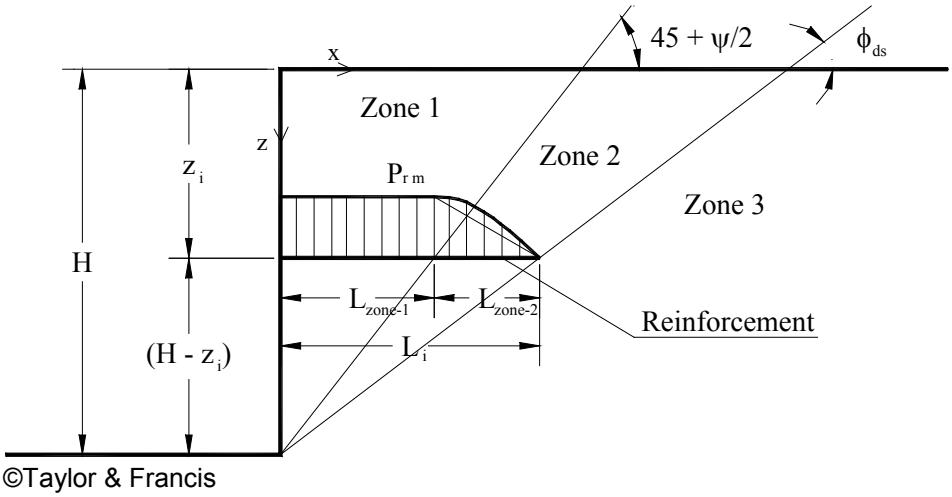

Figure 54. Illustration. Major zones of the reinforcement force in a GRS wall.[19]

The horizontal movement, Δ_h, of the wall face at depth z_i can be evaluated using figure 55 through figure 57.

$$\Delta_h = \Delta_{zone-1} + \Delta_{zone-2}$$

Figure 55. Equation. Horizontal movement.

$$\Delta_{zone-1} = \int_0^{L_{zone-1}} \frac{P_{rm}}{K_{reinf}} dx = \frac{P_{rm}}{K_{reinf}} L_{zone-1}$$

Figure 56. Equation. Lateral deformation in zone 1.

$$\Delta_{zone-2} = \int_{L_{zone-1}}^{L_{zone-1}+L_{zone-2}} \frac{P_r}{K_{reinf}} dx \approx \left(\frac{1}{2}\right) \frac{P_{rm}}{K_{reinf}} L_{zone-2}$$

Figure 57. Equation. Lateral deformation in zone 2.

Where:

K_{reinf} = Stiffness of the reinforcement.
P_{rm} = Maximum reinforcement force at depth z_i.
L_{zone-1} = Reinforcement length in zone 1 at depth z_i.
L_{zone-2} = Reinforcement length in zone 2 at depth z_i.

Substituting figure 56 and figure 57 into figure 55 results in figure 58.

$$\Delta_h = \frac{P_{rm}}{K_{reinf}} \left(L_{zone-1} + \frac{1}{2} L_{zone-2} \right)$$

Figure 58. Equation. Total horizontal movement of the wall face.

Substituting figure 59 and figure 60 into figure 58 results in figure 61.

$$L_{zone-1} = (H - z_i)\tan\left(45^o - \frac{\psi}{2}\right)$$

Figure 59. Equation. Reinforcement length in zone 1.

$$L_{zone-2} = (H - z_i)\left[\tan(90^o - \phi_{ds}) - \tan\left(45^o - \frac{\psi}{2}\right)\right]$$

Figure 60. Equation. Reinforcement length in zone 2.

$$\Delta_h = \frac{P_{rm}}{K_{re\,\inf}}\left\{(H - z_i)\tan\left(45^o - \frac{\psi}{2}\right) + \frac{1}{2}(H - z_i)\left[\tan(90^o - \phi_{ds}) - \tan\left(45^o - \frac{\psi}{2}\right)\right]\right\}$$

Figure 61. Equation. Total horizontal movement of the wall face substituting the components derived in figure 59 and figure 60.

Rearranging figure 61 results in figure 62 and figure 63.

$$\Delta_h = \frac{P_{rm}}{K_{re\,\inf}}(H - z_i)\left\{\tan\left(45^o - \frac{\psi}{2}\right) + \frac{1}{2}\left[\tan(90^o - \phi_{ds}) - \tan\left(45^o - \frac{\psi}{2}\right)\right]\right\}$$

Figure 62. Equation. Rearrangement of total horizontal movement of the wall face.

$$\Delta_h = \frac{P_{rm}}{K_{re\,\inf}}(H - z_i)\left\{\frac{1}{2}\left[\tan\left(45^o - \frac{\psi}{2}\right) + \tan(90^o - \phi_{ds})\right]\right\}$$

Figure 63. Equation. Factored down total horizontal movement of the wall face.

The value of Δ_h, the lateral displacement of a GRS wall at depth z_i, can be calculated directly from figure 64.

$$\Delta_h = \left(\frac{1}{2}\right)\left(\frac{P_{rm}}{K_{re\,\inf}}\right)(H - z_i)\left[\tan\left(45^0 - \frac{\psi}{2}\right) + \tan(90^0 - \phi_{ds})\right]$$

Figure 64. Equation. Simplified horizontal movement of the wall face.

Where:

K_{reinf} = Stiffness of the reinforcement.
P_{rm} = Maximum reinforcement force at depth z_i.
H = Wall height.
ϕ_{ds} = Effective direct shear friction angle of soil.
ψ = Angle of dilation of soil.

3.2.2. Connection Forces for GRS Walls with Modular Block Facing

The connection forces in figure 64 are defined as the forces in the reinforcement at the back face of the wall facing. The assumptions made for the determination of the connection forces include the following:

- The wall face is vertical or nearly vertical.
- There is only friction connection between adjacent facing blocks (i.e., there is no additional mechanical connection elements such as lips, keys, or pins).
- A uniform surcharge is being applied over the entire horizontal crest of the wall.
- Each facing block is a rigid body (i.e., movement is allowed but not the deformation). As a facing block moves, the frictional resistance between two adjacent blocks will reach the maximum resistance.

Consider the reinforcement at depth, z_i, sandwiched between two adjacent facing blocks, as shown in figure 65. The frictional forces, F, above and below these blocks are F_{i-1} and F_{i+1}. The horizontal resultant force of lateral Earth pressure acting on the two facing blocks is P_i. The tensile connection force in the reinforcement is T_i, W_i is the weight of the facing at location at depth Z_i, N_i is the normal force, and S_r is the reference spacing.

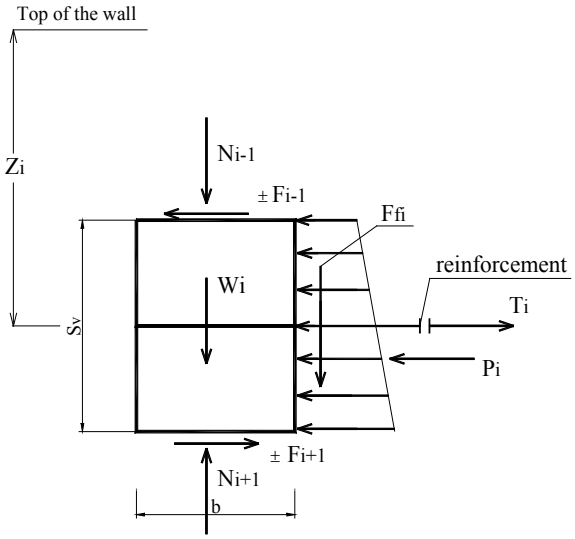

Figure 65. Illustration. Forces acting on two facing blocks at depth z_i.

The tensile connection force, T_i, in the reinforcement is shown in figure 66. P_i is calculated using figure 67.

$$T_i = P_i \pm (F_{i+1} - F_{i-1})$$

Figure 66. Equation. Tensile connection force.

$$P_i = K_h\left(\gamma_s z_i + q\right)S_v$$

Figure 67. Equation. Horizontal resultant force of lateral Earth pressure acting on the two facing blocks.

If $P_i \pm (F_{i+1} - F_{i-1}) < 0$, T_i should be set equal to 0, as geosynthetic reinforcement can resist only tensile forces (i.e., T_i is always greater than or equal to 0).

From figure 65, figure 68 to figure 70 are derived.

$$T_i = P_i \pm (N_{i+1} - N_{i-1})\tan\ \delta;\ T_i = 0 \text{ if } T_i \le 0$$

Figure 68. Equation. Tensile connection force substituting the components derived in figure 67.

Where N_{i+1} and N_{i-1} are normal forces on the top and the bottom of the two adjacent blocks.

$$T_i = P_i \pm (W_i + F_{fi})\tan\ \delta$$

Figure 69. Equation. Tensile connection force solved in terms of the weight of the facing block and friction between the soil and wall facing.

Or

$$T_i = P_i \pm (\gamma_b b S_v + \overline{p} S_v \tan\ \beta)\tan\ \delta$$

Figure 70. Equation. Simplified tensile connection force.

Where:

F_{fi} = Frictional resultant force between wall facing and soil.
γ_b = Unit weight of facing block.
b = Width of facing block.
S_v = Reinforcement spacing.
δ = Friction angle between modular block facing elements (δ can be the friction angle between facing blocks if there is no reinforcement between the blocks, or it can be the friction angle between facing block and geosynthetic if there is reinforcement sandwiched between blocks).
β = Friction angle between back face of wall and soil.
$\overline{p}$ = Average net Earth pressure acting on the facing due to Earth pressure on the facing and the pressure caused by the reinforcement force. The value of $\overline{p}$ can be estimated as shown in figure 71.

$$\overline{p}\ =\ \frac{F_{i+1} - F_{i-1}}{S_v}\ =\ \gamma_b\ b\ \tan\delta$$

Figure 71. Equation. Average net Earth pressure on the facing.

Substituting figure 71 into figure 70, T_i, the connection force at depth z_i, can be determined as shown in figure 72 and figure 73.

$$T_i = P_i \pm (\gamma_b b S_v + \gamma_b b S_v \tan\delta \tan\beta)\tan\delta$$

Figure 72. Equation. Tensile connection force at a given depth.

$$T_i = K_h(\gamma_s z_i + q)S_v \pm (\gamma_b b S_v + \gamma_b b S_v \tan\delta \tan\beta)\tan\delta$$

Figure 73. Equation. Tensile connection force substituting figure 67.

Therefore, the tensile connection force in the reinforcement at depth z_i can be expressed as shown in figure 74.

$$T_i = K_h(\gamma_s z_i + q)S_v \pm \gamma_b b S_v \tan\delta(1 + \tan\delta \tan\beta)\text{; T} = 0 \text{ if T} \le 0$$

Figure 74. Equation. Tensile connection force as a simplification of figure 73.

Note that if the friction between the back face of the wall facing and the soil behind the wall is ignored, the connection force at depth z_i is as shown in figure 75.

$$T_i = K_h(\gamma_s z_i + q)S_v \pm (\gamma_b b S_v)(\tan\delta)\text{; T} = 0 \text{ if T} \le 0$$

Figure 75. Equation. Tensile connection force ignoring the effect of fiction between the back of the block and soil.

Calculating the reinforcement connection forces in a GRS wall with modular block facing by a simple equation can eliminate a considerable amount of work designing a GRS wall. In designing GRS walls with segmental facing, the connection forces are involved. A series of experimental tests to measure the connection forces were conducted by many researchers. According to the results, if the blocks are heavy and well connected, the GRS walls with block facing would perform very well.[16,17] The values of the connection forces can be estimated by using figure 76 for a typical GRS wall with modular block facing.

$$T_i = K_h(\gamma_s z_i + q)S_v - (\gamma_b b S_v)(\tan\delta)$$

Figure 76. Equation. Connection force for a typical GRS wall with modular block facing.

The resistant connection force at depth z_i at facing can be estimated using figure 77.

$$F_r = 2\gamma_b b z_i(\tan\delta)$$

Figure 77. Equation. Resistant connection force.

Comparisons of connection forces and maximum friction capacity at facing blocks are shown in figure 78 and figure 79.

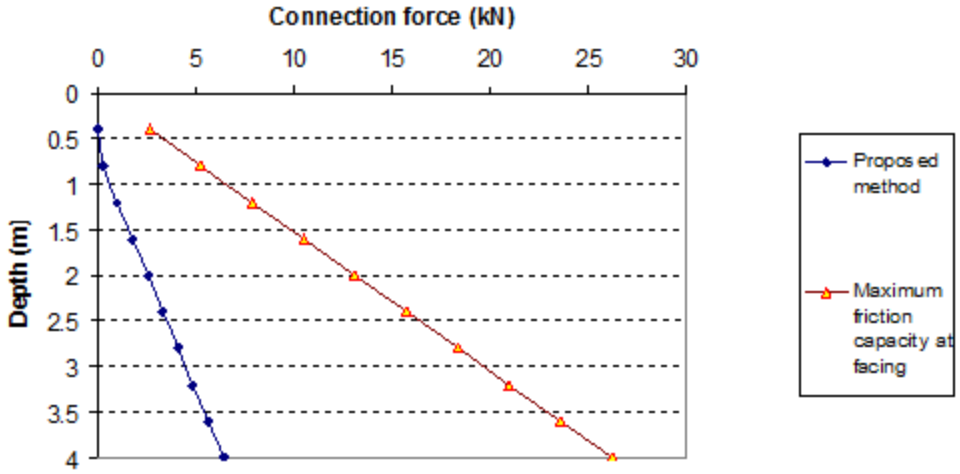

1 kN = 224.81 lbf
1 m = 3.28 ft

Figure 78. Graph. Connection forces in reinforcement (q = 0 kip/ft (0 kN/m)) (wall data from section 3.3.1 with ψ = 15 degrees).

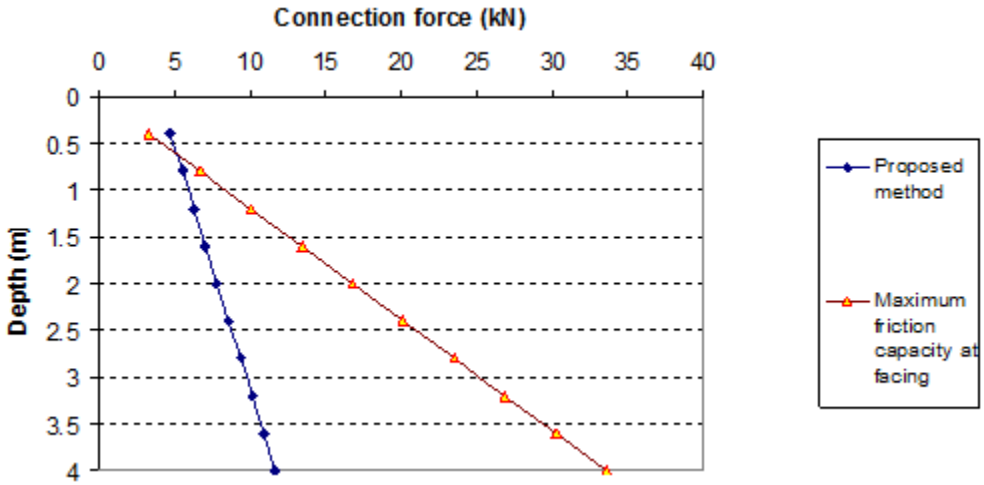

1 kN = 224.81 lbf
1 m = 3.28 ft

Figure 79. Graph. Connection forces in reinforcement (q = 3.4 kip/ft (50 kN/m)) (wall data from section 3.3.1 with ψ = 15 degrees).

Figure 78 and figure 79 show the values of connection forces with the maximum connection friction forces with a surcharge of 0 and 3.4 kip/ft (0 and 50 kN/m). For most of the cases, the lightweight blocks (without strong key connections between blocks) can be used for GRS walls. With the heavy surcharge, some blocks at the top of the wall may be unstable, as shown in figure 79.

3.2.3 Lateral Movement of GRS Walls with Modular Block Facing

From figure 64 and figure 76, the displacement of a GRS wall with modular block facing at depth z_i can be determined by figure 80.

$$\Delta_i = 0.5\left(\frac{K_h\left(\gamma_s z_i + q\right)S_v - \gamma_b b S_v \tan\delta(1+\tan\delta\tan\beta)}{K_{re\inf}}\right)\left(H - z_i\right)\left[\tan\left(45° - \frac{\psi}{2}\right) + \tan\left(90° - \varphi_{ds}\right)\right]$$

Figure 80. Equation. Lateral displacement of a GRS wall with modular block facing.

Figure 80 is the analytical model in this study. When the frictional resistance between the back face of the wall facing and the soil can be ignored, the displacement of the wall at depth z_i will reduce to figure 81.

$$\Delta_i = 0.5\left(\frac{K_h\left(\gamma_s z_i + q\right)S_v - \left(\gamma_b b S_v\right)\left(\tan\delta\right)}{K_{re\inf}}\right)\left(H - z_i\right)\left[\tan\left(45° - \frac{\psi}{2}\right) + \tan\left(90° - \varphi_{ds}\right)\right]$$

Figure 81. Equation. Lateral displacement of a GRS wall with modular block facing ignoring the effect of fiction between the back of the block and soil.

Note that the lateral movement calculated by figure 81 will be slightly larger than that calculated by figure 80.

3.2.4 Required Tensile Strength of Reinforcement of GRS Walls

The analytical model for estimating wall movement can also be used to determine the required reinforcement strength for a limiting value of maximum lateral wall movement (e.g., 2 inches (50 mm) or 1 percent of wall height, whichever is smaller) for any given backfill strength properties. The required reinforcement strength, $T_{required}$, can be determined from the maximum allowable lateral movement at the wall face, Δ_{max}, as shown in figure 82.

$$T_{required} = \frac{2\,\Delta_{\max} K_{re\inf}}{\left(H - z_i\right)\left[\tan\left(45° - \frac{\psi}{2}\right) + \tan\left(90° - \varphi_{ds}\right)\right]}$$

Figure 82. Equation. Required tensile reinforcement strength at a given allowable lateral movement of the wall face.

Figure 82 applies to any facing rigidity because the force T is related only to Δ_{max} and is unaffected by the facing rigidity.

3.3 VERIFICATION OF THE ANALYTICAL METHOD

To verify the analytical model developed in this study, the model calculation results were first compared to the Jewell-Milligan method for GRS walls with negligible facing rigidity. The model calculation results were then compared to measured data from a full-scale experiment.

3.3.1 Comparison to the Jewell-Milligan Method for Lateral Wall Movement

The model calculation results of wall movement from the analytical model were first compared to the results of the Jewell-Milligan method using an example.[19] The conditions of the wall in this example are as follows:

- **Wall height:** H = 13 ft (4.0 m).

- **Geosynthetic reinforcement**: Vertical spacing (S_v) = 1.3 ft (0.4 m) and stiffness (K_{reinf}) = 13.7 kip/ft (200 kN/m).

- **Backfill**: Free-draining granular soil unit weight (γ_s) = 0.11 kip/ft^3 (18 kN/m^3), cohesion (c) = 0, friction angle (ϕ_{ds}) = 35 degrees, and dilation angle (ψ) = 5 degrees.

- **Facing**: Modular concrete blocks width (b) = 1 ft (0.3 m), unit weight (γ_b) = 0, 0.13, and 0.19 kip/ft^3 (0, 20, and 30 kN/m^3).

- **Interface between adjacent blocks**: Cohesion (c) = 0 and friction angle (δ) = 25 degrees.

- **Interface friction between back face of facing and soil**: β = 0 degrees.

The results of the comparisons between the analytical model and the Jewell-Milligan method are shown in figure 83 through figure 94 for different weights of facing blocks (unit weight of block γ_b = 0, 0.06, 0.13, and 0.19 kip/ft^3 (0, 10, 20, and 30 kN/m^3)), each with different values of surcharge pressure (q = 0, 0.7, and 3.4 kip/ft (0, 10, or 50 kN/m)). The value q = 0.7 kip/ft (10 kN/m) represents a typical surcharge for highway design. These figures indicate that for all facing conditions (i.e., for different values of γ_b), the effect of surcharge on wall movement is significant. The deformed shape of the wall face is different at q = 0 and 3.4 kip/ft (0 and 50 kN/m). At q = 0 kip/ft (0 kN/m), the wall bulges at mid-height, but as the surcharge increases, the top of the wall face begins to move outward. At q = 3.4 kip/ft (50 kN/m), the largest wall movement occurs near the top of the wall.

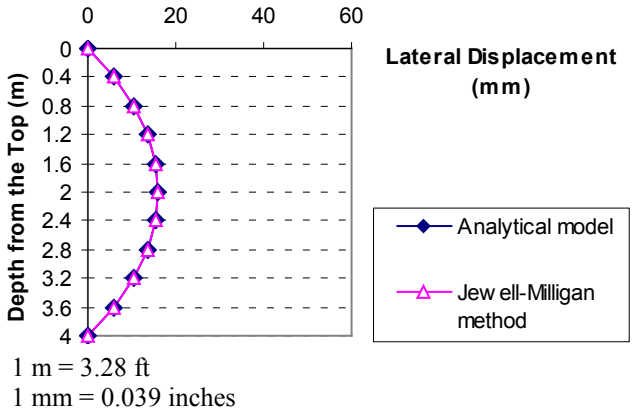

Figure 83. Graph. Lateral displacement calculated by the Jewell-Milligan method and the analytical model, γ_b = 0 kip/ft^3 (0 kN/m^3), q = 0 kip/ft (0 kN/m).

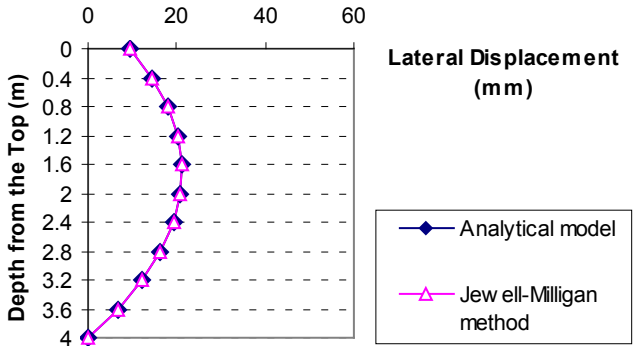

1 m = 3.28 ft
1 mm = 0.039 inches

Figure 84. Graph. Lateral displacement calculated by the Jewell-Milligan method and the analytical model, γ_b = 0 kip/ft^3 (0 kN/m^3), q = 0.7 kip/ft (10 kN/m).

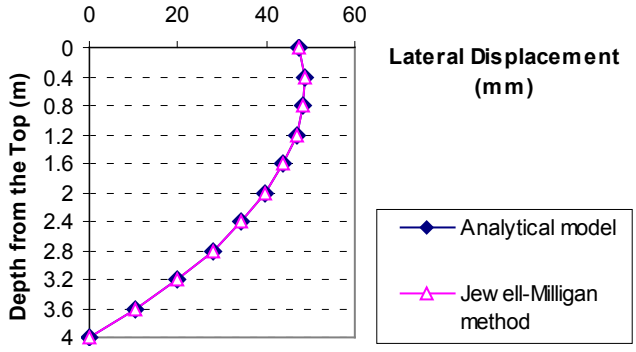

1 m = 3.28 ft
1 mm = 0.039 inches

Figure 85. Graph. Lateral displacement calculated by the Jewell-Milligan method and the analytical model, γ_b = 0 kip/ft^3 (0 kN/m^3), q = 3.4 kip/ft (50 kN/m).

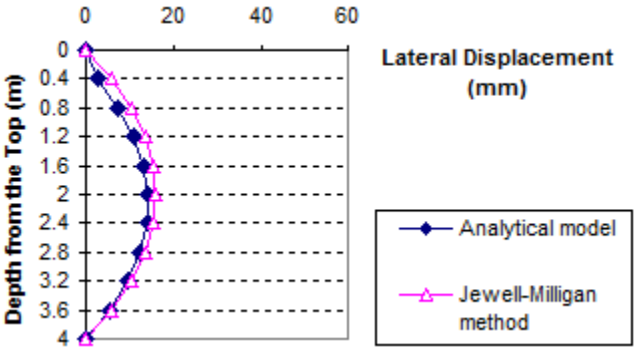

1 m = 3.28 ft
1 mm = 0.039 inches

Figure 86. Graph. Lateral displacement calculated by the Jewell-Milligan method and the analytical model, γ_b = 0.06 kip/ft^3 (10 kN/m^3), q = 0 kip/ft (0 kN/m).

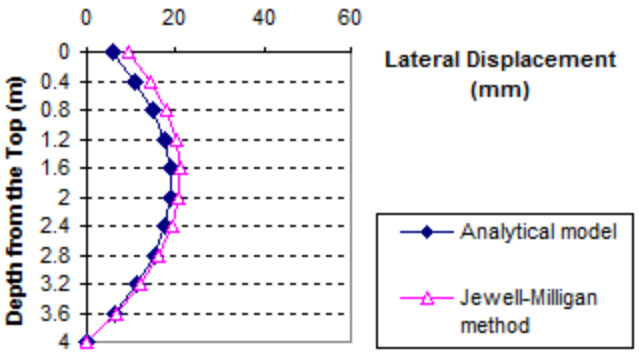

1 m = 3.28 ft
1 mm = 0.039 inches

Figure 87. Graph. Lateral displacement calculated by the Jewell-Milligan method and the analytical model, γ_b = 0.06 kip/ft^3 (10 kN/m^3), q = 0.7 kip/ft (10 kN/m).

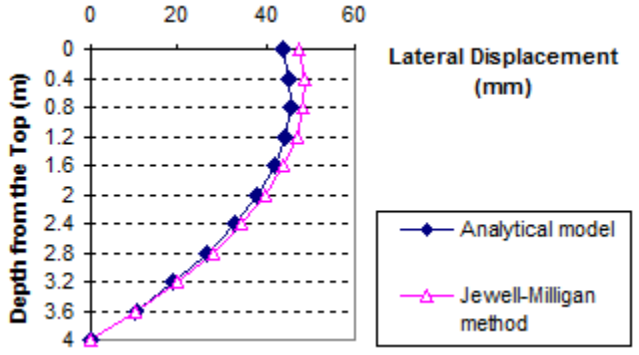

1 m = 3.28 ft
1 mm = 0.039 inches

Figure 88. Graph. Lateral displacement calculated by the Jewell-Milligan method and the analytical model, γ_b = 0.06 kip/ft^3 (10 kN/m^3), q = 3.4 kip/ft (50 kN/m).

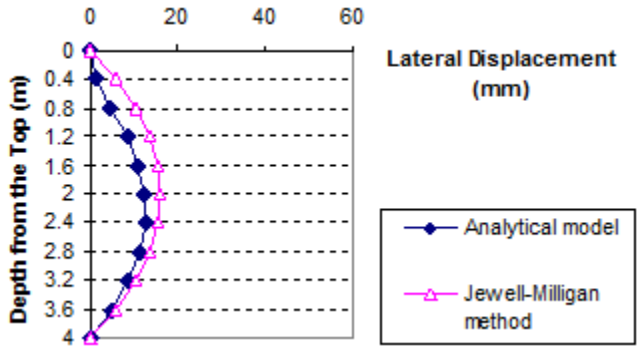

1 m = 3.28 ft
1 mm = 0.039 inches

Figure 89. Graph. Lateral displacement calculated by the Jewell-Milligan method and the analytical model, γ_b = 0.13 kip/ft^3 (20 kN/m^3), q = 0 kip/ft (0 kN/m).

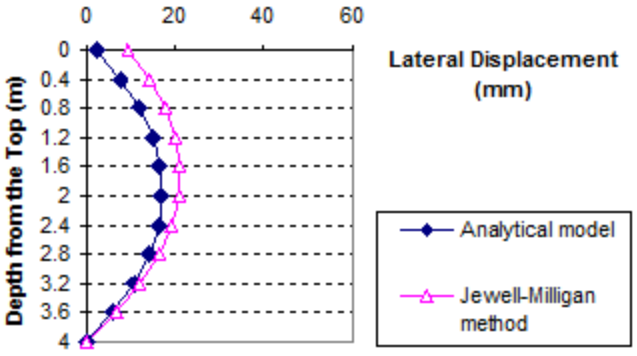

1 m = 3.28 ft
1 mm = 0.039 inches

Figure 90. Graph. Lateral displacement calculated by the Jewell-Milligan method and the analytical model, γ_b = 0.13 kip/ft^3 (20 kN/m^3), q = 0.7 kip/ft (10 kN/m).

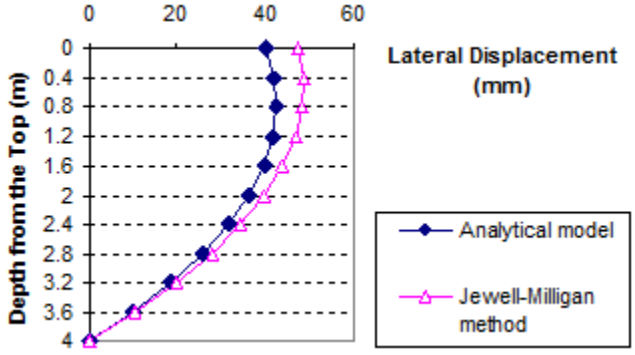

1 m = 3.28 ft
1 mm = 0.039 inches

Figure 91. Graph. Lateral displacement calculated by the Jewell-Milligan method and the analytical model, γ_b = 0.13 kip/ft^3 (20 kN/m^3), q = 3.4 kip/ft (50 kN/m).

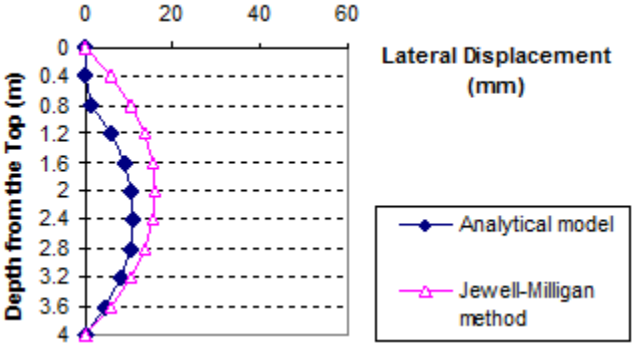

1 m = 3.28 ft
1 mm = 0.039 inches

Figure 92. Graph. Lateral displacement calculated by the Jewell-Milligan method and the analytical model, γ_b = 0.19 kip/ft^3 (30 kN/m^3), q = 0 kip/ft (0 kN/m).

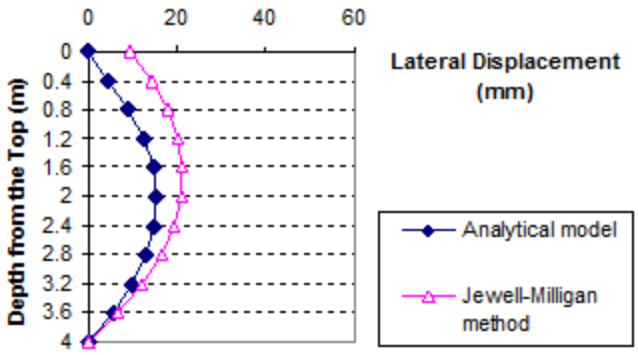

1 m = 3.28 ft
1 mm = 0.039 inches

Figure 93. Graph. Lateral displacement calculated by the Jewell-Milligan method and the analytical model, γ_b = 0.19 kip/ft^3 (30 kN/m^3), q = 0.7 kip/ft (10 kN/m).

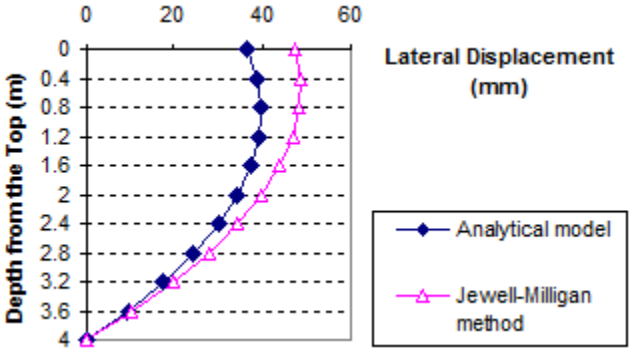

1 m = 3.28 ft
1 mm = 0.039 inches

Figure 94. Graph. Lateral displacement calculated by the Jewell-Milligan method and the analytical model, γ_b = 0.19 kip/ft^3 (30 kN/m^3), q = 3.4 kip/ft (50 kN/m).

As shown in figure 83 through figure 85, when the facing block is weightless (i.e., unit weight γ_b = 0 kip/ft^3 (0 kN/m^3)), the analytical model gives nearly identical lateral wall movement to the Jewell-Milligan method. This is to be expected because facing rigidity is ignored in the Jewell-Milligan method. The figures show that as the facing blocks becomes heavier (i.e., unit weight increases), the wall movement becomes smaller. When a heavy facing block (γ_b = 0.19 kip/ft^3 (30 kN/m^3)) is used, the maximum lateral wall movement can be as much as 35 percent smaller than a wall with negligible facing rigidity.

3.3.2 Comparison to Measured Data of Full-Scale Experiment by Hatami and Bathurst[16,17]

A full-scale experiment of a GRS wall with modular block facing is one of a series of laboratory experiments conducted by Hatami and Bathurst and was referred to as "wall 1" by the authors.[16,17] The parameters of the GRS wall are as follows:

- **Wall height**: H = 12 ft (3.6 m) high with a facing batter of 8 degrees from vertical and seated on a rigid foundation.

- **Soil**: A clean uniform beach sand (γ_s) = 0.107 kip/ft^3 (16.8 kN/m^3), ϕ_{ps} = 44 degrees, ψ = 11 degrees, and c = 0.3 psi (2 kPa).

- **Geosynthetic reinforcement**: A weak biaxial polypropylene geogrid, vertical spacing = 2 ft (0.6 m), reinforcement stiffness = 7.88 kip/ft (115 kN/m), and ultimate strength = 0.96 kip/ft (14 kN/m).

- **Facing**: Solid masonry concrete blocks (12 inches (300 mm) high by 6 inches (150 mm) wide by 8 inches (200 mm) deep) with a shear key on the top surface of block and γ_b = 0.13 kip/ft^3 (20 kN/m^3).

- **Interface between facing blocks**: Friction angle between blocks ($\delta_{b\text{-}b}$) = 57 degrees and cohesion between blocks ($c_{b\text{-}b}$) = 6.7 psi (46 kPa).

Because the analytical model requires that the direct shear friction angle be used in model calculations and assumes a vertical wall face, the direct shear friction angle of the soil and the facing batter factor were determined before using the analytical model to evaluate the lateral movement of the facing.

The direct shear friction angle was calculated as shown in figure 95.

$$\tan\varphi_{ds} = \frac{\sin\varphi_{ps}\cos\psi}{1-\sin\varphi_{ps}\sin\psi} = \frac{\sin 44^\circ \cos 11^\circ}{1-\sin 44^\circ \sin 11^\circ} = 40^\circ$$

Figure 95. Equation. Direct shear friction angle.

The empirical facing batter factor, Φ_{fb}, was calculated from Allen and Bathurst, with facing batter of 8 degrees, as shown in figure 96.[60]

$$\Phi_{fb} = \left(\frac{K_{abh}}{K_{avh}}\right)^d = 0.88$$

Figure 96. Equation. Empirical facing batter factor.

Where:

K_{abh} = The horizontal component of the active Earth pressure coefficient accounting for wall face batter.
K_{avh} = The horizontal component of the active Earth pressure coefficient for a vertical wall.
d = Constant coefficient.

Allen and Bathurst found that the value of d = 0.5 would yield the best fit for available T_{max} data and recommended using d = 0.5 for determining Φ_{fb}.[60]

Figure 97 and figure 98 show lateral movement of the GRS wall under surcharge pressures of 3.4 and 4.8 kip/ft (50 and 70 kN/m), respectively, for the mean value of measured displacement, the Jewell-Milligan method, and the analytical model.[17] The figures show that the lateral movement calculated by the analytical model is in close agreement with the measured values. Lateral wall movement given by the analytical model agrees much better with the measured values than that

calculated by the Jewell-Milligan method for both surcharge pressures. The lateral movement obtained by the Jewell-Milligan method was as much as 3.5 times as large as the measured movement. Note that the analytical model, not unlike the Jewell-Milligan method, produced a displacement profile that had lower bending stiffness than the measured profile. However, considering that the analytical model is a simplified model, the simulation is adequate.

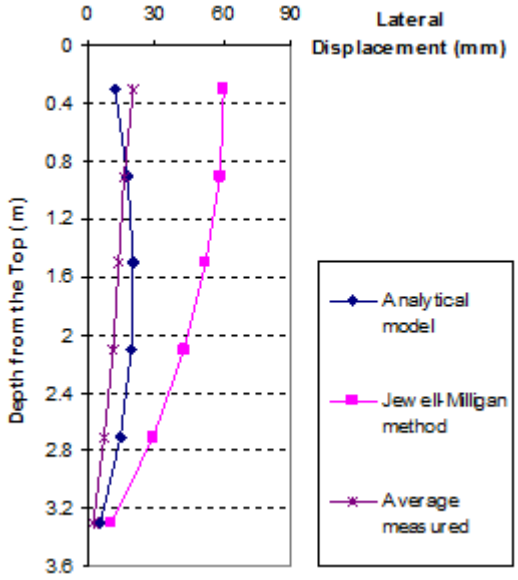

1 m = 3.28 ft
1 mm = 0.039 inches

Figure 97. Graph. Measured lateral displacements with Jewell-Milligan method and analytical model, *q* = 3.4 kip/ft (50 kN/m).

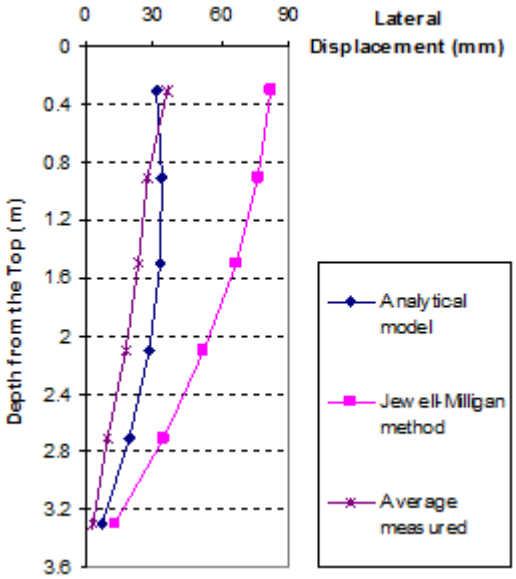

1 m = 3.28 ft
1 mm = 0.039 inches

Figure 98. Graph. Measured lateral displacements with Jewell-Milligan method and analytical model, *q* = 4.8 kip/ft (70 kN/m).

3.4 SUMMARY

An analytical model was developed to predict the profile of lateral movement of a GRS wall with modular block facing. The connection forces in the reinforcement can also be determined by a simple equation. The equation for the lateral movement can also be used in design where the required reinforcement strength can be determined for a prescribed value of maximum allowable lateral wall movement for a given backfill condition. The analytical model has been verified through comparisons with the Jewell-Milligan method. The Jewell-Milligan method is a special case of the analytical model for GRS walls with negligible facing rigidity. Comparisons were also made with a full-scale experiment of a GRS wall with modular block facing. The analytical model offers a simple and improved tool for predicting lateral movement of a GRS wall with modular block facing.

CHAPTER 4. GSGC TESTS

The understanding of GSGC behavior in reinforced soil structures has been lacking. As a result, current design methods have considered the geosynthetic layers simply as added tensile elements and have failed to account for the interaction between soil and geosynthetics. A series of GSGC laboratory tests were designed and conducted to examine the behavior of a GSGC with varying spacing and strength of reinforcement, provide test data for verifying the analytical model for calculating strength properties of a GRS composite as described in chapter 5, and provide test data for calibration of an FE model for a GRS mass. The GSGC tests were conducted at TFHRC in McLean, VA.

4.1 DIMENSIONS OF THE PLANE-STRAIN GSGC TEST SPECIMEN

A soil mass reinforced by layers of geosynthetic reinforcement is not a uniform mass. To investigate the behavior of GSGCs by conducting laboratory tests, it is necessary to determine the proper dimensions of the test specimen so that the test provides an adequate representation of GSGC behavior.

A number of factors were considered prior to determining the test specimen dimensions of the GSGC test, including the following:

- **Plane-strain condition:** Because most GRS structures resemble a plane-strain condition, the test should be conducted in a plane-strain condition.

- **Backfill particle size:** To alleviate the effects of particle size on the test specimen, the dimensions of a generic GRS mass should be at least 6 times as large as the maximum particle size of the soil specimen, as suggested by the U.S. Army Corps of Engineers, and 15 times larger than the average particle size (D_{50}).[(61)] The recommended maximum particle size for the backfill of GRS structures is 0.75 inches (19 mm).[(62)] The specimen dimension, therefore, should be at least 4.7 inches (120 mm).

- **Reinforcement spacing:** The reinforcement spacing plays an important role in the deformation behavior of GRS structures and the load-transfer mechanism of reinforced soil masses.[(63)] The height of a generic GRS mass should be able to accommodate the typical reinforcement spacing of 8 to 12 inches (200 to 300 mm) for GRS walls.

- **Size of reinforcement sheet:** The specimen dimensions in the plane-strain direction, referred to as the width, W, and in the longitudinal direction, referred to as length, L, should be sufficiently large to provide adequate representation of the geosynthetic reinforcement. For polymer grids, enough grid cells need to be included for a good representation of the polymer grid. For nonwoven geotextiles, the aspect ratio of the reinforcement specimen (i.e., the ratio of width to length) should be sufficiently large (e.g., greater than 4) to alleviate significant necking effect. There will be a little necking effect for woven geotextiles regardless of the aspect ratio.

Using Plaxis Version 8.2, a series of FE analyses were conducted to examine the effect of specimen dimensions on the resulting global stress-strain and volume change relationships of the

composites. The objective of the FE analyses was to determine proper dimensions of a GSGC that will produce load-deformation behavior sufficiently close to that of a large mass of soil-geosynthetic composite, referred to as the reference composite.

Figure 99 shows the typical geometric and loading conditions of the GSGC tests. The reference GSGC is taken as a reinforced soil mass with dimensions of 23 ft (7.0 m) high and 16 ft (4.9 m) wide in a plane-strain condition. Four different dimensions of GSSCs were analyzed with varying specimen heights (23, 6.6, 3.3, and 1.6 ft (7.0, 2.0, 1.0 and 0.5 m), while the width of the test specimen was kept as 0.7 × H. In these analyses, the soil was a dense sand. The sand was reinforced by a medium-strength woven geotextile (Geotex® 4×4) at 0.7 ft (0.2 m) vertical spacing. Table 2 lists the conditions and properties of the soil and reinforcement used in the analyses.

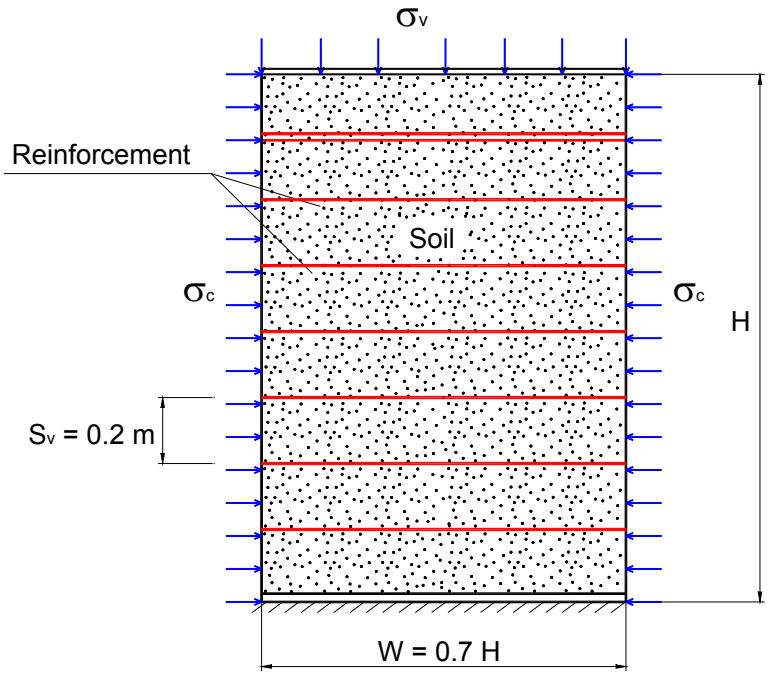

1 m =3.28 ft

Figure 99. Illustration. Typical geometric and loading conditions of a GSGC.

Table 2. Conditions and properties of the backfill and reinforcement used in FE analyses.

Element	Description
Soil	A dense sand where unit weight = 17 kN/m^3; cohesion = 5 kPa; angle of internal friction (ϕ) = 38 degrees; angle of dilation (ψ) = 8 degrees; soil modulus (E_{50}) = 40,000 kPa; and Poisson's ratio = 0.3
Reinforcement	Geotex® 4×4 axial stiffness (EA) = 1,000 kN/m; ultimate strength (T_{ult}) = 70 kN/m; and reinforcement spacing = 0.2 m
Confining pressure	Constant confining pressures of 0 and 30 kPa

1 kN/m^3 = 0.006 kip/ft^3
1 kPa = 0.145 psi
1 kN/m = 0.068 kip/ft
1 m = 3.28 ft

The global stress-strain curves obtained from the analyses are shown in figure 100 and figure 101 for confining pressures (σ_c) of 0 and 4.4 psi (0 and 30 kPa), respectively (a confining pressure of 4.4 psi (30 kPa) is representative of the lateral stress at the mid-height of a 23-ft (7.0-m)-high wall). The corresponding global volume change curves are shown in figure 102 and figure 103. The global vertical strain (ε_v) was calculated by figure 104.

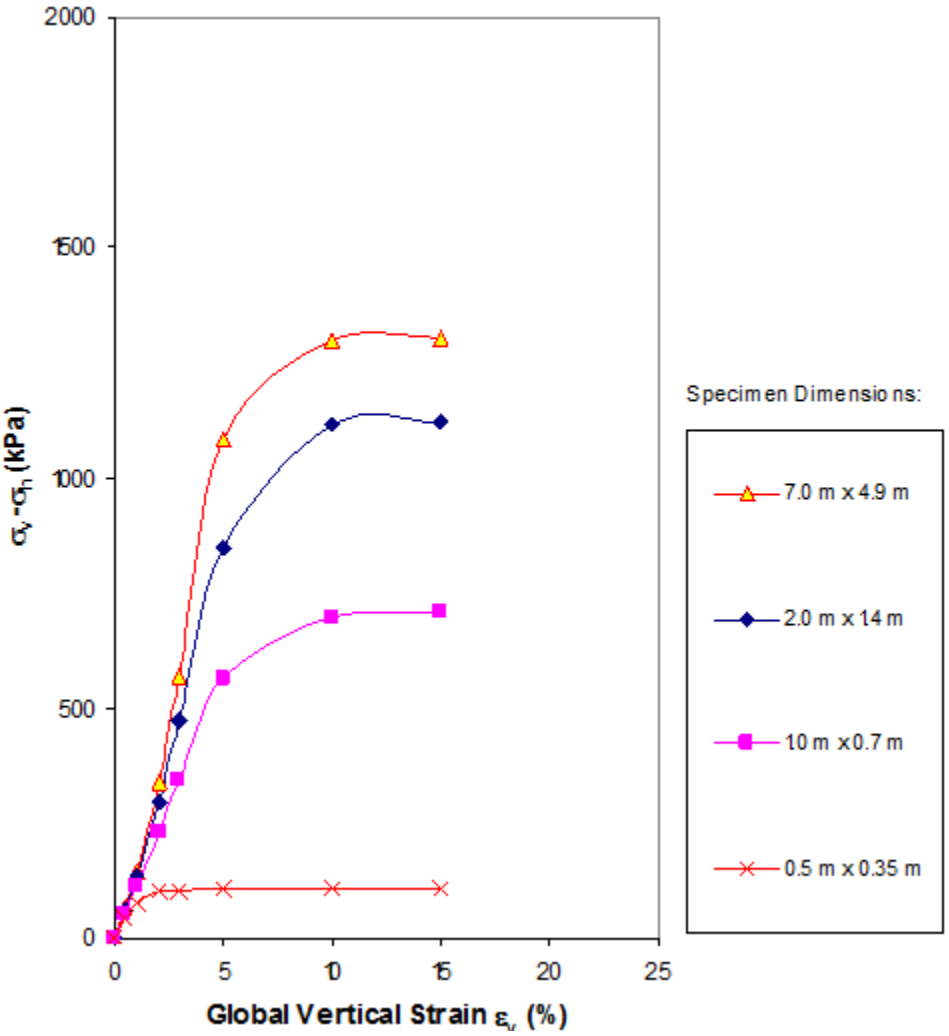

1 kPa = 0.145 psi
1 m = 3.28 ft

Figure 100. Graph. Global stress-strain curves for GSGCs of different dimensions under a confining pressure of 0 psi (0 kPa).

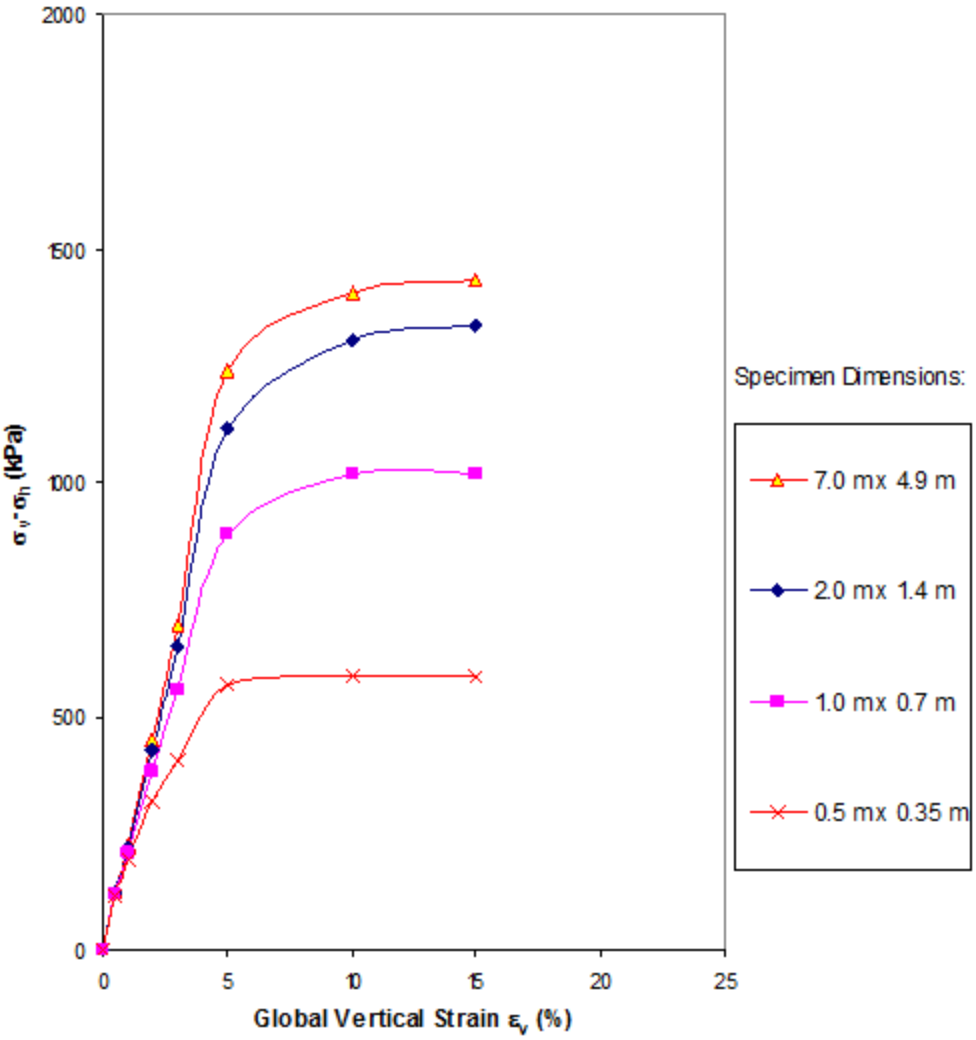

1 kPa = 0.145 psi
1 m = 3.28 ft

Figure 101. Graph. Global stress-strain curves for GSGCs of different dimensions under a confining pressure of 4.4 psi (30 kPa).

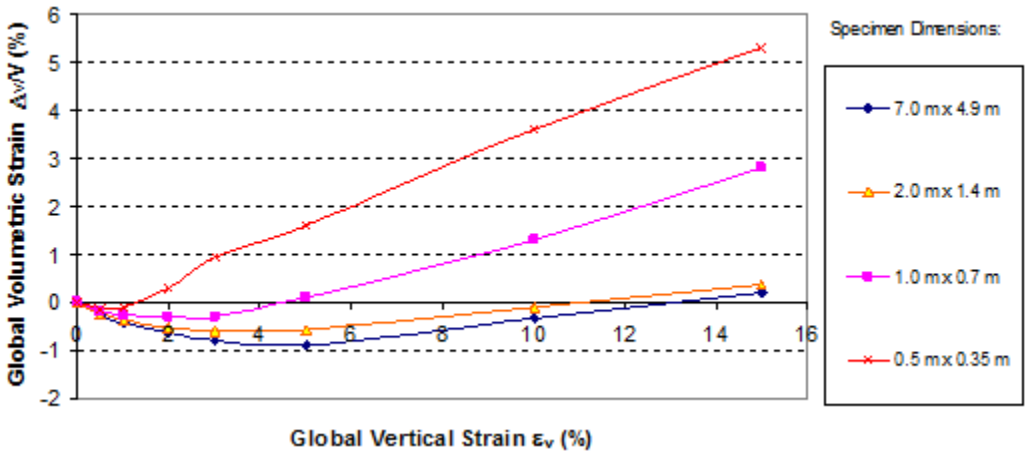

1 m = 3.28 ft

Figure 102. Graph. Global volume change curves for GSGCs of different dimensions under a confining pressure of 0 psi (0 kPa).

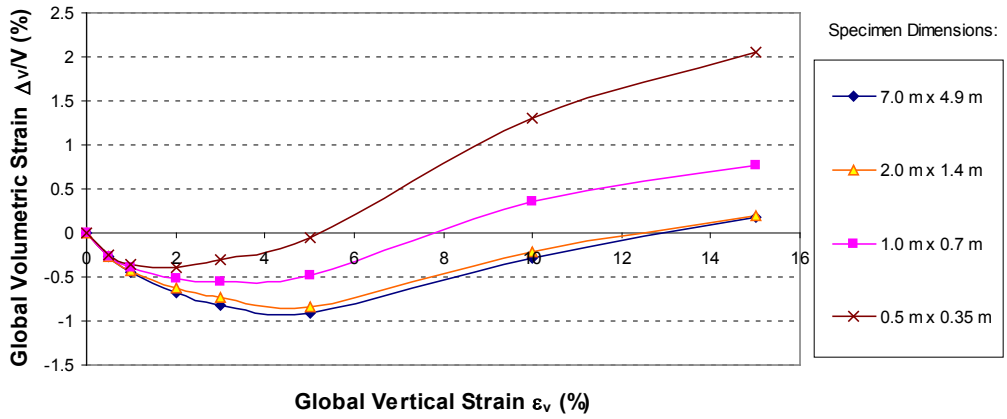

1 m = 3.28 ft

Figure 103. Graph. Global volume change curves for GSGCs of different dimensions under a confining pressure of 4.4 psi (30 kPa).

$$\varepsilon_v = \left(\frac{\Delta H}{H}\right) 100\%$$

Figure 104. Equation. Global vertical strain.

Where:

ΔH = Total vertical displacement of the specimen.
H = Initial height of the specimen.

Figure 100 and figure 101 indicate that a composite with a height of 6.6 ft (2.0 m), width of 4.6 ft (1.4 m), and confining pressure of 4.4 psi (30 kPa) yielded stress-strain and volume change relationships that were sufficiently close to those of the reference composite. Specimen sizes with heights of 3.3 and 1.6 ft (1.0 and 0.5 m) appeared too small to provide an adequate representation of the reference composite.

For comparison, additional analyses were conducted on unreinforced soil. Figure 105 and figure 106 show the global stress-strain curves and global volume change curves of the soil masses without any reinforcement for the different specimen dimensions. The results indicate that a specimen height as small as 1.6 ft (0.5 m) will yield nearly the same stress-strain and volume change relationships as the reference soil mass of height 23 ft (7.0 m) when reinforcement is not present.

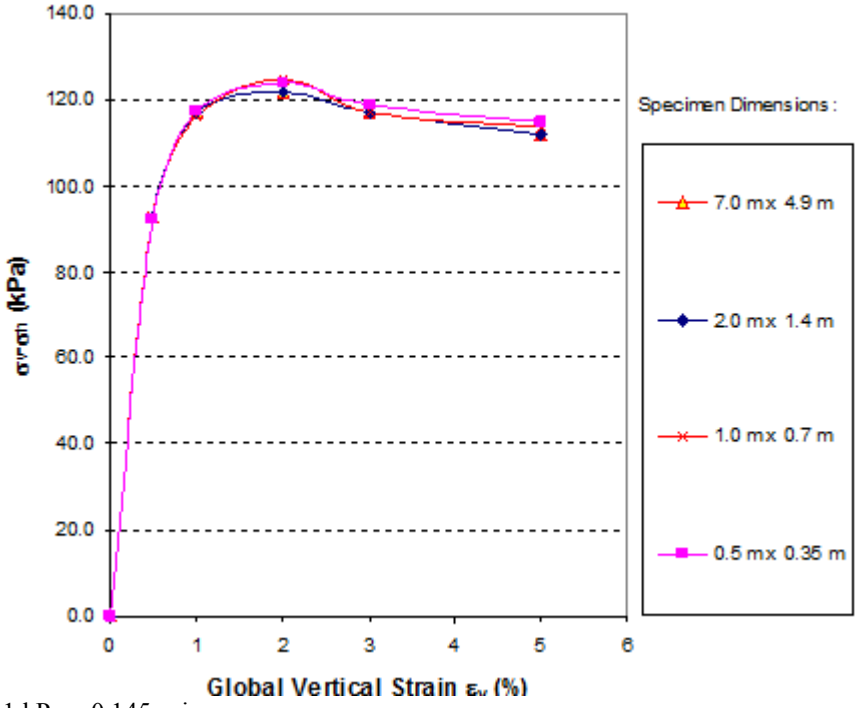

1 kPa = 0.145 psi
1 m = 3.28 ft

Figure 105. Graph. Global stress-strain curves of unreinforced soil under a confining pressure of 4.4 psi (30 kPa).

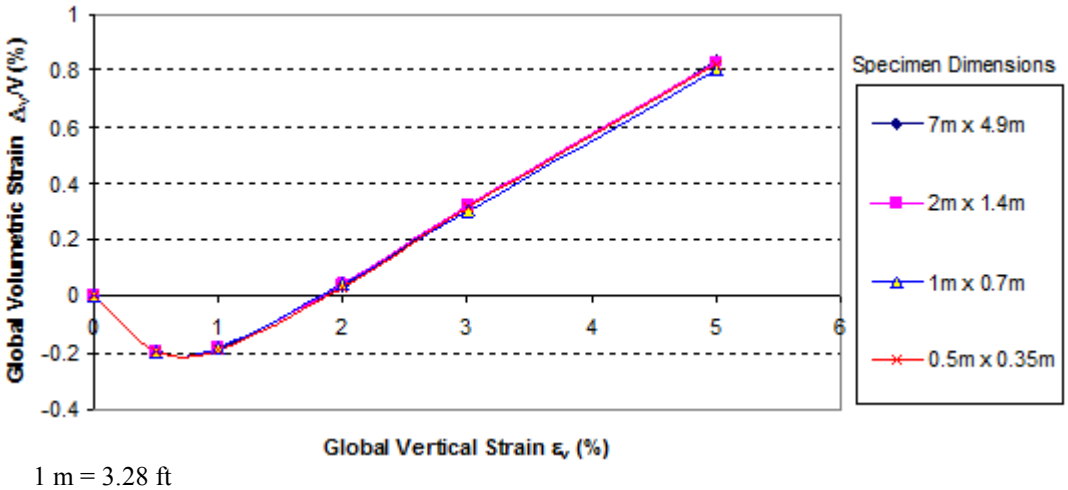

1 m = 3.28 ft

Figure 106. Graph. Global volume change curves of unreinforced soil under a confining pressure of 4.4 psi (30 kPa).

Based on the results of the FE analyses, a specimen height of 6.6 ft (2.0 m) and depth of 4.6 ft (1.4 m) with 0.7-ft (0.2-m) reinforcement spacing was selected for the GSGC tests. The actual specimen dimensions for the GSGC tests are shown in figure 107. Figure 108 and figure 109 show the front and plan views of the GSGC test setup.

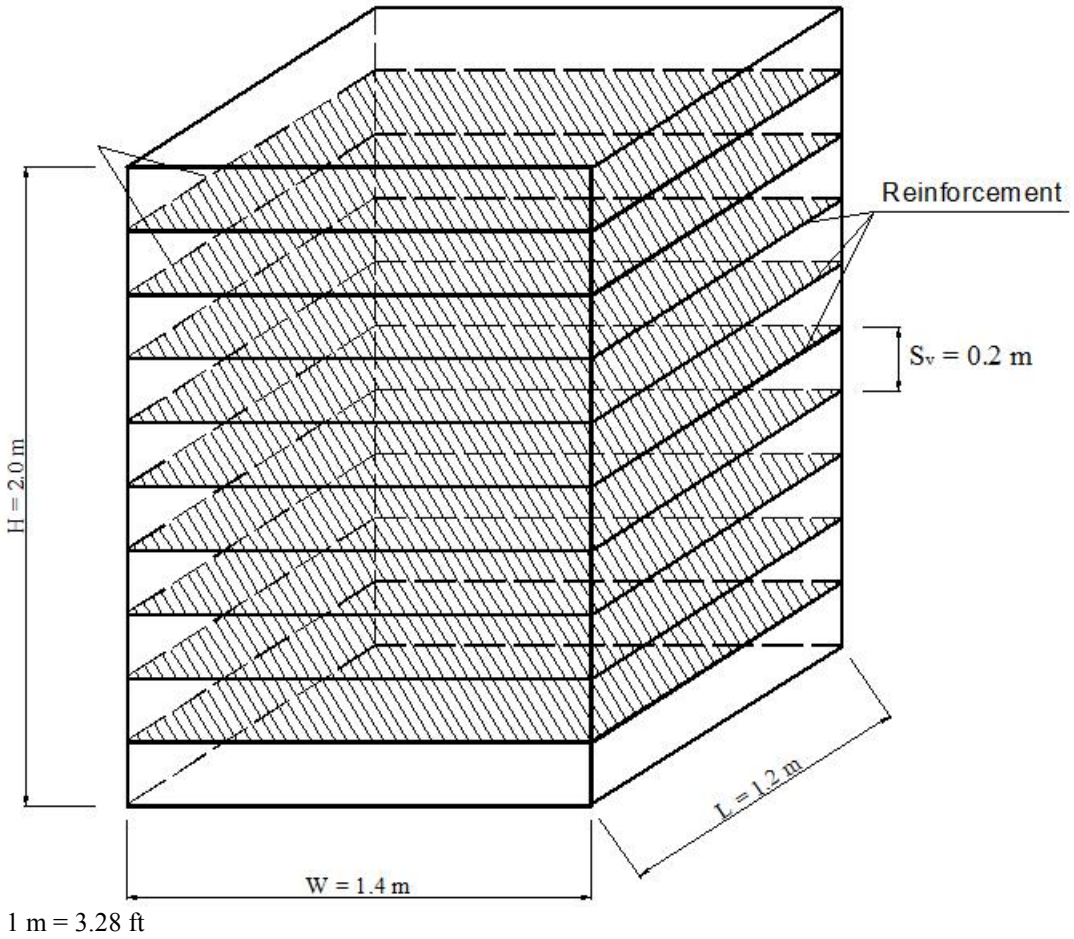

Figure 107. Illustration. Specimen dimensions for the GSGC tests.

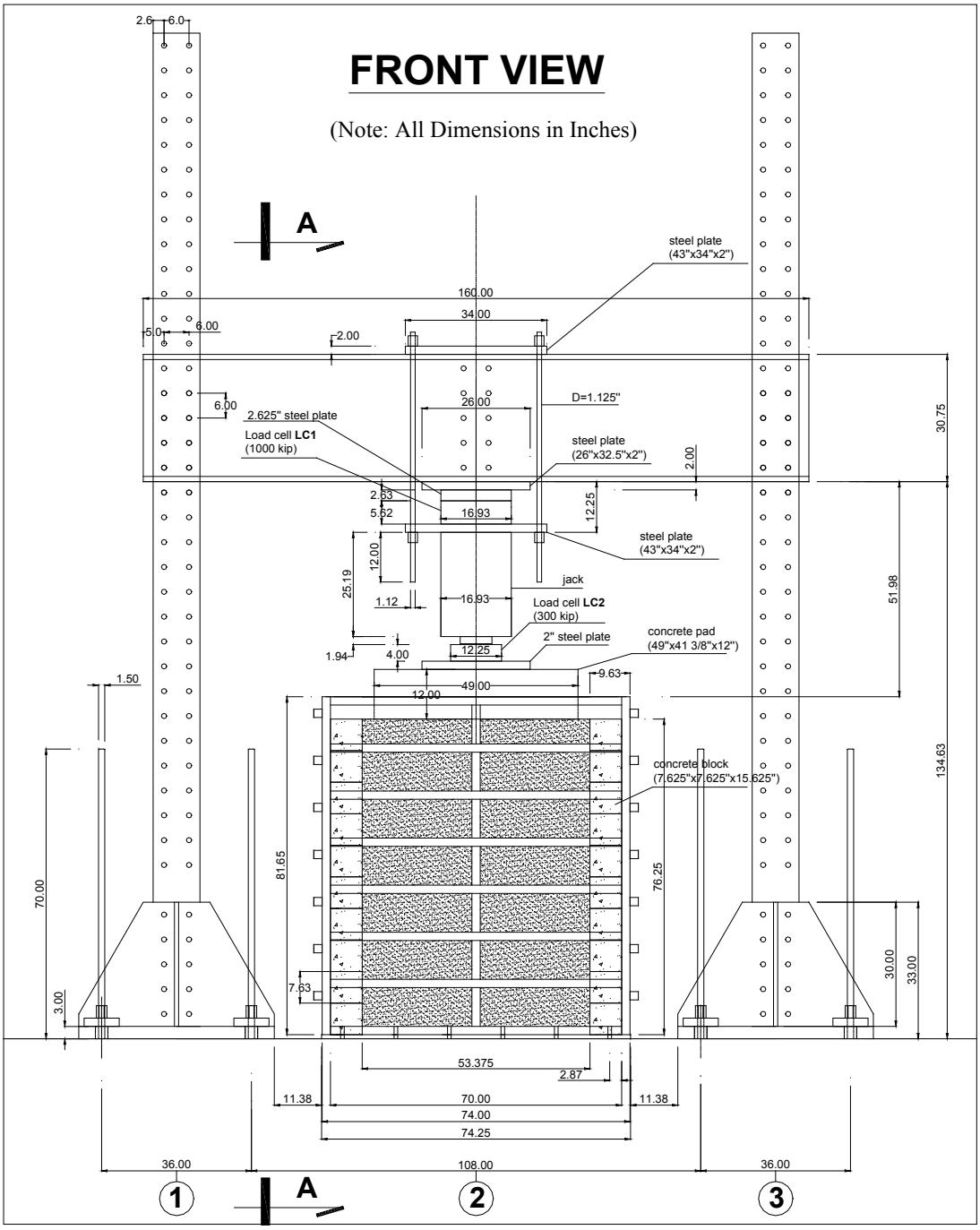

1 mm = 0.039 inches

Figure 108. Illustration. Front view of the test setup.

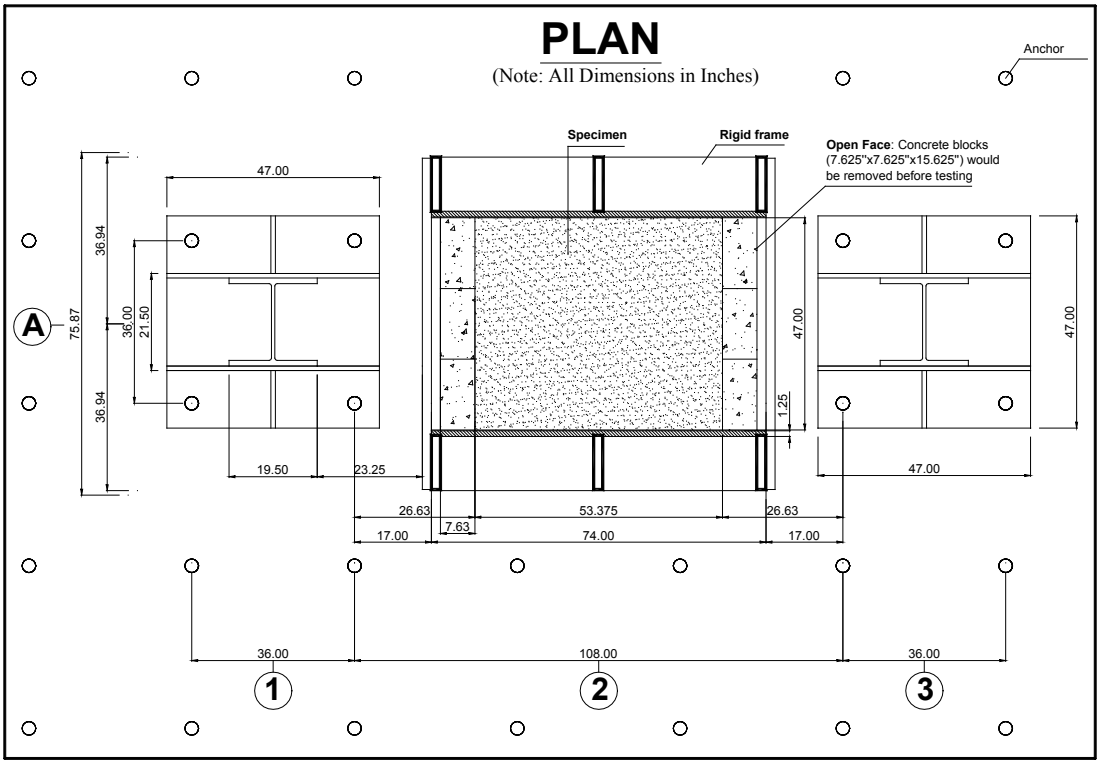

1 mm = 0.039 inches

Figure 109. Illustration. Plan view of the test setup.

4.2 APPARATUS FOR PLANE-STRAIN TEST

To maintain a plane-strain condition for the GSGC specimens throughout the tests, two major factors were considered: (1) the test bin needed to be sufficiently rigid to have negligible lateral deformation in the longitudinal direction (i.e., the length direction) and (2) the friction between the backfill and the side panels of the test bin needed to be minimized to nearly zero.

4.2.1 Lateral Deformation

Five GSGC masses were tested inside a test bin. The test bin was designed to experience little deformation for a surcharge pressure up to 410 psi (2,800 kPa). The test bin is shown in figure 110.

Figure 110. Photo. Test bin.

4.2.2 Friction

Two transparent Plexiglas® panels were attached inside the steel tubing frame to form the side surfaces of the test bin. To minimize the friction between the Plexiglas® and the backfill in these surfaces, a lubrication layer was created on the inside surfaces of the Plexiglas® panels. The lubrication layer consisted of a 0.02-inch (0.5-mm)-thick latex membrane and an approximately 0.04-inch (1 mm)-thick lubrication agent (Dow Corning® 4 Electrical Insulating Compound NSF 6). This procedure has been used successfully in many plane-strain tests conducted by Tatsuoka and his associates at University of Tokyo and by the lead author of this paper in many large-scale experiments. (See references 64–68.) The friction angle between the lubricant layer and the Plexiglas®, as determined by direct shear test, was less than 1 degree.

4.3 TEST MATERIAL

The backfill and geotextile reinforcement employed in the tests are described in the following sections.

4.3.1 Backfill

The backfill was a crushed diabase from a source near Washington, DC. Before conducting the GSGC tests, a series of laboratory tests was performed to determine the properties of the backfill, including the following:

- Gradation test.
- Specific gravity and absorption test of the coarse aggregates.
- Moisture-density tests (Proctor compaction) with rock correction.
- Large-sized triaxial tests with specimen diameter of 6 inches (152 mm).

A summary of some index properties is given in table 3. The grain size distribution of the soil is shown in figure 111. Two gradation tests were performed, and the results agreed well with each other.

Table 3. Summary of index properties of backfill.

Classification	Well-Graded Gravel: Soil Classification A-1a per AASHTO M-15 and Soil Classification GW-GM per ASTM D 2487[69,70]
Maximum dry unit weight	0.15 kip/ft^3 (24.1 kN/m^3)
Optimum moisture content	5.2 percent
Specific gravity of soil solids	3.03

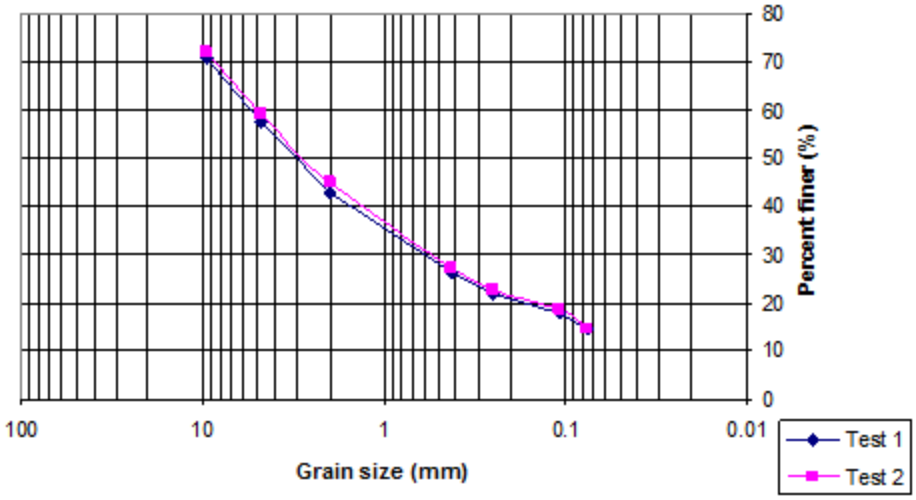

1 mm = 0.039 inches

Figure 111. Graph. Grain size distribution of backfill.

Four triaxial tests were conducted at confining pressures of 5, 15, 30, and 70 psi (34, 103, 207, and 482 kPa), and the results were compared with those performed at the University of Colorado Denver on the same soil. The soil specimen was approximately 6 inches (152 mm) in diameter and 12 inches (305 mm) in height. The shapes of a typical specimen before and after failure are shown in figure 112 and figure 113, respectively. Figure 114 and figure 115 present the stress-strain and volume change curves of the tests. The stress-strain curves obtained by Ketchart and Wu are included for comparison and to furnish a more complete set of data.[(68)] The stress-strain relationships agree well in trend with those by Ketchart and Wu.[(68)] The Mohr-Coulomb failure envelopes of the backfill are shown in figure 116. For confining pressures between 0 and 30 psi (0 and 103 kPa), the strength parameters are c = 10.3 psi (71.0 kPa) and ϕ = 50 degrees. For confining pressures between 30 and 110 psi (103 and 758 kPa), the strength parameters are c = 35.1 psi (242 kPa) and ϕ = 38 degrees.

Figure 112. Photo. Typical triaxial test specimen before test.

Figure 113. Photo. Typical triaxial test specimen after test.

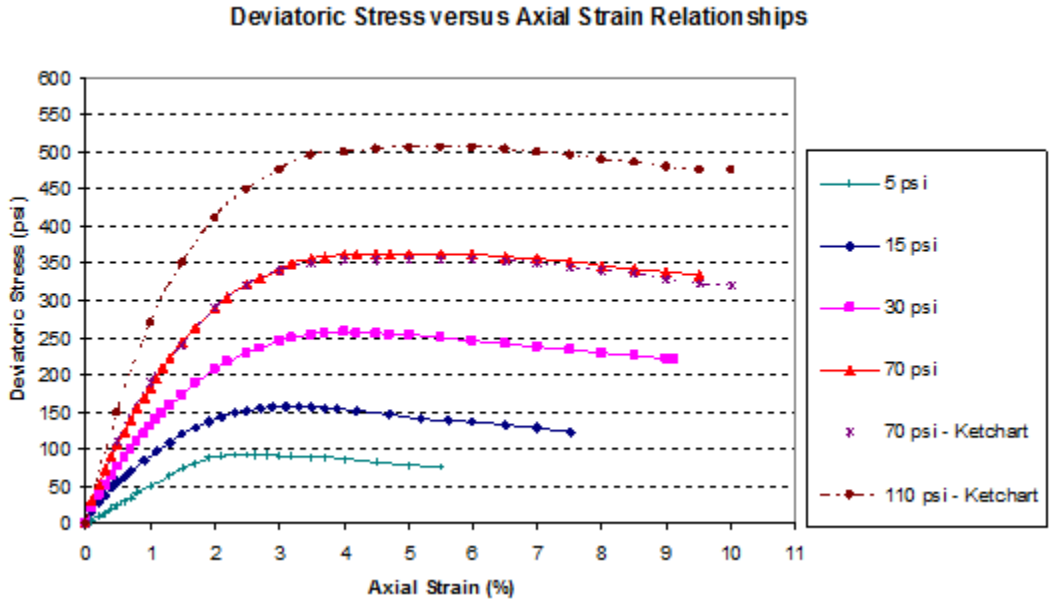

1 kPa = 0.145 psi

Figure 114. Graph. Triaxial test results: stress-strain curves of backfill at 0.15 kip/ft^3 (24.1 kN/m^3) dry density and 5.2 percent moisture.

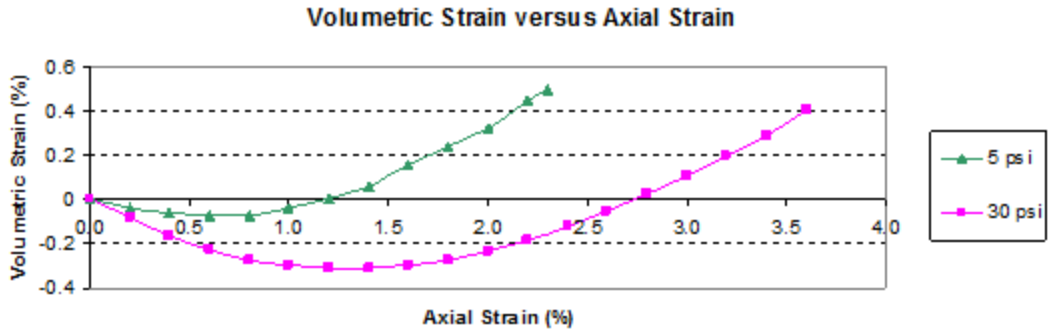

1 kPa = 0.145 psi

Figure 115. Graph. Triaxial test results: volume change curves of backfill at confining pressures of 5 and 30 psi (34.45 and 103.35 kPa).

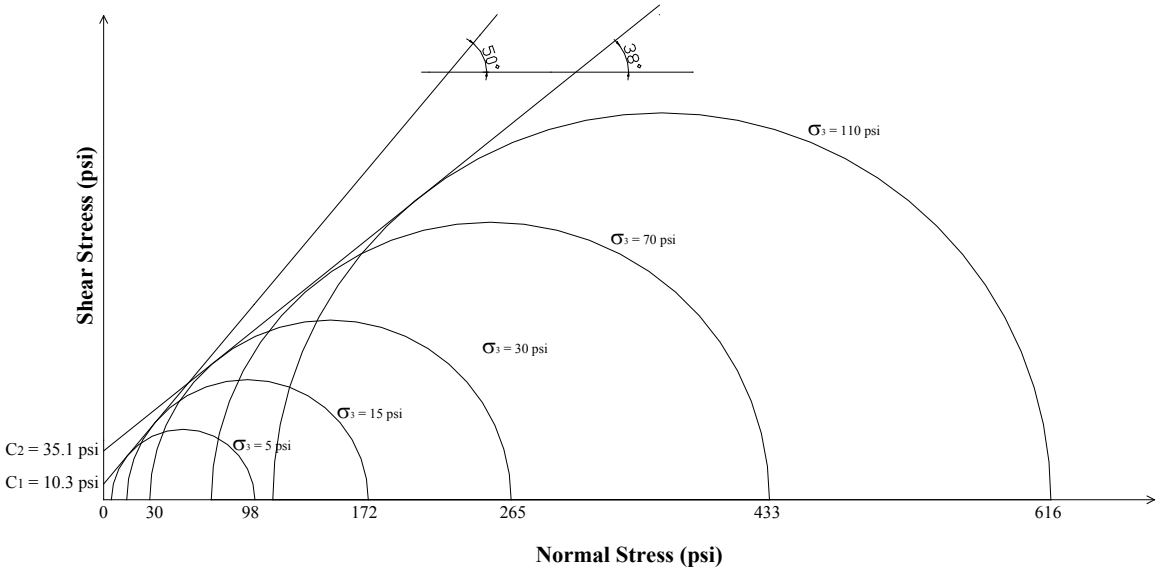

1 kPa = 0.145 psi

Figure 116. Graph. Mohr-Coulomb failure envelopes of backfill.

4.3.2 Geosynthetics

The geosynthetic used in the experiments was Geotex® 4×4 manufactured by Propex® (formally known as Amoco 2044). This geosynthetic is a woven polypropylene geotextile. Table 4 shows its strength properties as provided by the manufacturer.

Table 4. Summary of Geotex® 4×4 properties.

Property	Test Method	Machine Direction (i.e., Wrap Direction)	Cross Direction (i.e., Fill Direction)
Tensile strength (grab)	ASTM D4632[71]	0.6 kip (2.67 kN)	0.5 kip (2.22 kN)
Wide-width tensile ultimate strength	ASTM D4595[72]	400 lb/inch (70 kN/m)	400 lb/inch (70 kN/m)
Wide-width strength at 5 percent strain	ASTM D4595[72]	121 lb/inch (21 kN/m)	217 lb/inch (38 kN/m)
Wide-width ultimate elongation	ASTM D4595[72]	10 percent	10 percent
Puncture	ASTM D4833[73]	170 lb (0.8 kN)	
Trapezoid tearing strength	ASTM D4533[74]	250 lb (1.11 kN)	

Two types of geosynthetics were used for the experiments: a single sheet of Geotex® 4×4 and a double sheet Geotex® 4×4 (by gluing two sheets together using 3M® Super 77 spray adhesive). The double sheet was used to create a geosynthetic that was approximately twice as stiff (and as strong) while maintaining the same interface condition as that of the single-sheet geosynthetic. Geotex® 4×4 geotextile has been used in the construction of hundreds of GRS walls and in many full-scale experiments, including the FHWA GRS pier, Havana Yard Test abutment and pier, Blackhawk preloaded GRS bridge abutment, and National Cooperative Highway Research Program test abutments. (See references 6 and 75–77.)

Uniaxial tension tests were performed on both types of geosynthetic to determine the load-deformation behavior using a specimen 12 inches (305 mm) wide and 6 inches (152 mm) long (see figure 117). The stiffness and strength of the two geosynthetics are shown in table 5, and load-deformation curves are shown in figure 118. The stiffness and strength of the double-sheet Geotex® 4×4 were approximately twice as much as those of the single-sheet Geotex® 4×4 with the breakage strain almost the same.

Figure 117. Photo. Uniaxial tension test of Geotex® 4×4.

Table 5. Properties of Geotex® 4×4 in fill direction.

Geosynthetic	Wide-Width Tensile Strength per ASTM D4595[72]	
	Stiffness (kN/m) at 1 Percent Strain	Ultimate Strength (kN/m) (Percent at Break)
Single-sheet Geotex® 4×4	1,000	70 (12 percent)
Double-sheet Geotex® 4×4	1,960	138 (12 percent)

1 kN/m = 0.069 kip/ft

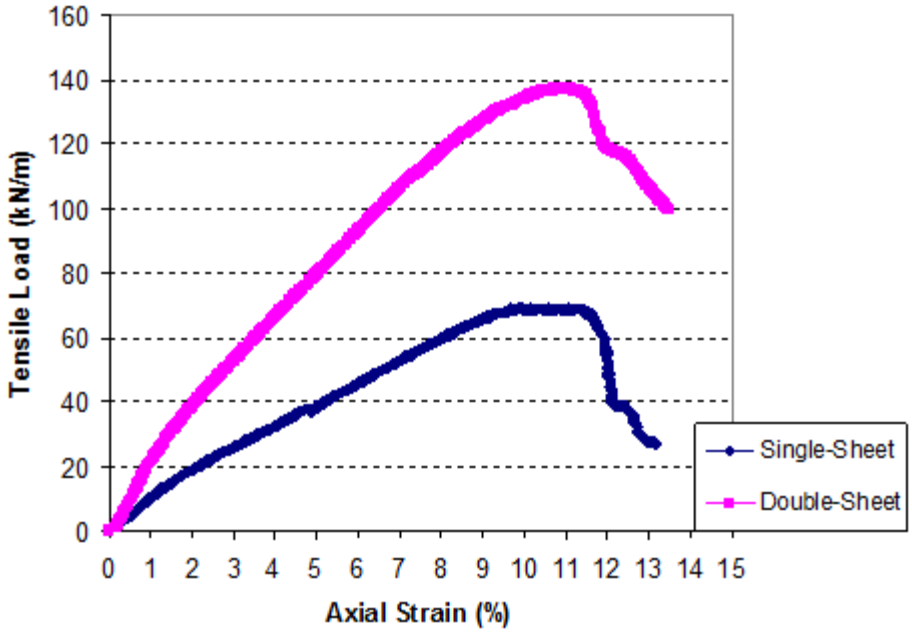

1 kN/m = 68.52 lbf/ft

Figure 118. Graph. Load deformation curves of the geosynthetics.

4.3.3. Facing Block

Blocks used for the facing of the GSGC mass during specimen preparation were hollow concrete blocks with dimensions of 15.625 by 7.625 by 7.625 inches (397 by 194 by 194 mm) and an average weight of 40 lb/block (18.1 kg/block).

4.4 TEST PROGRAM

The test program comprised five GSGC tests. Their test conditions are shown in table 6. The plate compactor used for the tests (MBW GP1200) had a weight of 120 lb (54 kg), plate dimensions of 12 by 21 inches (305 by 533 mm), centrifugal force of 1,500 lbf (6,700 N), rotation speed of 5,000 vibrations/min, and moving speed of 70 ft/min (21 m/min).

Table 6. Test program for GSGC tests.

Test Designation	Geosynthetic Reinforcement	Confining Pressure (kPa)	Wide-Width Strength of Reinforcement (kN/m)	Reinforcement Spacing, S_v (m)
Test 1	None	34	None	No reinforcement
Test 2	Geotex® 4×4	34	70	0.2
Test 3	Double-sheet Geotex® 4×4	34	140	0.4
Test 4	Geotex® 4×4	34	70	0.4
Test 5	Geotex® 4×4	0 (unconfined)	70	0.2

1 kPa = 0.145 psi
1 kN/m = 0.069 kip/ft
1 m = 3.28 ft

4.5 TEST CONDITIONS AND INSTRUMENTATION

4.5.1 Vertical Loading System

The vertical loads were applied to the test specimens by using a 1,000,000-lb- (454,000-kg)-capacity loading frame with a 1,000,000-lb (454,000-kg) hydraulic jack. Loads were measured by load cells and by hydraulic jack pressure gauges. For test 1, two load cells of 100,000 and 300,000 lb (45,400 and 136,200 kg) were used to measure the loads. For tests 2 through 5, a 1,000,000-lb (454,000-kg) load cell was used to measure the loads. A 12-inch (305-mm)-thick concrete pad was placed on top of the specimen before loading. Vertical loads were applied in equal increments with 10 min of elapsed time between increments to allow for equilibrium. The elapsed time also allowed manual recording of displacements of the test specimen. The vertical loads were applied until a failure condition was reached to determine the strength of the composite specimen. The applied pressures on the composite specimens were determined from the applied vertical loads divided by the surface areas of the composite specimens.

4.5.2 Confining Pressure

The confining pressure on the test specimens was applied by vacuuming. The entire surface area of the test specimen was vacuum-sealed with a 0.02-inch (0.5-mm)-thick latex membrane. A prescribed confining pressure of 5 psi (34 kPa) was applied for tests 1 through 4 by connecting the latex membrane to a suction device through two 0.234-inch (6-mm)-diameter flexible plastic tubes. Only test 5 was conducted without confining pressure.

4.5.3 Instrumentation

The specimens were instrumented to monitor their performance during tests. The instruments used include the following:

- **Vertical movement:** Three linear variable displacement transducers (LVDT) and two digital dial indicators were installed on the top of the concrete pad to measure the

vertical movement of the specimen during loading. The vertical movement was measured along the top surface of the concrete pad.

- **Lateral movement:** Ten LVDTs and two digital dial indicators were installed along the height of the specimen (two open sides of the specimen) to measure the lateral movement of the specimen. The location of the LVDTs and digital dial indicators are shown in figure 119.

- **Internal movement:** The internal movement of the soil at selected points in the soil mass was traced by marking the locations of preselected points on a 2-by-2-inch (51-by-51-mm) grid system drawn on the membrane.

- **Reinforcement strain:** To measure the strains in the geotextile, a number of high elongation strain gauges manufactured by Measurements Group, Inc. (type EP-08-250BG-120) were used. Each strain gauge was glued to the geotextile at only two ends to avoid inconsistent local stiffening of geotextile due to the adhesive. The strain gauge attachment technique was developed at the University of Colorado Denver. The gauge was first mounted on a 0.97-by-3.0-inch (25-by-76-mm) patch of a lightweight nonwoven geotextile (see figure 120 and figure 121). A microcrystalline wax and rubber coating (M-Coat B Nitrile Rubber) were used to protect the gauges from moisture. To check the effectiveness of the moisture protection technique, the geotextile specimens with the strain gauges were tested after immersion in water for 24 h. Before placing the reinforcement sheet in the test specimen, an M-Coat FB-2 butyl rubber tape was used to protect the gauges during compaction (see figure 121). To measure the strain distribution of the reinforcement, six strain gauges were mounted on each Geotex® 4×4 sheet (see figure 122).

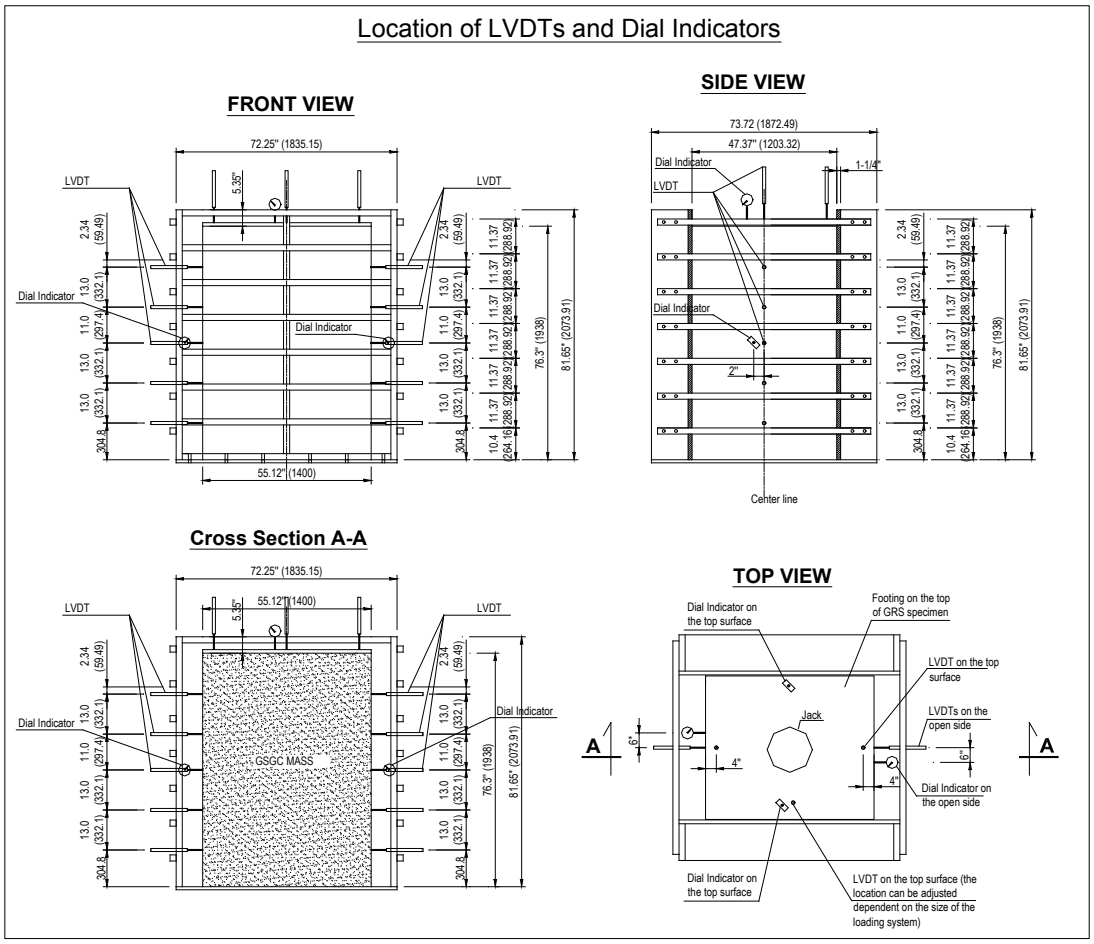

Figure 119. Illustration. Locations of LVDTs and digital dial indicators.

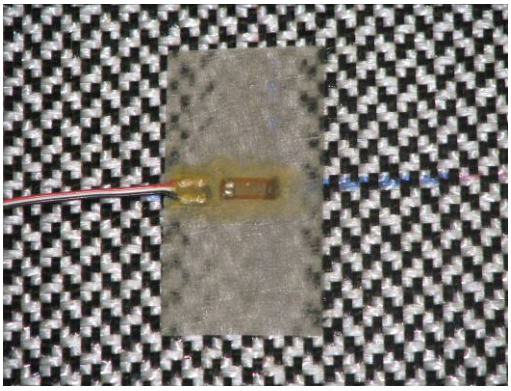

Figure 120. Photo. Strain gauge on Geotex® 4×4 geotextile before applying protection tape.

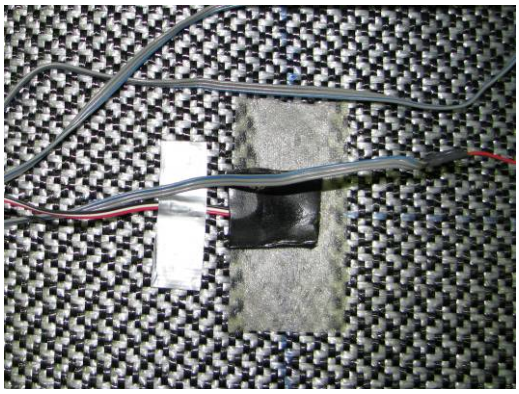

Figure 121. Photo. Strain gauge on Geotex® 4×4 geotextile after applying protection tape.

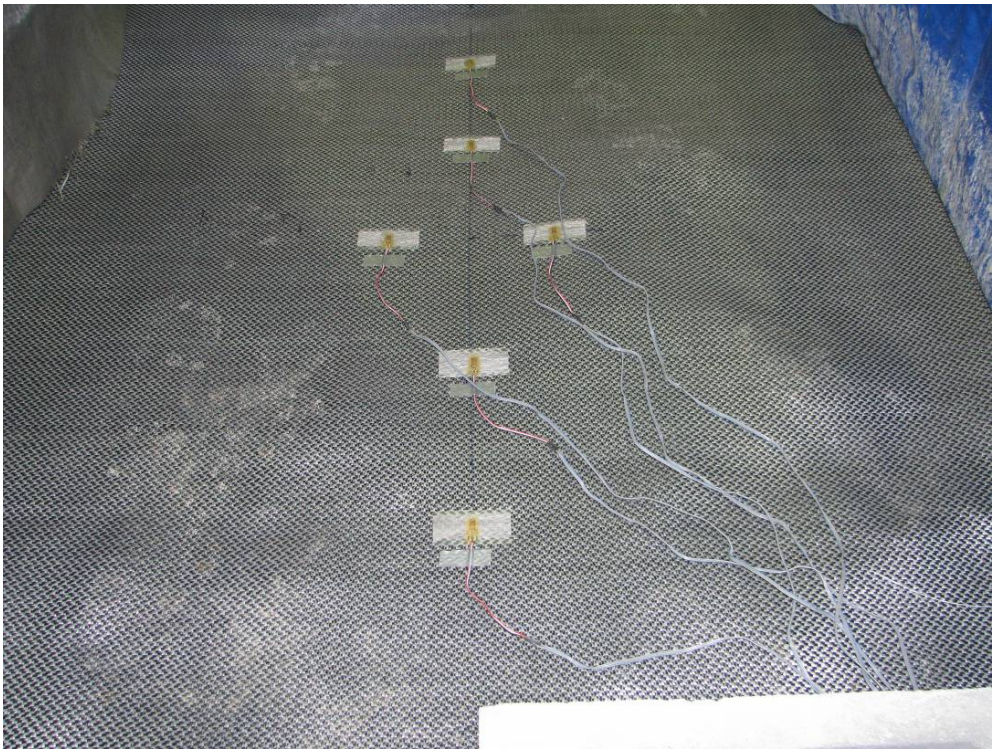

Figure 122. Photo. Strain gauges mounted on Geotex® 4×4 geotextile.

Due to the presence of the lightweight geotextile patch, calibration of the strain gauge was needed. The calibration tests were performed to relate the strain obtained from the strain gauge to the actual strain of the reinforcement. Figure 123 and figure 124 show the calibration curves along the fill direction of Geotex® 4×4 geotextile for the single-sheet and double-sheet specimens, respectively.

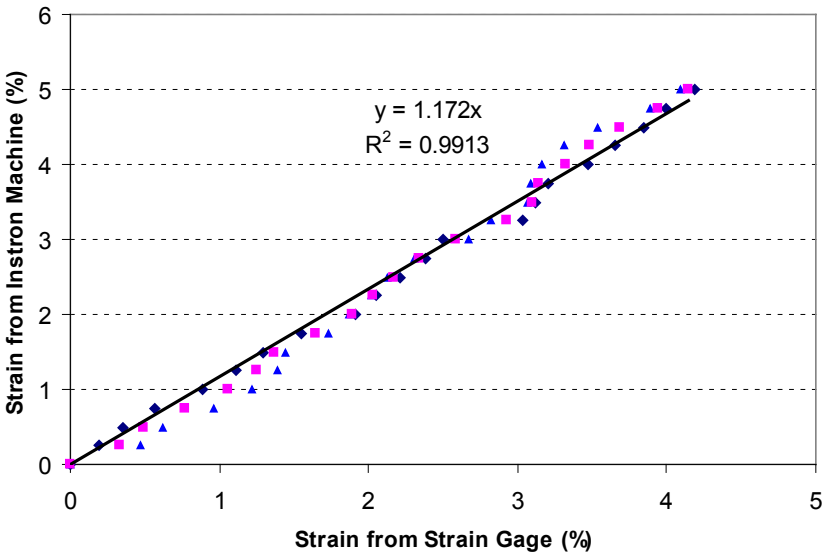

Figure 123. Graph. Calibration curve for single-sheet Geotex® 4×4.

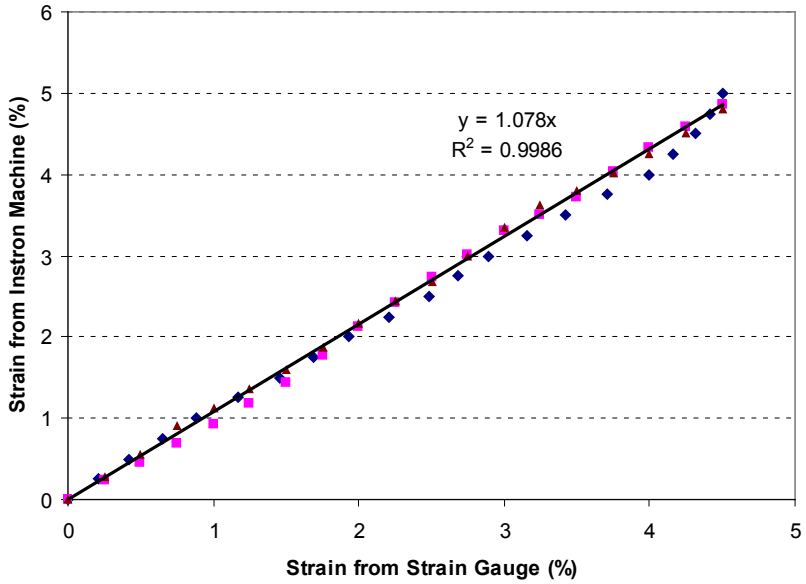

Figure 124. Graph. Calibration curve for double-sheet Geotex® 4×4.

4.5.4 Preparation of Test Specimen for GSGC Tests

The preparation procedure of a typical composite mass with the dimensions of 6.6 by 4.6 by 3.9 ft (2.0 by 1.4 by 1.2 m) is as follows:

1. Mark the anticipated location of the GSGC mass on the Plexiglas®.

2. Apply approximately 0.04-inch (1-mm)-thick lubricating agent (Dow Corning® 4 Electrical Insulating Compound NSF 61) evenly on the inside surfaces of the Plexiglas® (see figure 125).

Figure 125. Photo. Applying grease on Plexiglas® surfaces.

3. Attach a sheet of membrane (with 2.0-by-2.0-inch (51-by-51-mm) grid system predrawn on membrane) over each Plexiglas® and at the bottom of the specimen (see figure 126).

Figure 126. Photo. Attaching membrane.

4. Lay a course of the facing blocks on the open sides of the specimen (see figure 127).

Figure 127. Photo. Placement of the first course of facing block.

5. Place the backfill in the test bin and compact in 0.7-ft (0.2-m) lifts (see figure 128 and figure 129). If needed, check and adjust the backfill moisture before compaction to achieve the target moisture of 5.2 percent.

Figure 128. Photo. Compacting the first lift of backfill.

Figure 129. Photo. Placing backfill for the second lift.

6. Check the water content and dry unit weight of each lift by using a nuclear density gauge (Troxler 3440) by the direct transmission method.

7. Place the next layer of geosynthetic reinforcement (with strain gauges already mounted), covering the entire top surface area of compacted fill and the facing blocks (see figure 130).

Figure 130. Photo. Placing a reinforcement sheet.

8. Repeat steps 4 to 8 until the full height of the composite mass is reached.

9. Sprinkle a 0.2-inch (5-mm)-thick fine sand layer over the top surface of the completed composite mass to level the surface and protect the membrane from being punctured by gravel in the backfill (see figure 131).

Figure 131. Photo. Completion of compaction of the composite mass and leveling the top surface with 0.2-inch (5-mm)-thick sand layer.

10. Place a geosynthetic sheet on top of the composite mass (see figure 132).

Figure 132. Photo. Completed composite mass with a geotextile sheet on the top surface.

11. Glue a sheet of membrane to the top edge of the side membrane sheets (see figure 133).

Figure 133. Photo. Top surface of the composite mass covered with a sheet of membrane.

12. Remove all facing blocks and trim off the excess geotextile (see figure 134).

Figure 134. Photo. Removing facing blocks and trimming off excess geosynthetic reinforcement.

13. Insert strain gauge cables through the plastic openings that were already attached on the membrane sheets at prescribed locations (see figure 135).

Figure 135. Photo. Inserting strain gauge cables through the membrane sheet.

14. Glue membrane sheets to enclose entire composite mass.

15. Apply vacuum to the composite mass at a low pressure of 2.0 psi (14 kPa) (see figure 136).

Figure 136. Photo. Vacuuming the composite mass with a low pressure.

16. Seal the connection between cables and membrane with epoxy to prevent air leaks (see figure 137). The low vacuum pressure allows the epoxy to seal the connection well.

Figure 137. Photo. Sealing the connection between cable and membrane with epoxy to prevent air leaks.

17. Raise the vacuum pressure to 4.9 psi (34 kPa) and check air leaks under vacuuming (see figure 138). Measure the specimen dimensions (see table 7 for specimen dimensions of five tests).

Figure 138. Photo. Checking air leaks under vacuuming.

Table 7. Dimensions of the GSGC specimens before loading.

Test	Height, inches (m)	Width, inches (m)	Length, inches (m)
Test 1	76.25 (1.937)	57.00 (1.448)	47.00 (1.194)
Test 2	76.35 (1.939)	54.00 (1.372)	46.75 (1.187)
Test 3	76.35 (1.939)	53.00 (1.346)	46.75 (1.187)
Test 4	76.30 (1.938)	58.75 (1.492)	46.75 (1.187)
Test 5	76.35 (1.939)	49.00 (1.245)	46.75 (1.187)

Figure 139 shows the LVDTs to monitor the lateral movement of a test specimen. The locations of the selected points for the tests are depicted in figure 140. The measured dry unit weights of five tests are shown in figure 141.

Figure 139. Photo. LVDTs on an open side of test specimen.

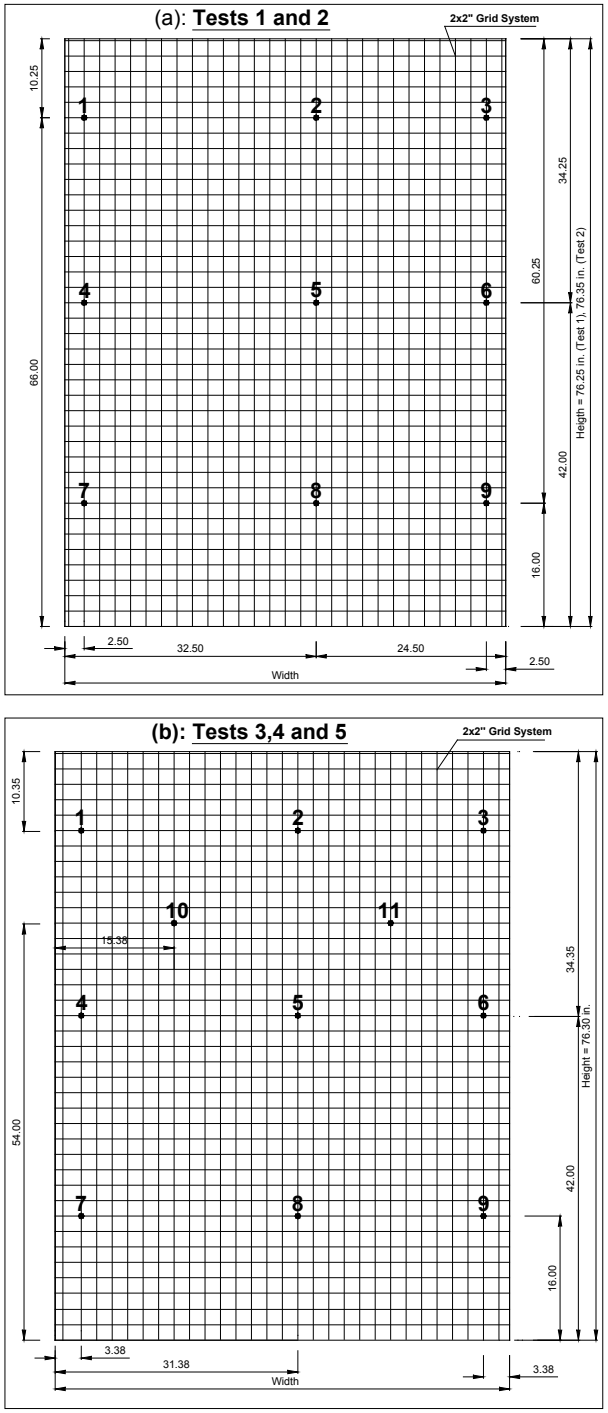

1 mm = 0.039 inches

Figure 140. Illustration. Locations of selected points to trace internal movement of tests 1–5.

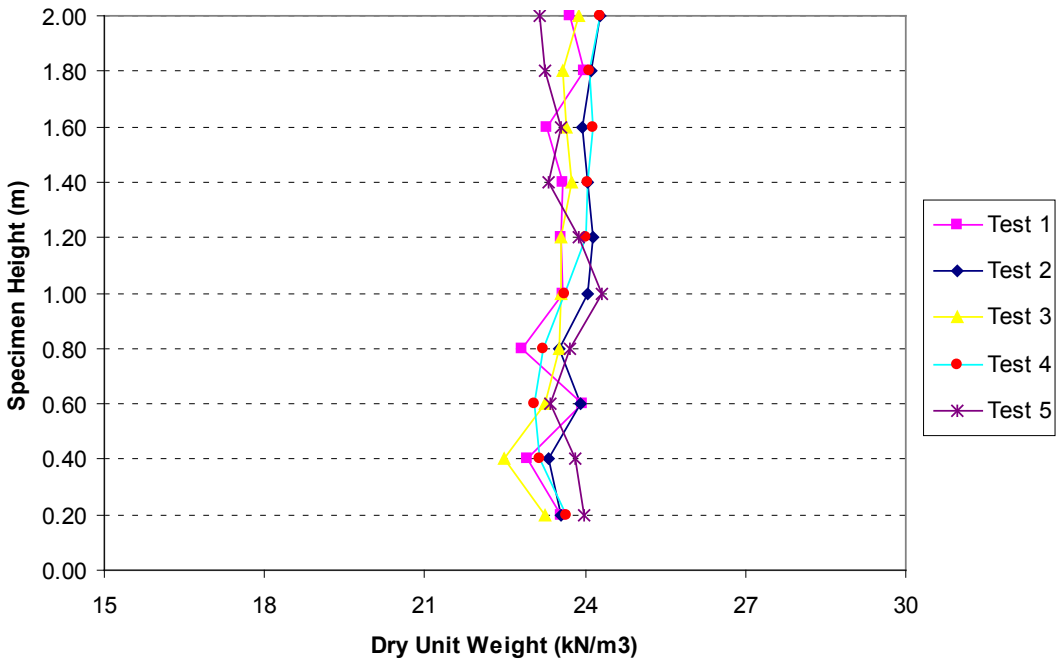

1 m = 3.28 ft
1 kN/m^3 = 0.006 kip/ft^3

Figure 141. Graph. Soil dry unit weight results during specimen preparation.

4.6 TEST RESULTS

4.6.1 Test 1—Unreinforced Soil

Test 1 is perhaps the largest plane-strain test for soil with a confining pressure. It was conducted as the baseline for the other four GSGC tests.

The loading sequence of the soil mass was as follows:

- Loading up to a vertical pressure of 36 psi (250 kPa) (nearly 1 percent vertical strain).
- Unloading to zero.
- Reloading until a failure pressure of 110 psi (770 kPa) was reached.

The soil mass at failure is shown in figure 142. Figure 143 shows the global vertical stress-strain relationship, and figure 144 shows the volume change relationships of the soil mass. The average lateral displacements on the open faces of the soil mass under different vertical stresses, measured by LVDTs, are presented in figure 145. The internal displacements of the soil at selected points under vertical applied pressures of 28, 45, 90, and 110 psi (190, 310, 620, and 770 kPa) are shown in figure 146. The test 1 results for unreinforced soil are summarized in table 8.

Figure 142. Photo. Soil mass at failure of test 1.

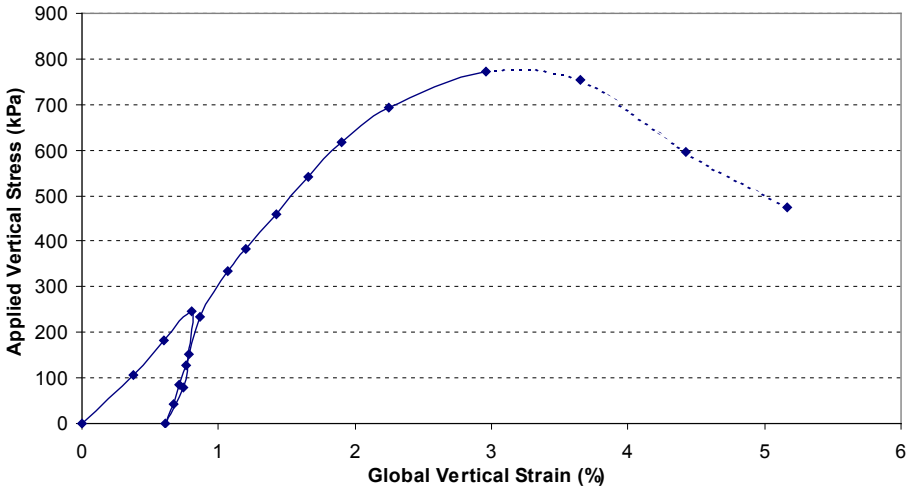

1 kPa = 0.145 psi

Figure 143. Graph. Test 1 unreinforced soil mass global vertical stress/vertical strain relationship.

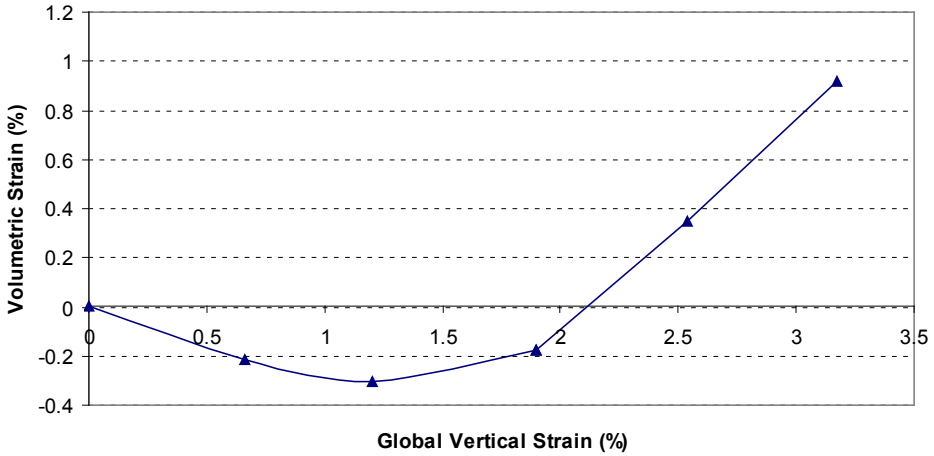

Figure 144. Graph. Test 1 unreinforced soil mass global volume change strain relationship.

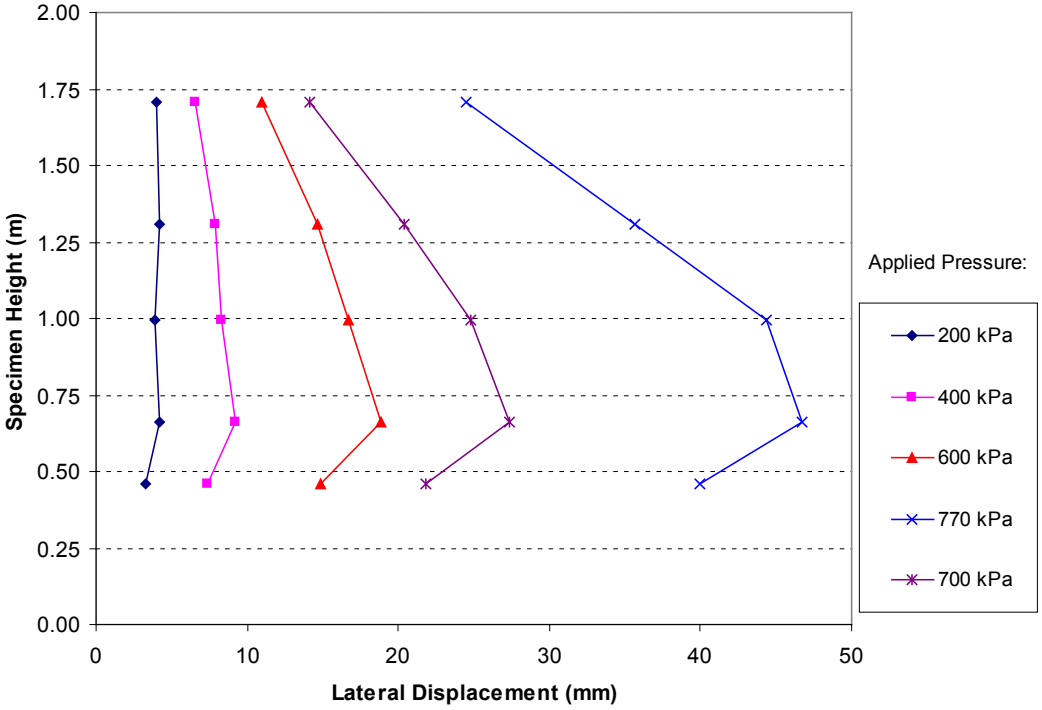

1 m = 3.28 ft
1 kPa = 0.145 psi

Figure 145. Graph. Lateral displacements on the open face of test 1.

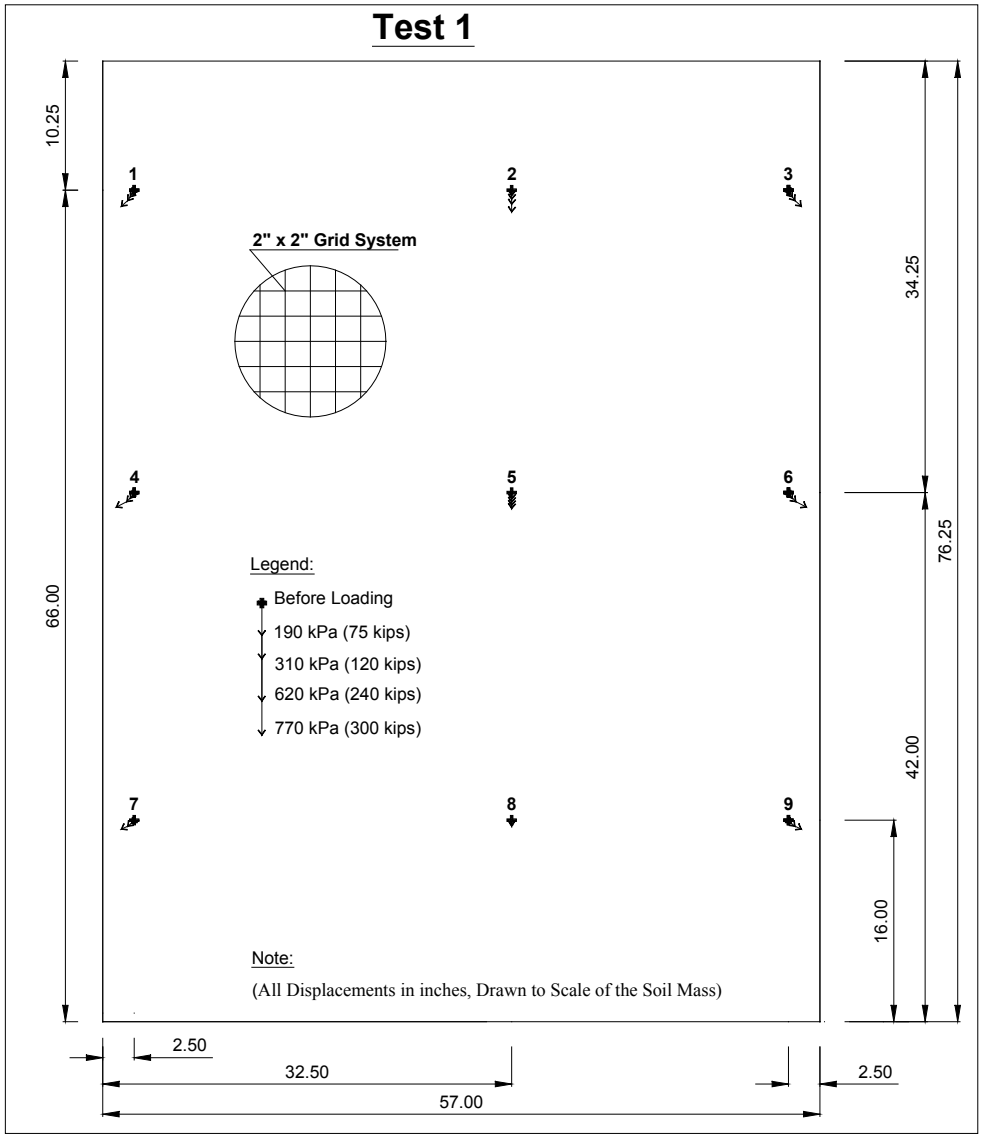

1 N = 0.00022 kip
1 mm = 0.039 inches

Figure 146. Illustration. Internal displacements of test 1.

Table 8. GSGC test 1 result summary.

Parameter		Measurement
Test condition	Geosynthetic reinforcement	None
	Wide-width strength of reinforcement	None
	Reinforcement spacing	No reinforcement
	Confining pressure	34 kPa
Test results	Applied stress at vertical strain of 1 percent	335 kPa
	Ultimate applied pressure	770 kPa
	Vertical strain at failure	3 percent
	Maximum lateral displacement of the open face at failure	47 mm
	Stiffness at 1 percent vertical strain ($E_{at\ 1\%}$)	33,500 kPa
	Stiffness for unloading-reloading (E_{ur})	87,100 kPa

1 mm = 0.039 inches
1 kPa = 0.145 psi

4.6.2 Test 2—GSGC Test (T, S_v)

In the second test, the GSGC mass was reinforced by nine sheets of single-sheet Geotex® 4×4 with spacing of 0.7 ft (0.2 m). The soil layer was compacted at 0.7-ft (0.2-m)-thick lifts. Each reinforcement sheet was mounted with 54 strain gauges.

The failure load in this test was 1,000,000 lb (454,000 kg). All nine reinforcement sheets were ruptured after testing. The composite mass after testing is shown in figure 147. The shear bands of the composite mass after testing are visible through the diagonal lines of the mass (see figure 147 and figure 148). Along the shear bands, the square grids of 2 by 2 inches (51 by 51 mm) were severely distorted after testing (see figure 148). These shear bands correspond exactly with the failure surfaces shown in figure 149.

Figure 147. Photo. Composite mass at failure of test 2.

Figure 148. Photo. Close-up of shear bands at failure of area A in figure 147.

Figure 149. Photo. Failure planes of the composite mass after testing in test 2.

The measured data from test 2 were as follows:

- **Global stress-strain relationship**: Figure 150 and figure 151 show the global stress-strain relationship of the composite up to and after failure. The maximum applied vertical pressure was about 390 psi (2,700 kPa), and the corresponding vertical displacement was 4.88 inches (125 mm) (6.5 percent vertical strain).

- **Lateral displacement:** The average lateral displacement profiles are on the open faces of the composite under different vertical pressures, as shown in figure 152. The lateral

displacements were nearly uniform along the height of the composite up to a pressure of about 87 psi (600 kPa). At vertical pressures between 110 and 220 psi (770 and 1,500 kPa), the maximum lateral displacement occurred at about $^{3}/_{8}$ *H* from the base, where *H* is the height of the composite mass. The locations of the maximum displacements were about the same as those of test 1 (unreinforced). The maximum lateral displacement at the mid-height of the composite under the applied pressure of 390 psi (2,700 kPa) was 2.3 inches (60 mm).

- **Internal displacement:** The internal displacements of the composite mass at selected points under vertical applied pressures of 39 to 390 psi (270 to 2,700 kPa) at increments of 39 psi (270 kPa) are shown in figure 153. At points near the open faces—1 and 3, 4 and 6, and 7 and 9—the displacements moved downward and outward with angles that were measured after testing of about 67, 47, and 31 degrees, respectively, to the horizontal. The vertical displacements of the points at the upper part of the soil mass were greater than those at the lower part. Along the center line, there were only vertical displacements for points 2, 5, and 8. There was almost no displacement at point 8 near the bottom and at the center line. The maximum lateral displacement in the soil body was 3.3 inches (60 mm) at mid-height on the open sides, and the maximum vertical displacement was 4.87 inches (125 mm) at the top of the specimen.

- **Reinforcement strain:** Figure 154 shows the locations of the strain gauges on the geosynthetic sheets. The strain in the reinforcement of the GSGC mass is shown in figure 155 through figure 163. Most of the strain gauges performed well at strains less than 4 percent. All reinforcement layers were found ruptured after the test was completed. The locations of the rupture lines can be seen from the aerial view of the reinforcement sheets exhumed from the composite after testing (see figure 164). Based on the locations of the rupture lines, the rupture planes can be constructed as shown in figure 165. This figure agrees perfectly with the shear bands shown in figure 149. The maximum strain in reinforcement at rupture was about 12 percent, while the measured data from the strain gauges were less than 4 percent. The strain distributions in figure 155 through figure 163 show that the locations of the maximum strain in reinforcement were different between layers. In reinforcement layers near at the mid-height of the GSGC mass (2.6 and 3.3 ft (0.8 and 1.0 m) from the base), the maximum reinforcement strains were close to the centerline. In the reinforcement layers near the top and the base of the GSGC mass (0.7 and 5.9 ft (0.2 and 1.8 m) from the base), the maximum reinforcement strains were at about 1 ft (0.3 m) from the edge of the composite mass. The maximum strain locations in all reinforcement layers were at the ruptured lines of reinforcement, as shown in figure 164 and figure 165.

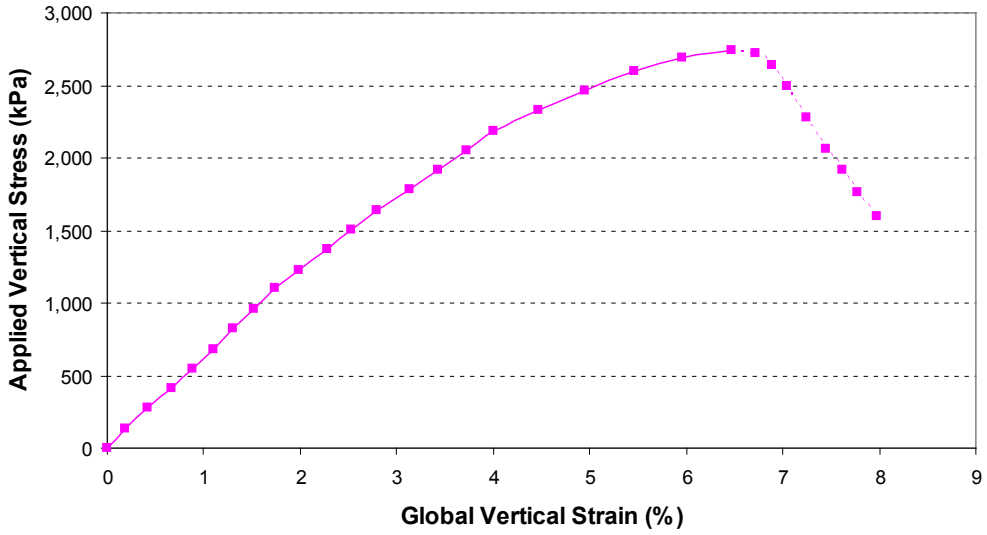

1 kPa = 0.145 psi

Figure 150. Graph. Test 2 reinforced soil mass global vertical stress-vertical strain relationship.

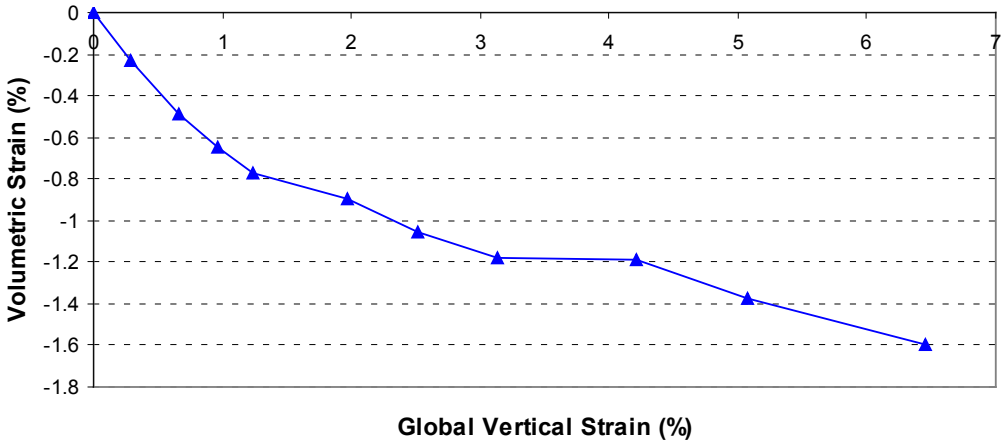

Figure 151. Graph. Test 2 reinforced soil mass global volume change strain relationship.

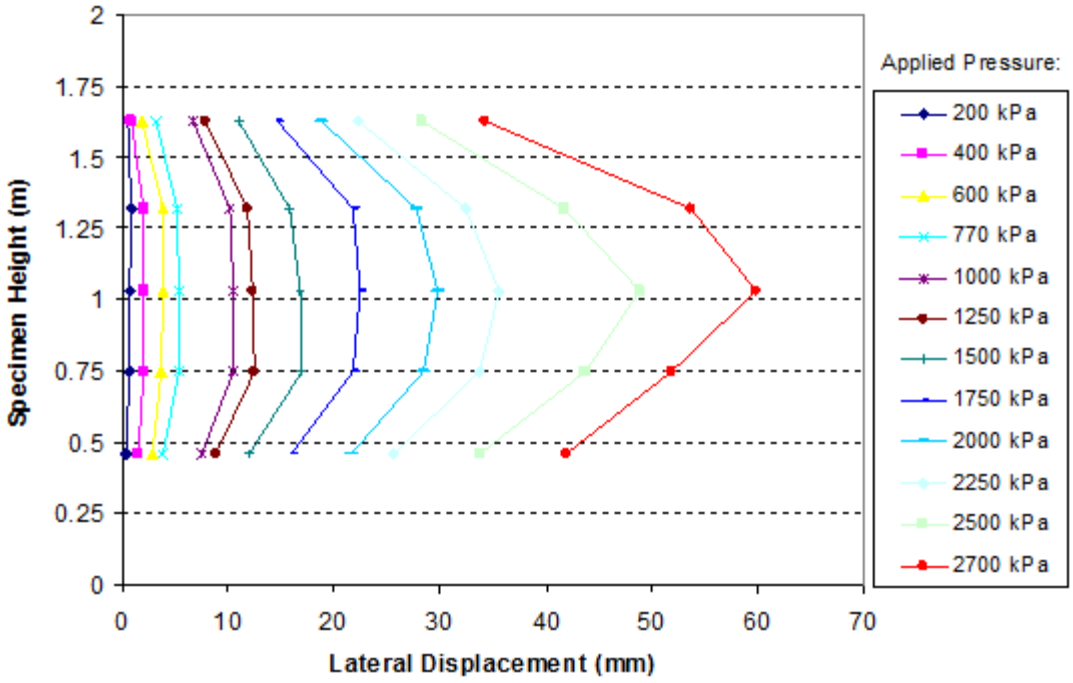

1 m = 3.28 ft
1 mm = 0.039 inches
1 kPa = 0.145 psi

Figure 152. Graph. Lateral displacements on the open face of test 2.

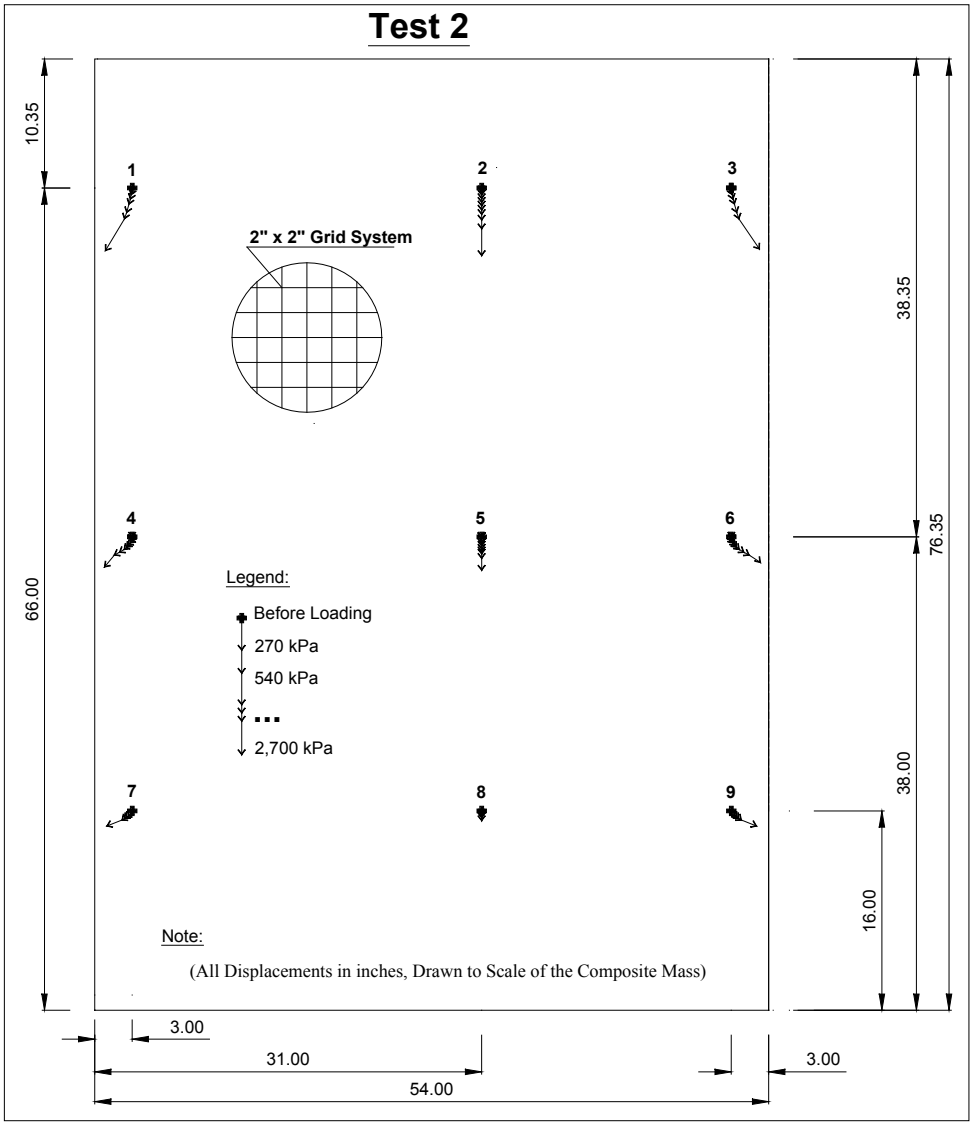

1 mm = 0.039 inches
1 kPa = 0.145 psi

Figure 153. Illustration. Internal displacements of test 2.

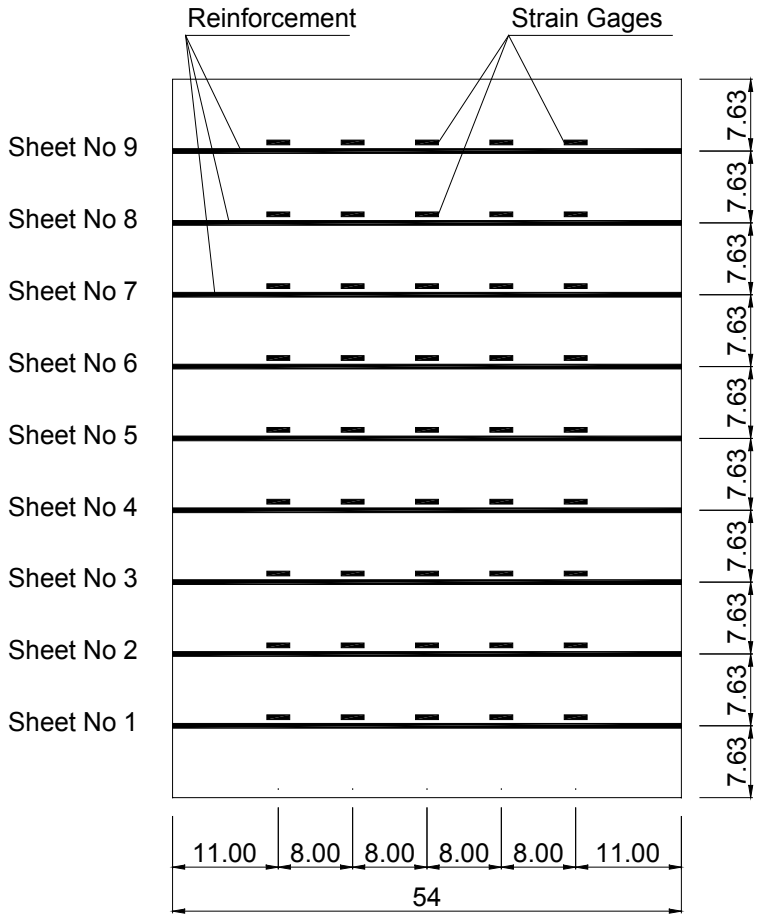

(Note: All Dimensions in inches)

1 mm = 0.039 inches

Figure 154. Illustration. Locations of strain gauges on geosynthetic sheets in test 2.

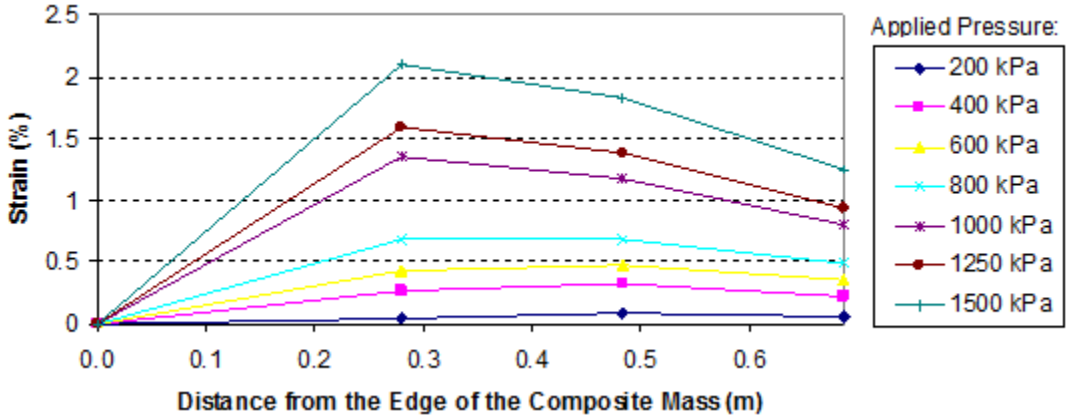

1 m = 3.28 ft

1 kPa = 0.145 psi

Figure 155. Graph. Reinforcement strain distribution of the composite mass in layer 1 of test 2 0.7 ft (0.2 m) from the base.

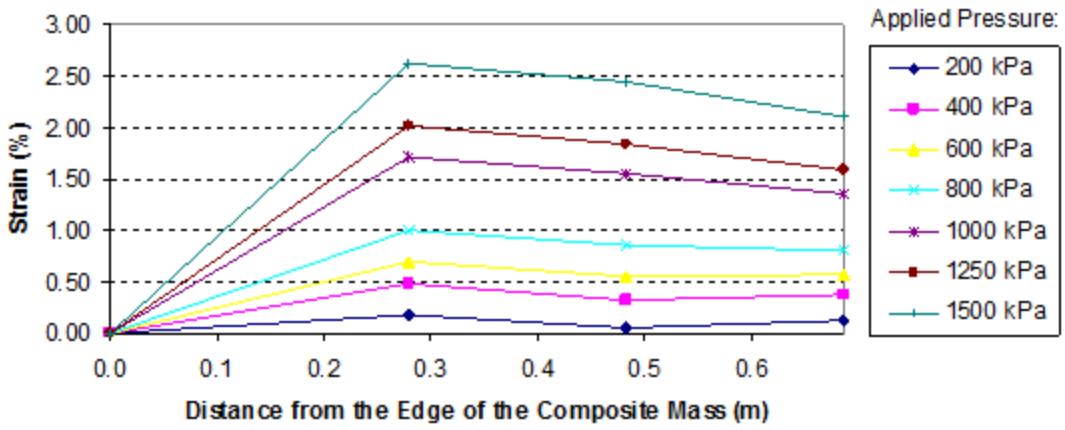

1 m = 3.28 ft
1 kPa = 0.145 psi

Figure 156. Graph. Reinforcement strain distribution of the composite mass in layer 2 of test 2 1.3 ft (0.4 m) from the base.

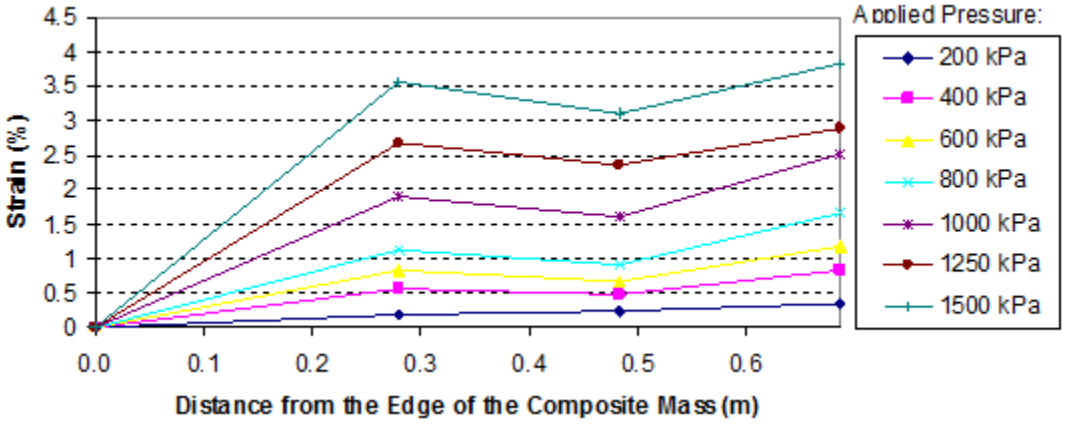

1 m = 3.28 ft
1 kPa = 0.145 psi

Figure 157. Graph. Reinforcement strain distribution of the composite mass in layer 3 of test 2 2 ft (0.6 m) from the base.

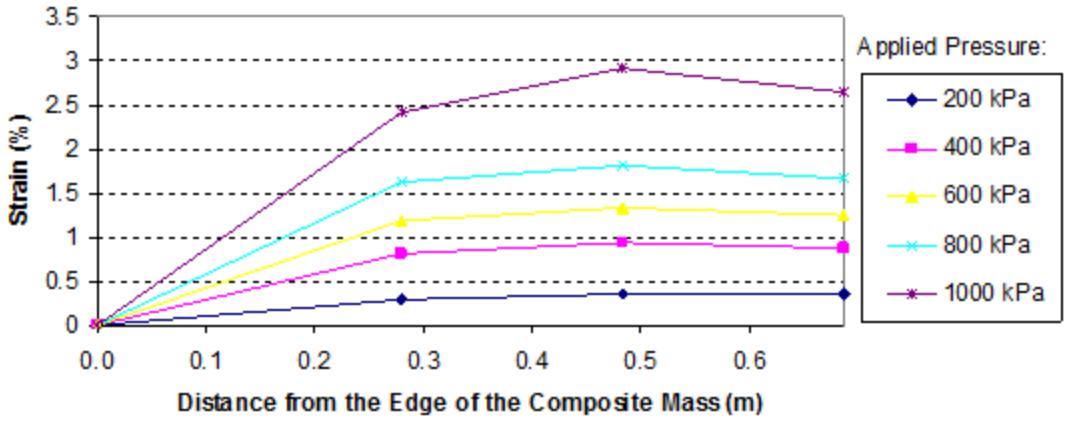

1 m = 3.28 ft
1 kPa = 0.145 psi

Figure 158. Graph. Reinforcement strain distribution of the composite mass in layer 4 of test 2 2.6 ft (0.8 m) from the base.

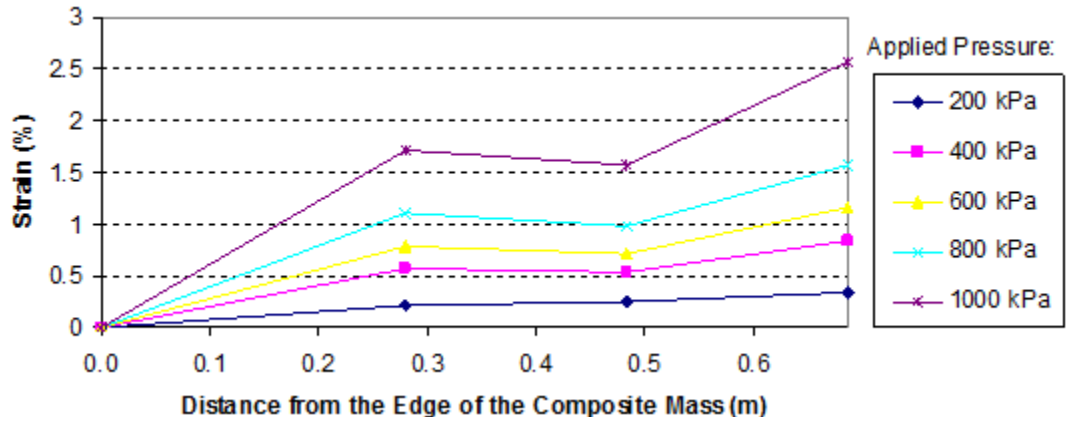

1 m = 3.28 ft
1 kPa = 0.145 psi

Figure 159. Graph. Reinforcement strain distribution of the composite mass in layer 5 of test 2 3.3 ft (1.0 m) from the base.

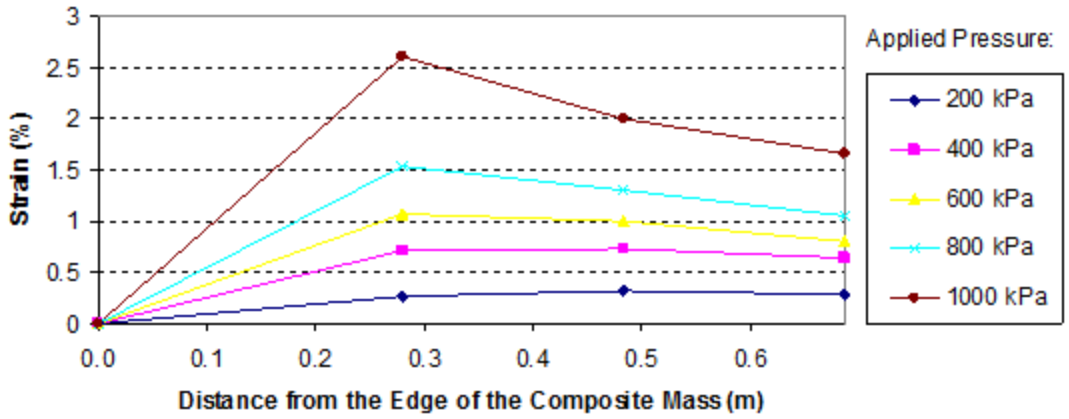

1 m = 3.28 ft
1 kPa = 0.145 psi

Figure 160. Graph. Reinforcement strain distribution of the composite mass in layer 6 of test 2 3.9 ft (1.2 m) from the base.

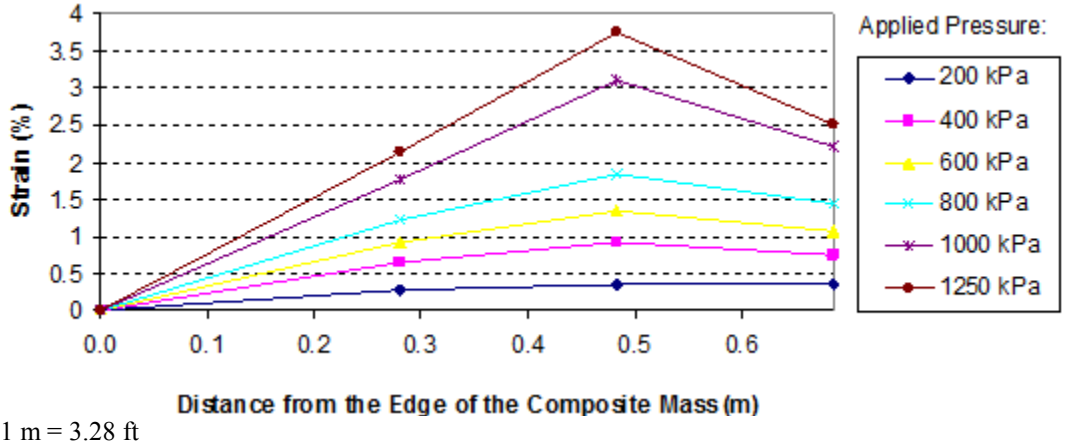

1 m = 3.28 ft
1 kPa = 0.145 psi

Figure 161. Graph. Reinforcement strain distribution of the composite mass in layer 7 of test 2 4.6 ft (1.4 m) from the base.

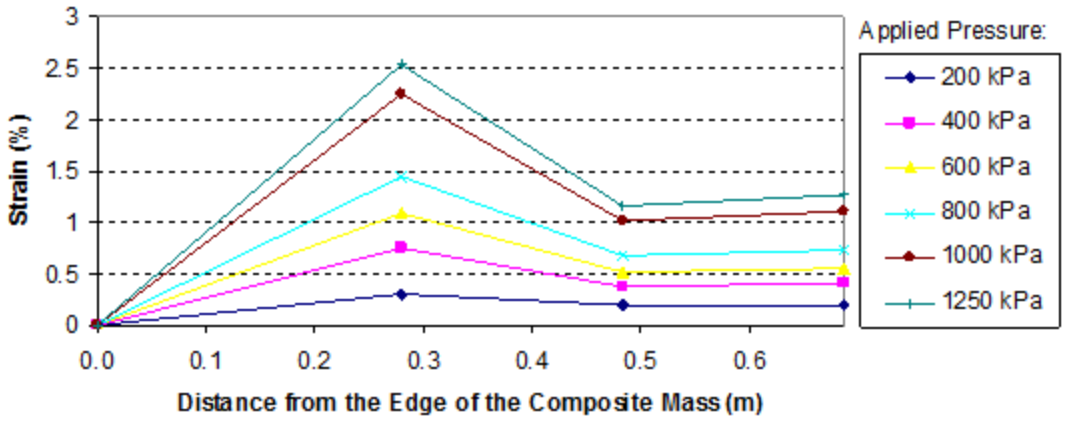

1 m = 3.28 ft
1 kPa = 0.145 psi

Figure 162. Graph. Reinforcement strain distribution of the composite mass in layer 8 of test 2 5.2 ft (1.6 m) from the base.

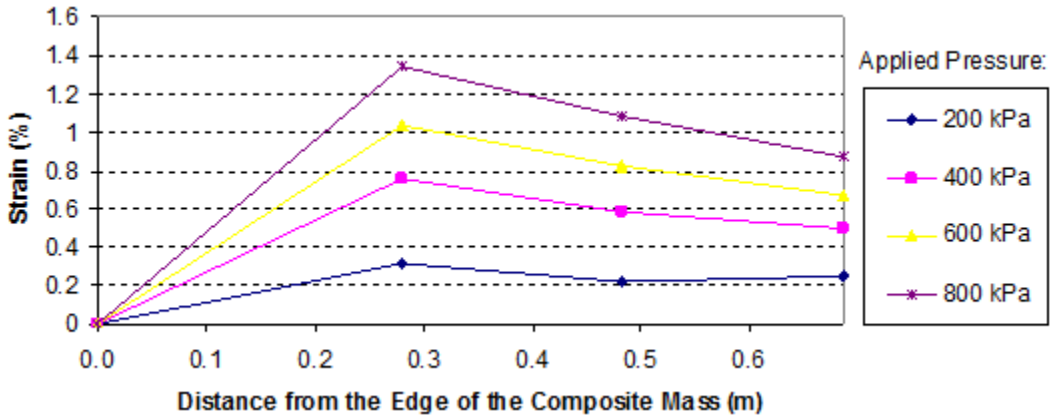

1 m = 3.28 ft
1 kPa = 0.145 psi

Figure 163. Graph. Reinforcement strain distribution of the composite mass in layer 9 of test 2 5.9 ft (1.8 m) from the base.

Figure 164. Photo. Aerial view of the reinforcement sheets exhumed from the composite mass after test 2 (numbers indicate sheet number).

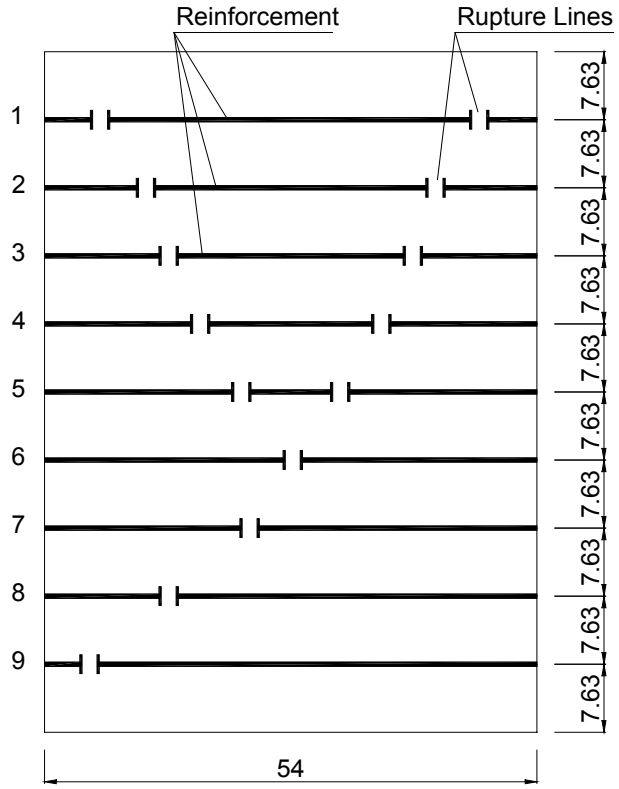

(Note: All Dimensions in inches, Drawn to Scale)

1 mm = 0.039 inches

Figure 165. Illustration. Locations of rupture lines of reinforcement in test 2 based on figure 164.

The results of test 2 are summarized in table 9.

Table 9. GSGC test 2 results summary.

Parameter		Measurement
Test condition	Geosynthetic reinforcement	Geotex® 4×4
	Wide-width strength of reinforcement	70 kN/m
	Reinforcement spacing	0.2 m
	Confining pressure	34 kPa
Test results	Ultimate applied pressure	2,700 kPa
	Vertical strain at failure	6.5 percent
	Maximum lateral displacement of the open face at failure	60 mm
	Stiffness at 1 percent vertical strain ($E_{at\ 1\%}$)	61,600 kPa
	Maximum strain in reinforcement at ruptured	12 percent
	Maximum measured strain in reinforcement	4.0 percent

1 kN/m = 0.069 kip/ft
1 m = 3.28 ft
1 kPa = 0.145 psi
1 mm = 0.039 inches

4.6.3 Test 3—GSGC Test ($2T$, $2S_v$)

In this test, the GSGC mass was reinforced by four double sheets of Geotex® 4×4 at a 1.31-ft (0.4-m) spacing. The strength and stiffness of the double-sheet reinforcement were nearly doubled compared to those of the single-sheet reinforcement used in test 2. The GSGC mass after testing is shown in figure 166.

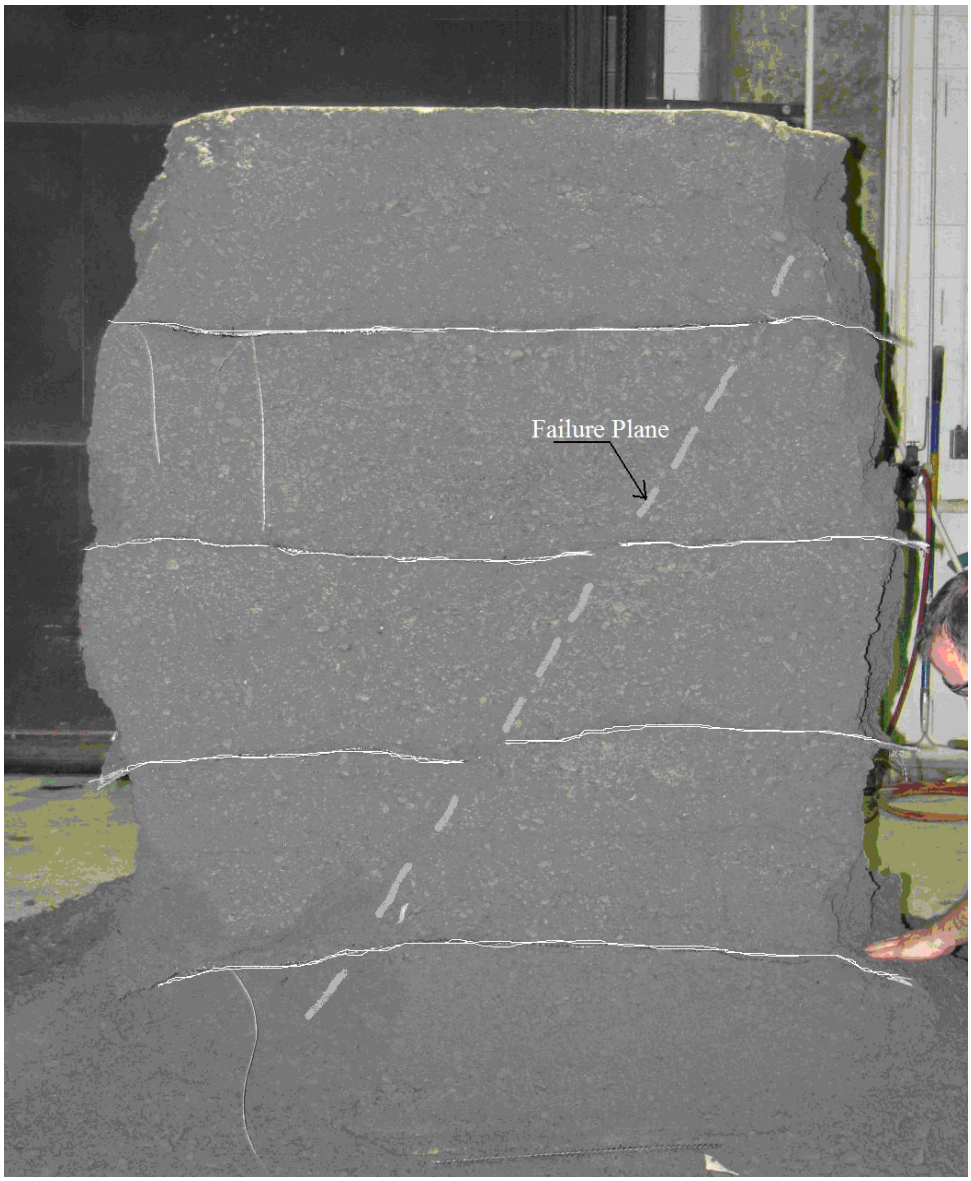

Figure 166. Photo. Composite mass after testing of test 3.

The measured data of test 3 were as follows:

- **Global stress-strain relationship**: The maximum applied vertical pressure was about 254 psi (1,750 kPa), as shown in figure 167. The vertical displacement at the failure pressure was 4.6 inches (118 mm) (6.1 percent global vertical strain).

- **Lateral displacement:** The average lateral displacement profiles on the open faces of the composite under different vertical pressures are shown in figure 168. The maximum lateral displacement under the failure pressure of 254 psi (1,750 kPa) was 2.1 inches (54 mm).

- **Internal displacement:** Internal displacements at selected points are shown in figure 169. The trend of the internal movements in test 3 was nearly the same as in test 2. For points 1, 3, 4, 5, 6, 7, and 9 near the open faces, the displacements moved downward and outward with angles from 49 to 71 degrees to the horizontal. For points 2, 5, and 8 along the center line, the displacements were almost vertical. The maximum vertical displacement at the top of the specimen was 4.6 inches (118 mm).

- **Reinforcement strain:** Figure 170 shows the locations of the strain gauges on the geosynthetic sheets. The strain in the reinforcement of the GSGC mass is shown in figure 171 through figure 174. Three reinforcement layers near the top of the composite were ruptured after testing. Figure 175 shows an aerial view of the locations of the rupture line on the reinforcement sheets exhumed from the composite after testing. Based on the locations of the rupture line, the rupture planes can be constructed, as shown in figure 176. This rupture line agrees perfectly with the failure line in figure 166. The maximum strain in reinforcement was 4 percent and was located near the ruptured line, as shown in figure 176.

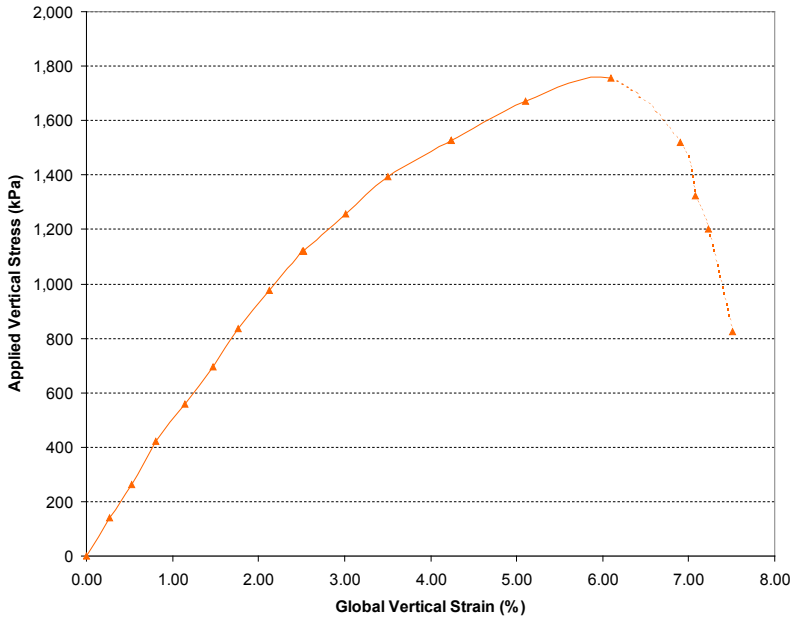

1kPa = 0.145 psi

Figure 167. Graph. Global stress-strain relationship of test 3.

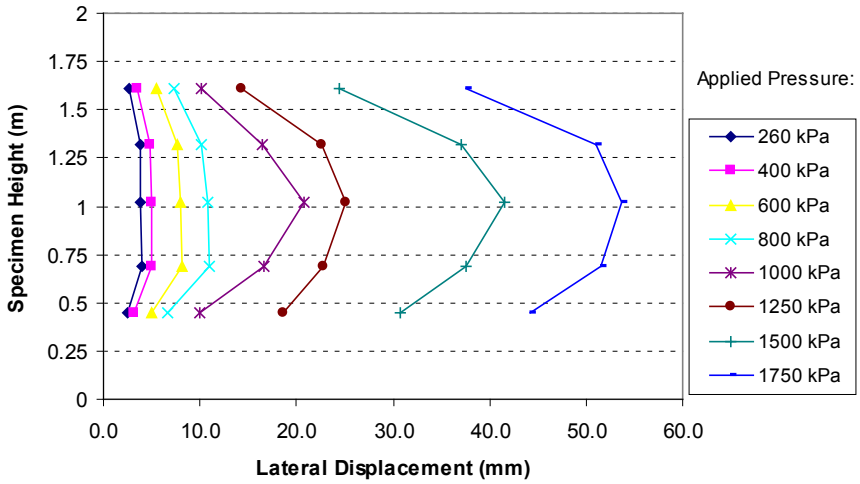

1 m = 3.28 ft
1 mm = 0.039 inches
1 kPa = 0.145 psi

Figure 168. Graph. Lateral displacements on the open face of test 3.

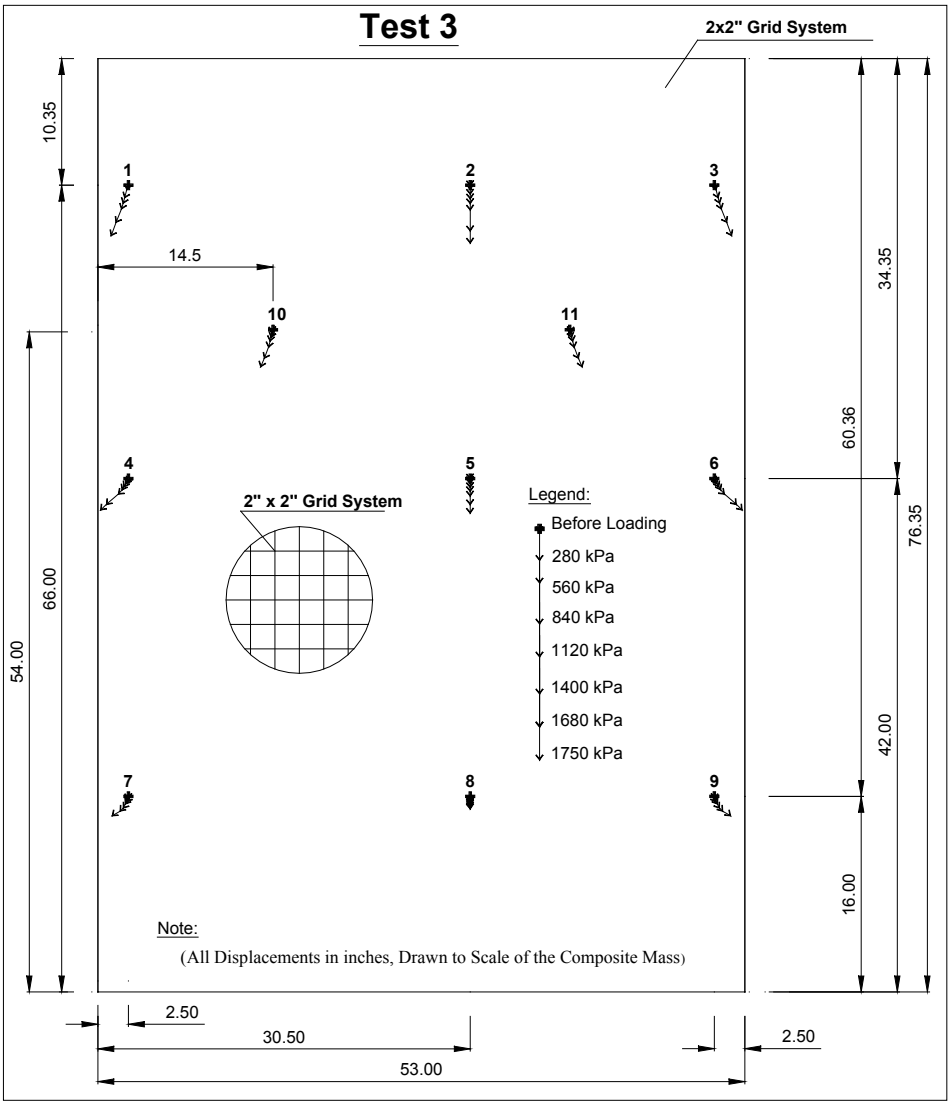

1 mm = 0.039 inches
1 kPa = 0.145 psi

Figure 169. Illustration. Internal displacements of test 3.

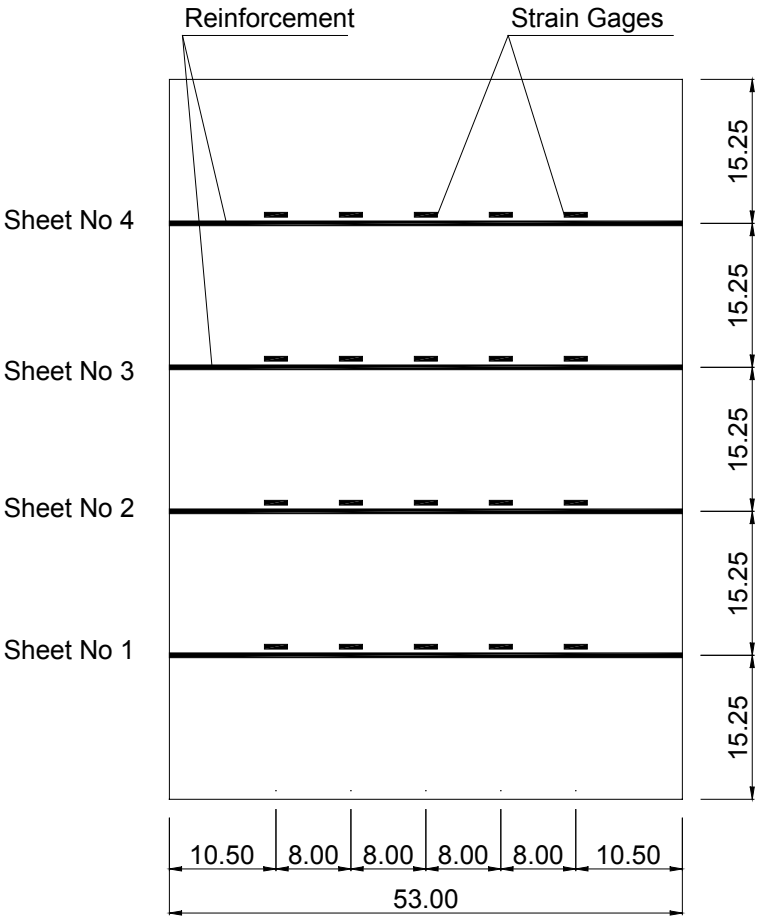

(Note: All Dimensions in inches)

1 mm= 0.039 inches

Figure 170. Illustration. Location of strain gauges on geosynthetic sheets in test 3.

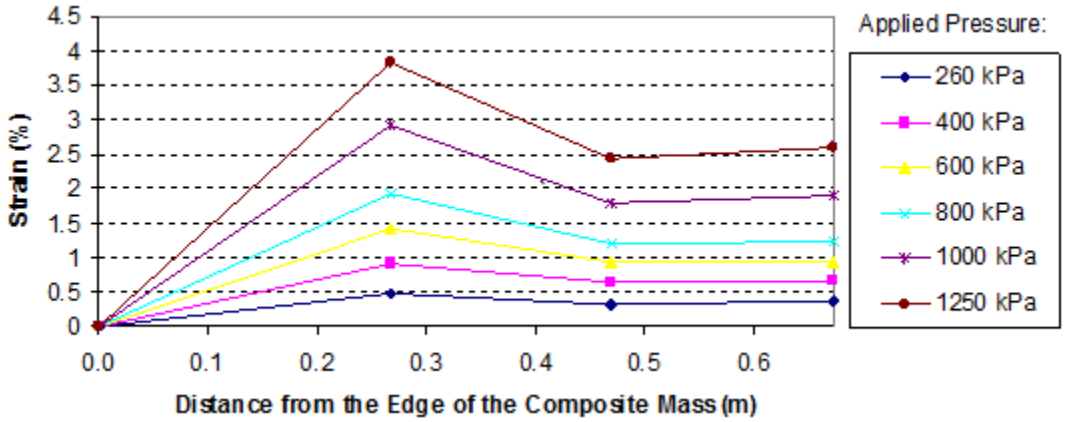

1 m = 3.28 ft

1 kPa = 0.145 psi

Figure 171. Graph. Reinforcement strain distribution of the composite mass in layer 1 of test 3 1.3 ft (0.4 m) from the base.

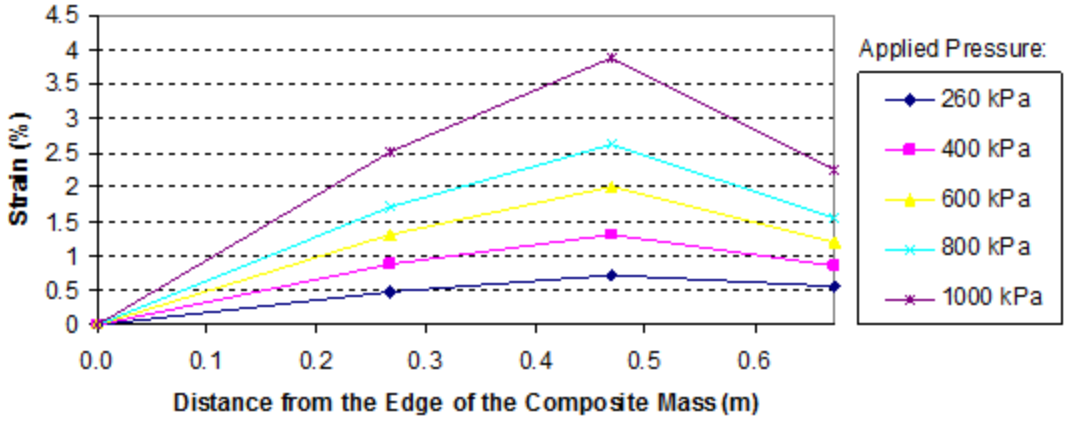

1 m = 3.28 ft
1 kPa = 0.145 psi

Figure 172. Graph. Reinforcement strain distribution of the composite mass in layer 2 of test 3 2.6 ft (0.8 m) from the base.

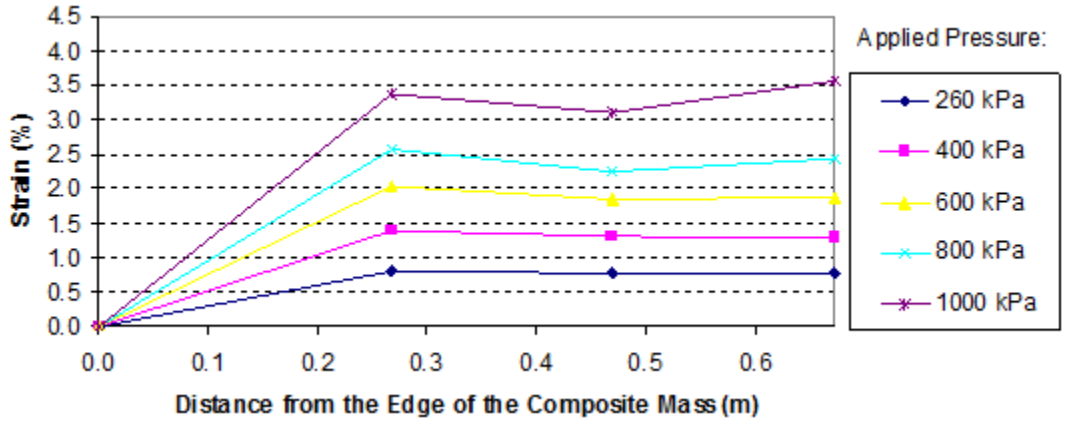

1 m = 3.28 ft
1 kPa = 0.145 psi

Figure 173. Graph. Reinforcement strain distribution of the composite mass in layer 3 of test 3 3.9 ft (1.2 m) from the base.

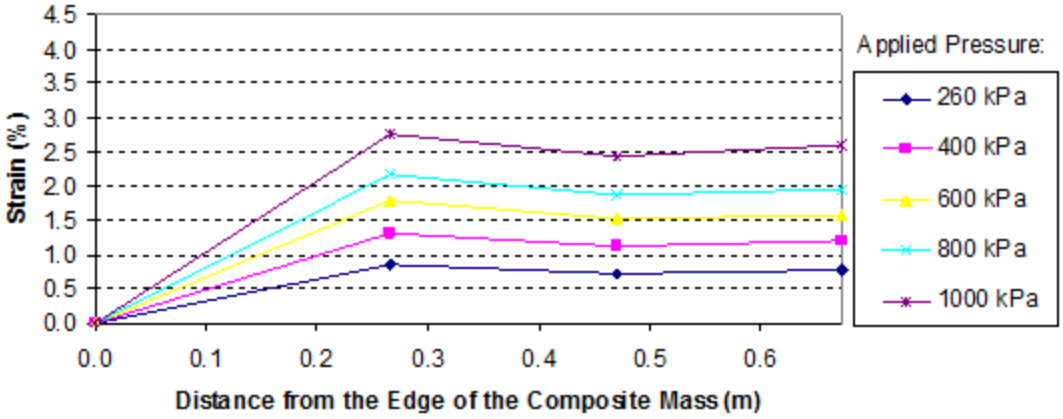

1 m = 3.28 ft
1 kPa = 0.145 psi

Figure 174. Graph. Reinforcement strain distribution of the composite mass in layer 4 of test 3 5.2 ft (1.6 m) from the base.

Figure 175. Photo. Aerial view of the reinforcement sheets exhumed from the composite mass after test 3 (numbers indicate sheet number).

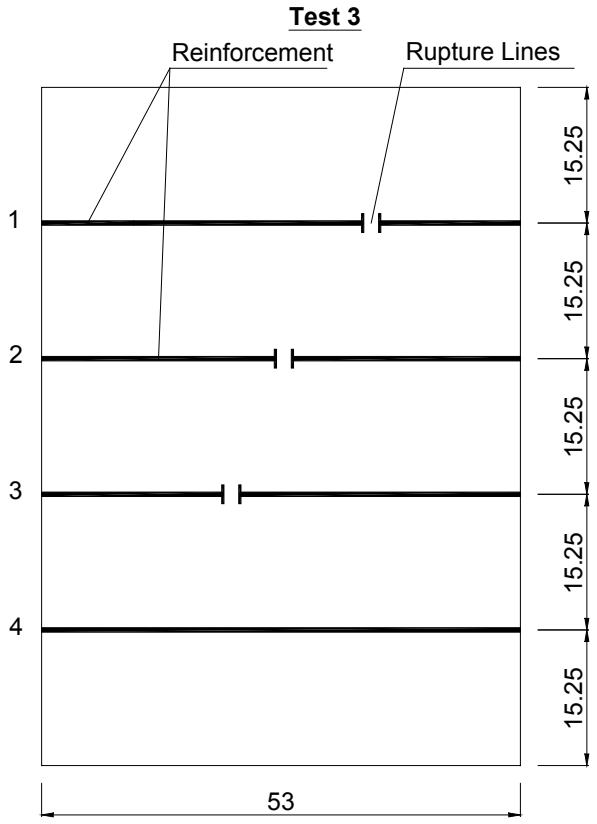

(Note: All Dimensions in inches, Drawn to Scale)

1 mm = 0.039 inches

Figure 176. Illustration. Locations of rupture lines of reinforcement in test 3 based on figure 175.

The results of test 2 are summarized in table 10.

Table 10. Test 3 result summary.

Parameter		Measurement
Test conditions	Geosynthetic reinforcement	Geotex® 4×4
	Wide-width strength of reinforcement	140 kN/m
	Reinforcement spacing	0.4 m
	Confining pressure	34 kPa
Test results	Ultimate applied pressure	1,750 kPa
	Vertical strain at failure	6.1 percent
	Maximum lateral displacement of the open face at failure	54 mm
	Stiffness at 1 percent vertical strain ($E_{at\ 1\%}$)	48,900 kPa
	Maximum strain in reinforcement at rupture	12 percent
	Maximum measured strain in reinforcement	4.0 percent

1 kN/m = 0.069 kip/ft
1 m = 3.28 ft
1 mm = 0.039 inches
1 kPa = 0.145 psi

4.6.4 Test 4—GSGC Test (*T*, 2S_v)

The reinforcement used in this test was a single sheet of Geotex® 4×4 at spacing of 1.3 ft (0.4 m). The composite mass after testing is shown in figure 177 and figure 178. The failure surfaces can be seen clearly in the figures.

Figure 177. Photo. Front view of failure planes of the composite mass after test 4.

Figure 178. Photo. Back view of failure planes of the composite mass after test 4.

The measured data for test 4 are as follows:

- **Global stress-strain relationship**: The maximum applied vertical pressure was about 190 psi (1,300 kPa), as shown in figure 179. The vertical displacement at the failure pressure was 3.0 inches (77 mm) (4.0 percent global vertical strain).

- **Lateral displacement:** The average lateral displacements on the open faces of the composite mass under different vertical pressures are shown in figure 180. The maximum lateral displacement under the failure pressure was 2.0 inches (52 mm).

- **Internal displacements:** Internal displacements at selected points are shown in figure 181. The trends of the internal movements in tests 2, 3, and 4 were identical. For points 1, 3, 4, 5, 6, 7, and 9 near the open faces, the displacements moved downward and outward with angles from 30 to 63 degrees to the horizontal. For points 2, 5, and 8 along the center line, the displacements were almost vertical. The maximum vertical displacement at the top of the specimen was 3.0 inches (77 mm).

- **Reinforcement strain:** Figure 182 shows the locations of the strain gauges on the geosynthetic sheets. The strain in the reinforcement of the GSGC mass is shown in figure 183 through figure 186. All reinforcement layers near the top of the composite were ruptured after the test was completed. The locations of the rupture lines are shown in figure 187. Based on the locations of the rupture line, the rupture planes can be constructed, as shown in figure 188. This rupture line agrees perfectly with the failure line in figure 177 and figure 178. The maximum strain in reinforcement at rupture was about 12 percent and located near the rupture line, as shown in figure 188.

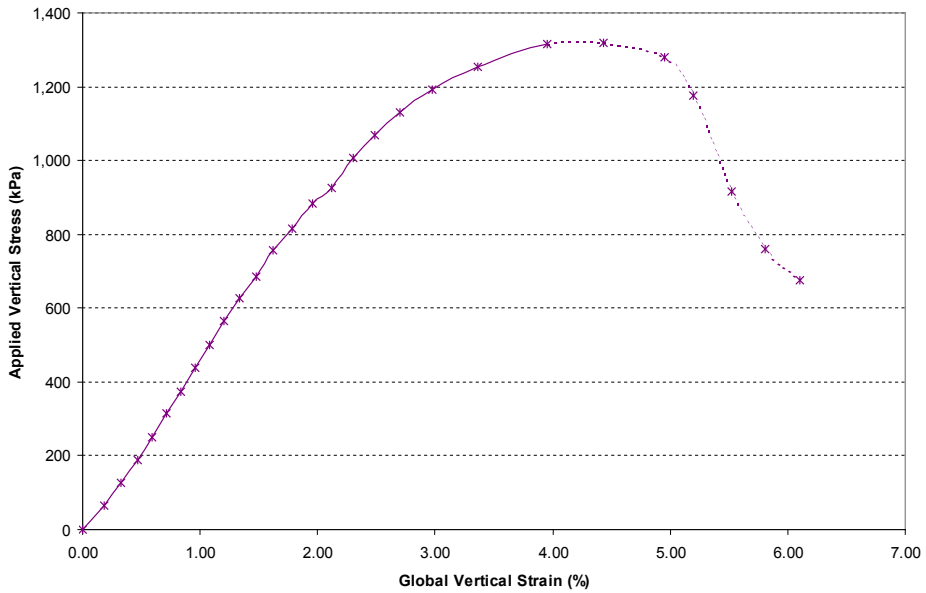

1 kPa = 0.145 psi

Figure 179. Graph. Global stress-strain relationship of test 4.

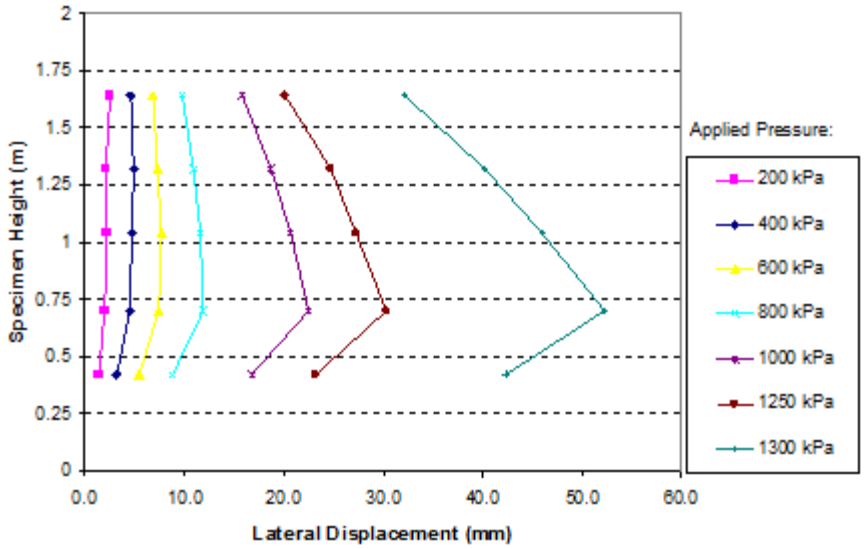

1 m = 3.28 ft
1 mm = 0.029 inches
1 kPa = 0.145 psi

Figure 180. Graph. Lateral displacements on the open face of test 4.

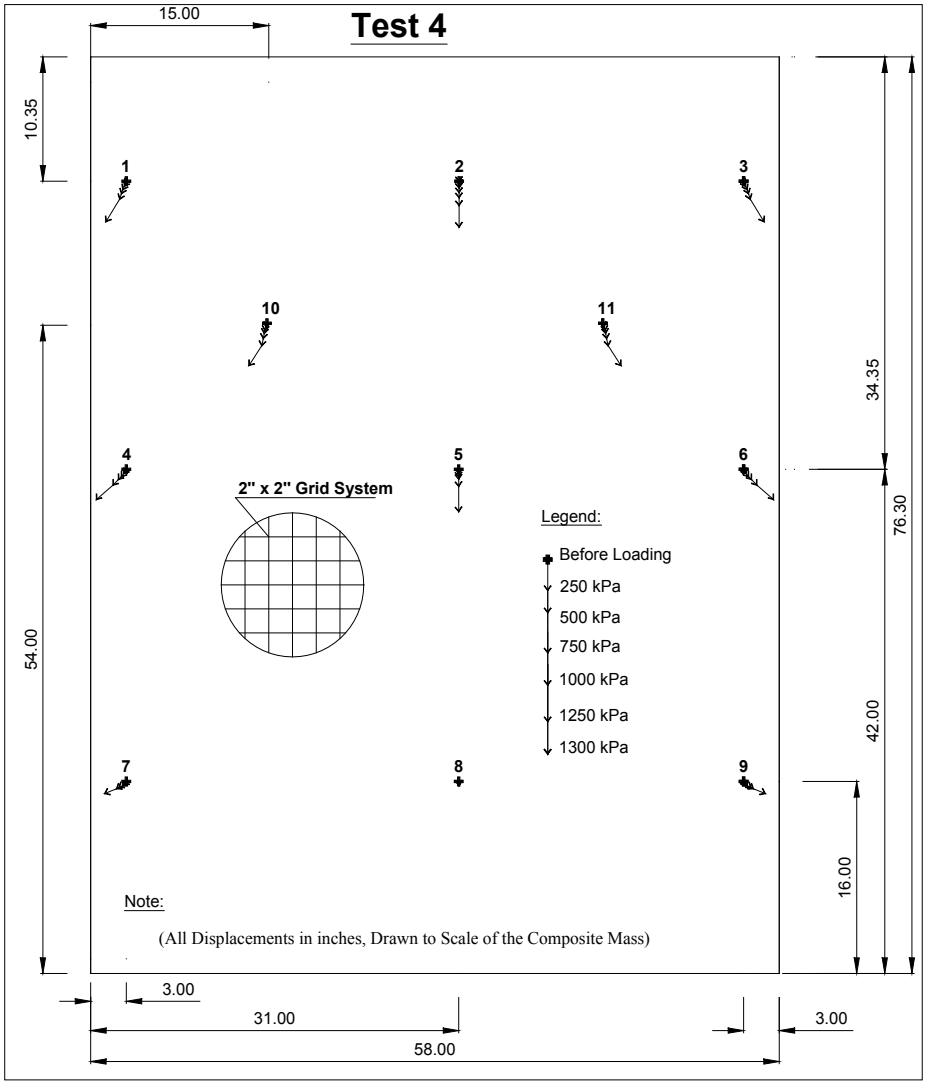

1 mm = 0.039 inches
1 kPa = 0.145 psi

Figure 181. Illustration. Internal displacements of test 4.

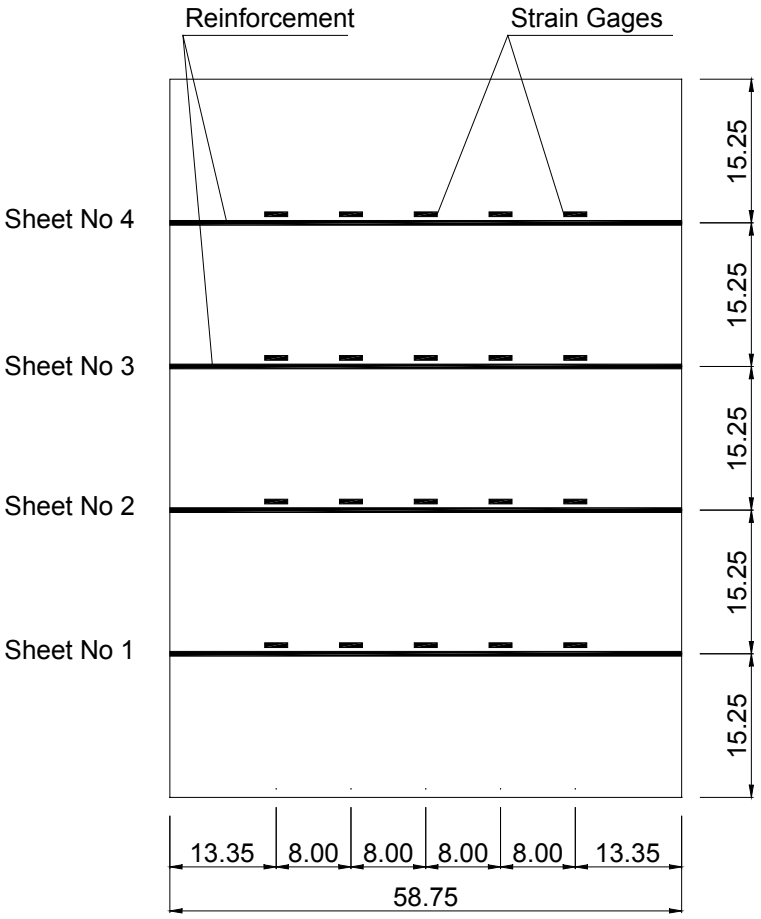

(Note: All Dimensions in inches)

1 mm = 0.039 inches

Figure 182. Illustration. Locations of strain gauges on geosynthetic sheets in test 4.

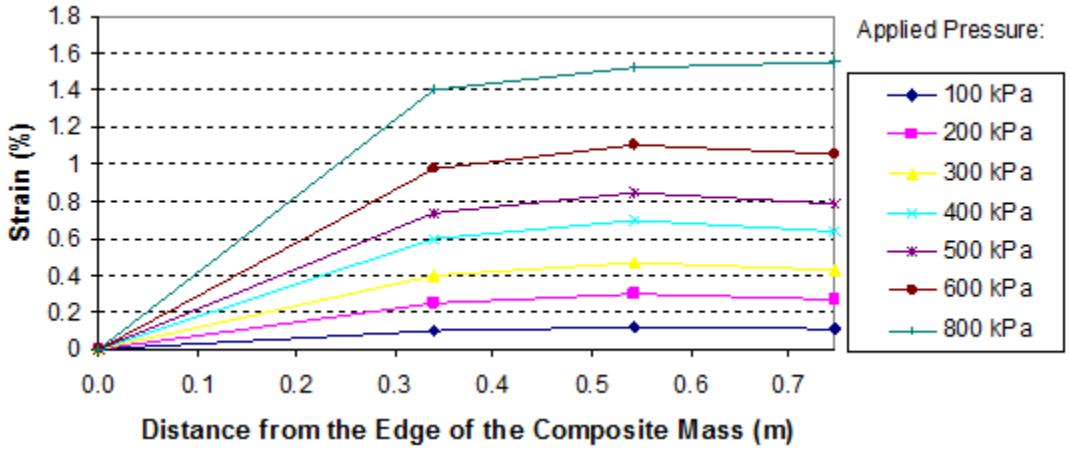

1 m = 3.28 ft

1 kPa = 0.145 psi

Figure 183. Graph. Reinforcement strain distribution of the composite mass in layer 1 of test 4 1.3 ft (0.4 m) from the base.

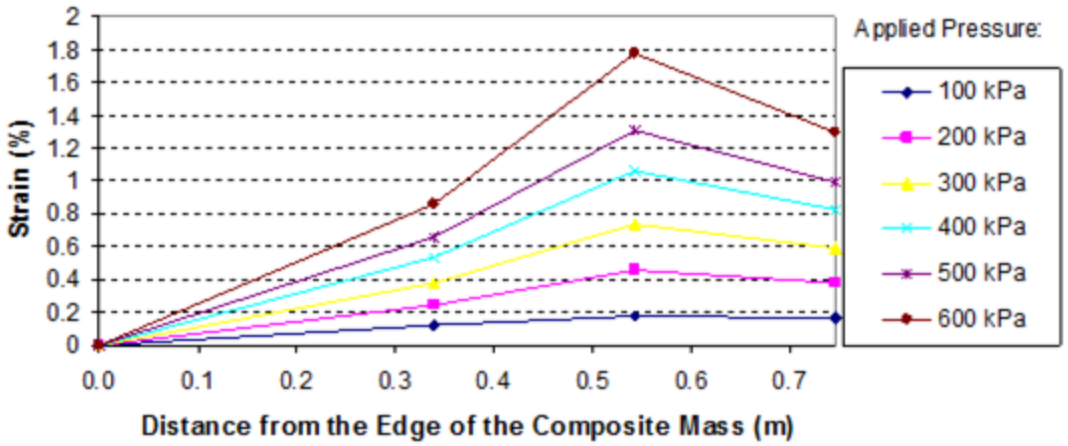

1 m = 3.28 ft
1 kPa = 0.145 psi

Figure 184. Graph. Reinforcement strain distribution of the composite mass in layer 2 of test 4 2.6 ft (0.8 m) from the base.

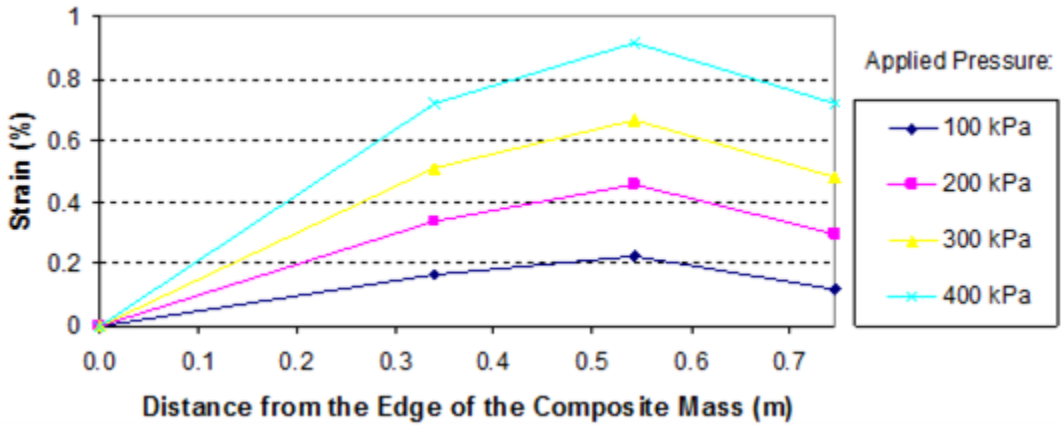

1 m = 3.28 ft
1 kPa = 0.145 psi

Figure 185. Graph. Reinforcement strain distribution of the composite mass in layer 3 of test 4 3.9 ft (1.2 m) from the base.

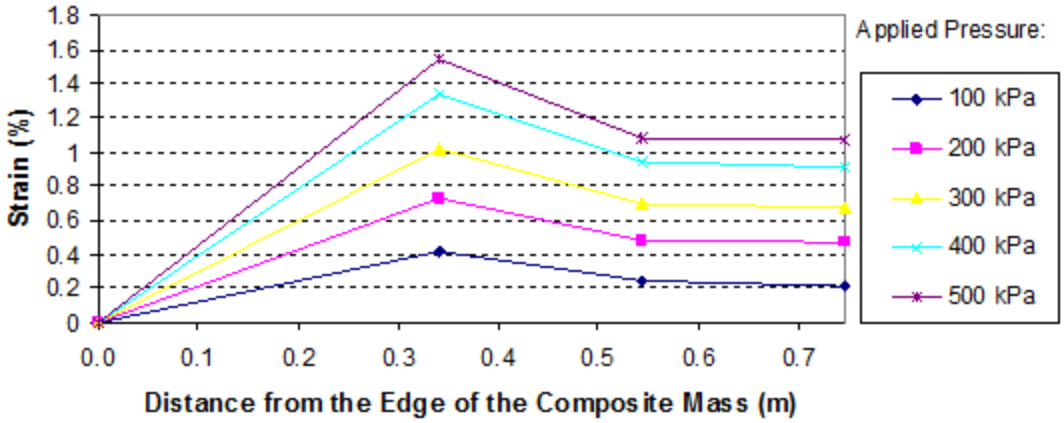

1 m = 3.28 ft
1 kPa = 0.145 psi

Figure 186. Graph. Reinforcement strain distribution of the composite mass in layer 4 of test 4 5.2 ft (1.6 m) from the base.

Figure 187. Photo. Aerial view of the reinforcement sheets exhumed from the composite mass after test 4 (numbers indicate sheet number).

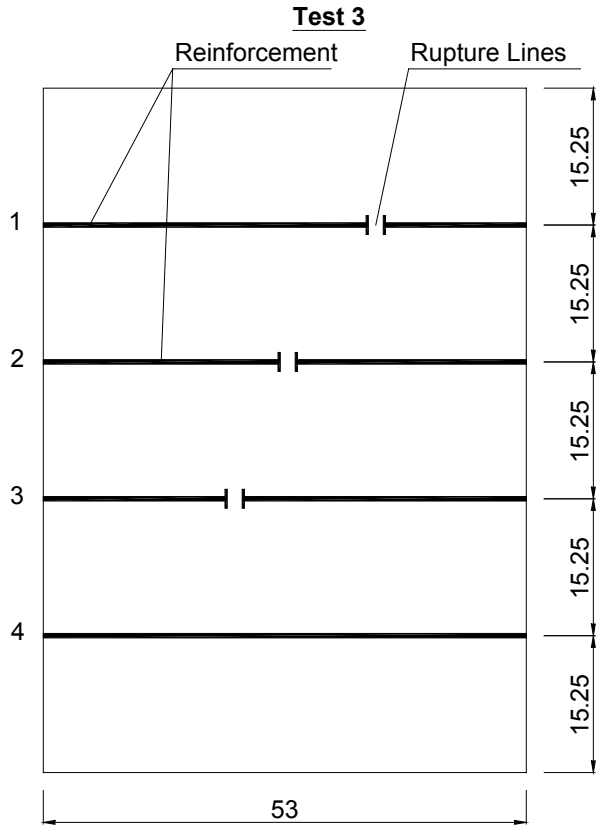

Figure 188. Illustration. Locations of rupture lines of reinforcement in test 4 based on figure 187.

The test 4 results are summarized in table 11.

Table 11. GSGC test 4 result summary.

Parameter		Measurement
Test conditions	Geosynthetic reinforcement	Geotex® 4×4
	Wide-width strength of reinforcement	70 kN/m
	Reinforcement spacing	0.4 m
	Confining pressure	34 kPa
Test results	Ultimate applied pressure	1,300 kPa
	Vertical strain at failure	4.0 percent
	Maximum lateral displacement of the open face at failure	53 mm
	Stiffness at 1 percent vertical strain ($E_{at\ 1\%}$)	46,600 kPa
	Maximum strain in reinforcement at rupture	12 percent
	Maximum measured strain in reinforcement	2.0 percent

1 kN/m = 0.069 kip/ft
1 m = 3.28 ft
1 mm = 0.039 inches
1 kPa = 0.145 psi

4.6.5 Test 5—GSGC Test (Unconfined with T, S_v)

The configuration of this test was the same as test 2. The reinforcement was single-sheet Geotex® 4×4 at a spacing of 0.6 ft (0.2 m). Confining pressure was not applied for this test. Without applying confining pressure, the soil on the open faces fell off continuously with increasing applied pressure. The composite mass and failure surfaces after testing are shown in figure 189 through figure 191.

Figure 189. Photo. Composite mass at failure of test 5.

Figure 190. Photo. Front view of failure planes of the composite mass after test 5.

Figure 191. Photo. Back view of failure planes of the composite mass after test 5.

The measured data of test 5 are as follows:

- **Global stress-strain relationship**: The maximum applied vertical pressure was about 270 psi (1,900 kPa), as shown in figure 192. The vertical displacement at the failure pressure was 4.33 inches (111 mm) (6.0 percent global vertical strain).

- **Lateral displacement**: The average lateral displacements on the open faces of the composite mass under different vertical pressures are shown in figure 193. The maximum lateral displacement at the open faces under the failure pressure could not be measured because the soil at these faces dropped during testing under the high applied pressures.

- **Internal displacements**: Internal displacements at selected points are shown in figure 194. The trend of the internal movements in test 5 was nearly the same as that in tests 2, 3, and 4. For points 1, 3, 4, 5, 6, 7, and 9 near the open faces, the displacements move downward and outward with angles of 35 to 63 degrees to the horizontal. For points 2, 5, and 8 along the center line, the displacements were almost vertical. The maximum vertical displacement at the top of the specimen was 4.33 inches (111 mm).

- **Reinforcement strain**: Figure 195 shows the locations of the strain gauges on the geosynthetic sheets. The strain in the reinforcement of the GSGC mass is shown in Figure 196 through figure 198. Eight reinforcement layers near the top of the composite were ruptured after testing. Figure 199 shows the locations of the rupture lines from an aerial view of the reinforcement sheets exhumed from the composite after testing. Based on the locations of the rupture line, the rupture planes can be constructed (see figure 200). This rupture line agrees perfectly with the failure line in figure 189. The maximum strain in reinforcement measured was 3.2 percent and located at near the rupture line, as shown in figure 200.

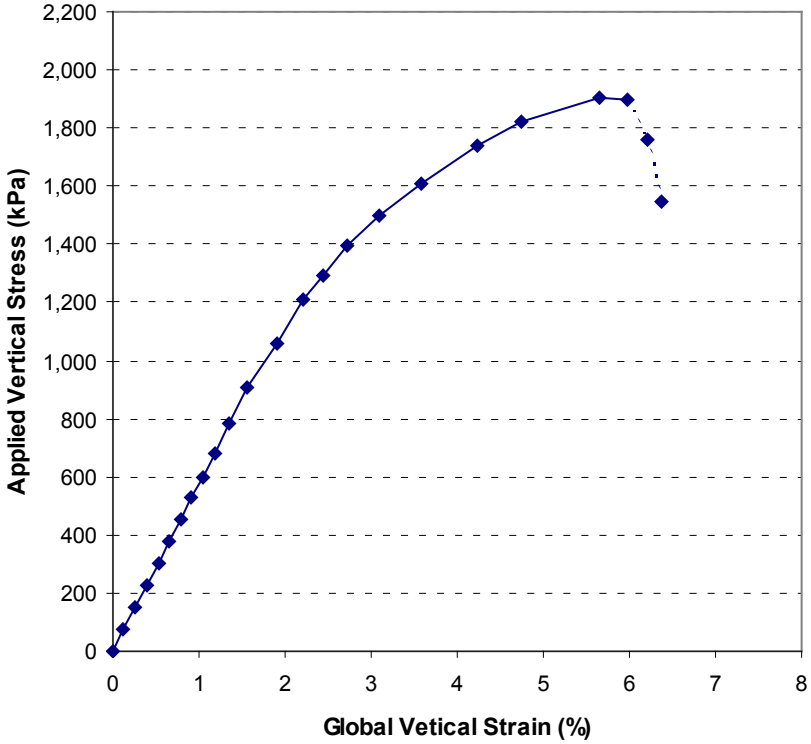

1 kPa = 0.145 psi

Figure 192. Graph. Global stress-strain relationship of test 5.

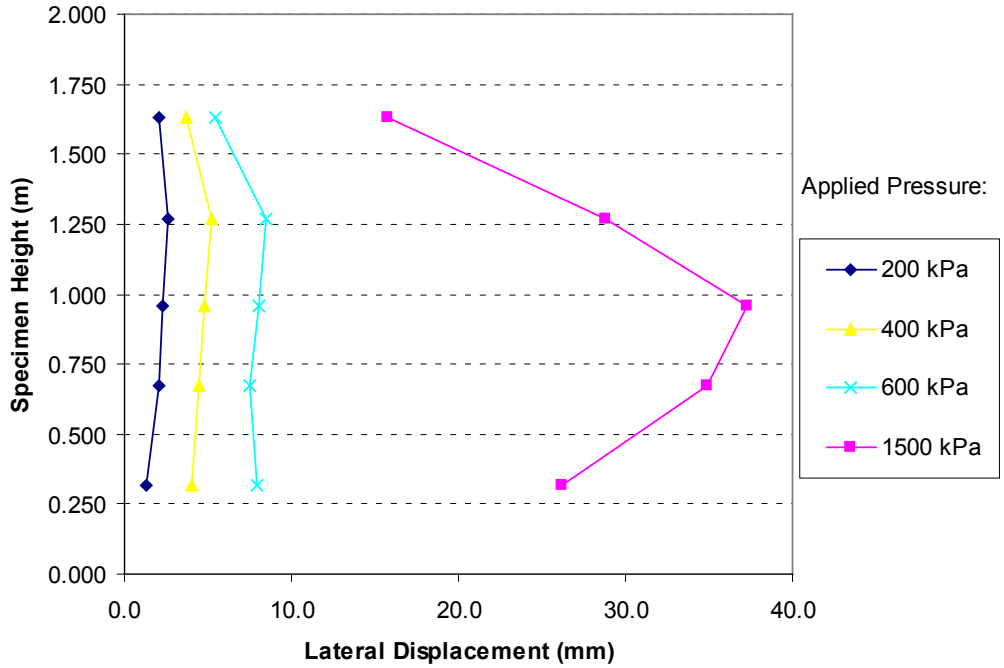

1 m = 3.28 ft
1 mm = 0.039 inches
1 kPa = 0.145 psi

Figure 193. Graph. Lateral displacements on the open face of test 5.

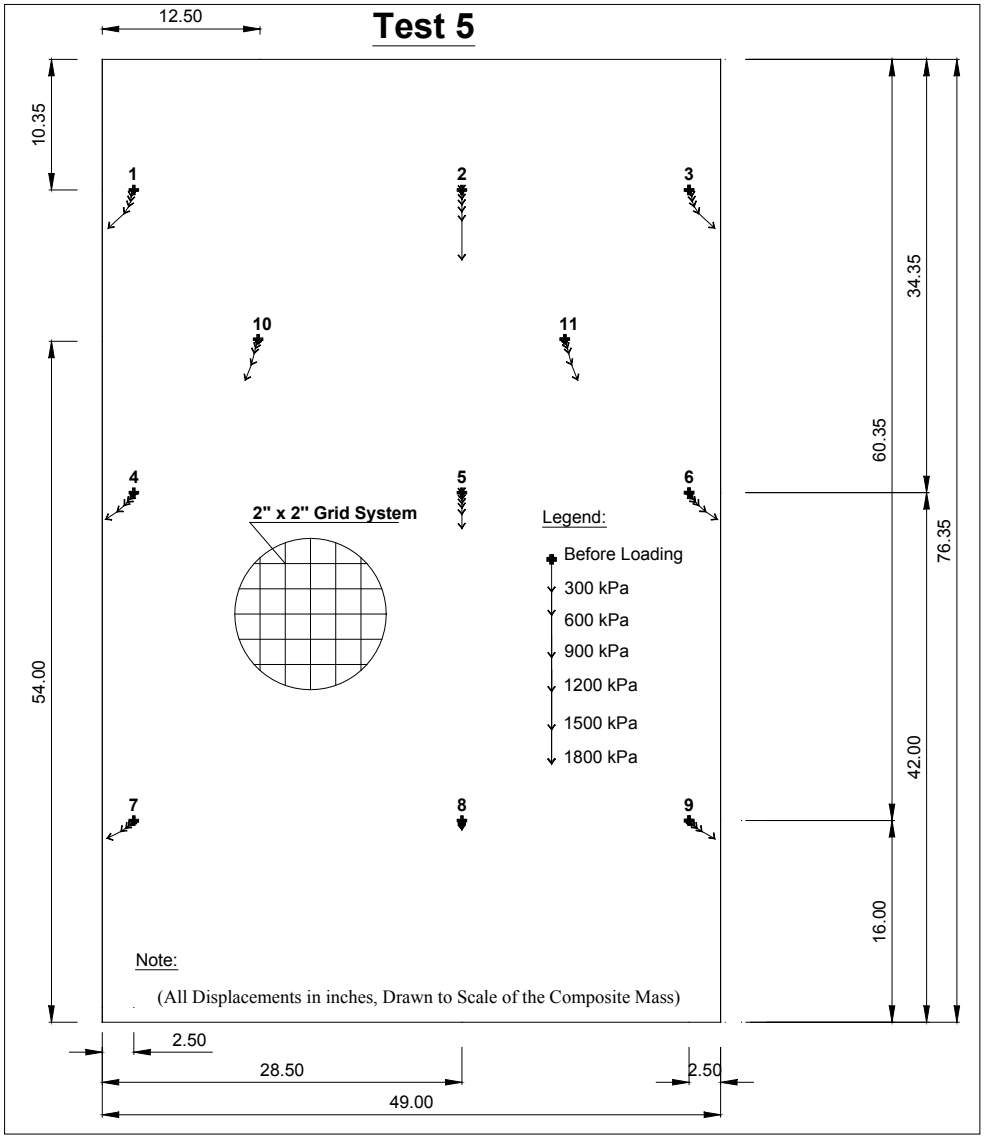

1 mm = 0.039 inches
1 kPa = 0.145 psi

Figure 194. Illustration. Internal displacements of test 5.

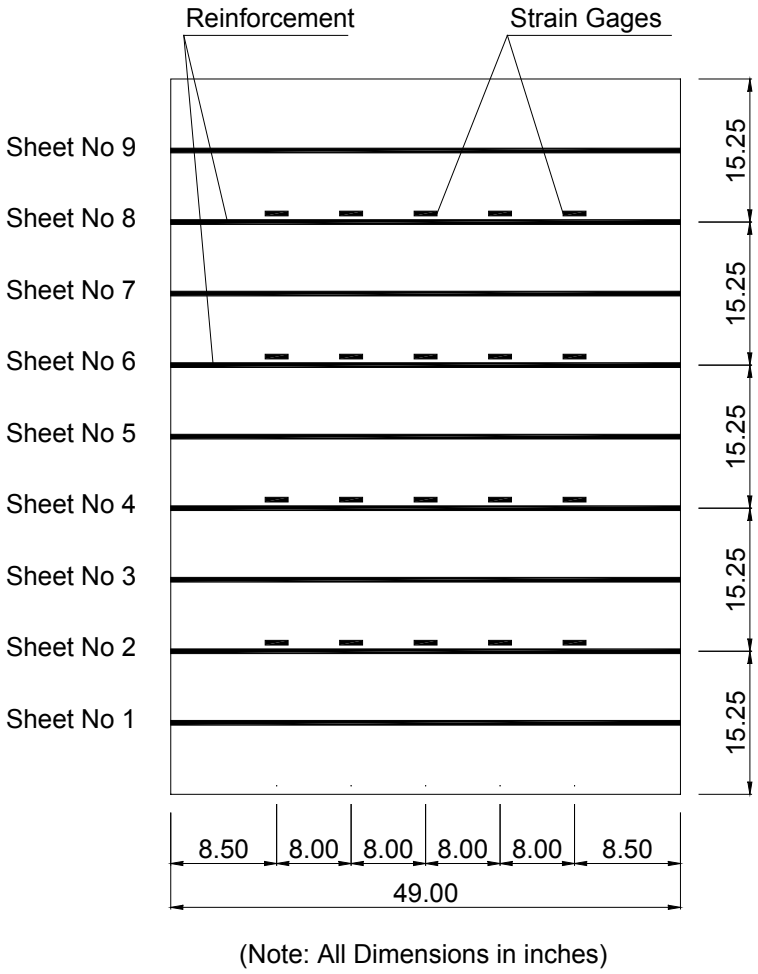

1 mm = 0.039 inches

Figure 195. Illustration. Locations of strain gauges on geosynthetic sheets in test 5.

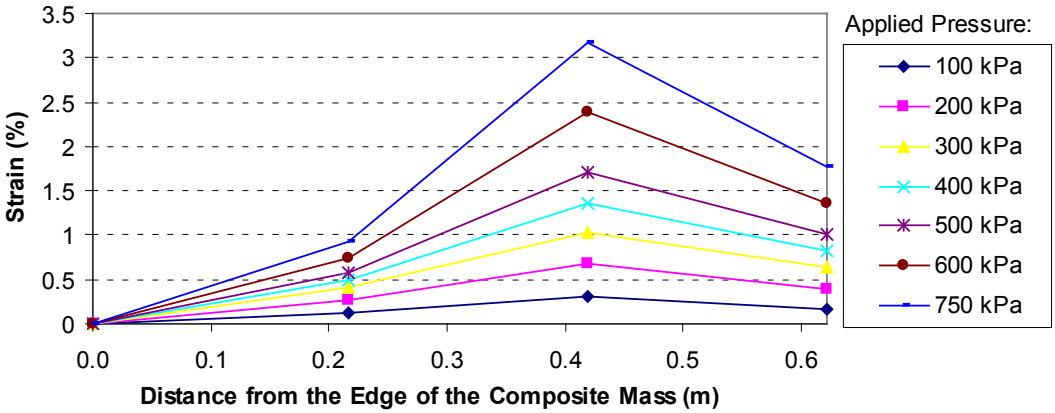

1 m = 3.28 ft
1 kPa = 0.145 psi

Figure 196. Graph. Reinforcement strain distribution of the composite mass in layer 1 of test 5 1.3 ft (0.4 m) from the base.

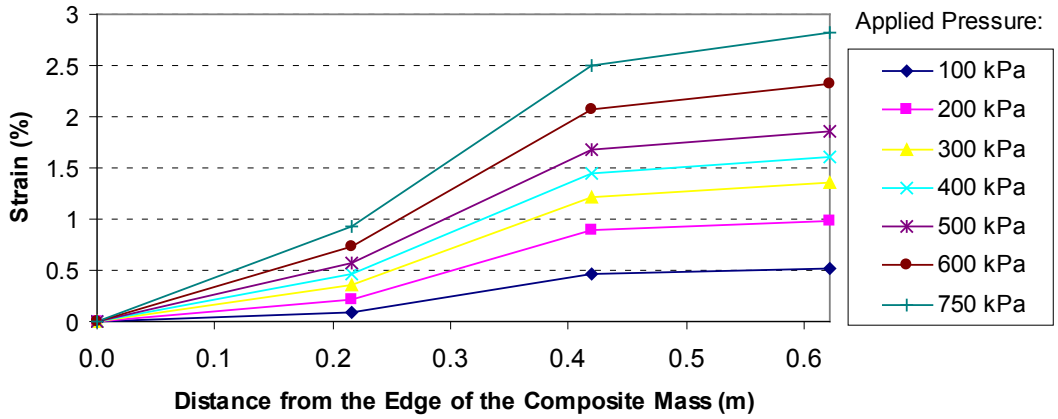

1 m = 3.28 ft
1 kPa = 0.145 psi

Figure 197. Graph. Reinforcement strain distribution of the composite mass in layer 2 of test 5 2.6 ft (0.8 m) from the base.

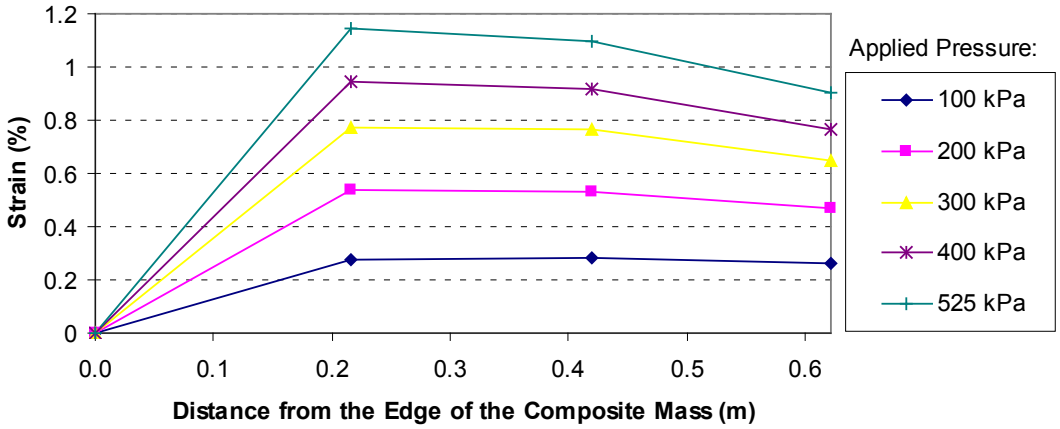

1 m = 3.28 ft
1 kPa = 0.145 psi

Figure 198. Graph. Reinforcement strain distribution of the composite mass in layer 3 of test 5 3.9 ft (1.2 m) from the base.

Figure 199. Photo. Aerial view of the reinforcement sheets exhumed from the composite mass after test 5 (numbers indicate sheet number).

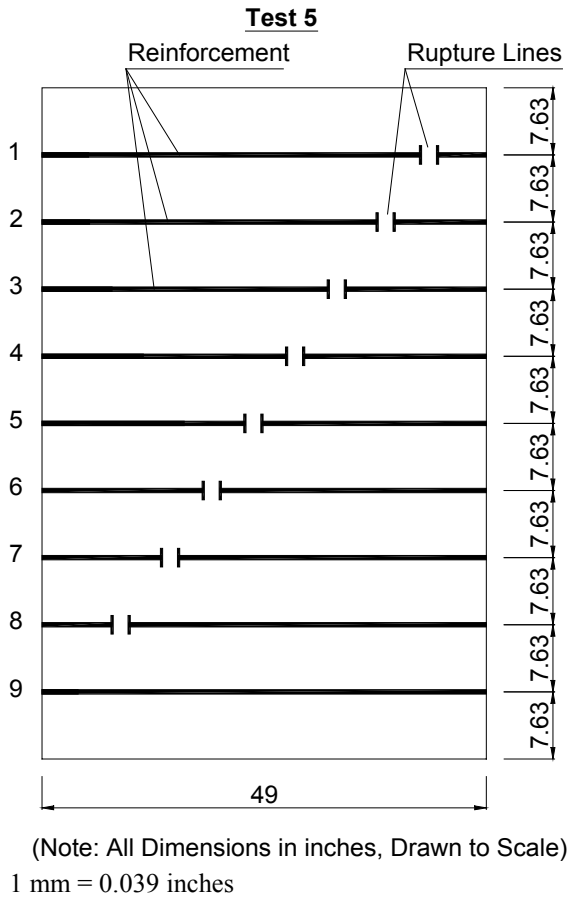

Figure 200. Illustration. Locations of rupture lines of reinforcement in test 5 based on figure 199.

The test results of test 5 are summarized in table 12.

Table 12. GSGC test 5 result summary.

Parameter		Measurement
Test condition	Geosynthetic reinforcement	Geotex® 4×4
	Wide-width strength of reinforcement	70 kN/m
	Reinforcement spacing	0.2 m
	Confining pressure	0
Test results	Ultimate applied pressure	1,900 kPa
	Vertical strain at failure	6.0 percent
	Maximum lateral displacement of the open face at failure	Not measured
	Stiffness at 1 percent vertical strain ($E_{at\ 1\%}$)	52,900 kPa
	Maximum strain in reinforcement at ruptured	12 percent
	Maximum measured strain in reinforcement	3.2 percent

1 kN/m = 0.069 kip/ft
1 m = 3.28 ft
1 kPa = 0.145 psi

4.7 DISCUSSION OF THE RESULTS

The results of the GSGC tests are discussed in terms of the following:

- Effects of geosynthetic inclusion (comparison between tests 1 and 2).
- Relationship between reinforcement spacing and reinforcement strength (comparison between tests 2 and 3).
- Effects of reinforcement spacing (comparison between tests 2 and 4).
- Effects of reinforcement stiffness (comparison between tests 3 and 4).
- Effects of confining pressure (comparison between tests 2 and 5).
- Composite strength properties.

4.7.1 Effects of Geosynthetic Inclusion (Comparison Between Tests 1 and 2)

Table 13 shows the result comparisons between an unreinforced soil mass (test 1) and a soil mass reinforced by Geotex® 4×4 at a 0.7-ft (0.2-m) spacing (test 2). The reinforced soil was much stronger than the unreinforced soil. The ultimate applied pressure for the GSGC mass was about 3.5 times as large as the strength of the soil mass without reinforcement. The stiffness of the unreinforced soil mass was 50 percent of that for the reinforced soil mass. In addition, the reinforced soil mass was much more ductile than the unreinforced soil mass. The global vertical strain was 6.5 percent at failure for test 2, whereas it was only 3.0 percent for test 1.

Table 13. Comparison between test 1 and test 2.

Parameter	Test 1	Test 2 (T, S_v)
Geosynthetic reinforcement	None	Geotex® 4×4
Wide-width strength of reinforcement	None	T_f = 70 kN/m
Reinforcement spacing	No reinforcement	S_v = 0.2 m
Confining pressure	34 kPa	34 kPa
Ultimate applied pressure	770 kPa	2,700 kPa
Vertical strain at failure	3 percent	6.5 percent
Maximum lateral displacement of the open face at failure	47 mm	60 mm
Stiffness at 1 percent vertical strain ($E_{at\ 1\%}$)	33,500 kPa	61,600 kPa
Stiffness for unloading-reloading (E_{ur})	87,100 kPa	Not applied

1 kN/m = 0.069 kip/ft
1 m = 3.28 ft.
1 kPa = 0.145 psi
1 mm = 0.039 inches

4.7.2 Relationship Between Reinforcement Spacing and Reinforcement Strength (Comparison Between Tests 2 and 3)

Comparing the results of tests 2 and 3 demonstrates the relationship between reinforcement spacing and reinforcement strength (see table 14). As noted in section 2.1, the current design methods are based on the concept that reinforcement spacing and reinforcement strength play an equal role in the performance of a GRS mass. In other words, a GRS wall with reinforcement strength T_f at spacing S_v will behave the same as the one with reinforcement strength of 2 × T_f at spacing 2 × S_v. The results of tests 2 and 3 demonstrate that this assumption is incorrect. Even with the same T_f/S_v ratio (7.3 kip/ft^2 (350 kN/m^2)) in tests 2 and 3, the stiffness and strength of test 2 (with T_f and S_v = 0.7 ft (0.2 m)) was much higher than that of test 3 (with 2T_f and S_v = 1.3 ft (0.4 m)). The strength of the composite mass in test 3 was only 65 percent of the strength in test 2. These results suggest that reinforcement spacing plays a more important role than strength of reinforcement in a reinforced soil mass.

Table 14. Comparison between test 2 and test 3 with the same T_f/S_v ratio.

Parameter	Test 2 (T, S_v)	Test 3 ($2T$, $2S_v$)
Wide-width strength of reinforcement (T_f)	70 kN/m	140 kN/m
Reinforcement spacing (S_v)	0.2 m	0.4 m
T_f/S_v	350 kPa	350 kPa
Confining pressure	34 kPa	34 kPa
Ultimate applied pressure	2,700 kPa	1,750 kPa
Stiffness at 1 percent vertical strain ($E_{at\ 1\%}$)	61,600 kPa	48,900 kPa
Vertical strain at failure	6.5 percent	6.1 percent
Maximum lateral displacement of the open face at failure	60 mm	54 mm

1 kN/m = 0.069 kip/ft
1 m = 3.28 ft
1 kPa = 0.145 psi
1 mm = 0.039 inches

4.7.3 Effects of Reinforcement Spacing (Comparison Between Tests 2 and 4)

The effects of reinforcement spacing can be seen by comparing the results of tests 2 and 4 (see table 15). All test conditions in the two tests were the same except the reinforcement spacing. The spacing was 1.3 ft (0.4 m) in test 4 and 0.65 ft (0.2 m) in test 2. The results demonstrate the importance of reinforcement spacing on the behavior of a GRS mass. With reinforcement spacing of 0.7 ft (0.2 m), the strength of the GRS mass was about twice as high as the one with the 1.3-ft (0.4-m) spacing. The corresponding increase in stiffness at 1 percent strain was about 30 percent. The GRS mass at the 0.7-ft (0.2-m) spacing also exhibited significantly higher ductility than at the 1.3-ft (0.4-m) spacing.

Table 15. Comparison between test 2 and test 4.

Parameter	Test 2 (T, S_v)	Test 4 (T, $2S_v$)
Wide-width strength of reinforcement (T_f)	70 kN/m	70 kN/m
Reinforcement spacing (S_v)	0.2 m	0.4 m
T_f/S_v	350 kPa	175 kPa
Confining pressure	34 kPa	34 kPa
Ultimate applied pressure	2,700 kPa	1,300 kPa
Vertical strain at failure	6.5 percent	4.0 percent
Maximum lateral displacement of the open face at failure	60 mm	53 mm
Stiffness at 1 percent vertical strain ($E_{at\ 1\%}$)	61,600 kPa	46,600 kPa

1 kN/m = 0.069 kip/ft
1 m = 3.28 ft
1 kPa = 0.145 psi
1 mm = 0.039 inches

4.7.4 Effects of Reinforcement Strength (Comparison Between Tests 3 and 4)

The effects of reinforcement strength can be seen by comparing the results of tests 3 and 4 (see table 16). All test conditions in the two tests were identical except that reinforcement strength in test 3 was almost twice as high as that in test 4. The results indicate that the increase in strength

of the GRS mass due to doubling the reinforcement strength was about 35 percent. This increase was much smaller than doubling the reinforcement spacing, where the increase in strength of the GRS mass was over 100 percent. The increase in stiffness at 1 percent strain due to doubling the reinforcement strength was only about 5 percent, compared to about a 30 percent increase due to doubling the reinforcement spacing.

Table 16. Comparison between test 3 and test 4.

Parameter	Test 3 ($2T$, $2S_v$)	Test 4 (T, $2S_v$)
Wide-width strength of reinforcement (T_f)	140 kN/m	70 kN/m
Reinforcement spacing (S_v)	0.4 m	0.4 m
T_f/S_v	350 kPa	175 kPa
Confining pressure	34 kPa	34 kPa
Ultimate applied pressure	1,750 kPa	1,300 kPa
Vertical strain at failure	6.1 percent	4.0 percent
Maximum lateral displacement of the open face at failure	54 mm	53 mm
Stiffness at 1 percent vertical strain ($E_{at\ 1\%}$)	48,900 kPa	46,600 kPa

1 kN/m = 0.069 kip/ft
1 m = 3.28 ft
1 kPa = 0.145 psi
1 mm = 0.039 inches

4.7.5 Effects of Confining Pressure (Comparison Between Tests 2 and 5)

The effects of confining pressure can be seen by comparing the test results of tests 2 and 5 (see table 17). All test conditions in the two tests were identical except that the confining pressure in test 2 was 4.9 psi (34 kPa) and test 5 was conducted without confinement. The results indicate that the increase in strength due to the confining pressure was about 40 percent. The increase in stiffness at 1 percent strain due to the confining pressure was about 15 percent.

Table 17. Comparison between test 2 and test 5.

Parameter	Test 2 (T, S_v)	Test 5 (T, S_v)
Wide-width strength of reinforcement (T_f)	70 kN/m	70 kN/m
Reinforcement spacing (S_v)	0.2 m	0.2 m
T_f/S_v	350 kPa	350 kPa
Confining pressure	34 kPa	0
Ultimate applied pressure	2,700 kPa	1,900 kPa
Vertical strain at failure	6.5 percent	6.0 percent
Maximum lateral displacement of the open face at failure	60 mm	Not measured
Stiffness at 1 percent vertical strain ($E_{at\ 1\%}$)	61,600 kPa	52,900 kPa

1 kN/m = 0.069 kip/ft
1 m = 3.28 ft
1 kPa = 0.145 psi
1 mm = 0.039 inches

4.7.6 Composite Strength Properties

Table 18 shows a comparison of the composite strength properties of the five GSGC tests as obtained from the measured data and calculated from Schlosser and Long's method by assuming the friction angle remains the same as unreinforced soil (i.e., the same ϕ value as in test 1).[25] The apparent cohesion, c_R, from Schlosser and Long's method is calculated as shown in figure 201.[25]

Table 18. Comparison of strength properties of five GSGC tests.

Parameter	Test 1 (unreinforced)	Test 2 (T, S_v)	Test 3 ($2T$, $2S_v$)	Test 4 (T, $2S_v$)	Test 5 (T, S_v)
Wide-width strength of reinforcement, T_f (kN/m)		70	140	70	70
Reinforcement spacing, S_v (m)		0.2	0.4	0.4	0.2
T_f/S_v (kPa)		350	350	175	350
Confining pressure (kPa)	34	34	34	34	0
Apparent cohesion, c_R, (kPa) by Schlosser and Long's method		550	550	310	550
Ultimate applied pressure (kPa) from measured data	770	2,700	1,750	1,300	1,900
Ultimate applied pressure (kPa) by Schlosser and Long's method		3,250	3,250	1,930	3,030
Difference in ultimate pressure between measured data and Schlosser and Long's method (percent)		20	86	48	59

1 kN/m = 0.069 kip/ft
1 m = 3.28 ft
1 kPa = 0.145 psi
Note: Blank cells indicate parameters for which there were no measurements.

$$c_R = \frac{T_f}{2\,S_v}\sqrt{K_p} + c$$

Figure 201. Equation. Apparent cohesion from Schlosser and Long.[25]

Where:

c = Cohesion of the backfill.
T_f = Strength of reinforcement.
S_v = Reinforcement spacing.
K_p = Coefficient of passive Earth pressure.

The values calculated from Schlosser and Long's method were higher than the measured values by 20 to 86 percent.

CHAPTER 5. ANALYTICAL MODELS FOR EVALUATING CIS, COMPOSITE STRENGTH PROPERTIES, AND REQUIRED REINFORCEMENT STRENGTH

This chapter describes analytical models for evaluating CIS in a GRS mass, strength properties of a GRS mass, and required tensile strength of reinforcement in the design of GRS structures.

The first analytical model is a simple compaction model that is capable of estimating CIS, or the increase of the horizontal stresses, in a GRS mass due to fill compaction. The model was developed by combining a compaction model developed by Seed, the companion hand-calculation procedure for an unreinforced soil mass by Duncan and Seed, and the theory of GRS composite behavior proposed by Ketchart and Wu.[11,12,20]

The second analytical model is for the determination of the strength properties of a GRS composite mass. With the analytical model, a new relationship between reinforcement strength and reinforcement spacing is introduced to reflect an observation made in actual construction and in controlled experiments regarding the relative effects of reinforcement spacing and reinforcement strength on the performance of GRS structures.

The third analytical model is for the determination of reinforcement strength in design. This model was also developed based on the relationship between reinforcement strength and reinforcement spacing.

5.1 EVALUATING CIS IN A GRS MASS

5.1.1 Conceptual Model for Simulation of Fill Compaction of a GRS Mass

Based on previous studies regarding CIS for unreinforced soil masses and very limited studies for reinforced soil masses, a conceptual stress path for loading-unloading-reloading of a GRS mass is shown in figure 202.

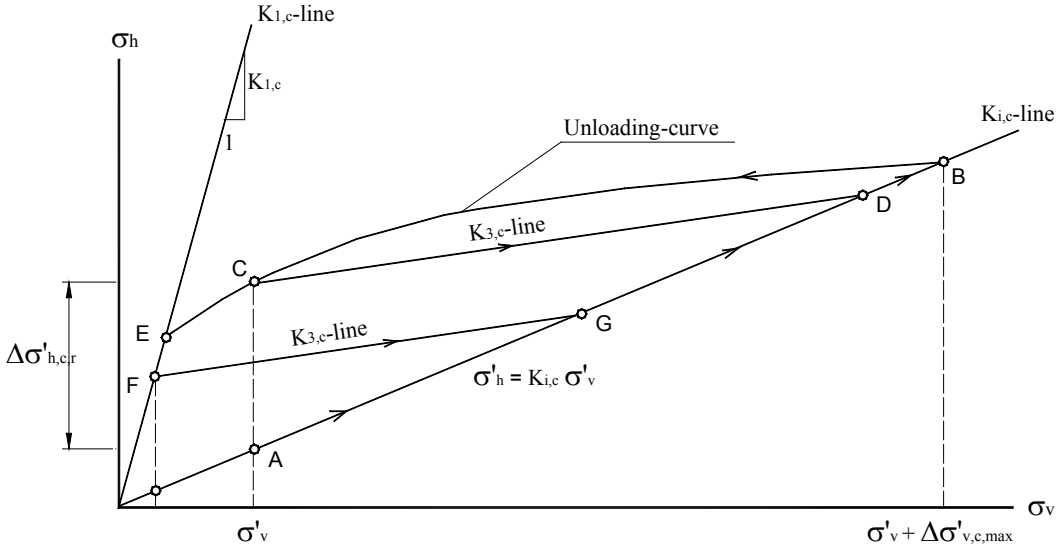

Figure 202. Illustration. Conceptual stress path for compaction of a GRS mass.

Elements in figure 202 are as follows:

- A GRS mass is loaded (due to application of compaction loads) from an initial state (point A) following the $K_{i,c}$ line (with horizontal stress, $\sigma'_h = K_{i,c}\,\sigma'_v$, where $K_{i,c}$ is the coefficient of lateral Earth pressure of the GRS mass for initial loading) up to point B. At point B, the GRS mass reaches a maximum stress state with the vertical stress of $\sigma'_{v,max} = \sigma'_v + \Delta\sigma'_{v,c,max}$ (σ'_v is the vertical stress at the initial stress and $\Delta\sigma'_{v,c,max}$ is the maximum increase in vertical stress due to compaction loading).

- Upon unloading (i.e., removal of the compaction loads), the stresses in the soil are reduced by following a nonlinear path from point B to point C.

- In cases of significant unloading in which the unloading path reaches the limiting line ($K_{1,c}$) at point E, further unloading stress path will follow line EF (with $\sigma'_h = K_{1,c}\,\sigma'_v$).

- Upon reloading due to the next cycle of compaction-load application, the stress follows a $K_{3,c}$ line (with $\sigma'_h = K_{3,c}\,\sigma'_v$) from either point C or point F until it meets the initial loading path (line AB).

- The subsequent cycles of unloading and reloading will not deviate much from the $K_{3,c}$ line, as suggested by Broms, Seed, and Ehrlich and Mitchell.[9,11,46] Therefore, the same K_3 line can be used for all subsequent cycles of reloading and unloading.

5.1.2 Simplified Model to Simulate Fill Compaction of a GRS Mass

A simplified compaction simulation model is proposed for simulation of fill compaction of a GRS mass, as depicted in figure 203. By using the proposed model, the increase of the horizontal stresses in a GRS mass due to compaction can be estimated. These stresses, namely CIS, are represented by the horizontal residual stresses, $\Delta\sigma'_{h,c,r}$, in figure 203. The proposed model is based on the bilinear compaction model for an unreinforced soil mass suggested by Seed and the companion hand-calculation procedure suggested by Duncan and Seed.[11,12] The proposed model considers the presence of geosynthetic inclusions.

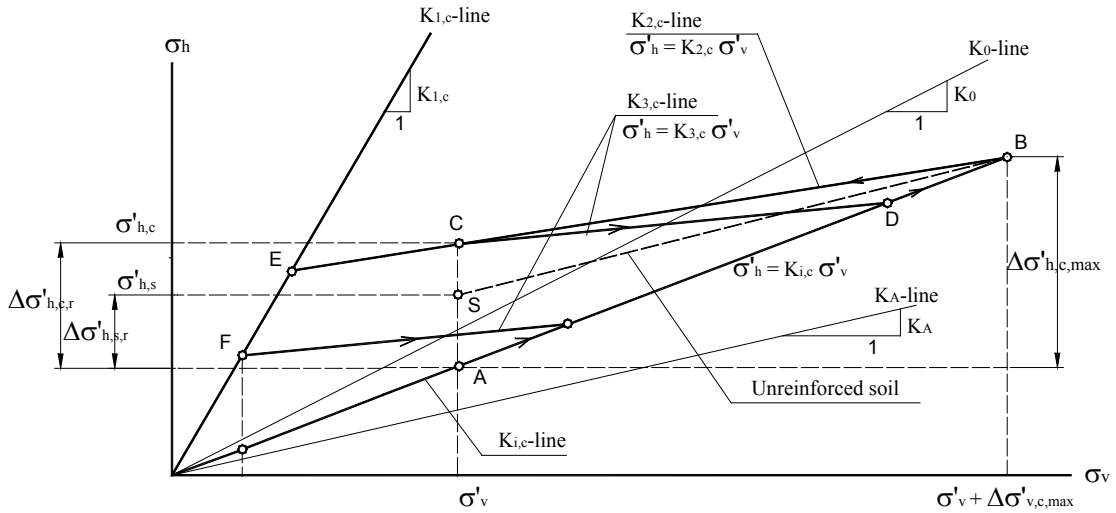

Figure 203. Illustration. Stress path of the proposed simplified model for fill compaction of a GRS mass.

The stress path for fill compaction of a GRS mass in the proposed model can be considered as a simplified form of the conceptual model described in section 5.1. The differences between the simplified model and the conceptual model are as follows:

- Upon removal of the compaction loads, the stresses in the soil are reduced by following the $K_{2,c}$ line from point B to point C, of which the vertical stress, σ'_v, is equal to that of point A. The horizontal residual stress due to the compaction loading is $\Delta\sigma'_{h,c,r}$.

- In the case of an unreinforced soil mass (or where the reinforcement stiffness is negligible), the stress in the soil in response to the removal of compaction loads will reduce to point S (instead of point C). The horizontal residual stress due to compaction loading will be $\Delta\sigma'_{h,s,r}$ with $\Delta\sigma'_{h,s,r} \leq \Delta\sigma'_{h,c,r}$.

- Upon application of the next cycle of compaction loads or placement of new fill layers, the reloading path will follow the $K_{3,c}$ line (with $\sigma'_h = K_{3,c}\,\sigma'_v$, and $K_{3,c} \leq K_{2,c}$). The stress path follows the $K_{3,c}$ line from point C or point F until it meets the initial loading path. It then follows the $K_{i,c}$ line to a new stress state.

5.1.3 Model Parameters of the Proposed Compaction Simulation Model

Four model parameters are needed for the proposed compaction simulation model: $K_{i,c}$, $K_{1,c}$, $K_{2,c}$, and $K_{3,c}$. These parameters can be estimated from soil and reinforcement properties using correlations shown in table 19. The empirical coefficients (e.g., α and F) are calibrated by the measured data from the GSGC tests described in chapter 4. Recommended values of the empirical coefficients are given for routine applications. Alternatively, the model parameters can be obtained directly from the results of GSGC tests. Note that the term $\left(0.7\frac{E_r}{E_s S_v - 0.7J_r}\right)$ for the estimation of $K_{2,c}$ is to account for the presence of reinforcement. For hand calculations, the

maximum increase of vertical stress due to compaction, $\Delta\sigma'_{v,c,\max}$, can be estimated simply by using Westergaard's solution as shown in figure 203.[78]

Table 19. Model parameters for the proposed compaction simulation model.

Parameter	Name	Range of the Parameter Values	Preliminary Estimation Based on Soil and Reinforcement Properties
$K_{i,c}$	Coefficient of lateral Earth pressure of a GRS mass for initial loading	$K_A \le K_{i,c} \le K_0$	$K_{i,c} \cong \beta\, K_A$ $1.0 \le \beta \le 1.5$ $K_A \cong \tan^2\left(45 - \frac{\phi'}{2}\right)$ $K_0 \cong 1 - \sin\phi'$
$K_{1,c}$	Limiting coefficient of lateral Earth pressure for unloading	$K_{1,c} \cong K_P$	$K_{1,c} \cong K_P \cong \tan^2\left(45 + \frac{\phi'}{2}\right)$
$K_{2,c}$	Coefficient of lateral Earth pressure for unloading	$0 \le K_{2,c} \le K_0$	$K_{2,c} \cong \left[1 - F\left(1 + 0.7\frac{E_r}{E_s S_v - 0.7E_r}\right)\right] K_{i,c}$ $F = 1 - \frac{\left(OCR - OCR^{\alpha}\right)}{\left(OCR - 1\right)};\ \alpha \cong \sin\phi'$
$K_{3,c}$	Coefficient of lateral Earth pressure for reloading	$0 \le K_{3,c} \le K_0$	$K_{3,c} \cong K_{2,c}$

K_o = Coefficient of at-rest lateral Earth pressure.
K_A = Coefficient of active lateral Earth pressure.
K_P = Coefficient of passive lateral Earth pressure.
OCR = Over-consolidation ratio.
E_s = Soil stiffness (kPa).
E_r = Reinforcement stiffness (kN/m).
S_v = Reinforcement spacing (m).

5.1.4 Simulation of Fill Compaction Operation

Fill compaction is a complex operation in terms of change in stresses. This section describes the maximum increase of vertical stress at depth *z* along a given section in a soil mass due to typical compaction operation. Consider the change of vertical stress at depth *z* in section I-I due to moving compaction loads, as shown in figure 204 through figure 207. The directions of the moving compaction plant may either be coming toward section I-I or moving away from section I-I. The compaction loads are simulated by loading and unloading at different locations (locations 1, 2, and i), as shown in figure 204 and figure 206. Figure 205 and figure 207 show the stress path of the stresses at depth *z* along section I-I.

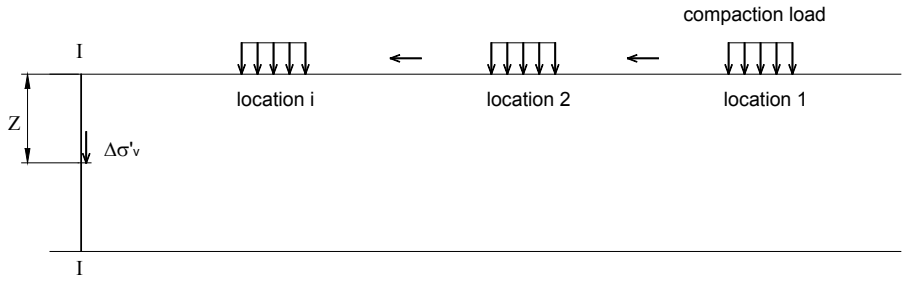

Figure 204. Illustration. Locations of compaction loads moving toward section I-I.

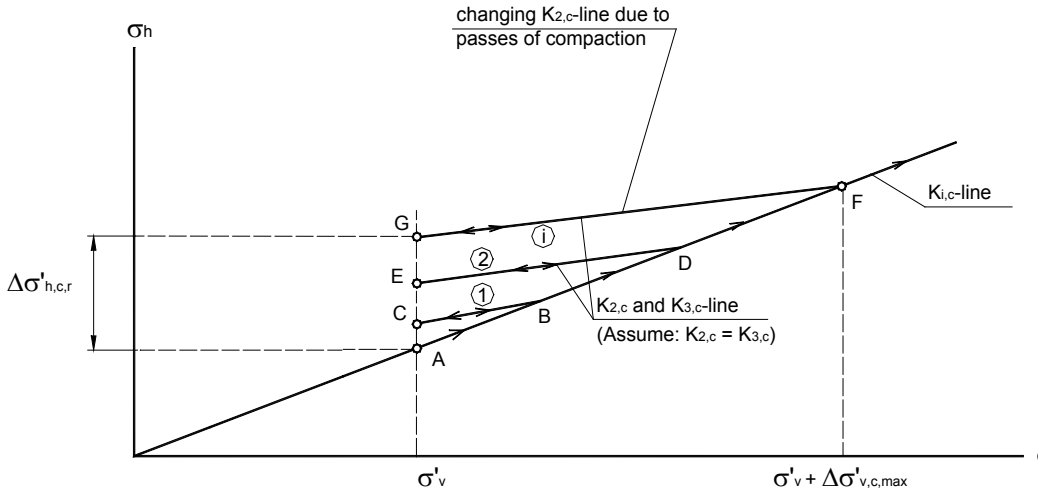

Figure 205. Illustration. Stress paths during compaction at depth *z* as compaction loads move toward section I-I.

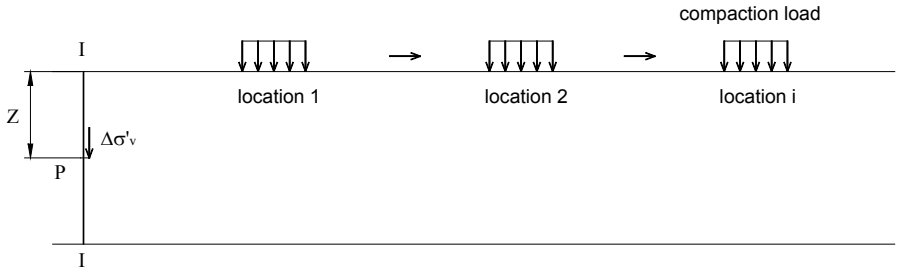

Figure 206. Illustration. Locations of compaction loads moving away from section I-I.

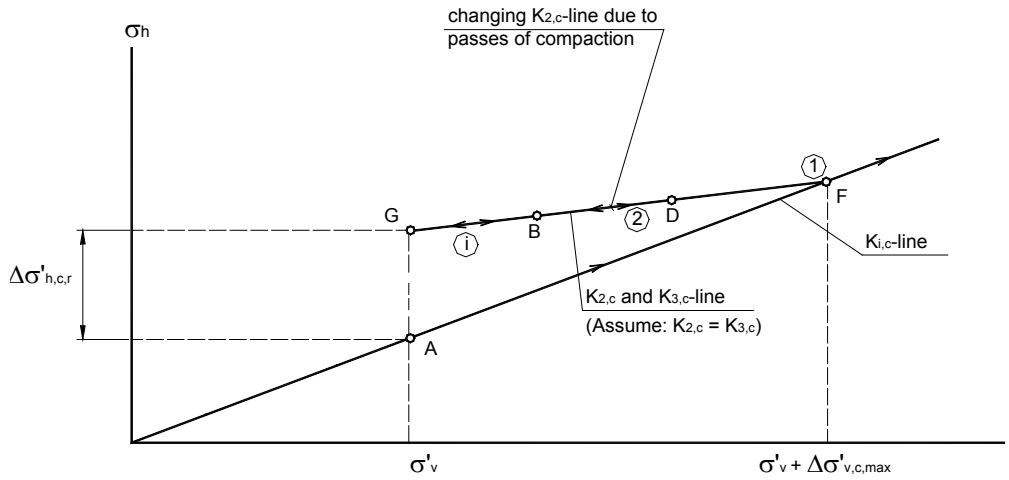

Figure 207. Illustration. Stress paths during compaction at depth *z* as compaction loads move away from section I-I.

Elements in figure 205 are as follows:

- The initial stress condition at depth *z* along section I-I is denoted by point A, with the initial vertical stress being σ_v.
- With the compaction loads at location 1, the stresses will increase by following the $K_{i,c}$ line to point B.
- As the compaction loads are removed from location 1, the stresses will reduce from point B to point C by following the $K_{2,c}$ line.
- When compaction loads move to a new location (location 2), the stresses will increase from point C through point B to point D.
- As the compaction loads are removed from location 2, the stresses will reduce from point D to point E by again following the $K_{2,c}$ line.
- The previous steps are repeated for all subsequent new locations as the compaction plant moves toward section I-I. As the compaction plant moves closer to section I-I, the vertical stress at depth *z* will become larger.
- The maximum vertical stress condition will be reached when the compaction plant is directly above section I-I. The corresponding stress condition is represented by point F. Upon removal of the compaction loads, the stress path will follow the K_2 line to point G.

In figure 206 and figure 207, the compaction plant moves away from section I-I. Initially, the compaction is located directly above section I-I, which causes the stresses to increase from point A to point F due to the compaction loads. As the compaction loads are removed from section I-I, the stresses are reduced from point F to point G, following the $K_{2,c}$ line. As the compaction plant moves away from section I-I, the stress conditions will move to points D and B along line FG. As the compaction plant is finally removed, the stress condition will be at point G.

As shown in figure 204 through figure 207, the residual stresses, denoted by the vertical distance AG, are the same for the two cases. This indicates that to determine the CIS at a certain section due to a moving compaction plant, only the residual lateral stresses need to be determined as the compaction loads are directly above the section under consideration.

Figure 208 shows the conceptual stress path on the effect of the number of compaction passes. For the first pass, the residual stress at point A is represented by point G. With the subsequent pass of the compaction plant, the slope of the K_2 line increases, and point G becomes point G'. As the number of compaction pass increases, the final residual stresses will move from G' to G" to G'".

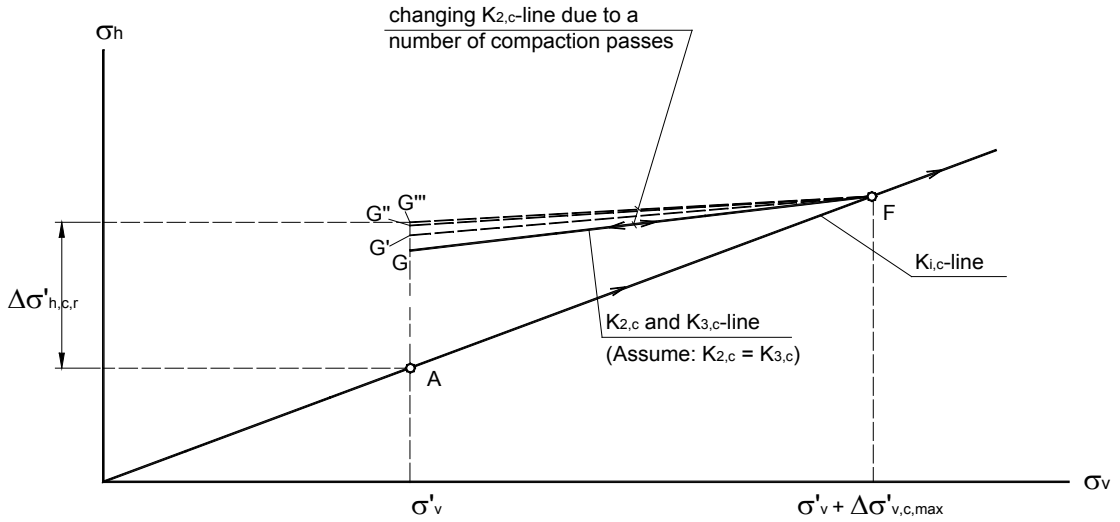

Figure 208. Illustration. Stress path at depth *z* when subject to multiple compaction passes.

5.1.5 Estimation of $K_{2,c}$

This section presents the estimation of $K_{2,c}$ in the proposed model for determining CIS in a GRS mass. Two stress reduction factors, F and A, are introduced (see figure 209). Factor F represents CIS for unreinforced soil in Seed's model, and factor A is considered the presence of the reinforcement in the GRS mass.[11]

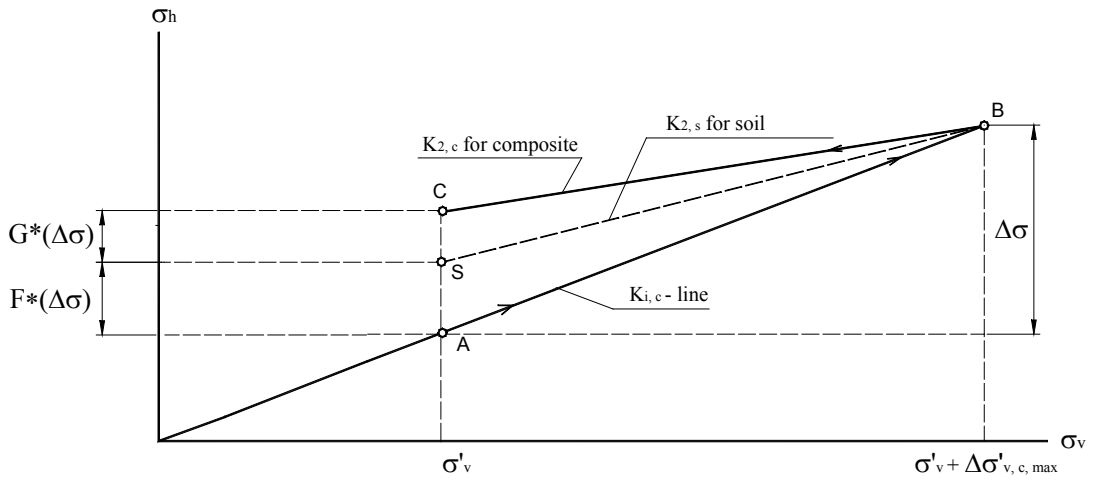

Figure 209. Illustration. Stress path of the proposed model for fill compaction of a GRS mass.

5.1.5.1 Compacted Soil

For an unreinforced soil fill, the coefficient of lateral Earth pressure for unloading in figure 203 can be estimated by using the expression in figure 210, as suggested by Seed.[11]

$$K_{2,s} = (1 - F)\, K_{i,c}$$

Figure 210. Equation. Coefficient of lateral Earth pressure.

Where:

$F = 1 - \dfrac{\left(OCR - OCR^{\alpha}\right)}{OCR - 1}$.

$\alpha \cong \sin \phi'$.

$OCR \cong 5$ for typical compacted sand.[11]

5.1.5.2 GRS Composite

For a GRS mass, total residual strain in the soil can be determined as shown in figure 211.

$$\varepsilon_s = \frac{(F + G)\,(\Delta\sigma)}{E_s}$$

Figure 211. Equation. Total residual strain.

Where:

F and G = Stress reduction factors shown in figure 209.
$\Delta\sigma$ = Increase in horizontal stress due to compaction.
E_s = Soil stiffness.

From figure 211, the reinforcement force, *T*, due to residual strain in the soil can be determined as shown in figure 212.

$$T = \left(\frac{(F+G)\,\Delta\sigma}{E_s} \right) E_r$$

Figure 212. Equation. Reinforcement force.

Where E_r is the reinforcement stiffness.

The average residual stress in the soil due to compaction, $G*(\Delta\sigma)$, is calculated as shown in figure 213 and figure 214.

$$G*\Delta\sigma = 0.7 \left(\frac{(F+G)\,\Delta\sigma}{E_s} \right) \frac{E_r}{S_v}$$

Figure 213. Equation. Average residual stress in the soil due to compaction.

$$G\,E_s\,S_v = 0.7\,F\,E_r + 0.7\,G\,E_r$$

Figure 214. Equation. Second equation for average residual stress in the soil due to compaction.

Figure 215 is a result of the previous two equations.

$$G = \frac{0.7\,F\,E_r}{E_s\,S_v - 0.7\,E_r}$$

Figure 215. Equation. Result of figure 213 and figure 214.

Substituting figure 215 into figure 216 results in figure 217.

$$K_{2,c} = [\,1 - (F+G)\,]\,K_{i,c}$$

Figure 216. Equation. First equation for estimation of $K_{2,c}$.

$$K_{2,c} \cong \left[1 - F\,\left(1 + \frac{0.7\,E_r}{E_s\,S_v - 0.7\,E_r} \right) \right] K_{i,c}$$

Figure 217. Equation. Second equation for estimation of $K_{2,c}$.

The factor 0.7 in figure 213 is explained in section 5.2.1. The increased horizontal stress in a GRS mass due to compaction can be estimated using figure 218.

$$\Delta\sigma_{h,c} = \Delta\sigma\,(G+F) = \Delta\sigma'_{v,c,\max}\,(K_{i,c} - K_{2,c})$$

Figure 218. Equation. Increased horizontal stress in a GRS mass due to compaction.

Substituting figure 217 into figure 218 results in figure 219 and figure 220.

$$\Delta\sigma_{h,c} = \Delta\sigma'_{v,c,\max}\left\{ K_{i,c}\left[1-1+F\left(1+\frac{0.7\ E_r}{E_s\ S_v - 0.7\ E_r}\right)\right]\right\}$$

Figure 219. Equation. Second equation of increased horizontal stress in a GRS mass due to compaction.

$$\Delta\sigma_{h,c} = \Delta\sigma'_{v,c,\max}\ \ K_{i,c}\,F\left(1+\frac{0.7\ E_r}{E_s\ S_v - 0.7\ E_r}\right)$$

Figure 220. Equation. Residual lateral stress in a GRS mass due to compaction and the effect of CIS in a GRS mass.

Figure 220 shows the calculation of the residual lateral stress in a GRS mass due to compaction as well as the effect of CIS in a GRS mass.

Using figure 220, the increase in lateral stress in a GRS mass can be estimated, and the increase in soil stiffness can be evaluated. For example, the stiffness of a soil can be evaluated using figure 221.

$$E_t = \left[1-\frac{R_f\ (1-\sin\phi)\left(\sigma_1 - \left(\sigma_3 + \Delta\sigma_{h,c}\right)\right)}{2\ c\ \cos\phi + 2\left(\sigma_3 + \Delta\sigma_{h,c}\right)\sin\phi}\right]^2 K\ P_a\left(\frac{\sigma_3 + \Delta\sigma_{h,c}}{P_a}\right)^n$$

Figure 221. Equation. Stiffness of a soil.

Where:

E_t = Tangent modulus.
R_f = Ratio of ultimate deviator stress to the failure deviator stress.
c = Cohesive strength.
ϕ = Angle of friction.
P_a = Atmospheric pressure.
K and n = Material parameters.

5.2 STRENGTH PROPERTIES OF GRS COMPOSITE

Schlosser and Long proposed the concepts of increase of apparent confining pressure and apparent cohesion of a GRS composite.[25] The Mohr circles of an unreinforced cohesive soil and a reinforced cohesive soil at failure are shown in figure 222.

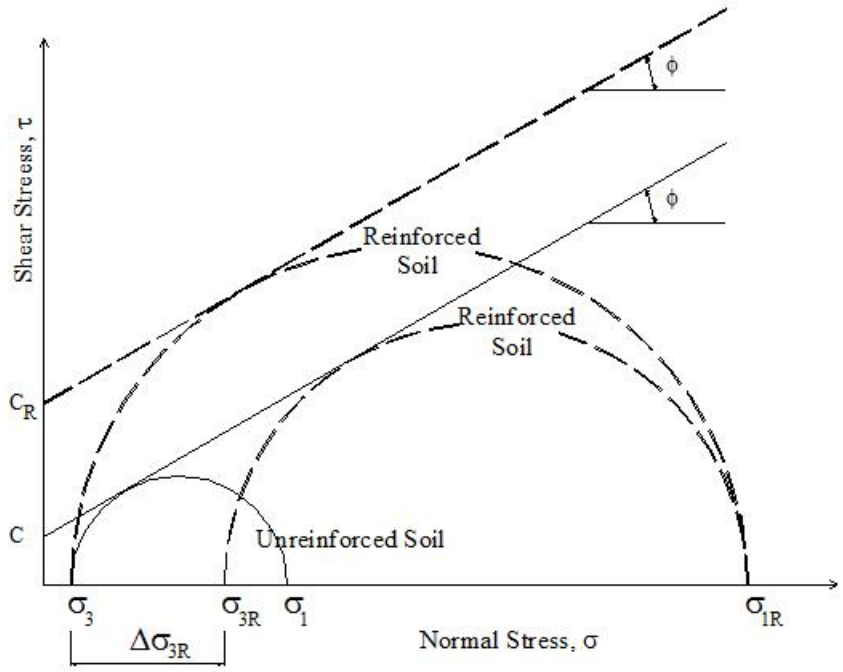

Figure 222. Illustration. Concept of apparent confining pressure and apparent cohesion of a GRS composite.

The apparent cohesion of a GRS composite can be determined as shown in figure 223.

$$c_R = \frac{\Delta\sigma_{3R}\sqrt{K_P}}{2} + c$$

Figure 223. Equation. Apparent cohesion of a GRS composite.

Where:

c_R = Apparent cohesion of a GRS composite.
c = Cohesion of soil.
K_p = Coefficient of passive Earth pressure.
$\Delta\sigma_{3R}$ = Increase of confining pressure due to reinforcement.

Schlosser and Long also proposed figure 224 to calculate increased confining pressure.[25]

$$\Delta\sigma_3 = \frac{T_f}{S_v}$$

Figure 224. Equation. Increased confining pressure.

This expression implies that an increase in reinforcement strength, T_f, has the same effect as a proportional decrease in reinforcement spacing, S_v. Many experimental test results have shown that figure 224 is not correct. Reinforcement spacing plays a more important role than reinforcement strength. (See references 6, 7, 30, 31, and 35.) This point is also supported by the experiments conducted as a part of this study and presented in chapter 4.

5.2.1 Increased Confining Pressure

A new method to estimate the increased confining pressure in soil due to the presence of reinforcement is expressed in figure 225.

$$\Delta\sigma_3 = W\left(\frac{T_f}{S_v}\right)$$

Figure 225. Equation. New method to estimate the increased confining pressure in soil due to the presence of reinforcement.

Where the factor, *W*, can be estimated as shown in figure 226.

$$W = r^{\left(\frac{S_v}{S_{ref}}\right)}$$

Figure 226. Equation. Estimation of the factor *W*.

Where:

T_f = Extensile strength of reinforcement.
r = Dimensionless factor.
S_v = Vertical spacing of reinforcement.
S_{ref} = Reference spacing.

To estimate the factor *r* in figure 226, the concept of average stresses proposed by Ketchart and Wu was employed.[20] However, instead of using average stresses, average reinforcement forces were used.

5.2.1.1 Average Stress in GRS Mass by Ketchart and Wu[20]

Ketchart and Wu developed a concept of average stress to determine the behavior of a GRS composite based on a load transfer analysis.[20] From a simplified preloading-reloading (SPR) model for GRS mass, the equations to calculate stresses and displacements of a GRS mass were developed using the idealized geometry of a plane-strain GRS mass and differential elements of soil and reinforcement for equilibrium equations, as shown in figure 227.

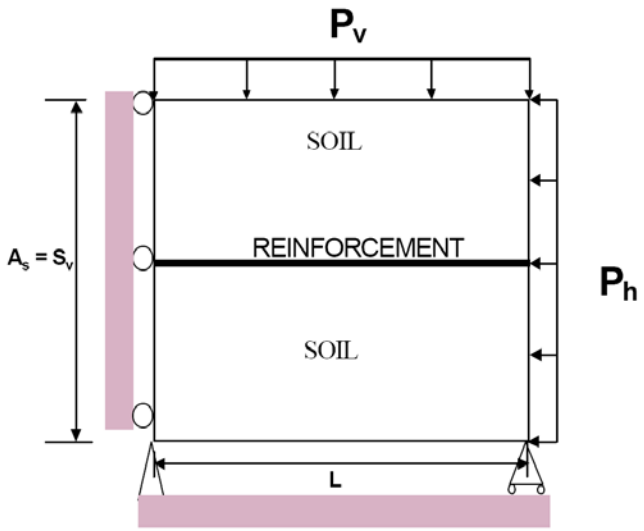

Figure 227. Illustration. Idealized plane-strain GRS mass for the SPR model.

Based on the equilibrium equations and several assumptions, the stresses in soil and the force in the reinforcement can be calculated using the following equations.

The force in the reinforcement is calculated with figure 228.

$$F_x = A_r\ E_r \left[\left(\frac{\upsilon_s}{1-\upsilon_s}\right) P_v - P_h\right]\left(\frac{1-\upsilon_s^{\,2}}{E_s}\right)\left(1-\frac{\beta}{\alpha^2}\right)\left(1-\frac{\cosh(\alpha\ x)}{\cosh(\alpha\ L)}\right)$$

Figure 228. Equation. Force in the reinforcement.

The horizontal stress in the soil is calculated with figure 229.

$$\sigma_x = -\left(\frac{\upsilon_s}{1-\upsilon_s}\right) P_v + \left(\left(\frac{\upsilon_s}{1-\upsilon_s}\right) P_v - P_h\right)\left(\frac{\beta}{\alpha^2}\frac{\cosh(\alpha\ x)}{\cosh(\alpha\ L)} + \left(1-\frac{\beta}{\alpha^2}\right)\right)$$

Figure 229. Equation. Horizontal stress in the soil.

Based on a load-transfer analysis, the average stresses were determined.

The average vertical stress, $\overline{\sigma}_v$, is assumed to be equal to the boundary vertical pressure, as shown in figure 230.

$$\overline{\sigma}_v = P_v$$

Figure 230. Equation. Average vertical stress.

The average horizontal stress, $\overline{\sigma}_h$, is as shown in figure 231 and figure 232.

$$\overline{\sigma}_h = \frac{\int_0^L \sigma_x(x)dx}{L}$$

Figure 231. Equation. First equation of average horizontal stress.

$$\overline{\sigma}_h = \left(\frac{\upsilon_s}{1-\upsilon_s}\right) P_v - \left(\left(\frac{\upsilon_s}{1-\upsilon_s}\right) P_v - P_h\right)\left(1+\frac{\beta}{\alpha^2}\left(\frac{\tanh(\alpha\, L)}{\alpha.L}-1\right)\right)$$

Figure 232. Equation. Second equation of average horizontal stress.

5.2.1.2. Average Reinforcement Forces in a GRS Mass

The equations of the forces in the reinforcement and the maximum force in the reinforcement are expressed as shown in figure 233 and figure 234.

$$F_x = A_r\ E_r \left[\left(\frac{\upsilon_s}{1-\upsilon_s}\right) P_v - P_h\right]\left(\frac{1-\upsilon_s{}^2}{E_s}\right)\left(1-\frac{\beta}{\alpha^2}\right)\left(1-\frac{\cosh(\alpha\, x)}{\cosh(\alpha\, L)}\right)$$

Figure 233. Equation. Forces in the reinforcement.

$$F_{\max} = A_r\ E_r \left[\left(\frac{\upsilon_s}{1-\upsilon_s}\right) P_v - P_h\right]\left(\frac{1-\upsilon_s{}^2}{E_s}\right)\left(1-\frac{\beta}{\alpha^2}\right)\left(1-\frac{1}{\cosh(\alpha\, L)}\right)$$

Figure 234. Equation. Maximum force in the reinforcement.

The average force in the reinforcement is calculated as shown in figure 235.

$$\overline{F} = \frac{\int_0^L F_x dx}{L}$$

Figure 235. Equation. Average force in the reinforcement.

Substituting figure 233 into figure 235 results in figure 236 and figure 237, which is simplified to figure 238.

$$\overline{F} = \frac{A_r\ E_r}{L}\int_0^L \left[\left(\frac{\upsilon_s}{1-\upsilon_s}\right) P_v - P_h\right]\left(\frac{1-\upsilon_s{}^2}{E_s}\right)\left(1-\frac{\beta}{\alpha^2}\right)\left(1-\frac{\cosh(\alpha\, x)}{\cosh(\alpha\, L)}\right) dx$$

Figure 236. Equation. Second equation of average force in the reinforcement.

$$\overline{F} = \frac{A_r.E_r}{L}\left[\left(\frac{\upsilon_s}{1-\upsilon_s}\right) P_v - P_h\right]\left(\frac{1-\upsilon_s{}^2}{E_s}\right)\left(1-\frac{\beta}{\alpha^2}\right)\int_0^L \left(1-\frac{\cosh(\alpha\, x)}{\cosh(\alpha\, L)}\right) dx$$

Figure 237. Equation. Third equation of average force in the reinforcement.

$$\overline{F} = \frac{A_r . E_r}{L}\left[\left(\frac{\upsilon_s}{1-\upsilon_s}\right)P_v - P_h\right]\left(\frac{1-\upsilon_s{}^2}{E_s}\right)\left(1-\frac{\beta}{\alpha^2}\right)\left(L-\frac{\sinh(\alpha\, x)}{\alpha\cosh(\alpha\, L)}\right)$$

Figure 238. Equation. Fourth equation of average force in the reinforcement.

Introducing a factor $r = \frac{\overline{F}}{F_{\max}}$ and using figure 234 and figure 238, *r* can be determined using figure 239.

$$r = \frac{\alpha\, L\cosh(\alpha\, L) - \sinh(\alpha\, L)}{\alpha\, L\left(\cosh(\alpha\, L) - 1\right)}$$

Figure 239. Equation. Estimation of factor *r*.

Table 20 shows the values of factor *r* for different applied pressures and reinforcement lengths using the data from the calculation example in the SPR model.[20]

Table 20. Values of factor *r* under different applied pressure and reinforcement lengths.

Increment of Vertical Pressure (P_v) (kPa)	Reinforcement Length, *L* (m)	α	$(\mathbf{r} = \frac{\overline{\mathbf{F}}}{\mathbf{F_{max}}})$
9.0	0.127	13.875	0.698
18.0	0.127	14.616	0.701
9.0	0.225	6.851	0.691
18.0	0.225	6.966	0.692

1 kPa = 0.145 psi
1 m = 3.28 ft

Table 20 shows that the average reinforcement forces are about 70 percent of the maximum reinforcement force. The highest value of the maximum reinforcement force, F_{max}, cannot exceed the tensile strength of reinforcement, T_f, as shown in figure 240.

$$F_{\max} = T_f$$

Figure 240. Equation. Maximum reinforcement force.

The average reinforcement force is as shown in figure 241.

$$T_{avg} = 0.7\, T_f$$

Figure 241. Equation. Average reinforcement force.

Figure 226 becomes figure 242.

$$W = 0.7^{\left(\frac{S_v}{S_{ref}}\right)}$$

Figure 242. Equation. Second estimation of the factor *W*.

5.2.2 Apparent Cohesion and Ultimate Pressure Carrying Capacity of a GRS Mass

Substituting figure 242 into figure 225, the increased confining pressure in a GRS mass is calculated in figure 243.

$$\Delta\sigma_3 = W\left(\frac{T_f}{S_v}\right) = \left[0.7^{\left(\frac{S_v}{S_{ref}}\right)}\right]\left(\frac{T_f}{S_v}\right)$$

Figure 243. Equation. Increased confining pressure in a GRS mass.

Therefore, the apparent cohesion, c_R, of a GRS composite can be evaluated using figure 244.

$$c_R = \frac{\Delta\sigma_3}{2}\sqrt{K_p} + c = \left[0.7^{\left(\frac{S_v}{S_{ref}}\right)}\right]\frac{T_f}{2\,S_v}\sqrt{K_p} + c$$

Figure 244. Equation. Apparent cohesion.

Where:

c = Cohesion of soil.
K_p = Coefficient of passive Earth pressure.
T_f = Extension strength of reinforcement.
S_v = Vertical spacing of reinforcement.
S_{ref} = Reference spacing, which can be calculated using figure 245.

$$S_{ref} = 6\,d_{\max}$$

Figure 245. Equation. Reference spacing.

Where:

d_{max} = Maximum particle/grain size of soil.

Therefore, the ultimate pressure carrying capacity, σ_{1R}, of a soil-geosynthetic composite mass is calculated using figure 246.

$$\sigma_{1R} = \left(\sigma_3 + W\frac{T_f}{S_v}\right)K_p + 2\,c\sqrt{K_p}$$

Figure 246. Equation. Pressure carrying capacity.

Where σ_3 is the confining pressure.

5.3 VERIFICATION OF THE ANALYTICAL MODEL WITH MEASUREMENT DATA

Verification of the proposed analytical model for GRS composite strength properties was made by comparing the model calculation results with the measured data from GSGC tests presented in chapter 4 and with the measured data by Elton and Patawaran.[31]

5.3.1 Comparison Between the Analytical Model and GSGC Test Results

The dimensions of the GSGC tests were 6.6 ft (2 m) high and 4.6 ft (1.4 m) wide in a plane-strain condition. The soil mass in the tests was reinforced with Geotex® 4×4 geotextile at 0.7- and 1.3-ft (0.2- and 0.4-m) spacing. For the diabase soil used in GSGC tests, the maximum particle size was about 1.3 inches (66 mm). Therefore, $S_{ref} = 6\ d_{max} = 7.8$ inches (0.2 m). Comparisons of the results between the analytical model and the GSGC tests are presented in table 21. The deviatoric stresses at failure calculated from the analytical model are in good agreement with those of the GSGC tests, with differences of less than 10 percent.

Table 21. Comparison of the results of the analytical model and the GSGC tests.

Parameter	Test 2 (*T*, *S*)	Test 3 (2*T*, 2*S*)	Test 4 (*T*, 2*S*)
T_f (kN/m)	70	140	70
S_v (m)	0.2	0.4	0.4
$\Delta\sigma_3$ (kN/m^2) by the analytical model	245	172	86
c_R (kN/m^2) by the analytical model	407	305	188
$(\sigma_{1R} - \sigma_3)$ (kN/m^2) from measured data	2,700	1,750	1,300
$(\sigma_{1R} - \sigma_3)$(kN/m^2) by the analytical model	2,460	1,900	1,250
Difference between analytical model and measured data	-9 percent	+8 percent	-4 percent

1 kN/m = 0.069 kip/ft
1 m = 3.28 ft
1 kN/m^2 = 0.021 kip/ft^2
Note: Internal friction angle of soil = 50 degrees and cohesion of soil = 10.15 psi (70 kPa).

For reference purposes, comparisons of the results between Schlosser and Long's method and the GSGC tests are presented in table 22. The deviatoric stresses at failure calculated from Schlosser and Long's method are about 20 to 86 percent larger than the measured values.

Table 22. Comparison of the results of Schlosser and Long's method and the GSGC tests.

Parameter	Test 2 (*T*, *S*)	Test 3 (2*T*, 2*S*)	Test 4 (*T*, 2*S*)
T_f (kN/m)	70	140	70
S_v (m)	0.2	0.4	0.4
$\Delta\sigma_3$ (kN/m^2) by Schlosser and Long's method	350	350	175
c_R (kN/m^2) by Schlosser and Long's method	550	550	310
$(\sigma_{1R} - \sigma_3)$ (kN/m^2) from measured data	2,700	1,750	1,300
$(\sigma_{1R} - \sigma_3)$ (kN/m^2) by Schlosser and Long's method	3,250	3,250	1,930
Difference between Schlosser and Long's method and measured data	+20 percent	+86 percent	+48 percent

1 kN/m = 0.069 kip/ft
1 m = 3.28 ft
1 kN/m^2 = 0.021 kip/ft^2
Note: Internal friction angle of soil = 50 degrees and cohesion of soil = 10.15 psi (70 kPa).

5.3.2 Comparison Between the Analytical Model and Elton and Patawaran's Test Results

Elton and Patawaran conducted seven large-size triaxial tests for reinforced soil 5 ft (1.5 m) in height and 2.5 ft (0.76 m) in diameter.[31] All the tests were conducted under an unconfined condition. The properties of the tests were as follows:

- **Backfill**: The soil used in the test was a poorly graded sand with the gradation test results shown in figure 247. The maximum dry unit weight, γ_{dry}, was 121 pcf (1,900 kg/m^3), the optimum moisture content, w_{opt}, was 9.3 percent, the internal friction, ϕ, was 40 percent, and the cohesion, c, was 4 psi (27 kPa).

- **Reinforcement**: Six types of reinforcement (TG500, TG600, TG700, TG800, TG1000, and TG028) were used for the tests with reinforcement spacing of 6 and 12 inches (150 and 300 mm).

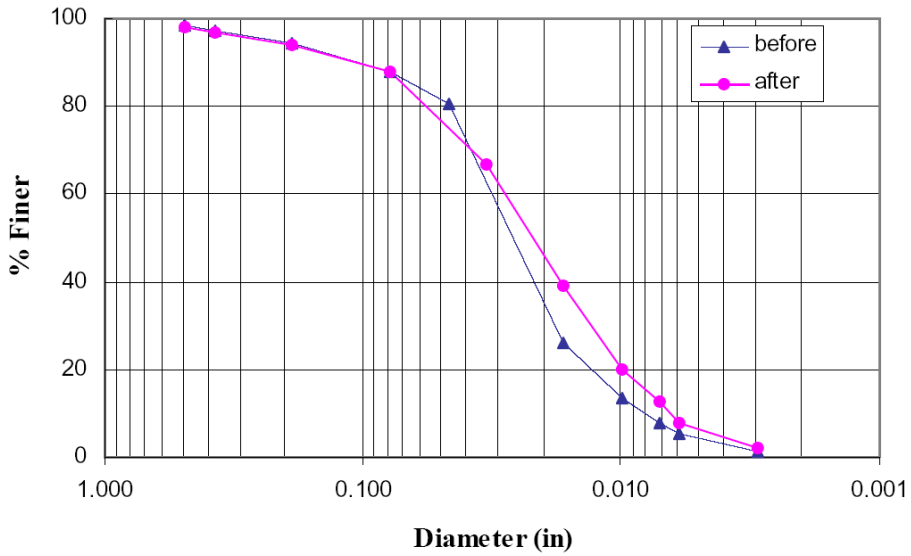

1 mm = 0.039 inches

Figure 247. Graph. Backfill grain size distribution before and after large-size triaxial tests.[31]

The maximum particle size of the backfill in the large-size triaxial tests was d_{max} = 0.5 inches (12.7 mm). Therefore, S_{ref} = 6 d_{max} = 3 inches (0.08 m). The measured results are shown in figure 248. The comparisons of Elton and Patawaran's tests results with the analytical model and with Schlosser and Long's method are presented in table 23 and table 24, respectively.

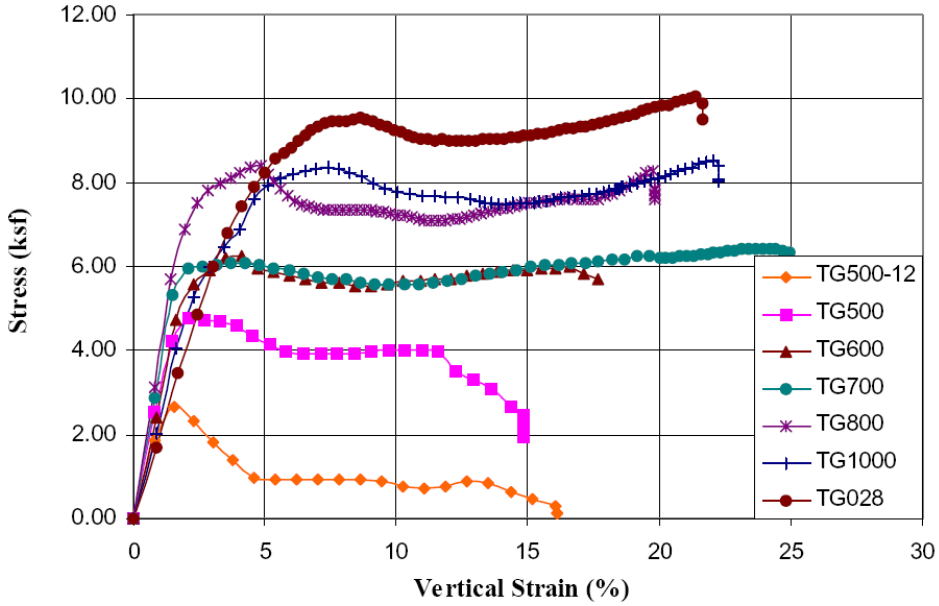

1 ksf = 47.88 kPa

Figure 248. Graph. Large-size triaxial test results.[31]

Table 23. Comparison of the results of the analytical model and Elton and Patawaran's tests.[31]

Parameter	TG 500	TG 500	TG 600	TG 700	TG 800	TG 1000	TG 028
T_f (kN/m)	9	9	14	15	19	20	25
S_v (m)	0.15	0.30	0.15	0.15	0.15	0.15	0.15
$\Delta\sigma_3$ (kN/m^2) by the analytical model	30	8	47	48	62	67	83
c_R (kN/m^2) by the analytical model	60	36	78	79	94	99	116
$(\sigma_{1R} - \sigma_3)$ (kN/m^2) from measured data	230	129	306	292	402	397	459
$(\sigma_{1R} - \sigma_3)$ (kN/m^2) by the analytical model	256	153	333	341	402	426	498
Difference between the analytical model and measured data (percent)	11	18	9	17	0	7	8

1 kN/m = 0.069 kip/ft
1 m = 3.28 ft
1 kN/m^2 = 0.021 kip/ft^2
Note: Internal friction angle of soil = 40 degrees and cohesion of soil = 4.0 psi (27.6 kPa).

Table 24. Comparison of the results of Schlosser and Long's method and Elton and Patawaran's tests.[31]

Parameter	TG 500	TG 500	TG 600	TG 700	TG 800	TG 1000	TG 028
T_f (kN/m)	9	9	14	15	19	20	25
S_v (m)	0.15	0.30	0.15	0.15	0.15	0.15	0.15
$\Delta\sigma_3$ (kN/m^2) by Schlosser and Long's method	59	30	92	95	122	132	163
c_R (kN/m^2) by Schlosser and Long's method	91	59	126	130	158	169	202
$(\sigma_{1R} - \sigma_3)$ (kN/m^2) from measured data	230	129	306	292	402	397	459
$(\sigma_{1R} - \sigma_3)$ (kN/m^2) by Schlosser and Long's method	390	254	541	557	678	726	868
Difference between Schlosser and Long's method and measured data (percent)	70	97	77	91	69	83	89

1 kN/m = 0.069 kip/ft
1 m = 3.28 ft
1 kN/m^2 = 0.021 kip/ft^2
Note: Internal friction angle of soil = 40 degrees; cohesion of soil = 4.0 psi (27.6 kPa).

The differences in the deviatoric stresses at failure calculated from the analytical model and Elton and Patawaran's measured data are less than 18 percent. The results calculated from Schlosser and Long's method are 69 to 97 percent larger than the measured values.

5.3.3 Comparison Between the Analytical Model and FE Results

FE analyses were conducted to provide additional data for verifying the analytical model. The test conditions and material properties used for the FE analyses were the same as those used in

GSGC test 2 but with confining pressures of 4.9, 10, 15, and 29 psi (34, 70, 100, and 200 kPa). The confining pressure used in GSGC test 2 was 4.9 psi (34 kPa). The comparison shown in table 25 indicates that the results of the analytical model are in good agreement with those obtained from the FE analyses at the different confining pressures. The largest difference in terms of the deviatoric stress at failure is 9 percent.

Table 25. Comparison of the results of analytical model and GSGC test 2 with different confining pressures from FE analyses.

Parameter	σ_3 = 34 kPa	σ_3 = 70 kPa	σ_3 = 100 kPa	σ_3 = 200 kPa
$\Delta\sigma_3$ (kN/m^2) by the analytical model	245	245	245	245
c_R (kN/m^2) by the analytical model	407	407	407	407
$(\sigma_{1R} - \sigma_3)$ (kN/m^2) from FE analysis	2,700	2,970	3,190	3,860
$(\sigma_{1R} - \sigma_3)$ (kN/m^2) by the analytical model	2,490	2,760	2,990	3,740
Difference between the analytical model and FE analyses	-8 percent	-7 percent	-6 percent	-3 percent

1 kPa = 0.145 psi
1 kN/m^2 = 0.021 kip/ft^2
Note: Internal friction angle of soil = 50 degrees, cohesion of soil = 10.15 psi (70 kPa), reinforcement strength = 4.83 kip/ft (70 kN/m), and reinforcement spacing = 0.65 ft (0.2 m).

5.4 REQUIRED REINFORCEMENT STRENGTH IN DESIGN

In this section, an analytical model for determining required tensile strength in reinforcement is developed, the analytical model is compared with the current design equation, and verification of the analytical model is presented.

5.4.1 Proposed Model for Determining Reinforcement Force

In current design methods, figure 249 is used to determine the required reinforcement strength for the design of GRS structures.

$$T_{required} = \sigma_h * S_v * F_s$$

Figure 249. Equation. Required strength for reinforcement.

Where:

$T_{required}$ = Required strength for reinforcement at depth z.
σ_h = Horizontal stress in a GRS mass at depth z.
F_s = Safety factor.

Assuming F_s = 1, then $T_{required} = T_f$, the ultimate strength of reinforcement, and figure 249 becomes figure 250.

$$\frac{T_f}{S_v} = \sigma_h$$

Figure 250. Equation. T_f divided by S_v.

Note that when the horizontal stress, σ_h, is a constant, the ratio T_f/S_v becomes a constant (i.e., T_f is linearly proportional to S_v). Using figure 225, a new expression for the increase of confining pressure due to tensile inclusion, a modified equation for determination of required reinforcement strength can be obtained. The horizontal stress, σ_h, in a GRS structure at depth z is calculated using figure 251 or figure 252.

$$\sigma_h = \sigma_3 + \Delta\sigma_3$$

Figure 251. Equation. First equation for horizontal stress in a GRS structure.

$$\Delta\sigma_3 = \sigma_h - \sigma_3$$

Figure 252. Equation. Second equation for horizontal stress in a GRS structure.

Substituting figure 225 into figure 250 leads to figure 253 and figure 254.

$$\sigma_h - \sigma_3 = W\frac{T_f}{S_v}$$

Figure 253. Equation. Third equation for horizontal stress in a GRS structure.

$$\frac{T_f}{S_v} = \frac{(\sigma_h - \sigma_3)}{W}$$

Figure 254. Equation. Second equation for T_f divided by S_v.

Substituting figure 241 into figure 254 results in figure 255.

$$\frac{T_f}{S_v} = \frac{(\sigma_h - \sigma_3)}{0.7^{\left(\frac{S_v}{6\,d_{\max}}\right)}}$$

Figure 255. Equation. Third equation for T_f divided by S_v.

For a GRS wall with modular block facing, the lateral constraint pressure, σ_3, at depth z, can be estimated as shown in figure 256.

$$\sigma_3 = \gamma_b b \tan\delta$$

Figure 256. Equation. Lateral constraint pressure.

Where:

γ_b = Unit weight of facing block.
b = Width of facing block.
δ = Friction angle between modular block facing elements (δ can be the friction angle between facing blocks if there is no reinforcement between the blocks or it can be the friction angle between facing block and geosynthetic if there is reinforcement sandwiched between blocks).
d_{max} = Maximum grain size of the backfill.

The required tensile strength of the reinforcement in design is shown in figure 257.

$$T_{required} = \left[\frac{\sigma_h - \sigma_3}{0.7^{\left(\frac{S_v}{6\, d_{\max}} \right)}} \right] * S_v * F_s$$

Figure 257. Equation. Required tensile strength of the reinforcement in design.

Where σ_h is the maximum lateral stress in a GRS mass and can be evaluated as the Rankin active Earth pressure. Note that $T_{required}$ is always equal or greater than zero. For a GRS mass without lateral constraint (e.g., a wrapped wall), σ_3 equals 0, and figure 257 becomes figure 258.

$$T_{required} = \left[\frac{\sigma_h}{0.7^{\left(\frac{S_v}{6\, d_{\max}} \right)}} \right] * S_v * F_s$$

Figure 258. Equation. Second equation for required tensile strength of the reinforcement in design.

5.4.2 Comparison of Reinforcement Strength Between the Analytical Model and Current Design Equation

A comparison of reinforcement forces was made between the proposed model (figure 257) and the current design equation (figure 249). The reinforcement forces in a 20-ft (6.0-m)-high GRS wall, as determined by the two equations, are shown in table 26. Note that the facing stiffness is ignored in the current design method, while the facing rigidity, as denoted by the lateral constraint pressure, σ_3, can be accounted for in the proposed model.

Table 26. Comparison of reinforcement forces in proposed model and current design equation for a GRS wall.

	$T_{required}$ (kN/m) for $F_s = 1$			
		Proposed Model		
z (m)	Current Design Equation	No Facing	Modular Block Facing with $\delta_{b-b} = 35$ degrees	Modular Block Facing with $\delta_{b-b} = 54$ degrees
0.4	0.3	0.4	0.0	0.0
0.8	0.6	0.9	0.0	0.0
1.2	1.0	1.3	0.0	0.0
1.6	1.3	1.8	0.3	0.0
2.0	1.6	2.2	0.8	0.0
2.4	1.9	2.7	1.2	0.0
2.8	2.3	3.1	1.7	0.3
3.2	2.6	3.5	2.1	0.7
3.6	2.9	4.0	2.5	1.2
4.0	3.2	4.4	3.0	1.6
4.4	3.6	4.9	3.4	2.0
4.8	3.9	5.3	3.9	2.5
5.2	4.2	5.8	4.3	2.9
5.6	4.5	6.2	4.8	3.4
6.0	4.9	6.6	5.2	3.8

1 kN/m = 0.069 kip/ft
1 m = 3.28 ft
δ_{b-b} = Friction angle between facing blocks.
Note: Internal friction angle of soil = 38 degrees, cohesion of soil = 0, reinforcement spacing = 0.65 ft (0.2 m), maximum grain size of soil = 1.48 inches (38 mm), unit weight of soil = 0.11 kip/ft^3) (17 kN/m^3), unit weight of facing block = 0.16 kip/ft^3 (25 kN/m^3), and width of blocks = 0.98 ft (0.3 m).

5.4.3 Verification of the Analytical Model for Determining Reinforcement Strength

Verification of the analytical model for determination of reinforcement strength was made by comparing the forces in reinforcement at failure from the GSGC tests with the data measured by Elton and Patawaran and with a typical GRS wall.[31]

Table 27 shows a comparison of the results from the proposed model and measured data from the GSGC tests. Note that cohesion, *c*, was included in model calculations. The largest difference in reinforcement forces between the two is 16 percent, whereas there is 47 percent difference between the current design methods and the test data.

Table 27. Comparison of reinforcement forces in the proposed model and the GSGC tests.

Parameter	Test 2 (*T*, *S*)	Test 3 (2*T*, 2*S*)	Test 4 (*T*, 2*S*)	Test 5 (*T*, *S*)
Reinforcement force at failure, T_f (kN/m)	70	140	70	70
Reinforcement spacing, S_v (m)	0.2	0.4	0.4	0.2
Measured failure pressure (kPa)	2,700	1,750	1,300	1,900
Lateral constraint pressure σ_3 (kPa)	34	34	34	0
Maximum reinforcement force from current design equation (kN/m)	62.4	74.4	50.5	41.2
Difference between current design equation and T_f (percent)	-11	-47	-28	-41
Maximum reinforcement force from proposed model (kN/m)	79.4	124.1	75.4	58.8
Difference between proposed model and T_f(percent)	+13	-11	+8	-16

1 kN/m = 0.069 kip/ft
1 m = 3.28 ft
1 kPa = 0.145 psi
Note: Internal friction angle of soil = 50 degrees, cohesion of soil = 10.15 psi (70 kPa), unit weight of soil = 0.15 kip/ft^3 (24 kN/m^3), and maximum grain size of soil = 1.29 inches (33 mm).

A comparison of the reinforcement forces between the proposed model and the measured data from Elton and Patawaran's tests is shown in table 28.[31] The largest difference in reinforcement forces between the two is 13 percent, whereas it was as high as 74 percent between the current design method and the test results. The proposed model clearly gives a much improved value for estimating reinforcement strength compared to the current design methods.

Table 28. Comparison of reinforcement forces between proposed model and test data from Elton and Patawaran.[31]

Parameter	TG 500	TG 500	TG 600	TG 700	TG 800	TG 1000	TG 028
Reinforcement force at failure, T_f (kN/m)	9	9	14	15	19	20	25
Reinforcement spacing, S_v (m)	0.15	0.30	0.15	0.15	0.15	0.15	0.15
Measured failure pressure (kPa)	230	129	306	292	402	397	459
Maximum reinforcement force from current design equation (kN/m)	4.47	2.35	6.95	6.49	10.08	9.91	11.94
Difference between current design equation and T_f(percent)	-50	-74	-50	-57	-47	-50	-52
Maximum reinforcement force from proposed model (kN/m)	9.02	9.56	14.02	13.10	20.34	20.01	24.09
Difference between proposed model and T_f(percent)	0	+6	0	-13	+7	0	-4

1 kN/m = 0.069 kip/ft
1 m = 3.28 ft
1 kPa = 0.145 psi
Note: Internal friction angle of soil = 40 degrees, cohesion of soil = 4.0 psi (27.6 kPa), unit weight of soil = 0.12 kip/ft^3 (18.8 kN/m^3), lateral constraint pressure = 0 psi (0 kPa), and maximum grain size of soil = 0.49 inches (12.7 mm).

CHAPTER 6. FE ANALYSES

The GSGC tests described in chapter 4 were simulated using the FE method of analysis. The behavior of the reinforced soil mass in GSGC test 2 under different confining pressures, which was not part of the experimental program, was investigated using the FE model. The angle of dilatation of a GRS composite was studied. In addition, the analytical model developed for evaluation of CIS in a GRS mass was verified by comparing the model results with those obtained from the FE analyses.

Many FE codes are available for the analysis of soil-structure interaction problems, including Abaqus, FLAC, LS-Dyna®, Plaxis, Sage Crisp®, and Sigma/W® (Geoslope). Plaxis 8.2 code was selected for the analysis in this study due primarily to the author's familiarity with the code. This code has been used successfully for the analysis of various Earth structures, including GRS structures.[79–81]

6.1 PLAXIS 8.2

Version 8.2 of Plaxis is an FE code intended for 2D analysis of deformation and stability problems in geotechnical engineering. The details of Plaxis 8.2 can be found in the software manual.[81] Following is a brief description of some key features of the program:

- **Graphical input of geometry models:** The input of layers, structures, construction stages, loads, and boundary conditions is based on computer-aided design drawing procedures, which allows for a detailed modeling of the geometry. From the geometry model, a 2D FE mesh is easily generated.

- **Automatic mesh generation:** Plaxis allows for automatic generation of 2D FE meshes with options for global and local mesh refinement.

- **High-order elements*:*** Quadratic 6-node and fourth-order 15-node triangle elements are available to describe the stress-deformation behavior of the soil.

- **Plates/beams:** Special beam elements can be used to model the bending of retaining walls, tunnel linings, shells, and other slender structures. The behavior of these elements is defined using a flexural rigidity, a normal stiffness, and an ultimate bending moment. Plates with interfaces can also be used to model the behavior of structures.

- **Interfaces:** Joint elements are available to model soil-structure interface behavior. For example, joint elements can be used to simulate the thin zone of intensely shearing material at the contact between a retaining wall and the surrounding soil, a tunnel lining and the soil, or reinforcement and surrounding soil. Values of the interface friction angle and adhesion are generally not the same as the friction angle and cohesion of the surrounding soil.

- **Anchors:** Elastoplastic spring elements can be used to model anchors and struts. The behavior of these elements is defined using a normal stiffness and a maximum force.

A special option exists for the analysis of prestressed ground anchors and excavation supports.

- **Geogrids/geotextiles:** Geogrids or geotextiles in GRS structures can be simulated in Plaxis by special tension elements. It is often convenient to combine these elements with joint elements to model the interaction between geosynthetic reinforcement and the surrounding soil.

- **Tunnels:** Plaxis offers a convenient option for creating circular and non-circular tunnels using arcs and lines. Plates and interfaces may be used to model the tunnel lining and the interaction with the surrounding soil. Fully isoparametric elements can be used to model the curved boundaries within the mesh. Various methods are available for the analysis of the deformation caused by various methods of tunnel construction.

- **Mohr-Coulomb model:** This non-linear model is based on soil parameters that are well-known in geotechnical engineering practice. Not all non-linear features of soil behavior are included in this model; however, the Mohr-Coulomb model can be used to compute realistic support pressures for tunnel faces, ultimate loads for footings, etc. It can also be used to calculate safety factors using a phi-c reduction approach.

- **Advanced soil models:** In addition to the Mohr-Coulomb model, Plaxis offers a variety of advanced soil models. A general second-order model called the hardening soil model, an elastoplastic type of hyperbolic model, is available. To accurately model the time-dependent and logarithmic compression behavior of normally consolidated soft soils, a creep model is also available, referred to as the soft soil creep model. In addition, a special model is available for the analysis of anisotropic behavior of jointed rock.

- **User-defined soil models:** A special feature in Plaxis 8.2 is a user-defined soil model option. This feature enables users to include self-programmed soil models for the analysis.

- **Staged construction:** This feature enables realistic simulation of construction of Earth structures by activating and deactivating compaction loads and simulation of excavation processes by activating and deactivating clusters of elements, application of loads, changing of water tables, etc. The procedure allows for a realistic assessment of stresses and displacements caused by, for example, compaction loads or soil excavation during underground construction.

6.2 CIS IN A GRS MASS

The residual lateral stresses in a GRS mass due to compaction can be evaluated by figure 259. (See section 5.15 for details.)

$$\Delta\sigma_3 = \Delta\sigma_{v,c,\max} \quad K_{i,c} F \left(1 + \frac{0.7\ E_r}{E_s\ S_v - 0.7\ E_r} \right)$$

Figure 259. Equation. Residual lateral stresses in a GRS mass due to compaction.

To illustrate how to compute the residual lateral stresses, or CIS, in a GRS mass, a 19.68-ft (6-m)-high GRS mass was used as an example. The parameters for the calculation of CIS are as follows:

- **Soil:** A dense sand with unit weight= 0.11 kip/ft^3 (17 kN/m^3), angle of internal friction = 45 degrees, soil modulus = 4,400 psi (30,000 kPa), and compaction lift = 0.7 ft (0.2 m).

- **Geosynthetics:** E_r = 290 psi (2,000 kPa) and S_v = 0.7 ft (0.2 m).

The vertical maximum pressures of 6.4, 15, 29, 44, and 73 psi (44, 100, 200, 300, and 500 kPa) due to compaction were used for the calculation of the residual stresses. Note that the maximum vertical compaction stress of 6.4 psi (44 kPa) was the contact pressure used in the GSGC tests described in chapter 4.

Figure 260 shows the distribution of the residual lateral stresses with depth due to the different maximum compaction pressures. The values of the lateral residual stresses in this figure were calculated based on figure 258 with the assumption that the compaction lift of 0.7 ft (0.2 m) is small compared to the dimensions of the compaction plant. As a result, the distribution of the lateral residual stress within the 0.7-ft (0.2-m)-thick lift due to compaction is constant. Near the surface, the lateral residual stresses will follow the limiting lateral Earth pressure for the unloading condition (i.e., the $K_{1,c}$ line, as shown in figure 203 and table 19).

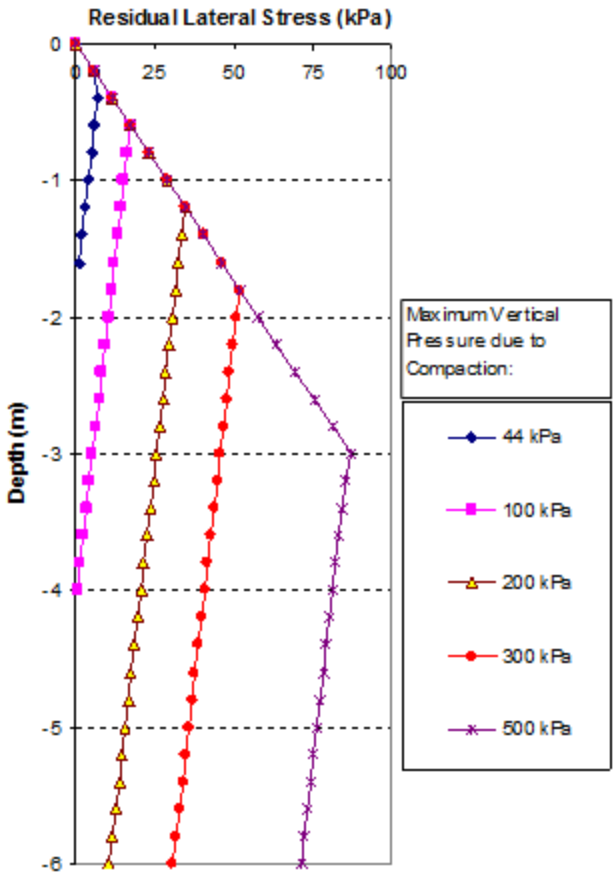

1 m = 3.28 ft
1 kPa = 0.145 psi

Figure 260. Graph. Distribution of residual lateral stresses of a GRS mass with depth due to fill compaction.

6.3 FE SIMULATION OF THE GSGC TESTS

Plaxis 8.2 was used for the simulation of GSGC tests 1, 2, and 3, as described in chapter 4. The backfill of all GSGC test specimens was compacted at 0.7-ft (0.2-m) lifts using an MBW GP1200 plate compactor with a contact pressure of 6.4 psi (44 kPa). The soil stiffness, E_{50}^{ref}, can be estimated from triaxial tests using Janbu's equation.[82] The Poisson's ratio of the backfill can be estimated as shown in figure 261 for uniaxial tests and figure 262 for triaxial tests.

$$\frac{\Delta V}{V} = \varepsilon_x + \varepsilon_y + \varepsilon_z = (1-2\nu)\frac{\sigma_z}{E}$$

Figure 261. Equation. Poisson's ratio of the backfill for uniaxial tests.

$$\frac{\Delta V}{V} = \varepsilon_x + \varepsilon_y + \varepsilon_z = \frac{(1+\nu)(1-2\nu)\sigma_z}{E(1-\nu)}$$

Figure 262. Equation. Poisson's ratio of the backfill for triaxial tests.

For GSGC test 1 (unreinforced soil), the soil model and parameters used in the analysis are as follows:

- Soil hardening model.
- Dry unit weight, γ_d = 0.15 kip/ft^3 (24 kN/m^3), wet unit weight, and γ_t = 0.16 kip/ft^3 (25 kN/m^3).
- Angle of internal friction = 50 degrees, angle of dilation = 17.5 degrees, and cohesion = 10 psi (70 kPa) (for confining pressure less than 30 psi (206.7 kPa)).
- Soil modulus, E_{50}^{ref} = 9,000 psi (62,000 kPa), unloaded-reloaded reference modulus, E_{ur}^{ref} = 18,000 psi (124,000 kPa), and Poisson's ratio, ν = 0.37.
- Power, m = 0.5.

For the GSGC tests, the backfill stiffness was increased due to CIS as follows:

1. Place the first lift of facing blocks and soil. The compaction lift thickness was 0.7 ft (0.2 m).
2. Apply a uniform vertical stress of 6.4 psi (44 kPa) over the entire surface of each newly placed soil layer before analysis, and remove it afterwards. This step was employed to simulate the compaction operation.
3. Place a sheet of reinforcement at preselected reinforcement spacing to cover the entire backfill surface plus the facing blocks.
4. Place another lift of facing blocks and soil.
5. Repeat steps 2 to 4 until the fill reached the total height of the specimen.
6. Remove facing blocks.
7. Apply a prescribed confining pressure.
8. Apply vertical stresses on the top of the specimen at equal increments until failure.

The properties of the backfill were modified due to compaction effects. The Poisson's ratio under plane-strain condition was reduced to ν_{min}, as suggested by Hatami and Bathurst. [17] Soil modulus E_{50}^{ref} was calculated using the increase in confining pressure due to compaction. The value of E_{50}^{ref} can be estimated by using equation 80 with $\sigma'_3 = \sigma'_{3S} + \Delta\sigma_3$, where $\Delta\sigma_3$ can be estimated by figure 221. Note that the elastic modulus was increased by factor of 2.25 for walls 1 and 2 in Hatami and Bathurst's numerical analyses and by a factor of 10 in the FE analyses by Morrison, et al.[17,18]

The conditions and properties of the backfill and reinforcement of GSGC tests 2 and 3 used in the FE analyses are shown in table 29.

Table 29. Parameters and properties of the GSGC tests used in FE analyses.

Category	Description
Soil	Material, diabase; Soil model, hardening soil model; dry unit weight, γ_d = 24 kN/m^3; wet unit weight, γ_w = 25 kN/m^3; cohesion, c = 70 kPa; angle of internal friction, ϕ = 50 degrees; angle of dilation, ψ = 17 degrees; soil modulus, E_{50}^{ref} = 63,400 kPa, E_{ur}^{ref} = 126,800 kPa; Poisson's ratio, ν = 0.2; power, m = 0.5
Reinforcement	GSGC test 2: Single-sheet Geotex® 4×4: axial stiffness, EA = 1,000 kN/m; ultimate strength, T_{ult} = 70 kN/m; reinforcement spacing, S_v = 0.2 m
	GSGC test 3: Double-sheet Geotex® 4×4: axial stiffness, EA = 2,000 kN/m; ultimate strength, T_{ult} = 140 kN/m; reinforcement spacing, S_v = 0.4 m
Facing block	FE model, linear elastic model; modulus, $E = 3*10^7$ kPa; unit weight, γ = 12.5 kN/m^3 (hollow blocks); Poisson's ratio, ν = 0.
Block-block interface	FE model, Mohr-Coulomb model; modulus, $E = 3*10^6$ kPa; unit weight, γ = 0 kN/m^3; cohesion, c = 2 kPa; angle of internal friction, ϕ = 33 degrees; Poisson's ratio, ν = 0.45
Confining pressure	Constant confining pressures of 34 kPa for the GSGC tests 1–4

1 kN/m^3 = 0.006 kip/ft^3
1 kPa = 0.145 psi
1 kN/m = 0.069 kip/ft
1 m = 3.28 ft
Note: Soil-reinforcement interface was assumed to be fully bonded in the analyses.

Figure 263 through figure 268 show the steps in the FE analyses. The first 20 steps were used for modeling the preparation of the specimen. The loading began from step 21.

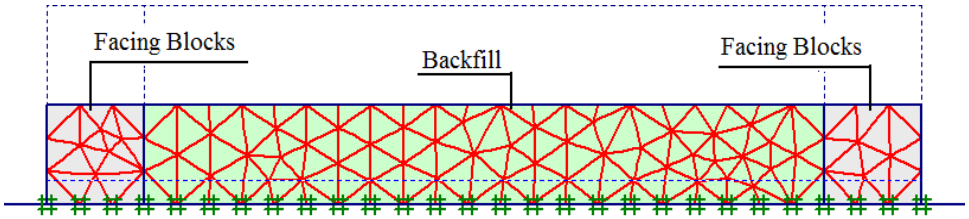

Figure 263. Illustration. Step 1 of analysis for the GSGC tests—placement of first layer.

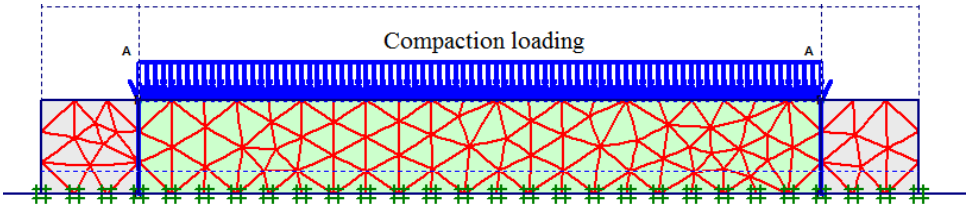

Figure 264. Illustration. Step 2 of analysis for the GSGC tests—compaction of first layer.

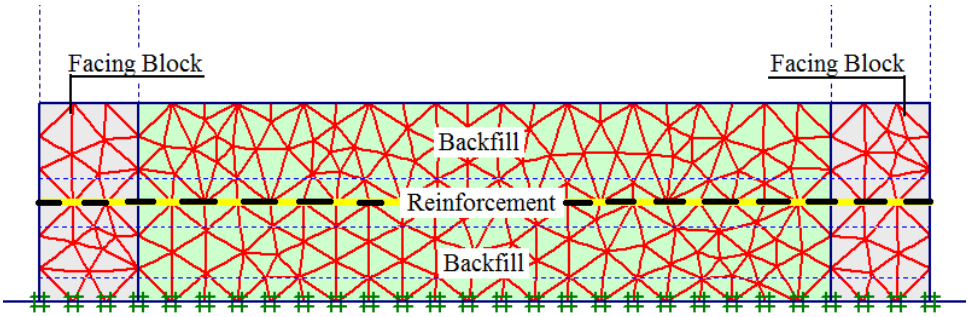

Figure 265. Illustration. Step 3 of analysis for the GSGC tests—placement of second layer.

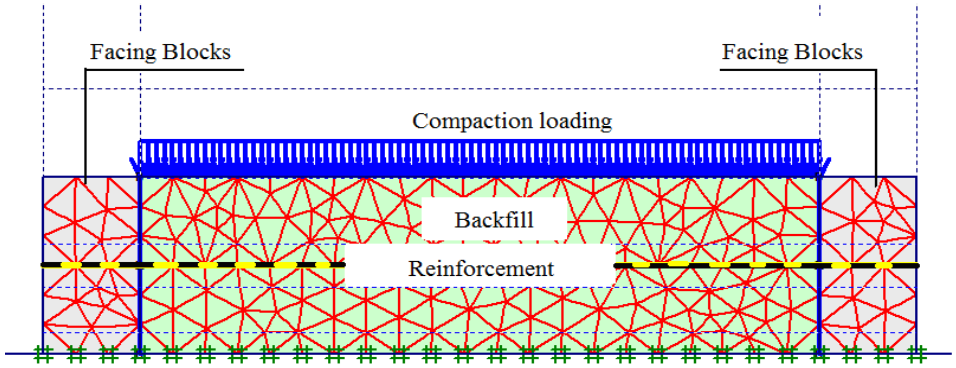

Figure 266. Illustration. Step 4 of analysis for the GSGC tests—compaction of second layer.

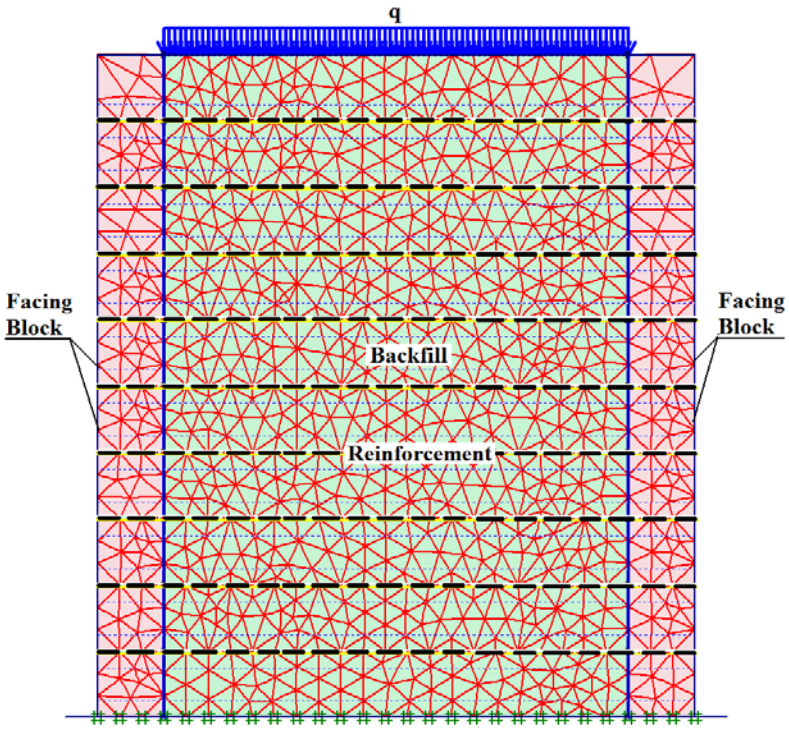

Note: The full height of the GSGC mass was reached at the last step of the specimen preparation.

Figure 267. Illustration. Step 20 of analysis for the GSGC tests—placement of surcharge.

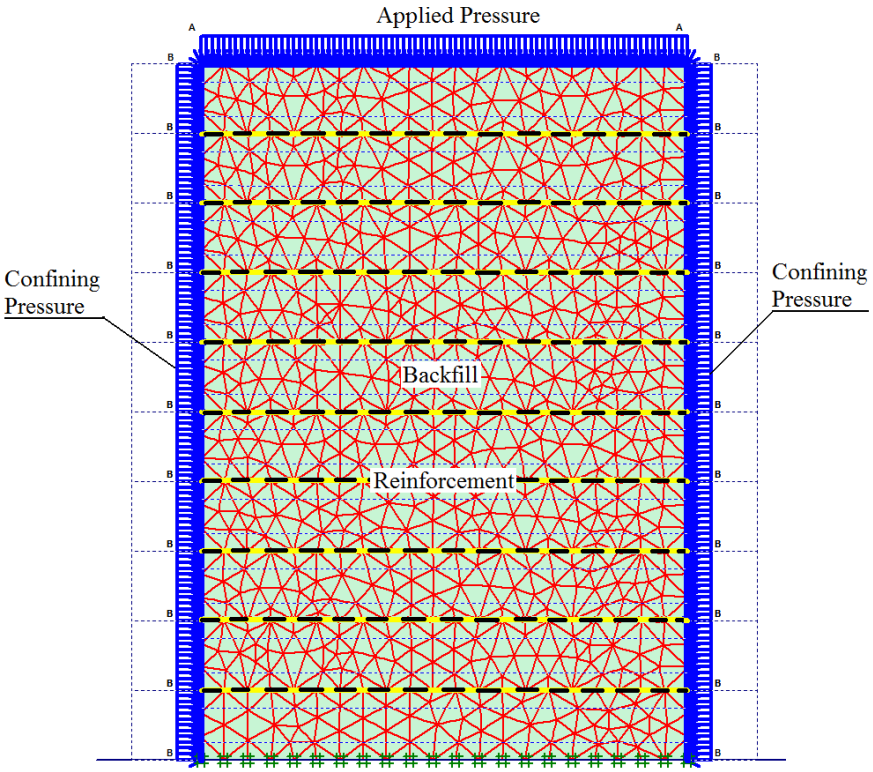

Note: The facing blocks were removed and confining pressure and vertical pressures were applied (during loading).

Figure 268. Illustration. Step 21 of analysis for the GSGC tests—placement of surcharge and confining stress.

6.3.1 Simulation of GSGC Test 1

The global stress-strain relationship and volume change relationship obtained from FE analysis and the GSGC tests are shown in figure 269 and figure 270. The analysis results are in good agreement with the measured data. The maximum differences of the results between the FE analysis and the tests were about 5 percent. Figure 271 shows the lateral movements on the open faces of the specimen at 29, 58, 87, and 110 psi (200, 400, 600, and 770 kPa). These results from FE analyses and the tests are also in good agreement.

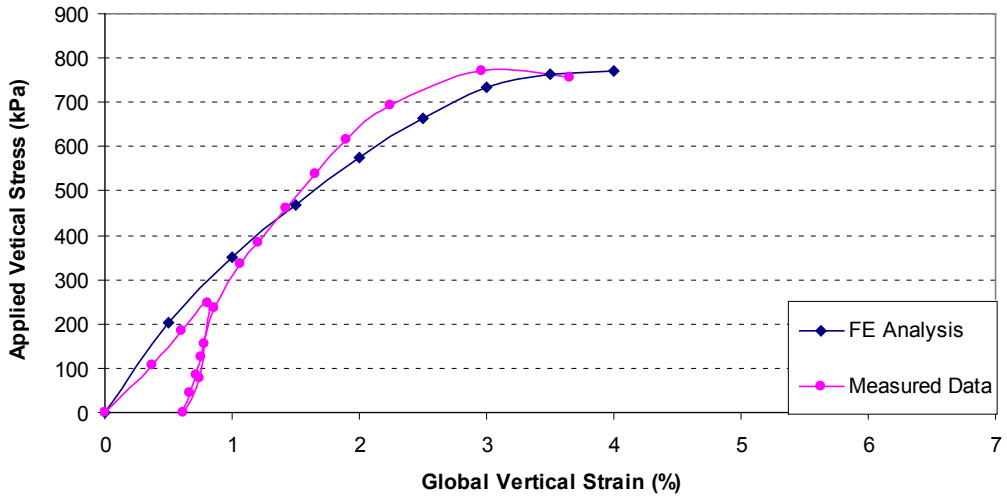

1 kPa = 0.145 psi

Figure 269. Graph. Comparison of results for GSGC test 1, global vertical stress-strain relationship.

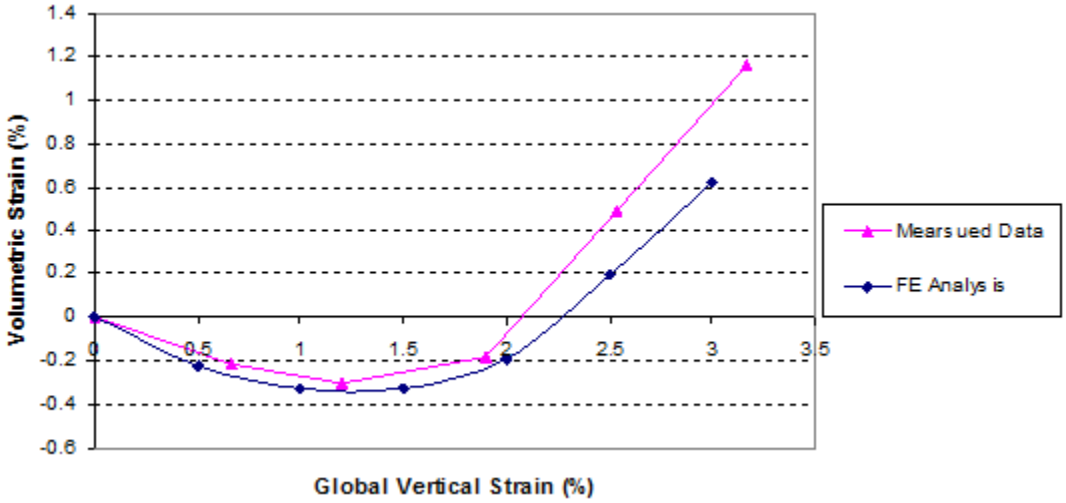

Figure 270. Graph. Comparison of results for GSGC test 1, volume change relationship.

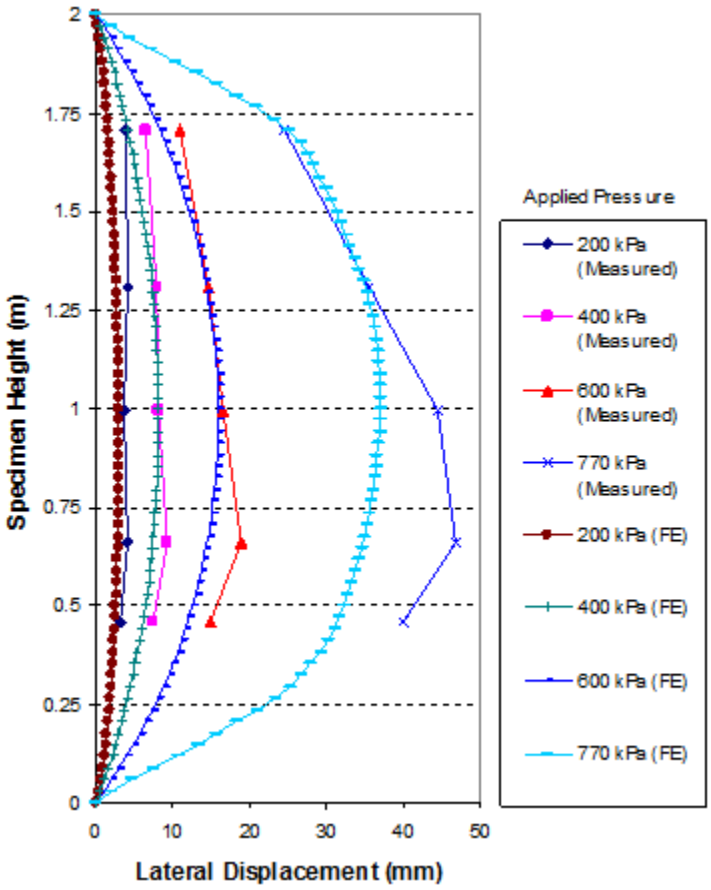

1 m = 3.28 ft
1 kPa = 0.145 psi

Figure 271. Graph. Comparison of lateral displacements on open face of GSGC test 1.

6.3.2 Simulation of GSGC Test 2

The global stress-strain relationships, as obtained from FE analysis and the GSGC tests, are shown in figure 272. The results of the FE analysis with and without consideration of CIS are included in the figure. The results with consideration of CIS give a slightly better simulation of the stress-strain curve. It should be noted that the compaction energy used in the GSGC tests was very low. As a result, the magnitude of CIS was very small and the effect of CIS on the global stress-strain relationship was not significant.

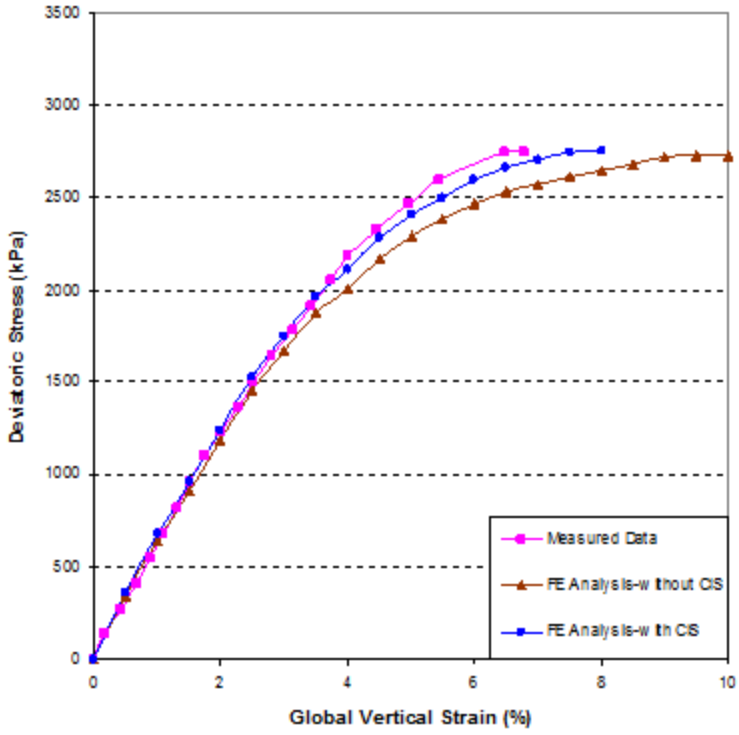

1 kPa = 0.145 psi

Figure 272. Graph. Comparison of global stress-strain relationship of GSGC test 2.

Figure 273 shows the lateral displacements on the open faces of the specimen at applied pressures of 58, 145, 290, and 360 psi (400, 1,000, 2,000, and 2,500 kPa). The simulated lateral displacements are no more than 5 percent greater than the measured values.

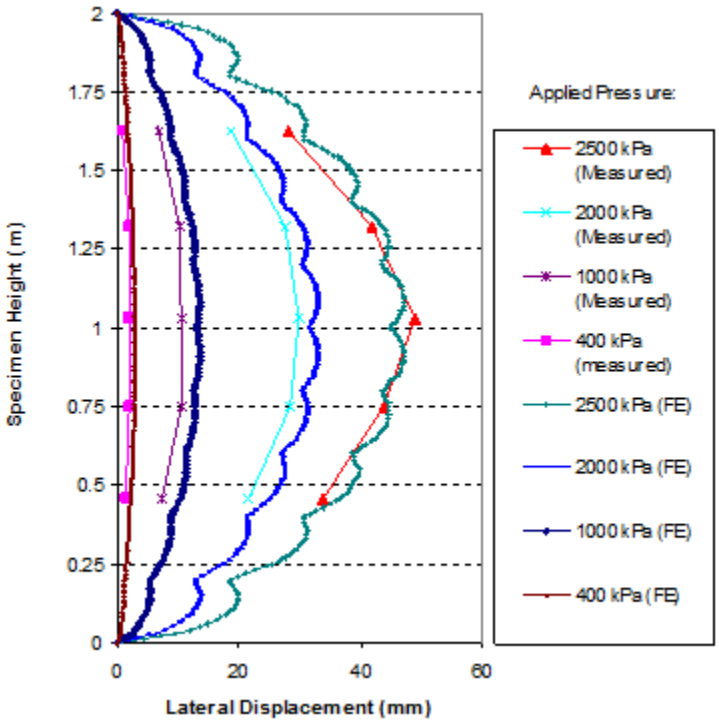

1 m = 3.28 ft
1 mm = 25.4 inches
1 kPa = 0.145 psi

Figure 273. Graph. Comparison of lateral displacement at open face of GSGC test 2.

Figure 274 shows the simulated and measured displacements of the GSGC mass at selected points in figure 153. The simulated displacements are in agreement with the measured values.

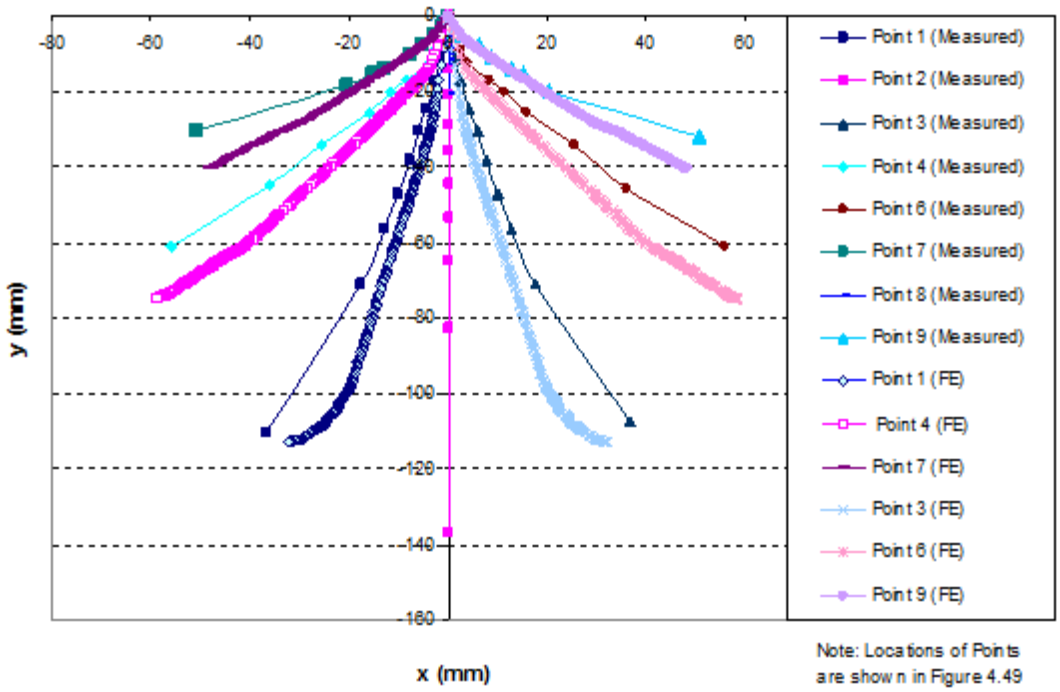

1 mm = 0.039 inches

Figure 274. Graph. Comparison of internal displacements of GSGC test 2.

A comparison of the distribution of strains in the reinforcement in GSGC test 2 between the FE analyses and measured data are shown in figure 275 and figure 276. The simulated strains are in good agreement with the measured values.

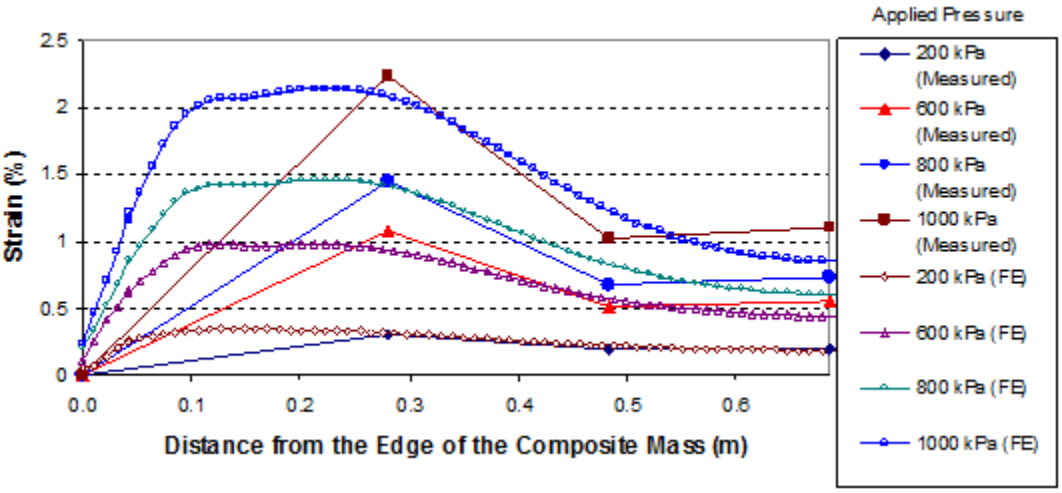

1 m = 3.28 ft
1 kPa = 0.145 psi

Figure 275. Graph. Comparison of results for GSGC test 2 at reinforcement layer 5.25 ft (1.6 m) from the base.

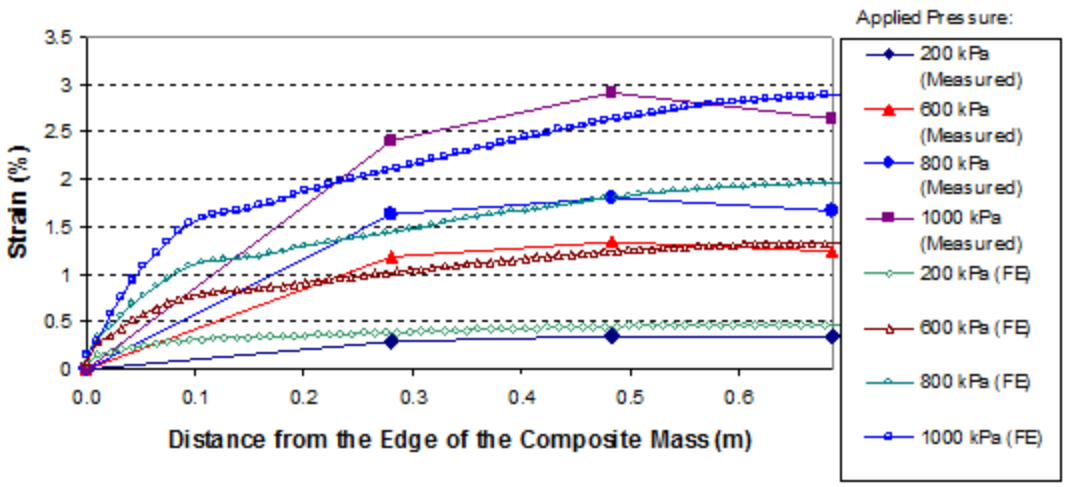

1 m = 3.28 ft
1 kPa = 0.145 psi

Figure 276. Graph. Comparison of results for GSGC test 2 at reinforcement layer 2.62 ft (0.8 m) from the base.

6.3.3 Simulation of GSGC Test 3

A comparison of the global stress-strain relationships obtained from FE analysis and measured data of GSGC test 3, are shown in figure 277. The FE results are in agreement with the measured data. The lateral displacements on the open faces at applied pressures of 58, 87, 116, 145, and 180 psi (400, 600, 800, 1,000, and 1,250 kPa) are shown in figure 278. Figure 279 shows a comparison of simulated and measured internal displacements of the GSGC test 3 specimen at selected points in figure 169. Once again, the results from FE analyses are in good agreement with the measured values.

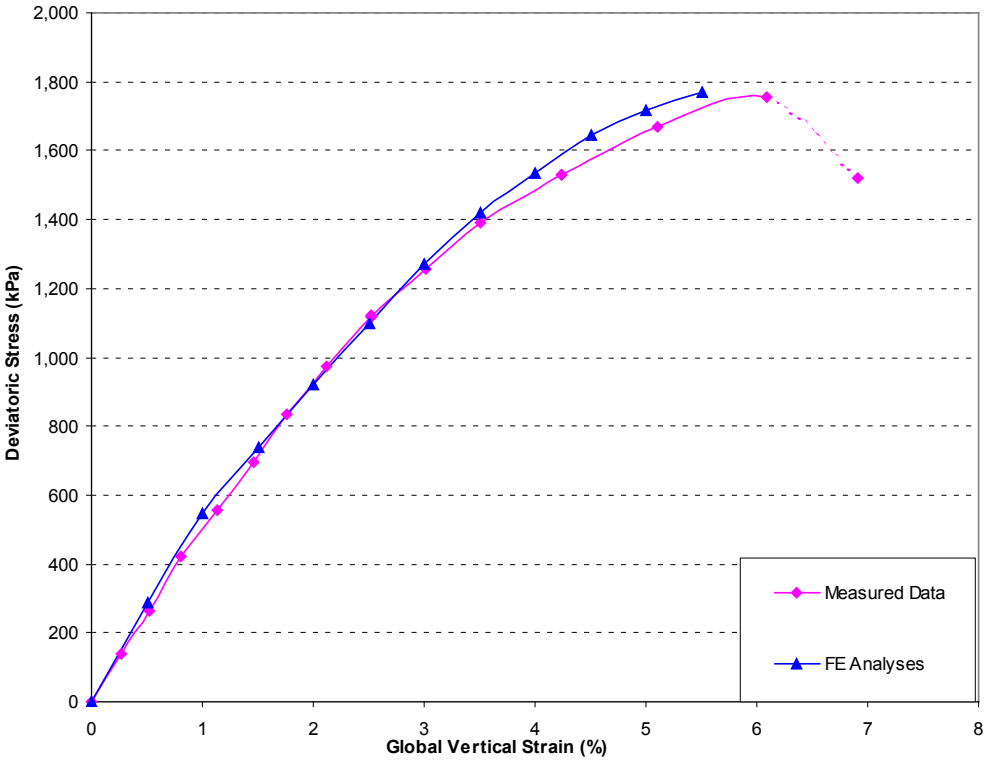

1 kPa = 0.145 psi

Figure 277. Graph. Comparison of global stress-strain relationship of GSGC test 3.

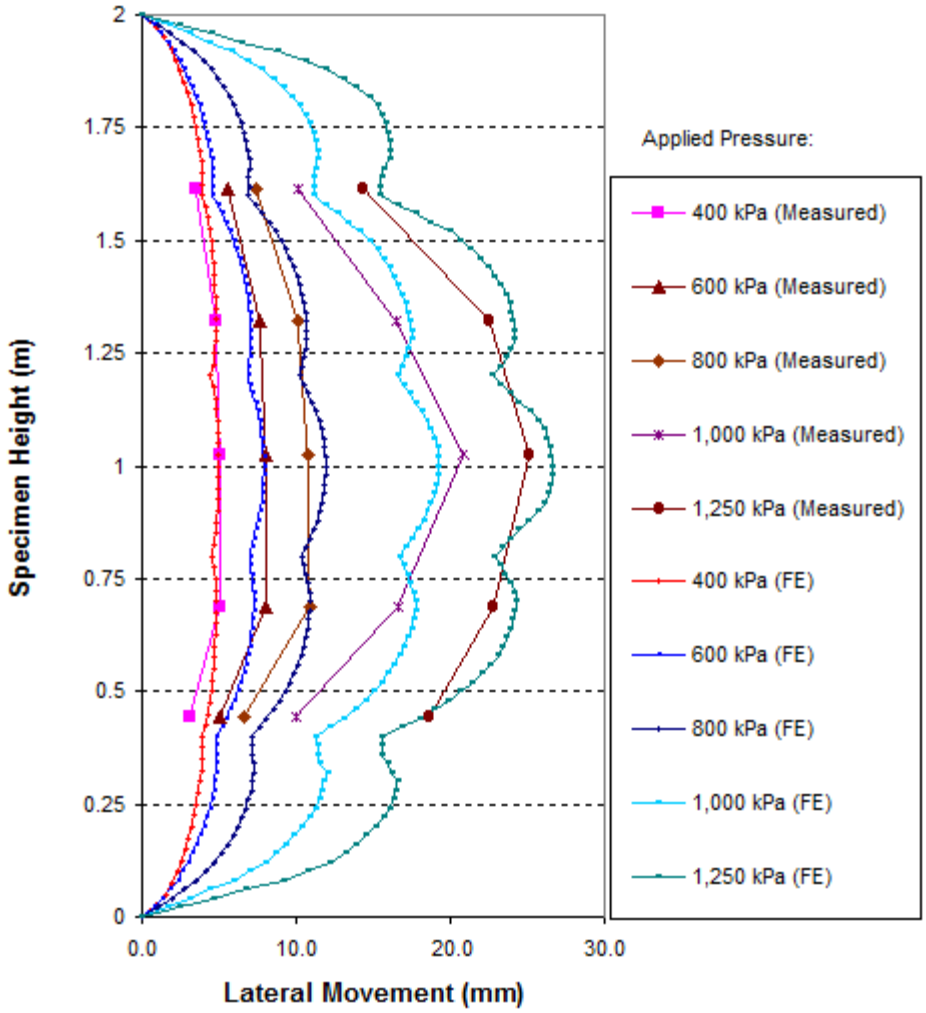

1 m = 3.28 ft
1 mm = 0.039 inches
1 kPa = 0.145 psi

Figure 278. Graph. Comparison of lateral displacement at open face of GSGC test 3.

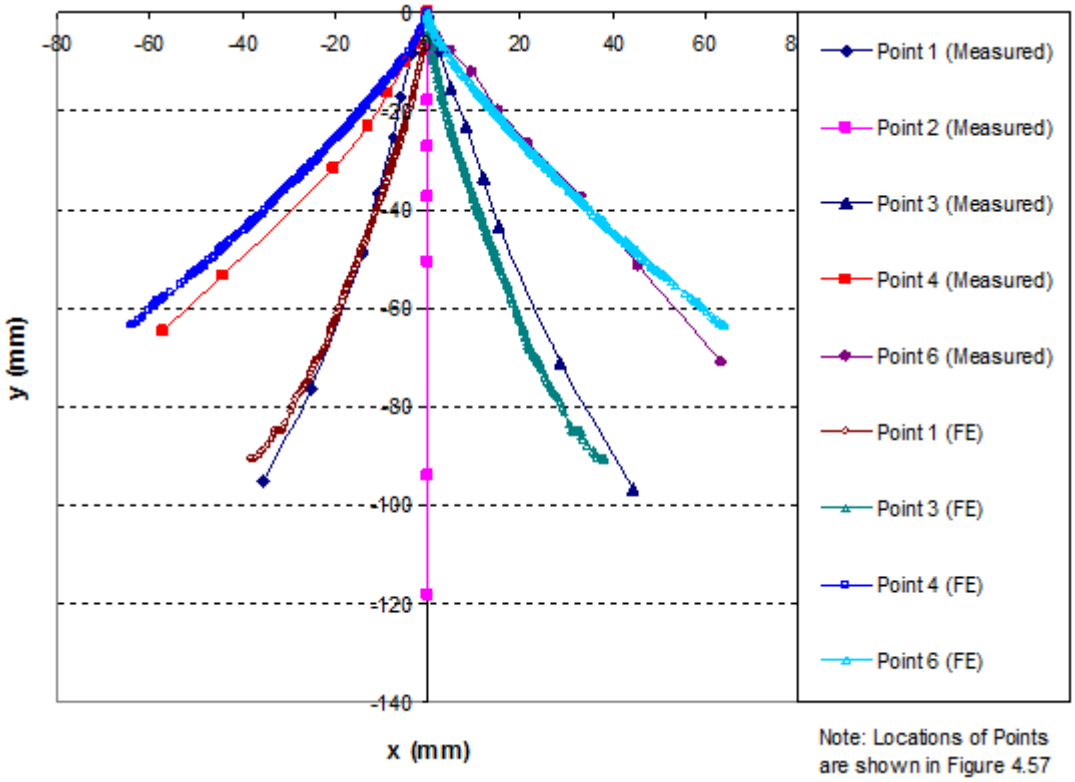

1 mm = 0.039 inches

Figure 279. Graph. Comparison of internal displacements of GSGC test 3.

The comparisons of the distribution of strains in the reinforcement in GSGC test 3 between FE analyses and measured data are shown in figure 280 and figure 281. The simulated strains are in agreement with the measured values.

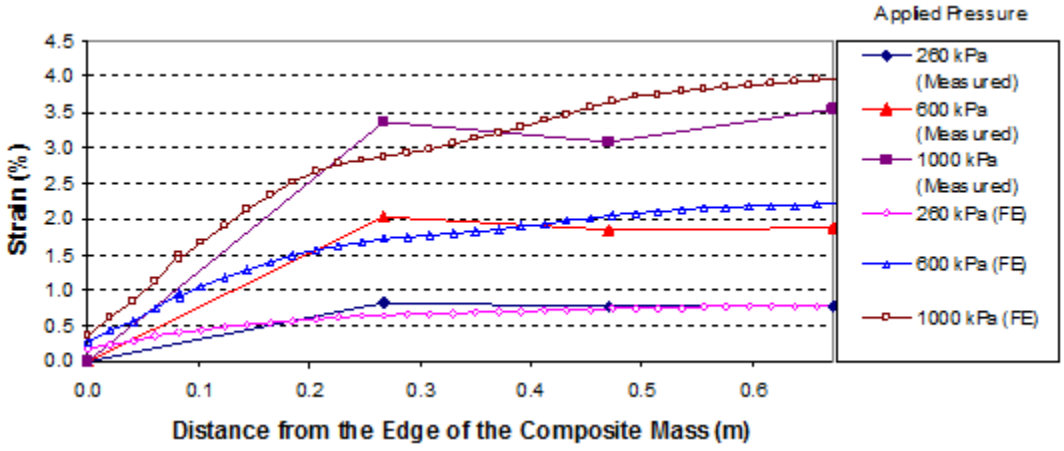

1 m = 3.28 ft
1 kPa = 0.145 psi

Figure 280. Graph. Comparison of results for GSGC test 3 at reinforcement layer 3.94 ft (1.2 m) from the base.

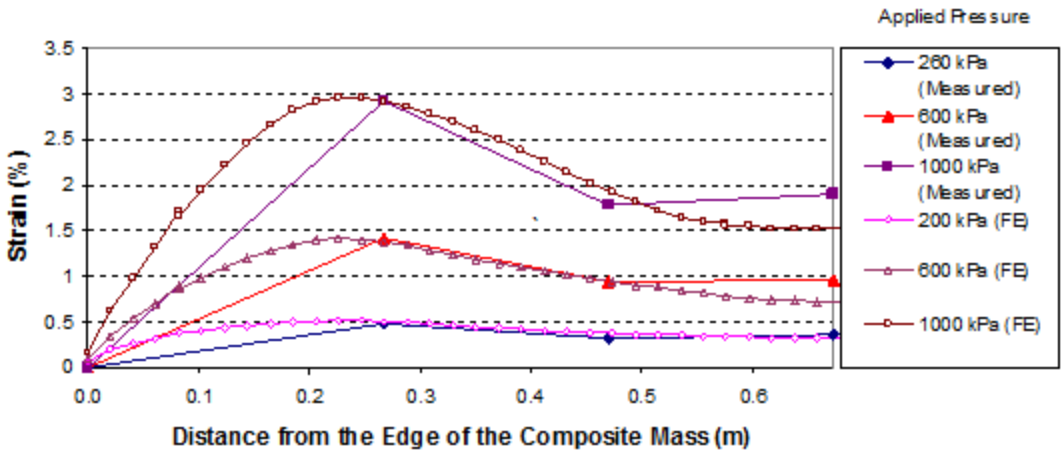

1 m = 3.28 ft
1 kPa = 0.145 psi

Figure 281. Graph. Comparison of results for GSGC test 3 at reinforcement layer 1.3 ft (0.4 m) from the base.

6.4 FE ANALYSIS OF GSGC TEST 2 UNDER DIFFERENT CONFINING PRESSURES AND DILATION ANGLE OF SOIL-GEOSYNTHETIC COMPOSITES

Figure 282 shows a comparison of the global stress-strain relationship obtained from FE analysis and the measured data of GSGC test 2. Figure 283 shows a comparison of the volume change relationships. GSGC test 2 was conducted under a confining pressure of 4.9 psi (34 kPa). The global stress-strain and volume change relationships under the confining pressure of 4.9 psi (34 kPa) as obtained from FE analysis are in good agreement with the measured data. To provide additional data under different confining pressures, the FE model was used to generate data under confining pressures of 15 and 29 psi (100 and 200 kPa), as shown in the figures.

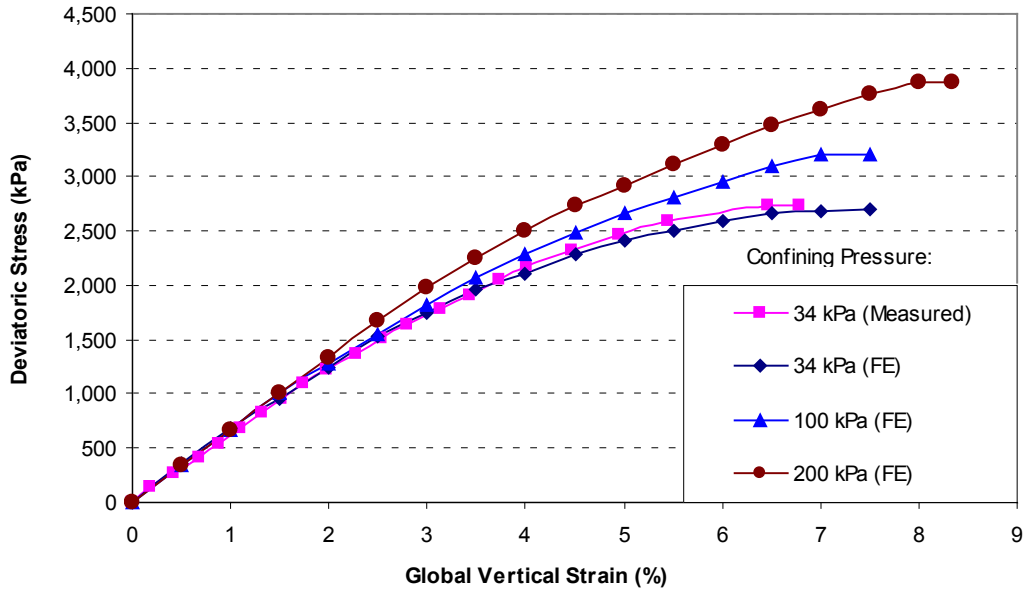

1 kPa = 0.145 psi

Figure 282. Graph. FE analyses of GSGC test 2 under different confining pressures—global stress-strain relationship.

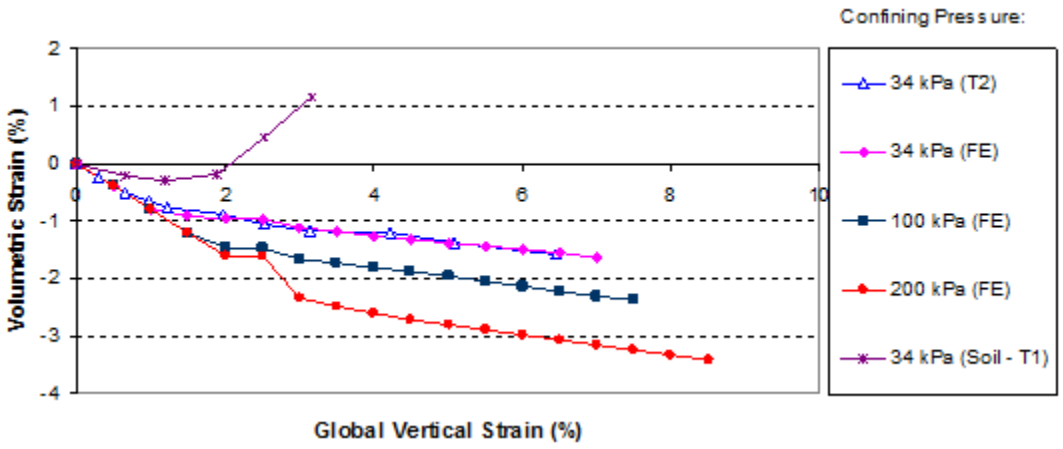

1 kPa = 0.145 psi

Figure 283. Graph. FE analyses of GSGC test 2 under different confining pressures—volume change curves.

It is interesting to note that the reinforcing mechanism of a GRS mass can be viewed in terms of the angle of dilation. The angle of dilation of a GRS mass is smaller than the angle of dilation of an unreinforced soil mass. Using the data in figure 282 and figure 283 as an example, the angles of dilation of the soil-geosynthetic composites were approximately -8, -11, and -12 degrees (a negative dilation angle means no dilation; the greater the absolute value, the less likely the material will dilate) under confining pressures of 4.9, 15, and 29 psi (34, 100, and 200 kPa), respectively. The angle of dilation of the unreinforced soil was +17 degrees under a confining pressure up to 29 psi (200 kPa). This suggests that the presence of geosynthetic reinforcement has a tendency to suppress dilation of the surrounding soil. A soil having less

tendency to dilate will become stronger. The dilation behavior offers a new explanation of the reinforcing mechanism, and the angle of dilation provides a quantitative measure of the degree of reinforcing effect of a GRS mass.

6.5 VERIFICATION OF CIS MODEL

The analytical model for evaluating CIS, as described in section 3.2, was verified using the FE method of analysis. The FE analysis was carried out by using Plaxis 8.2.[81] To verify the CIS model, a 20-ft (6-m)-high GRS mass was chosen as an example. The parameters used for the calculation of CIS in the analytical model and the FE analysis are as follows:

- **Soil:** A dense sand with mass unit weight = 0.12 kip/ft^3 (17 kN/m^3), angle of internal friction= 45 degrees, loading modulus = 4,400 psi (30,000 kPa), unloading modulus = 13,000 psi (90,000 kPa), Poisson ratio = 0.2, and compaction lift = 0.7 ft (0.2 m). (The behavior of the soil was simulated in FE analysis by using the hardening soil model in plane-strain condition.)

- **Geosynthetics:** Tensile modulus = 290 psi (2,000 kPa) and reinforcement spacing = 0.7 ft (0.2 m).

- **Interface:** The interface between the soil and geosynthetic reinforcement is fully bonded.

The very fine mesh of an FE analyses to simulate CIS in a GRS mass is shown in figure 284. Figure 285 and figure 286 show the lateral stress distributions at the center line of the GRS mass without considering CIS and with CIS under the maximum compaction pressures of 29 and 73 psi (200 and 500 kPa). The compaction operation was simulated by loading and unloading at different locations on the surface area of each lift. The residual lateral stresses were the differences between the lateral stresses with simulating CIS and those without CIS at the same location, as shown in figure 285 and figure 286.

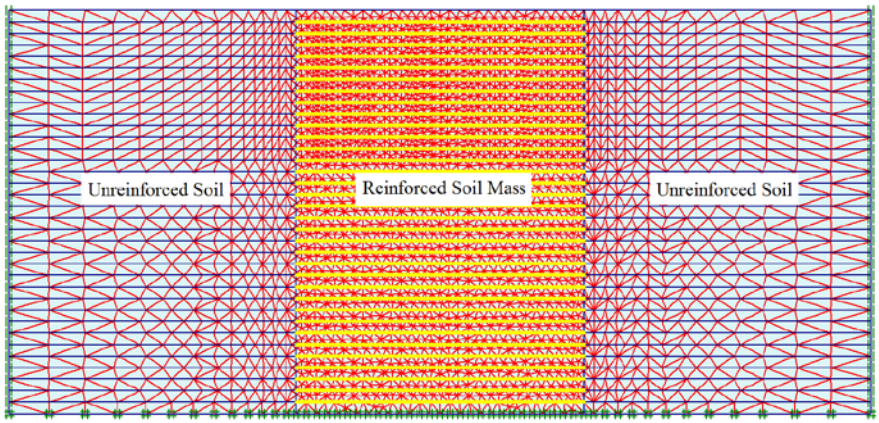

Figure 284. Illustration. FE mesh to simulate CIS in a reinforced soil mass.

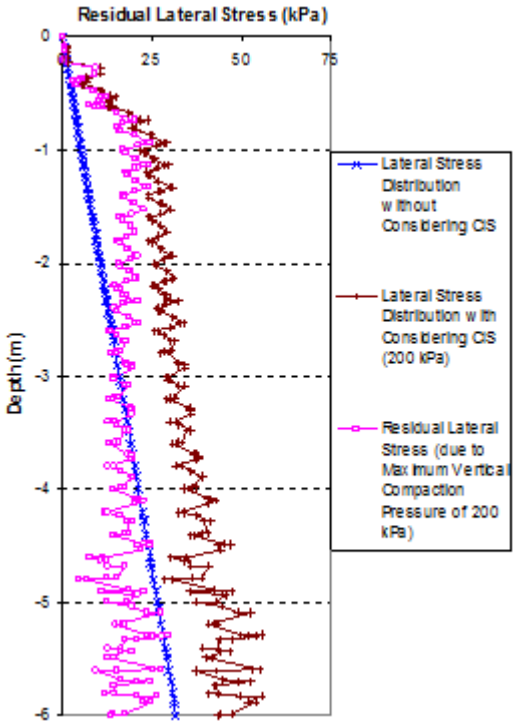

1 m = 3.28 ft
1 kPa = 0.145 psi

Figure 285. Graph. Lateral stress distribution of a GRS mass from FE analyses with maximum vertical compaction pressures of 29 psi (200 kPa).

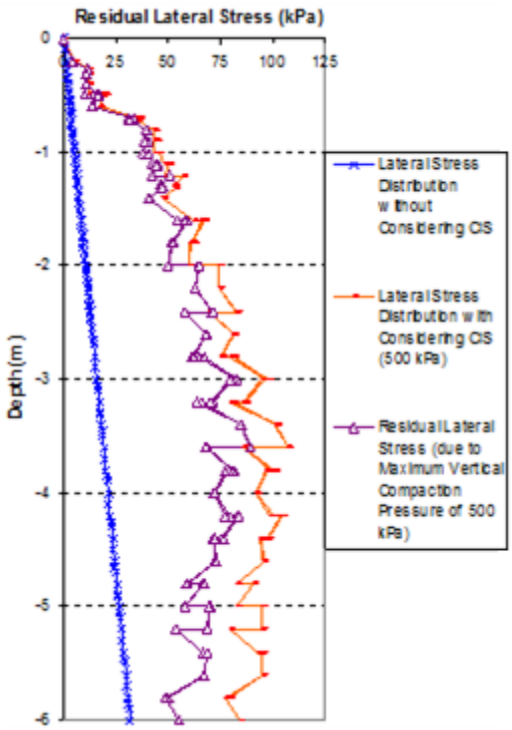

1 m = 3.28 ft
1 kPa = 0.145 psi

Figure 286. Graph. Lateral stress distribution of a GRS mass from FE analyses with maximum vertical compaction pressures of 72.5 psi (500 kPa).

Comparisons of residual lateral stress distribution resulting from compaction pressures of 29 and 73 psi (200 and 500 kPa) between the CIS model and the FE analysis are shown in figure 287. The CIS calculated from the hand computation model are in good agreement with the values obtained from the FE analysis. Note that the residual lateral stresses in a GRS mass are higher under a higher vertical compaction pressure. In actual construction, the maximum vertical pressure of compaction is in the range of 29 to 73 psi (200 to 500 kPa). As shown in figure 287, the effects of CIS can be significant in actual construction. The zigzag of the FE analyses lines in figure 287 was caused by the thickness of compaction lift of 0.7 ft (0.2 m). A larger compaction lift indicates a larger amplitude of the zigzag, and the effect of CIS is smaller.

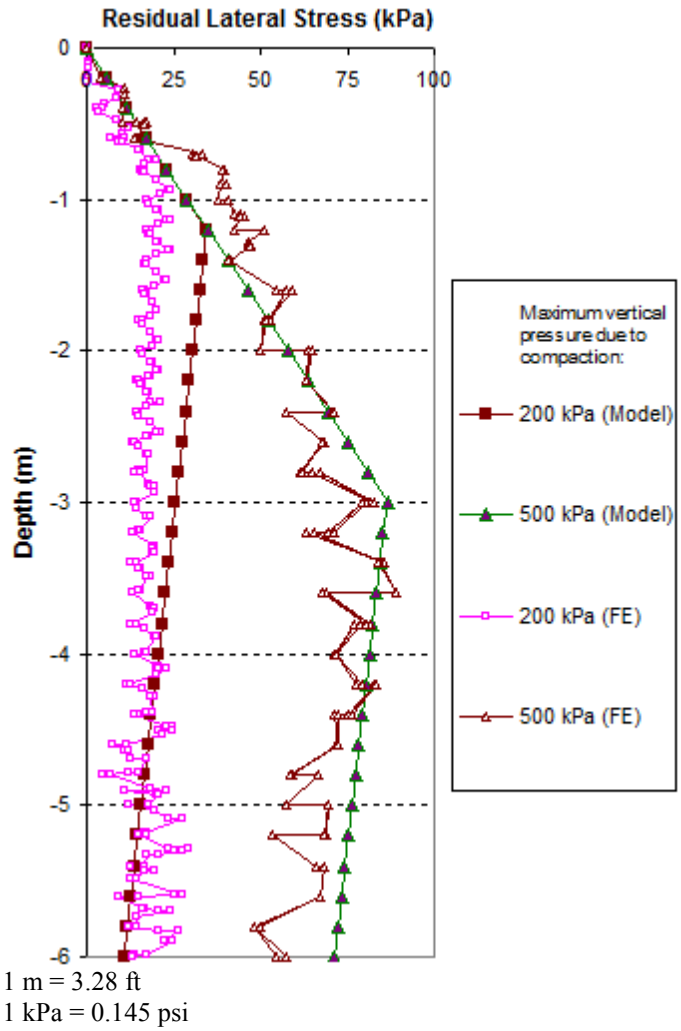

Figure 287. Graph. Comparison of residual lateral stresses of a GRS mass due to fill compaction between FE analysis with very fine mesh and the analytical model.

The FE analyses are more accurate with finer meshes, but the results for one curve from the FE analysis took more than 20 h of inputting data and running the program with a strong computer configuration (e.g., dual core 1.86 GHz, 3 GB RAM). Conversely, the analytical model is simple and can use hand calculations. To speed up the FE analysis process, a coarse mesh can be used with somewhat tolerated error. Figure 288 shows the comparison between FE results with a coarse mesh and the analytical model. The FE results were obtained from simulating the compaction operation by applying the compaction pressure over the entire surface area of the GRS mass at each compaction lift. Figure 287 and figure 288 show that the fine mesh should be used when analyzing GRS structures.

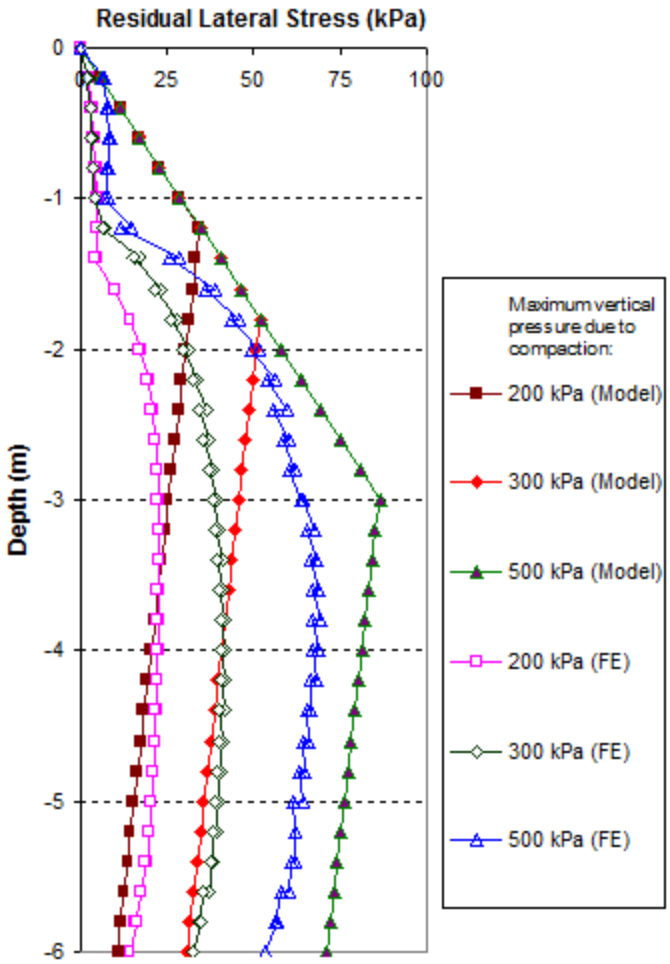

1 m = 3.28 ft
1 kPa = 0/145 psi

Figure 288. Graph. Comparison of residual lateral stresses of a GRS mass due to fill compaction between FE analysis with coarse mesh and the analytical model.

CHAPTER 7. SUMMARY AND CONCLUSIONS

7.1 SUMMARY

This study investigated the composite behavior of a GRS mass. It focused on the strength of a GRS mass, CIS in a GRS mass, the lateral deformation of a GRS wall with modular block facing, and the development of a rational design procedure for determining the required reinforcement strength of a GRS wall by considering both lateral stresses in the fill and lateral wall deformation of the wall system.

The following tasks were carried out:

- Reviewed previous studies on composite behavior of a GRS mass and CIS in an unreinforced soil mass and a GRS mass.

- Designed a GSGC test for investigating the composite behavior of a GRS mass and conducted five GSGC tests with well-controlled conditions and extensive instrumentation to monitor behavior under different reinforcement spacing, reinforcement strength, and confining pressure.

- Developed an analytical model for the relationship between reinforcement strength and reinforcement spacing and derived an equation for calculating composite strength properties.

- Developed a hand computation analytical model for simulation of CIS in a GRS mass.

- Performed FE analyses to simulate the GSGC tests, generate additional data (with different confining pressures) for verifying the analytical models in this study, and investigate the behavior of GRS composites.

- Verified the analytical models using measured data from the GSGC tests, relevant test data available in the literature, and FE analyses.

- Developed an analytical model for predicting lateral movement of GRS walls with modular block facing.

7.2 FINDINGS AND CONCLUSIONS

The findings and conclusions of this study are as follows:

- The results of the GSGC tests were consistent and appear very reliable. The tests provide direct observation of the behavior of a GRS mass as related to reinforcement strength and spacing. The tests also provide a better understanding of the composite behavior of a GRS mass and can be used for validation of analytical models in this study and other models of GRS structures in the future.

- An equation describing the relative effects of reinforcement spacing and reinforcement strength was developed and verified. Based on the equation, the required reinforcement strength in a GRS wall can be determined, as can the composite strength properties and ultimate pressure carrying capacity of a GRS mass.

- An analytical model for calculating lateral deformation of a GRS wall with modular block facing was developed and verified. The required tensile strength of reinforcement in design can be determined for a prescribed value of the maximum allowable lateral movement of a wall.

- An analytical model for simulating compaction operation of a GRS mass was developed. The model allows CIS in the fill to be determined.

- The presence of geosynthetic reinforcement has a tendency to suppress dilation of the surrounding soil and reduce the angle of dilation of the soil mass. The dilation behavior offers a new explanation of the reinforcing mechanism, and the angle of dilation provides a quantitative measure of the degree of reinforcing effect of a GRS mass.

REFERENCES

1. Adams, M., Nicks, J., Stabile, T., Wu, J., Schlatter, W., and Hartmann, J. (2012). *Geosynthetic Reinforced Soil Integrated Bridge System Interim Implementation Guide*, Report No. FHWA-HRT-11-026, Federal Highway Administration, Washington, DC.

2. Wu, J.T.H. (1994). *Design and Construction of Low Cost Retaining Walls: The Next Generation in Technology*, Report No. CTI-UCD-1-94, Colorado Transportation Institute, Denver, CO.

3. Holtz, R.D., Christopher, B.R., and Berg, R. (1997). *Geosynthetic Engineering*, BiTech Publishers, Ltd., Richmond, BC.

4. Bathurst R.J., Cai, Z., Alfaro, M., and Pelletier, M. (1997). "Seismic Design Issues for Geosynthetic Reinforced Segmental Retaining Walls," *Proceedings of the International Symposium on Mechanically Stabilized Backfill*, J.T.H. Wu (Ed.), Balkema, Rotterdam, Netherlands.

5. Wu, J.T.H. (2001). *Revising the AASHTO Guidelines for Design and Construction of GRS Walls*, Report No. CDOT-DTD-R-2001-6, Colorado Department of Transportation, Denver, CO.

6. Adams, M.T. (1997). "Performance of a Prestrained Geosynthetic Reinforced Soil Bridge Pier," *Proceedings of the International Symposium on Mechanically Stabilized Backfill*, J.T.H. Wu (Ed.), Balkema, Rotterdam, Netherlands.

7. Adams, M.T., Ketchart, K., and Wu, J.T.H. (2007). "Mini Pier Experiments: Geosynthetic Reinforcement Spacing and Strength as Related to Performance," *Proceedings of Geo-Denver 2007*, American Society of Civil Engineers, Denver, CO.

8. Rowe, P.W. (1954). "A Stress-Strain Theory for Cohesionless Soil with Applications to Earth Pressures at Rest and Moving Walls," *Geotechnique*, *4*(2), 70–88, Institution of Civil Engineers, London, United Kingdom.

9. Broms, B. (1971). "Lateral Earth Pressure Due to Compaction of Cohesionless Soils," *Proceedings, 4th Budapest Conference on Soil Mechanics and Foundation Engineering*, 373–384, Akademiai Kiado, Budapest.

10. Aggour, M.S. and Brown, C.B. (1974). "The Prediction of Earth Pressure on Retaining Walls Due to Compaction," *Geotechnique*, *24*(4), 489–502, Institution of Civil Engineers, London, United Kingdom.

11. Seed, R.M. (1983). *Compaction-Induced Stresses and Deflections on Earth Structure*, PhD Thesis, University of California, Berkeley, CA.

12. Duncan, J.M. and Seed, R.M. (1986). "Compaction-Induced Earth Pressures Under K_o-Conditions," *Journal of Geotechnical Engineering*, *112*(1), 1–22, American Society of Civil Engineers, Reston, VA.

13. Duncan, J.M., Williams, G.W., Sehn, A.L., and Seed R.M. (1991). "Estimation Earth Pressures Due to Compaction," *Journal of Geotechnical Engineering*, *117*(12), 1833–1847, American Society of Civil Engineers, Reston, VA.

14. Duncan, J.M., Williams, G.W., Sehn, A.L., and Seed R.M. (1993). "Closure to Estimation Earth Pressures Due to Compaction," *Journal of Geotechnical Engineering*, *119*(7), 1172–1177, American Society of Civil Engineers, Reston, VA.

15. Katona, M.G. (1978). "The Analysis of Long Span Culverts by the Finite Element Method," *Transportation Research Record 678*, 59–66, Transportation Research Board, Washington, DC.

16. Hatami, K. and Bathurst, R.J. (2005). "Development and Verification of a Numerical Model for the Analysis of Geosynthetic Reinforced-Soil Segment Walls," *Canadian Geotechnical Journal*, *42*(4), 1066–1085, NRC Research Press, Ottawa, ON.

17. Hatami K. and Bathurst R.J. (2006). "Numerical Model for Reinforced Soil Segmental Walls Under Surcharge Loading," *Journal of Geotechnical and Geoenvironmental Engineering*, *132*(6), 673–684, American Society of Civil Engineers, Reston, VA.

18. Morrison, K.F., Harrison, F.E., Collin, J.G., Dodds, A., and Arndt, B. (2006). *Shored Mechanically Stabilized Earth (SMSE) Wall Systems Design Guidelines*, Report No. FHWA-CFL/TD-06-001, Federal Highway Administration, Lakewood, CO.

19. Jewell, R.A. and Milligan, G.W. (1989). "Deformation Calculation for Reinforced Soil Walls," *International Conference on Soil Mechanics and Foundation Engineering*, 1259–1262.

20. Ketchart, K. and Wu, J.T.H. (2001). *Performance Test for Geosynthetic Reinforced Soil Including Effects of Preloading*, Report No. FHWA-RD-01-018, Federal Highway Administration, Washington, DC.

21. Yang, Z. (1972). *Strength and Deformation Characteristics of Reinforced Sand*, PhD. Thesis, University of California at Los Angeles, Los Angeles, CA.

22. Yang, Z. and Singh, A. (1974). *Strength and Deformation Characteristics of Reinforced Sand*, International Meeting on Water Resources Engineering, Los Angeles, CA.

23. Ingold, T.S. (1982). *Reinforced Earth*, Thomas Telford Ltd., London, United Kingdom.

24. Athanasopoulos, G.A. (1994). "On the Enhanced Confining Pressure Approach to the Mechanics of Reinforced Soil," *Geotechnical and Geological Engineering 12*, 122–132, Springer, Netherlands.

25. Schlosser, F. and Long, N.T. (1974). "Recent Results in French Research on Reinforced Earth," *Journal of Construction Division*, *100*, 223–237, American Society of Civil Engineers, Reston, VA.

26. Hausmann, M.R. (1976). "Strength of Reinforced Earth," *ARRB Proceedings, 8*, ARRB Group, Melbourne, Australia.

27. Gray, D.H. and Ohashi, H. (1983). "Mechanics of Fiber Reinforcement in Sand," *Journal of Geotechnical Engineering*, *109*, 335–353, American Society of Civil Engineers, Reston, VA.

28. Maher, M.H. and Woods, R.D. (1990). "Dynamic Response of Sand Reinforced with Randomly Distributed Fibers," *Journal of Geotechnical Engineering*, *116*, 1116–1131, American Society of Civil Engineers, Reston VA.

29. Athanasopoulos, G.A. (1993). "Effect of Particle Size on the Mechanical Behavior of Sand-Geotextile Composite," *Geotextiles and Geomembranes*, *12*, 255–273, International Geosynthetics Society, West Palm Beach, FL.

30. Elton, D.J. and Patawaran, M.A.B. (2004). "Mechanically Stabilized Earth Reinforcement Tensile Strength from Tests of Geotextile-Reinforced Soil," *Journal of the Transportation Research Board 1868*, 81–88, National Research Council, Washington, DC.

31. Elton, D.J. and Patawaran, M.A.B. (2005). *Mechanically Stabilized Earth (MSE) Reinforcement Tensile Strength from Tests of Geotextile Reinforced Soil*, Report to the Alabama Highway Research Center, Auburn University, Auburn, AL.

32. Bassett, A.K. and Last, N.C. (1978). "Reinforcing Earth Below Footings and Embankments," *Proceedings of the ASCE Spring Convention and Exhibit*, Pittsburgh, PA.

33. Broms, B. (1977). "Triaxial Tests with Fabric-Reinforced Soil," *Proceedings of the International Conference on the Use of Fabric in Geotechnics*, *3*, 129–134, Paris, France.

34. Gray, D.H. and Al-Refeai, T.O. (1986). "Behavior of Fabric- Versus Fiber-Reinforced Sand," *Journal of Geotechnical Engineering Division*, *112*(GT8), 804–820, American Society of Civil Engineers, Reston, VA.

35. Ziegler, M., Heerten, G., and Ruiken. G. (2008). *Progress in the Understanding of Geosynthetic/Soil Composite Material Behaviour in Geosynthetic Reinforced Earth Structures*, Presented at The First Pan American Geosynthetics Conference and Exhibition, Cancun, Mexico.

36. Lee, W.F. (2000). *Internal Stability Analyses of Geosynthetic Reinforced Retaining Walls*, Ph.D. Thesis, University of Washington, Seattle, WA.

37. Chen, T.C, Chen, R.H, and Lin, S.S. (2000). "A Nonlinear Homogenized Model Applicable to Reinforced Soil Analysis," *Geotextile and Geomembranes*, *18*, 349–366, International Geosynthetics Society, West Palm Beach, FL.

38. Holtz, R.D. and Lee, W.F. (2002). *Internal Stability Analyses of Geosynthetic Reinforced Retaining Walls*, Report No. WA-RD 532.1, Washington State Department of Transportation, Olympia, WA.

39. Zhang, M.X., Javadi, A.A., Lai, Y.M., and Sun, J. (2006). "Analysis of Geosynthetic Reinforced Soil Structures with Orthogonal Anisotropy," *Geotechnical and Geological Engineering*, *24*, 903–917, Springer, Netherlands.

40. Vulova, C. and Leshchinsky, D. (2003). *Effect of Geosynthetic Reinforcement Spacing on the Performance of Mechanically Stabilized Earth Walls*, Report No. FHWA-RD-03-048, Federal Highway Administration, McLean, VA.

41. Itasca International, Inc. (1998). *FLAC3D, Fast Lagrangian Analysis of Continua in 3 Dimensions*, Version 3.40, Arlington, VA.

42. Terzaghi, K. (1943). "Large Retaining Wall Tests (I): Pressure of Dry Sand," *Engineering News Record*, *112*, 136–140, McGraw Hill Construction, New York, NY.

43. Seed, R.M. and Duncan, J.M. (1986). "FE Analyses: Compaction-Induced Stresses and Deformations," *Journal of Geotechnical Engineering*, *112*(1), 23–43, American Society of Civil Engineers, Reston, VA.

44. Schmidt, B. (1967). "Lateral Stresses in Uniaxial Strain," *Bulletin No. 23*, 5–12, Danish Geotechnical Institute, Copenhagen, Denmark.

45. Ingold, T.S. (1979). "The Effect of Compaction on Retaining Walls," *Geotechnique*, *29*(3), 265–283, Institution of Civil Engineers, London, United Kingdom.

46. Ehrlich, M. and Mitchell, J.K. (1994). "Working Stress Design Method for Reinforced Soil Walls," *Journal of Geotechnical Engineering*, *120*(4), 625–645, American Society of Civil Engineers, Reston, VA.

47. Jaky, J. (1944). "The Coefficient of Earth Pressure at Rest," *Journal of the Society of Hungarian Architects and Engineering*, 355–358, Budapest, Hungary.

48. Gotteland, P., Gourc, J.P., and Villard, P. (1997). "Geosynthetics Reinforced Structures as Bridge Abutments: Full Scale Experimentation and Comparison with Modelisations," *Mechanically Stabilized Backfill*, J.T.H. Wu (Ed.), 25–34, A.A. Balkema, Rotterdam, Netherlands.

49. Tatsuoka, F. (1993). "Roles of Facing Rigidity in Soil Reinforcing," *Earth Reinforcement Practice*, Ochiai, Hayashi, and Otani (Eds.), 831–867, A.A. Balkema, Rotterdam, Netherlands.

50. Rowe, R.K. and Ho, S.K. (1998). "Horizontal Deformation in Reinforced Soil Walls," *Canadian Geotechnical Journal*, *35*, 312–327, NRC Research Press, Ottawa, ON.

51. Helwany, M.B., Tatsuoka, F., Tateyama, M., and Kojima, K. (1996). "Effects of Facing Rigidity on the Performance of Geosynthetic-Reinforced Soil Retaining Walls," *Soil and Foundations*, *36*(1), 27–38, Japanese Geotechnical Society, Tokyo, Japan.

52. Bathurst, R.J., Vlachopoulos, N., Walters, D.L., Burgess, P.G., and Allen, T.M. (2006). "The Influence of Facing Stiffness on the Performance of Two Geosynthetic Reinforced Soil Retaining Walls," *Canadian Geotechnical Journal*, *43*, 1225–1237.

53. Christopher, B.R., Gill, S.A., Giroud, J.P, Mitchell, J.K., Schlosser, F., and Dunnicliff J. (1989). *Reinforced Soil Structures Vol. 1: Design and Construction Guidelines*, Report No. FHWA-RD-89-043, Federal Highway Administration, Washington, DC.

54. Giroud, J.P. (1989). *Geotextile Engineering Workshop-Design Examples*, Report No. FHWA-HI-89-002, Federal Highway Administration, Washington, DC.

55. Macklin, P.M. (1994). *A Comparison of Five Methods for Calculation Lateral Deformation of Geosynthetic Reinforced Soil (GRS) Walls*, Master Thesis, University of Colorado at Denver, Denver, CO.

56. Jewell, R.A. (1988). "Reinforced Soil Wall Analysis and Behavior," *The Application of Polymeric Reinforcement in Soil Retaining Structures*, NATO Advanced Research Workshop, Kluwer, Netherlands.

57. Ho, S.K. and Rowe, R.K. (1997). "Effect of Wall Geometry on the Behavior of Reinforced Soil Walls," *Geotextiles and Geomembranes 14*, 521–541, International Geosynthetics Society, West Palm Beach, FL.

58. Rowe, R.K. and Ho, S.K. (1993). "Some Insights into Reinforced Wall Behavior on Finite Element Analysis," *Earth Reinforcement Practice*, Ochiai, Hayashi, and Otani (Eds.), 485–490, A.A. Balkema, Rotterdam, Netherlands.

59. American Association of State Highway and Transportation Officials. (2002). *Standard Specifications for Highway Bridges*, 17th Ed., Washington, DC.

60. Allen, T.M. and Bathurst, R.J. (2001). *Application of the K_o-Stiffness Method to Reinforced Soil Wall Limit State Design*, Final Research Report to Washington State Department of Transportation, Seattle, WA.

61. Jewell, R.A. (1990). *Strength and Deformation in Reinforced Soil Design*, Presented at the Fourth International Conference on Geotextiles, Geomembranes, and Related Products, The Hague, Netherlands.

62. Elias, V. and Christopher, B.R. (1996). *Mechanically Stabilized Earth Walls and Reinforced Soil Slope Design and Construction Guidelines*, Report No. FHWA-SA-96-071, Federal Highway Administration, Washington, DC.

63. Abramento, M. and Whittle, A.J. (1993). "Shear-Lag Analysis of Planar Soil Reinforcement in Plane-Strain Compression," *Journal of Engineering Mechanics*, *119*(2), 270–291, American Society of Civil Engineers, Reston, VA.

64. Huang, C. and Tatsuoka, F. "Bearing Capacity of Reinforced Horizontal Sandy Ground," *Geotextiles and Geomembranes*, *9*(1), 51–82, International Geosynthetics Society, West Palm Beach, FL.

65. Wu, J.T.H. (1992). "Measured Behavior of the Denver Walls," *International Symposium on Geosynthetic-Reinforced Soil Retaining Walls*, 31–41, A.A. Balkema, Rotterdam, Netherlands.

66. Wu, J.T.H. and Helwany, S. (2001). "Examining the Effects of Reinforcement in U.S. Forest Service Deep-Patch Landslide Repair Technique: Full-Scale Model Tests," *Transportation Research Record 1772*, 203–210, Transportation Research Board, Washington, DC.

67. Ketchart, K. and Wu, J.T.H. (2002). "A Modified Soil-Geosynthetic Interactive Performance Test for Evaluating Deformation Behavior of GRS Structures," *ASTM Geotechnical Testing Journal*, *25*(4), 405–413, ASTM International, West Conshohocken, PA.

68. Ketchart, K. and Wu, J.T.H. (1997). *Loading Test of a GRS Wall Reinforced with a AMOCO Geotextile*, Research Report, Department of Civil Engineering, University of Colorado at Denver, Denver, CO.

69. AASHTO M-145. (2008). *Standard Specification for Classification of Soils and Soil-Aggregate Mixtures for Highway Construction Purposes*, American Association of State Highway Transportation Officials, Washington, DC.

70. ASTM D2487. (2011). "Standard Practice for Classification of Soils for Engineering Purposes (Unified Soil Classification System)," *Annual Book of Standards Volume 4.08*, ASTM International, West Conshohocken, PA.

71. ASTM D4632. (2008). "Standard Test Method for Grab Breaking Load and Elongation of Geotextiles," *Annual Book of Standards Volume 4.13*, ASTM International, West Conshohocken, PA.

72. ASTM D4595. (2006). "Standard Test Method for Tensile Properties of Geotextiles by the Wide-Width Strip Method," *Annual Book of Standards Volume 4.13*, 40–50, ASTM International, West Conshohocken, PA.

73. ASTM D4833. (2007). "Standard Test Method for Index Puncture Resistance of Geomembranes and Related Products," *Annual Book of Standards Volume. 4.13*, ASTM International, West Conshohocken, PA.

74. ASTM D4533. (2011). "Standard Test Method for Trapezoid Tearing Strength of Geotextiles," *Annual Book of Standards Volume 4.13*, ASTM International, West Conshohocken, PA.

75. Wu, J.T.H. and Ketchart, K. (2008). *Investigating Failure of a Geosynthetic-Reinforced Soil Wall in Black Hawk, Colorado*, Presented at the Sixth International Conference on Case Histories in Geotechnical Engineering, Arlington, VA.

76. Wu, J.T.H., Lee, K.Z.Z., Helwany, S.B., and Ketchart, K. (2006). *Design and Construction Guidelines for GRS Bridge Abutment with a Flexible Facing*, Report No. 556, National Cooperative Highway Research Program, Washington, DC.

77. Westergaard, C.M. (1938). “A Problem of Elasticity Suggested by a Problem in Soil Mechanics: A Soft Material Reinforced by Numerous Strong Horizontal Sheet,” *Contributions to the Mechanics of Solids, Stephen Timoshenko 60th Anniversary Volume*, 268–277, Macmillan, New York, NY.

78. Hermann, L.R. and Al-Yassin, Z. (1978). “Numerical Analysis of Reinforced Soil Systems,” *ASCE Proceedings of the Symposium on Earth Reinforcement*, 428–457, Pittsburgh, PA.

79. Christopher, B.R., Leshchinsky, D., and Stulgis, R. (2005). “Geosynthetic-Reinforced Soil Walls and Slopes: US Perspective,” *GSP 141 International Perspectives on Soil Reinforcement Applications*, American Society of Civil Engineers, Reston, VA.

80. Morrison, K.F., Harrison, F.E., Collin, J.G., and Anderson, S.A. (2007). “Full-Scale Testing of a Shored Mechanically-Stabilized Earth (SMSE) Wall Employing Short Reinforcements,” *Proceedings of Geo-Denver 2007*, American Society of Civil Engineers, Denver CO.

81. PLAXIS. (2002). *Plaxis 2D—Version 8 Manual*, A.A. Balkema, Rotterdam, Netherlands.

82. Janbu, N. (1963). “Soil Compressibility as Determined by Oedometer and Triaxial Tests,” *Proceedings of ECSMFE I*, 19–25, Wiesbaden, Germany.

HRDI-40/07-13(WEB)E